ΕΘΝΙΚΟ ΜΕΤΣΟΒΙΟ ΠΟΛΥΤΕΧΝΕΙΟ

ΣΧΟΛΗ ΕΦΑΡΜΟΣΜΕΝΩΝ ΜΑΘΗΜΑΤΙΚΩΝ

ΚΑΙ ΦΥΣΙΚΩΝ ΕΠΙΣΤΗΜΩΝ

ΜΕΛΕΤΗ ΔΙΑΦΟΡΙΚΩΝ ΕΝΕΡΓΩΝ ΔΙΑΤΟΜΩΝ ΚΑΤΑΛΛΗΛΩΝ ΓΙΑ EBS ΚΑΙ NRA

ΔΙΔΑΚΤΟΡΙΚΗ ΔΙΑΤΡΙΒΗ

ΒΑΛΕΝΤΙΝΑ ΠΑΝΕΤΑ

Διπλωματούχος Σχολής Εφαρμοσμένων Μαθηματικών και Φυσικών Επιστημών, Ε.Μ.Π.
Μεταπτυχιακό Δίπλωμα Ειδίκευσης, Φυσική και Τεχνολογικές Εφαρμογές, Ε.Μ.Π.

.

ΑΘΗΝΑ, ΜΑΡΤΙΟΣ 2015

ΕΘΝΙΚΟ ΜΕΤΣΟΒΙΟ ΠΟΛΥΤΕΧΝΕΙΟ

ΣΧΟΛΗ ΕΦΑΡΜΟΣΜΕΝΩΝ ΜΑΘΗΜΑΤΙΚΩΝ

ΚΑΙ ΦΥΣΙΚΩΝ ΕΠΙΣΤΗΜΩΝ

ΜΕΛΕΤΗ ΔΙΑΦΟΡΙΚΩΝ ΕΝΕΡΓΩΝ ΔΙΑΤΟΜΩΝ ΚΑΤΑΛΛΗΛΩΝ ΓΙΑ EBS ΚΑΙ NRA

ΔΙΔΑΚΤΟΡΙΚΗ ΔΙΑΤΡΙΒΗ

ΒΑΛΕΝΤΙΝΑ ΠΑΝΕΤΑ

Διπλωματούχος Σχολής Εφαρμοσμένων Μαθηματικών και Φυσικών Επιστημών, Ε.Μ.Π.
Μεταπτυχιακό Δίπλωμα Ειδίκευσης, Φυσική και Τεχνολογικές Εφαρμογές, Ε.Μ.Π.

ΤΡΙΜΕΛΗΣ ΣΥΜΒΟΥΛΕΥΤΙΚΗ ΕΠΙΤΡΟΠΗ

1. Μ. Κόκκορης, Αναπλ. Καθ. ΕΜΠ (επιβλέπων)
2. Α. Λαγογιάννης, Ερευνητής Β΄ ΕΚΕΦΕ «Δημόκριτος»
3. A.F. Gurbich, Καθ. IPPE Obninsk, Ρωσία

ΕΠΤΑΜΕΛΗΣ ΣΥΜΒΟΥΛΕΥΤΙΚΗ ΕΠΙΤΡΟΠΗ

1. Μ. Κόκκορης, Αναπλ. Καθ. ΕΜΠ (επιβλέπων)
2. Α. Λαγογιάννης, Ερευνητής Β΄ ΕΚΕΦΕ «Δημόκριτος»
3. A.F. Gurbich, Καθ. IPPE Obninsk, Ρωσία
4. Ρ. Βλαστού-Ζάννη, Καθ. ΕΜΠ
5. Π. Μισαηλίδης, Καθ. ΑΠΘ
6. Ν. Πατρώνης, Επίκ. Καθ. Παν/μιο Ιωαννίνων
7. M. Chiari, Ερευνητής, INFN Firenze, Ιταλία

ΑΘΗΝΑ, ΜΑΡΤΙΟΣ 2015

NATIONAL TECHNICAL UNIVERSITY OF ATHENS

SCHOOL OF APPLIED MATHEMATICAL AND PHYSICAL SCIENCES

DEPARTMENT OF PHYSICS

STUDY OF DIFFERENTIAL CROSS SECTIONS SUITABLE FOR EBS AND NRA

DOCTORAL DISSERTATION

VALENTINA PANETA

Diploma, School of Applied Mathematical and Physical Sciences, N.T.U.A.
M.Sc., Physics and Technological Applications, N.T.U.A.

ATHENS 2015

NATIONAL TECHNICAL UNIVERSITY OF ATHENS

SCHOOL OF APPLIED MATHEMATICAL AND PHYSICAL SCIENCES

DEPARTMENT OF PHYSICS

STUDY OF DIFFERENTIAL CROSS SECTIONS SUITABLE FOR EBS AND NRA

DOCTORAL DISSERTATION

VALENTINA PANETA

Diploma, School of Applied Mathematical and Physical Sciences, N.T.U.A.
M.Sc., Physics and Technological Applications, N.T.U.A.

ADVISORY COMMITTEE

1. M. Kokkoris,
   Assoc. Professor NTUA (supervisor)
2. A. Lagoyannis,
   Researcher, NCSR "Demokritos"
3. A.F. Gurbich, Professor IPPE Obninsk

EXAMINATION COMMITTEE

1. M. Kokkoris,
   Assoc. Professor NTUA (supervisor)
2. A. Lagoyannis, Researcher,
   NCSR "Demokritos"
3. A.F. Gurbich, Professor IPPE Obninsk
4. R. Vlastou-Zanni, Professor NTUA
5. P. Misaelides, Professor AUTh
6. N.Patronis, Assist. Professor UoI
7. M. Chiari, Researcher, INFN, Firenze

ATHENS, MARCH 2015

στον πατέρα μου…

ACKNOWLEDGMENTS

First of all, I would like to express my deepest appreciation and gratitude to my supervisor Associate Professor Michael Kokkoris and to Researcher Anastasios Lagoyannis for their valuable guidance and constant encouragement throughout the course of this study. For their continuous support, trust and dedicated involvement in every step of the way, I am indeed truly thankful.

I would also like to express my gratitude to Professor Alexander F. Gurbich, whose contribution in the preparation of this dissertation both in the experimental and theoretical parts has been more than enlightening and valuable. The constructive discussions with Professor Roza Vlastou-Zanni, along with her constant encouraging, have been of vital importance and for that I am deeply thankful.

The overall interaction I had with all the above has been a source of inspiration and motivation throughout all these years.

Moreover, I would like to express my deep appreciation to Principal Researcher Massimo Chiari for his interest and support, and also to Assistant Professor Nikolas Patronis and Professor Panagiotis Misaelides for their constructive contributions. Also to Dr Sotirios Harissopulos, Head of the Tandem laboratory and I.N.P.P. for his vision and inspiration. Part of the experimental work was carried out in Surrey and my sincere gratitude goes to Principal Researcher Chris Jeynes and Post Doc Research Associate Julien Coloaux for their fruitful collaboration and hospitality in their laboratory.

I would also like to especially thank Post Doc Research Associate Michael Axiotis for his valuable help and support in the Tandem laboratory, where along with all the members of the group, including the technicians, the best working “office” was formed. I am truly thankful for the scientific and moral support of Drs. George Provatas, Varvara Foteinou and Vicky Kantarellou and also for the most valuable technical contribution of Miltiades Andrianes, during the experimental runs at “Demokritos”.

My deep gratitude also goes to my friends Mary Diakaki, Froso Androulakaki and George Eleftheriou, who worked with me at NTUA all these years, with mutual support and care. I am truly thankful for their friendship and constant encouragement, while their help and constructive

discussions, along with the contribution of all the members of the “NTUA group” are highly appreciated.

The NTUA group along with the one at Demokritos constituted a model of team work and collaboration in the friendliest and warmest atmosphere.

Finally, I would like to thank and express my deepest gratitude to my friends, my people, my family. For their support and patience. For always being there for me.

CONTENTS

ΠΕΡΙΛΗΨΗ

Η ανάλυση δειγμάτων χρησιμοποιώντας δέσμη φορτισμένων σωματιδίων (Ion Beam Analysis –IBA) αποτελεί τη λιγότερο (σχεδόν καθόλου) καταστροφική μέθοδο που χρησιμοποιείται για την μελέτη της επιφανειακής σύνθεσης για την εύρεση του προφίλ της επιφανειακής κατανομής ενός στοιχείου σε ένα δείγμα και βρίσκει σήμερα μεγάλες και διαρκώς διευρυνόμενες εφαρμογές σε θέματα υψηλής τεχνολογίας, βιομηχανικών εφαρμογών, αλλά και γεωλογίας, πολιτιστικής κληρονομιάς και περιβάλλοντος.

Οι πυρηνικές τεχνικές που χρησιμοποιούνται στο πεδίο αυτό, βασίζονται στην ανίχνευση των σωματιδίων ή της ακτινοβολίας που προκύπτει μετά την αλληλεπίδραση των σωματιδίων της δέσμης με τα άτομα και τους πυρήνες του υπό μελέτη στόχου. Συγκεκριμένα, για την ποσοτική ανάλυση ελαφρών στοιχείων, που αποτελεί το μεγαλύτερο πρόβλημα για όλες τις τεχνικές, χρησιμοποιείται κυρίως η φασματοσκοπία ελαστικής οπισθοσκέδασης (EBS – Elastic Backscattering Spectrometry) και η μέθοδος πυρηνικών αντιδράσεων (NRA – Nuclear Reaction Analysis), ανάλογα με την αντίδραση που μελετάται. Για την υλοποίηση των τεχνικών αυτών είναι απαραίτητη η χρήση της διαφορικής ενεργού διατομής της υπό μελέτη αντίδρασης. Δεδομένου όμως ότι, για τις τυπικές ενέργειες των σωματιδίων που προέρχονται από επιταχυντές, δεν υπάρχει αναλυτικός τρόπος να υπολογιστούν θεωρητικά οι αντίστοιχες ενεργές διατομές ειδικά στην περίπτωση που ο στόχος αποτελείται από ελαφρά στοιχεία, η ανάλυση βασίζεται στα αντίστοιχα πειραματικά δεδομένα που υπάρχουν στη βιβλιογραφία. Σε πολλές περιπτώσεις όμως τα δεδομένα αυτά παρουσιάζουν σημαντικές διαφορές μεταξύ τους ή/και είναι πολύ αραιά σε ενεργειακά βήματα. Είναι σαφές ότι οι πιο αξιόπιστες τιμές διαφορικών ενεργών διατομών που μπορούν να χρησιμοποιηθούν για εφαρμογές υψηλής ακρίβειας είναι αυτές που προκύπτουν από θεωρητικούς υπολογισμούς και μοντέλα, βασισμένα πάνω σε υπάρχοντα ακριβή πειραματικά δεδομένα σε μεγάλο εύρος ενεργειών και γωνιών ανίχνευσης (φαινομενολογική προσέγγιση, evaluation). Τέτοια δεδομένα όμως είναι διαθέσιμα για περιορισμένες αντιδράσεις και αφορούν γενικά ένα μικρό εύρος ενεργειών.

Η συμβολή της παρούσας διατριβής στο πεδίο αυτό απαρτίζεται από τρία μέρη. Το πρώτο αφορά τον πειραματικό προσδιορισμό διαφορικών ενεργών διατομών για τις παρακάτω πυρηνικές αντιδράσεις, που αποτελούν χαρακτηριστικές περιπτώσεις όπου παρουσιάζονται ελλείψεις ή/και σημαντικές διαφορές στα αντίστοιχα δεδομένα στη βιβλιογραφία για την υλοποίηση των αντίστοιχων EBS και NRA τεχνικών:

- $^{7}Li(p,p_0)^{7}Li$, $^{7}Li(p,p_1)^{7}Li$, $^{7}Li(p,\alpha_0)^{4}He$ και $^{19}F(p,p_0)^{19}F$,$^{19}F(p,\alpha_0)^{16}O$, $^{19}F(p,\alpha_{1,2})^{16}O$ σε ενεργειακό εύρος 1.5–7 MeV και σε αρκετές γωνίες οπισθοσκέδασης.
- $^{nat}Mg(d,d_0)$, $^{24}Mg(d,p_0,p_1,p_2)^{25}Mg$ σε ενεργειακό εύρος 1300–2050 keV και σε αρκετές γωνίες σκέδασης.

Στο δεύτερο μέρος παρουσιάζεται η μεθοδολογία που αναπτύχθηκε στα πλαίσια της παρούσας εργασίας για τον έλεγχο της αξιοπιστίας των διαφορικών ενεργών διατομών (benchmarking), καθώς και η υλοποίησή της στον έλεγχο των προσδιορισμένων τιμών των παραπάνω αντιδράσεων, αλλά και των ενεργών διατομών για άλλες σημαντικές επιλεγμένες πυρηνικές αντιδράσεις (αναφέρονται παρακάτω). Η διαδικασία αυτή είναι πολύ σημαντική για τον πρόσθετο λόγο ότι παρέχει πληροφορίες για την κατάλληλη ρύθμιση των παραμέτρων που χρησιμοποιούνται στα θεωρητικά πρότυπα για την αναπαραγωγή των διαφορικών ενεργών διατομών, ενώ παράλληλα επιτρέπει την επέκταση των θεωρητικών αναλύσεων σε μεγαλύτερο ενεργειακό εύρος. Επίσης επιτρέπει την απόδοση ρεαλιστικών αβεβαιοτήτων (σφαλμάτων) στις υπολογιζόμενες ενεργές διατομές.

Το τρίτο μέρος της διατριβής αφορά τη φαινομενολογική προσέγγιση (στα πλαίσια της θεωρίας R-matrix) για τον υπολογισμό διαφορικών ενεργών διατομών, καθώς και την εφαρμογή της διαδικασίας υπολογισμού στην περίπτωση της ελαστικής σκέδασης πρωτονίων από πυρήνες ^{19}F με τη χρήση του κώδικα AZURE.

Πιο αναλυτικά, η παρούσα εργασία είναι δομημένη σε 3 αντίστοιχες ενότητες, που συμπληρώνονται από το θεωρητικό υπόβαθρο που τις πλαισιώνει.

1. Θεωρητικό υπόβαθρο

Στα θεμελιώδη στοιχεία της Ion Beam Analysis περιλαμβάνεται το αντίστοιχο θεωρητικό υπόβαθρο για τους μηχανισμούς αντίδρασης των φορτισμένων σωματιδίων με τα άτομα και τους πυρήνες του στόχου και τη θεωρία σκέδασης, αλλά και τα αντίστοιχα στοιχεία φασματοσκοπίας. Η υλοποίηση των τεχνικών EBS (Elastic Backscattering Spectroscopy – Φασματοσκοπία ελαστικής σκέδασης) και NRA (Nuclear Reaction Analysis – Ανάλυση πυρηνικών αντιδράσεων) βασίζεται στον ανιχνευόμενο αριθμό σωματιδίων (στο καταγραφόμενο φάσμα) που, μεταξύ των άλλων (όπως θα φανεί παρακάτω), εξαρτάται κυρίως από τις αντίστοιχες ενεργές διατομές.

Ξεκινώντας όμως από την αρχή της αλληλεπίδρασης, από τη στιγμή δηλαδή που η δέσμη προσπίπτει στο στόχο, τέσσερα σημαντικά φαινόμενα λαμβάνουν χώρα και πρέπει να ληφθούν υπόψη. Αρχικά, τα σωματίδια της δέσμης χάνουν ενέργεια όσο διαπερνούν το στόχο, αλληλεπιδρώντας με τα άτομά του (κυρίως με το ηλεκτρονιακό νέφος), μέχρι να αλληλεπιδράσουν με κάποιον πυρήνα. Η απώλεια ενέργειας της δέσμης μέσα στον στόχο (ισχύς ανάσχεσης - stopping power S και stopping cross section ε) οδηγεί στην αντίληψη του βάθους-πάχους του στόχου και γενικά προσεγγίζεται θεωρητικά από τη γνωστή σχέση Bethe-Bloch, ενώ οι στατιστικές διακυμάνσεις του φαινομένου αυτού οδηγούν στον ενεργειακό διασκεδασμό (energy straggling) της δέσμης που σε συνδυασμό με άλλες πειραματικές παραμέτρους, όπως η διακριτική ικανότητα του ανιχνευτή, θέτει περιορισμούς στην επιτεύξιμη διακριτική ικανότητα ανάλυσης μαζών και βάθους. Η αλληλεπίδραση, τέλος, ενός σωματιδίου της δέσμης με έναν

πυρήνα του στόχου και η ανίχνευση του αντίστοιχου εξερχόμενου/εκπεμπόμενου σωματιδίου (ή ακτινοβολίας) εξαρτάται από την πιθανότητα να συμβεί η συγκεκριμένη αντίδραση (διαφορική ενεργός διατομή $\frac{d\sigma}{d\Omega}$) επιτρέποντας μας να αναλύουμε ποσοτικά ένα στόχο. Η ενέργεια του εξερχόμενου σωματιδίου εξαρτάται βέβαια από την κινηματική της αντίδρασης (παράγοντας K) για την ελαστική σκέδαση, αλλά και τη διαφορά μαζών (Q-value) στην περίπτωση πυρηνικής αντίδρασης, ενώ η τελική ενέργεια των σωματιδίων που φτάνουν στον ανιχνευτή εξαρτάται και από την επιπρόσθετη απώλεια ενέργειας διασχίζοντας το στόχο από το σημείο (βάθος) της αντίδρασης «πίσω» προς τον ανιχνευτή.

Τα ανιχνευόμενα σωματίδια καταγράφονται με τη βοήθεια των κατάλληλων ηλεκτρονικών μονάδων σε ένα φάσμα, ανάλογα με την ενέργεια τους (αντιστοιχία σε κανάλι, energy interval – channel). Όπως φαίνεται στο Σχήμα 1.1, οι τεχνικές EBS και NRA βασίζονται ακριβώς στην ανάλυση και τη συσχέτιση του ύψους του φάσματος H (height) ή Y (yield) σε κάθε ενέργεια με το αντίστοιχο στρώμα του στόχου που έχει πάχος τ και αριθμό ατόμων ανά επιφάνεια Nt σε βάθος x, από όπου εκπέμπονται τα αντίστοιχα σωματίδια. Το ύψος αυτό (counts/channel) στην περίπτωση ενός μονοστοιχειακού στρώματος κοντά στην επιφάνεια του στόχου, που αντιστοιχεί σε ανιχνευόμενα σωματίδια ενέργειας E_1, δίνεται από την απλοποιημένη σχέση 1.1 [4]. όπου Q είναι ο αριθμός των σωματιδίων της δέσμης που προσπίπτουν στο στόχο (φορτίο), Ω είναι η στερεά γωνία ανίχνευσης, E η ενέργεια των σωματιδίων της δέσμης ακριβώς πριν τη σκέδαση/αντίδραση στο βάθος με συνολική απώλεια ενέργειας $[\varepsilon(E)]$, δE το ενεργειακό εύρος ενός καναλιού και θ_1 η γωνία πρόσπτωσης της δέσμης. Η ολοκληρωμένη περιγραφή του ύψους του φάσματος στην ενέργεια E_1 δίνεται από τη σχέση 1.2 [65], συμπεριλαμβάνοντας και την ενεργειακή κατανομή της δέσμης από τον επιταχυντή $g(E',E_0)$ γύρω από τη μέση ενέργεια E_0, την απώλεια ενέργειας στο στόχο Δ και τον ενεργειακό διασκεδασμό $W(E,E',E'')$.

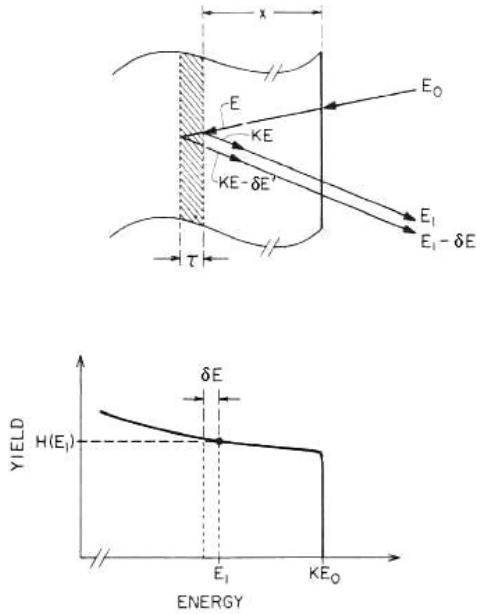

Σχήμα 1.1: Οπισθοσκέδαση στο βάθος x ενός μονοστοιχειακού στόχου και το αντίστοιχο καταγραφόμενο φάσμα [4].

$$H(E_1) = \frac{d\sigma}{d\Omega}(E,\theta)Q\Omega\frac{\delta E}{[\varepsilon(E)]cos\theta_1} \quad 1.1$$

$$H(E_1) = \int_{E_0-\Delta}^{E_0}\int_0^{\infty}\int_0^{\infty}\frac{d\sigma}{d\Omega}(E'',\theta)Q\Omega\frac{\delta E}{[\varepsilon(E'')]cos\theta_1}g(E',E_0)W(E,E',E'')dE''dE'dE \quad 1.2$$

Η αλληλεπίδραση των φορτισμένων σωματιδίων της δέσμης με τους πυρήνες του στόχου εξελίσσεται σταδιακά, ανάλογα την κάθε περίπτωση, και μπορεί να αποτελείται από διάφορους μηχανισμούς αντίδρασης που συνδέονται χρονικά, όπως απεικονίζεται στο Σχήμα 1.2 που ακολουθεί. Μετά την πρώτη αλληλεπίδραση, όπως φαίνεται στο Σχήμα 1.2, το βλήμα μπορεί να διαφύγει αμέσως (μέσα σε ~10^{-22} s) μέσω μιας άμεσης (direct) αντίδρασης, ή να αλληλεπιδράσει με ένα νουκλεόνιο του πυρήνα ξεκινώντας μια αλληλουχία αλληλεπιδράσεων (cascade) νουκλεονίου-νουκλεονίου, από όπου (κατάσταση προ-ισορροπίας) μπορεί να συμβεί εκπομπή σωματιδίου (pre-compound emission). Κατά τη διάρκεια του cascade η ενέργεια μοιράζεται σε όλο και περισσότερα νουκλεόνια μέχρι το σχηματισμό του σύνθετου πυρήνα (compound nucleus), ο οποίος αποδιεγείρεται τελικά μέσω των επιτρεπόμενων (ενεργειακά) καναλιών. Η συνεισφορά του κάθε μηχανισμού αντίδρασης εξαρτάται από το είδος και την ενέργεια των φορτισμένων σωματιδίων της δέσμης και τον εκάστοτε πυρήνα.

Ο συνδυασμός της άμεσης ελαστικής σκέδασης (shape elastic ή potential scattering) με την compound ελαστική σκέδαση δίνει την πιθανότητα, δηλαδή την ενεργό διατομή, της ελαστικής σκέδασης, ενώ τα υπόλοιπα ανελαστικά κανάλια δίνουν τις αντίστοιχες ανελαστικές ενεργές διατομές.

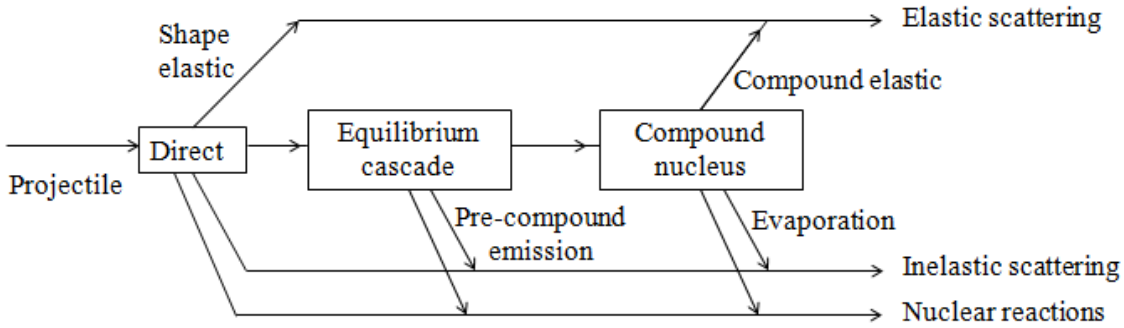

Σχήμα 1.2: Μηχανισμοί αντίδρασης των σωματιδίων της δέσμης με τους πυρήνες του στόχου [1].

Μόνο στην περίπτωση σκέδασης Rutherford (άμεση αντίδραση – σκέδαση δυναμικού) μπορεί να υπολογιστεί αναλυτικά η διαφορική ενεργός διατομή χρησιμοποιώντας τον αντίστοιχο τύπο του Rutherford. Για τη μελέτη όμως ελαφρών στοιχείων, που είναι το αντικείμενο της παρούσας εργασίας, και για τις τυπικές ενέργειες των σωματιδίων που

προέρχονται από επιταχυντές, η διαφορική ενεργός διατομή ελαστικής σκέδασης δεν ακολουθεί την σχέση του Rutherford, λόγω της συνεισφοράς του μηχανισμού σύνθετου πυρήνα και πρέπει να προσδιοριστεί, όπως και οι ανελαστικές ενεργές διατομές, για κάθε συνδυασμό δέσμης-πυρήνα, καθώς και για κάθε ενέργεια δέσμης και γωνίας ανίχνευσης για την υλοποίηση της αντίστοιχης τεχνικής EBS ή/και NRA. Οι διαφορικές ενεργές διατομές αυτές μπορούν να προσδιοριστούν πειραματικά, αλλά και με θεωρητικούς υπολογισμούς που βασίζονται σε πρότερη πειραματική μελέτη (φαινομενολογία).

Οι υπόλοιποι παράγοντες στις σχέσεις 1.1 και 1.2, δηλαδή ο παράγοντας QΩ, η απώλεια ενέργειας στο στόχο και το εύρος δE, μπορούν να προσδιοριστούν ή να υπολογιστούν με σχετικά αρκετά καλή ακρίβεια. Η υλοποίηση και η αξιοπιστία άρα των τεχνικών EBS και NRA εξαρτάται τελικά κυρίως από τη διαθεσιμότητα και την ακρίβεια της διαφορικής ενεργού διατομής της μελετούμενης αντίδρασης.

2. Μετρήσεις διαφορικών ενεργών διατομών

Οι διαφορικές ενεργές διατομές ($\frac{d\sigma}{d\Omega}$) που υπολογίστηκαν στα πλαίσια της παρούσας διατριβής αφορούν τα συστήματα p+^{7}Li, p+^{19}F και d+^{nat}Mg και την εφαρμογή των αντίστοιχων IBA τεχνικών για την ποσοτικοποίηση και την κατά βάθος κατανομή του ^{7}Li, ^{19}F και ^{nat}Mg σε ένα υλικό. Τα στοιχεία αυτά, τα οποία χρησιμοποιούνται ευρέως σε τεχνολογικές και βιομηχανικές εφαρμογές, αλλά και για ερευνητικούς σκοπούς, παρουσιάζουν, όπως τα περισσότερα ελαφρά στοιχεία, μεγάλη δυσκολία ανίχνευσης και ποσοτικοποίησης εξαιτίας της συνύπαρξης τους με άλλα βαρύτερα στοιχεία σε πολύπλοκες μήτρες. Η χρήση των αντίστοιχων EBS και NRA τεχνικών (και ειδικά η συνδυασμένη/ταυτόχρονη εφαρμογή EBS και NRA ανάλυσης) είναι η πιο κατάλληλη σε αυτές τις περιπτώσεις. Για τα παραπάνω συστήματα όμως, τα διαθέσιμα πειραματικά δεδομένα στην υπάρχουσα βιβλιογραφία παρουσιάζουν μεγάλες ελλείψεις ή/και αποκλίσεις. Να σημειωθεί εδώ ότι για την περίπτωση της ελαστικής σκέδασης ^{19}F(p,p) υπάρχουν θεωρητικά-evaluated δεδομένα από το SigmaCalc [25] που φτάνουν μέχρι τα 1730 keV (ενέργεια δέσμης).

Η συμβολή της παρούσας εργασίας στο πεδίο αυτό έγκειται συγκεκριμένα στον πειραματικό προσδιορισμό διαφορικών ενεργών διατομών για τις εξής αντιδράσεις:

- ^{7}Li(p,p$_0$)^{7}Li, ^{7}Li(p,p$_1$)^{7}Li, ^{7}Li(p,α$_0$)^{4}He και ^{19}F(p,p$_0$)^{19}F,^{19}F(p,α$_0$)^{16}O, ^{19}F(p,α$_{1,2}$)^{16}O στο ενεργειακό εύρος 1500–7000 keV και γωνίες οπισθοσκέδασης 140°, 150°, 160° και 170°.
- ^{nat}Mg(d,d$_0$)^{nat}Mg, ^{24}Mg(d,p$_0$,p$_1$,p$_2$)^{25}Mg στο ενεργειακό εύρος 1300–2050 keV και γωνίες ανίχνευσης 55°, 70°, 90°, 125°, 140°, 150°, 160° και 170°.

Οι μετρήσεις πραγματοποιήθηκαν στο εργαστήριο του Ινστιτούτου Πυρηνικής και Σωματιδιακής Φυσικής του ΕΚΕΦΕ “Δημόκριτος” χρησιμοποιώντας τον επιταχυντή 5.5 MV

Tandem και την πειραματική γραμμή που καταλήγει στο θάλαμο σκέδασης με το γωνιόμετρο (διαμέτρου 70cm). Σε όλα τα πειράματα η δέσμη πρωτονίων από τον επιταχυντή προσπίπτει στο στόχο, ο οποίος είναι τοποθετημένος στο κέντρο του θαλάμου, με διάμετρο (beam size) ~2mm, ενώ τα εξερχόμενα σωματίδια από το στόχο ανιχνεύονται από ανιχνευτές πυριτίου (Silicon Surface Barrier) που τοποθετούνται γύρω από το στόχο στις επιθυμητές γωνίες ανίχνευσης, πάνω στο γωνιομετρικό τραπέζι, σε απόσταση τέτοια ώστε το γωνιακό άνοιγμά τους να είναι περίπου ±1°. Συγκεκριμένα, για τις μετρήσεις διαφορικών ενεργών διατομών για τα συστήματα $p+^{7}Li$, $p+^{19}F$ και $d+^{nat}Mg$, χρησιμοποιήθηκαν 4-6 ανιχνευτές Silicon Surface Barrier, με ενεργειακή διακριτική ικανότητα 15-20 keV και πάχος 300-1000μm. Οι στόχοι που χρησιμοποιήθηκαν κατασκευάστηκαν στο εργαστήριο με τη μέθοδο της εξάχνωσης και αποτελούνταν από ένα λεπτό στρώμα LiF πάνω σε ένα φύλλο άνθρακα για το πείραμα p+LiF και αντίστοιχα από ένα λεπτό στρώμα $Mg+MgCl_2$ πάνω σε φύλλο άνθρακα για τη μελέτη του μαγνησίου. Πάνω στους στόχους αυτούς εξαχνώθηκε επιπλέον ένα λεπτό στρώμα Au για την πρώτη μελέτη (LiF) κ αντίστοιχα ένα λεπτό στρώμα Ta για τη μελέτη του μαγνησίου με δευτέρια, για λόγους κανονικοποίησης, όπως φαίνεται στις παρακάτω σχέσεις για τον υπολογισμό των ενεργών διατομών.

Χρησιμοποιώντας λεπτό στόχο (δηλαδή στόχο που οδηγεί σε πολύ μικρή απώλεια ενέργειας (κάτω από ~4 keV) των σωματιδίων της δέσμης) ο αριθμός των ανιχνευόμενων σωματιδίων Y, εντός της στερεάς γωνίας ανίχνευσης Ω, από μια αντίδραση x στη γωνία θ, για ενέργεια δέσμης E, δίνεται από τη σχέση 2.1, σε αναλογία με την εξίσωση 1.1.

$$Y_x = \left(\frac{d\sigma}{d\Omega}\right)_x (Q\Omega) N_{t,x} \qquad 2.1$$

Το αντίστοιχο φάσμα που καταγράφεται αποτελείται από λεπτές κορυφές που αντιστοιχούν στα εξερχόμενα (ανιχνευόμενα) σωματίδια από όλες τις αντιδράσεις μέσα στο στόχο. Ολοκληρώνοντας (ή κάνοντας προσαρμογή (fit) αν χρειάζεται) την κορυφή που αντιστοιχεί στην αντίδραση υπό μελέτη (Y) και χαρακτηρίζοντας το στόχο (επιφανειακή πυκνότητα – πάχος στόχου N_t), η διαφορική ενεργός διατομή προσδιορίζεται από την σχέση 2.2, διαιρώντας την 2.1 με την αντίστοιχη σχέση για την σκέδαση στο βαρύ στοιχείο του στόχου (Au ή Ta) που υπολογίζεται από την σχέση του Rutherford.

$$\left(\frac{d\sigma}{d\Omega}\right)_x = \left(\frac{d\sigma}{d\Omega}\right)_{Au} \frac{Y_x}{Y_{Au}} \frac{N_{t,Au}}{N_{t,x}} \qquad 2.2$$

Μετά τη βαθμονόμηση του επιταχυντή σε όρους ενέργειας, η ενέργεια της δέσμης για κάθε μέτρηση προσδιορίζεται στο μέσο του στόχου, λαμβάνοντας υπόψη την απώλεια ενέργειας μέχρι το αντίστοιχο σημείο, όπως υπολογίζεται από το SRIM [5].

2.1 . Μελέτη p+^{7}Li και p+^{19}F

Από την κινηματική των υπό μελέτη αντιδράσεων, όλες οι κορυφές που έπρεπε να αναλυθούν στα φάσματα ήταν απομονωμένες, όπως φαίνεται στο τυπικό φάσμα του Σχήματος 2.1, σε όλο το ενεργειακό εύρος μελέτης, εκτός από ελάχιστες περιπτώσεις επικάλυψης κορυφών (π.χ. οι κορυφές από τις αντιδράσεις ^{7}Li(p,α_0)^{4}He και ^{19}F(p,α_0)^{16}O συμπίπτουν/επικαλύπτονται για ενέργειες πρωτονίων ~2550-2750 keV στις 150°), καθιστώντας αδύνατη την αντίστοιχη ανάλυση, αλλά και την περίπτωση των ^{19}F(p,α_1)^{16}O και ^{19}F(p,α_2)^{16}O αντιδράσεων. Οι κορυφές που προέρχονταν από τις δύο αυτές αντιδράσεις δεν ξεχώριζαν ικανοποιητικά στα φάσματα (οι αντίστοιχες ενεργειακές στάθμες του ^{16}O είναι στα 6049 και 6130 keV) με αποτέλεσμα την ανάλυση των δύο αυτών κορυφών ως μια, αντιστοιχώντας την στην αντίδραση ^{19}F(p,$\alpha_{1,2}$)^{16}O.

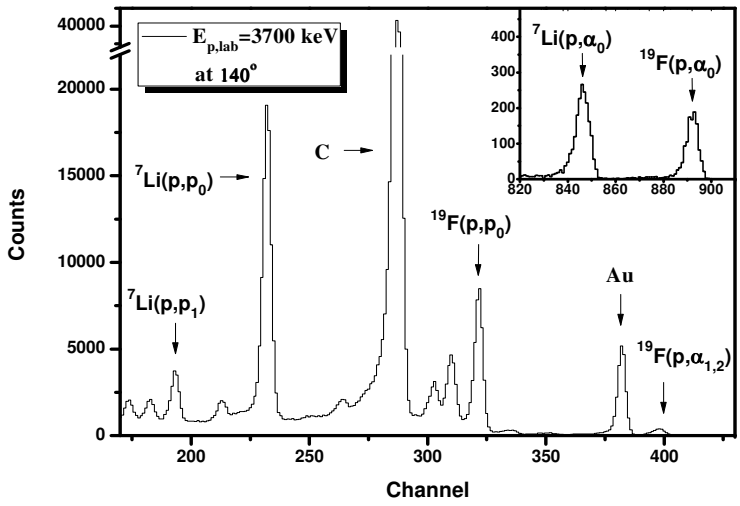

Σχήμα 2.1: Τυπικό πειραματικό φάσμα για $E_{p,lab}$= 3700 keV στις 140° μαζι με την αντίστοιχη αναγνώριση κορυφών.

Το πάχος του χρυσού στο στόχο LiF που χρησιμοποιήθηκε, προσδιορίστηκε με την τεχνική XRF (X-ray Fluorescence) και βρέθηκε ίσο με (4.4 ± 0.3) μg/cm^2, ενώ ο υπολογισμός του πάχους του ^{19}F βασίστηκε στα υπάρχοντα evaluated δεδομένα (SigmaCalc) για την ελαστική σκέδαση ^{19}F(p,p) για ενέργεια δέσμης 1600 keV στις 160°. Ο έλεγχος του στόχου μετά την εξάχνωση έδειξε ότι η στοιχειομετρία του παρέμεινε 1:1 σε LiF εντός 3%, όπως αναμενόταν, όποτε το πάχος του ^{7}Li θεωρήθηκε ίσο με αυτό του ^{19}F. Ο λόγος των παχών που χρησιμοποιήθηκε τελικά σε όλους τους υπολογισμούς ήταν ίδιος και ίσος με:

$$\frac{N_{t,Au}}{N_{t,Li,F}} = 0.028 \pm 0.001$$

Τα αποτελέσματα επομένως για όλες τις αντιδράσεις των πρωτονίων με ^{7}Li και ^{19}F που μελετήθηκαν είναι συσχετισμένα μεταξύ τους (για κάθε γωνία και ενέργεια), αφού μόνο ο αριθμός των ανιχνευόμενων γεγονότων (Y_x) αλλάζει στον κάθε υπολογισμό (σχέση 2.2). Η συσχέτιση αυτή παίζει πολύ σημαντικό ρόλο στον έλεγχο της ορθότητας των αποτελεσμάτων, όπως περιγράφεται αναλυτικότερα στην επόμενη ενότητα.

Το συνολικό στατιστικό σφάλμα των διαφορικών ενεργών διατομών που προσδιορίστηκαν για την ελαστική σκέδαση των πρωτονίων από τους πυρήνες ^{7}Li και ^{19}F κυμάνθηκε περίπου από 1 έως 4%, ενώ η αβεβαιότητα για τις τιμές που προσδιορίστηκαν για τις υπόλοιπες αντιδράσεις κυμάνθηκε στο ~4-7%. Το συστηματικό σφάλμα του πάχους του στόχου βρέθηκε ίσο με 4%, ενώ ένα επιπλέον 3% συστηματικό σφάλμα αποδίδεται στα αποτελέσματα που αφορούν το ^{7}Li, λόγω της στοιχειομετρίας του στόχου.

Οι διαφορικές ενεργές διατομές που προσδιορίστηκαν στην παρούσα εργασία για τις αντιδράσεις ^{7}Li(p,p$_0$)^{7}Li, ^{7}Li(p,p$_1$)^{7}Li και ^{7}Li(p,α$_0$)^{4}He παρουσιάζονται στα Σχήματα 2.2, 2.3 και 2.4 αντίστοιχα. Σε κάθε περίπτωση, τα πειραματικά αποτελέσματα παρουσιάζονται με τα αντίστοιχα δεδομένα της βιβλιογραφίας, όπου αυτά υπάρχουν. Η σύγκριση με τα διαθέσιμα δεδομένα της βιβλιογραφίας για όλες τις αντιδράσεις του ^{7}Li δείχνει γενικά αρκετά καλή συμφωνία, ενώ ισχυρή γωνιακή εξάρτηση παρουσιάστηκε μόνο στην περίπτωση της ελαστικής σκέδασης για ενέργειες δέσμης από ~3MeV έως ~5 MeV, που αντιστοιχούν σε περιοχή με επικαλυπτόμενα ενεργειακά επίπεδα του σύνθετου πυρήνα ^{8}Be. Αξίζει να σημειωθεί εδώ πως ο εμπλουτισμός της βιβλιογραφίας από τις διαφορικές ενεργές διατομές που προσδιορίστηκαν στην παρούσα μελέτη, και ειδικά για την αντίδραση ^{7}Li(p,α$_0$), όπου μόνο ένα σετ δεδομένων ήταν διαθέσιμο, ενισχύει σε πολύ σημαντικό βαθμό την υλοποίηση της EBS και NRA τεχνικής για την ανάλυση ^{7}Li σε ένα δείγμα, καθώς και την ταυτόχρονη/συνδυασμένη εφαρμογή τους.

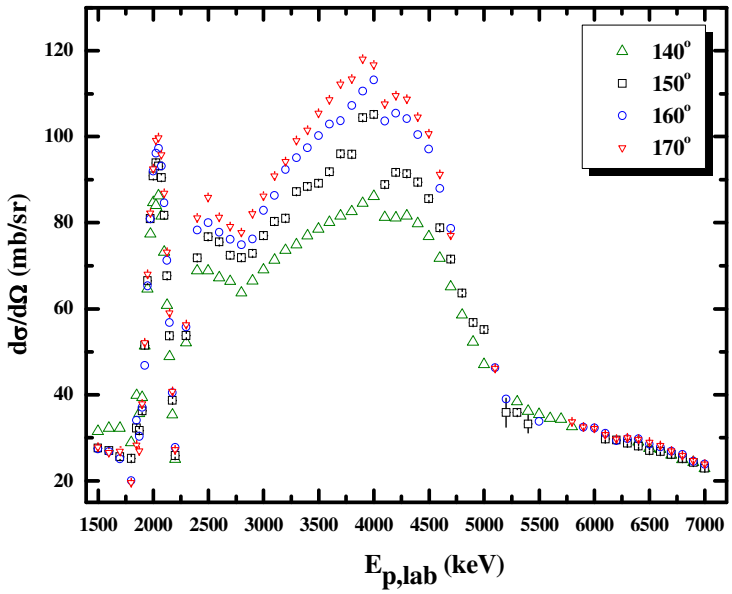

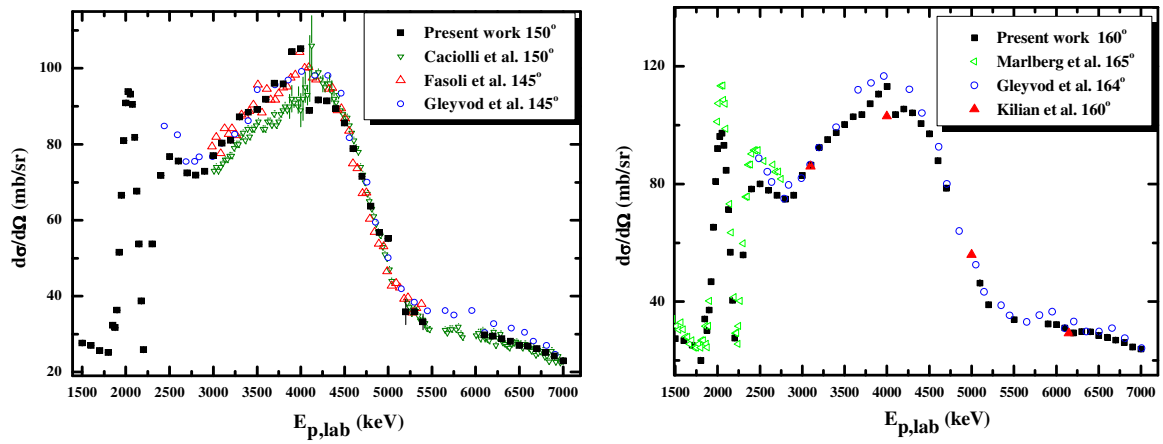

Σχήμα 2.2: Διαφορικές ενεργές διατομές για την αντίδραση $^{7}Li(p,p_0)^{7}Li$ στις 140°, 150°, 160° και 170° μαζί με τα διαθέσιμα δεδομένα από τη βιβλιογραφία.

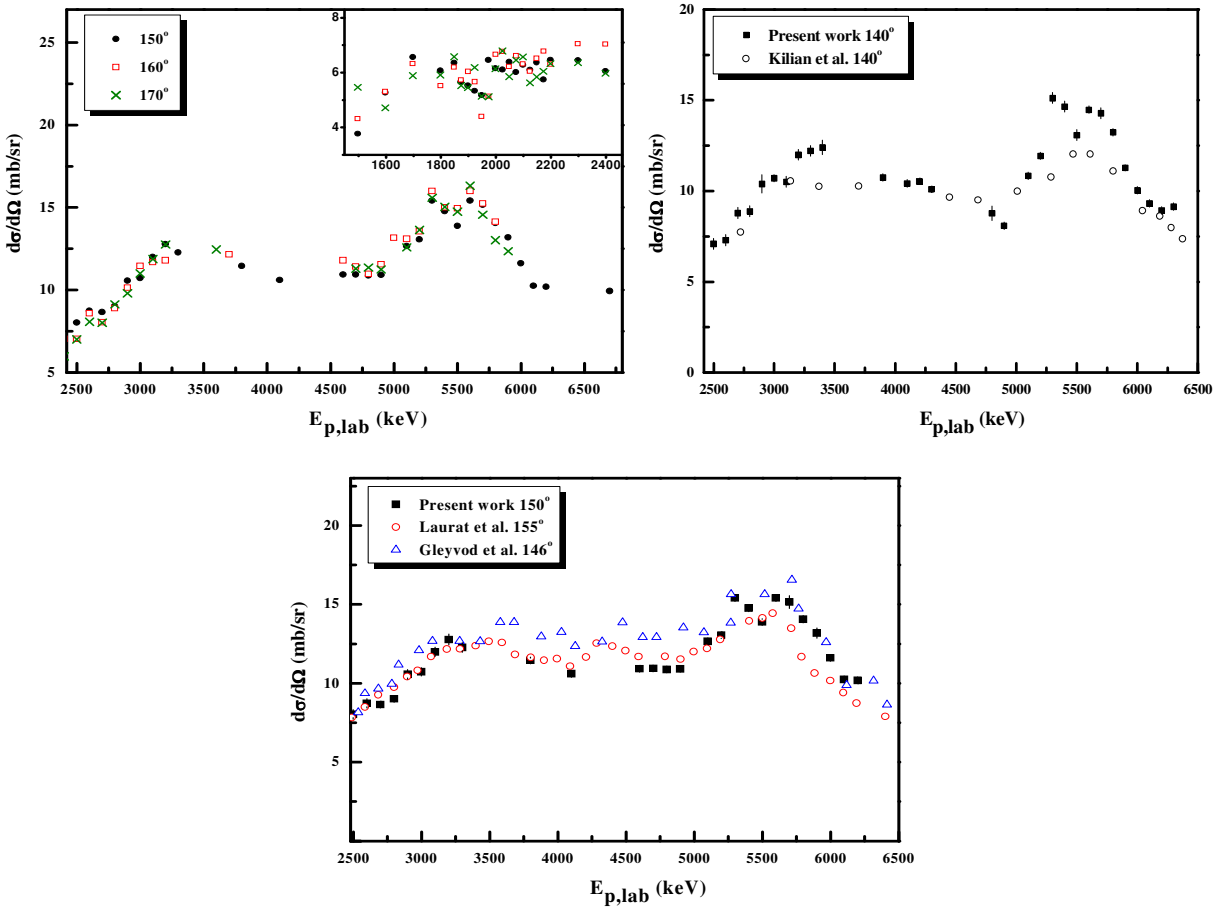

Σχήμα 2.3: Διαφορικές ενεργές διατομές για την αντίδραση $^{7}Li(p,p_1)^{7}Li$ στις 140°, 150°, 160° και 170° μαζί με τα διαθέσιμα δεδομένα από τη βιβλιογραφία.

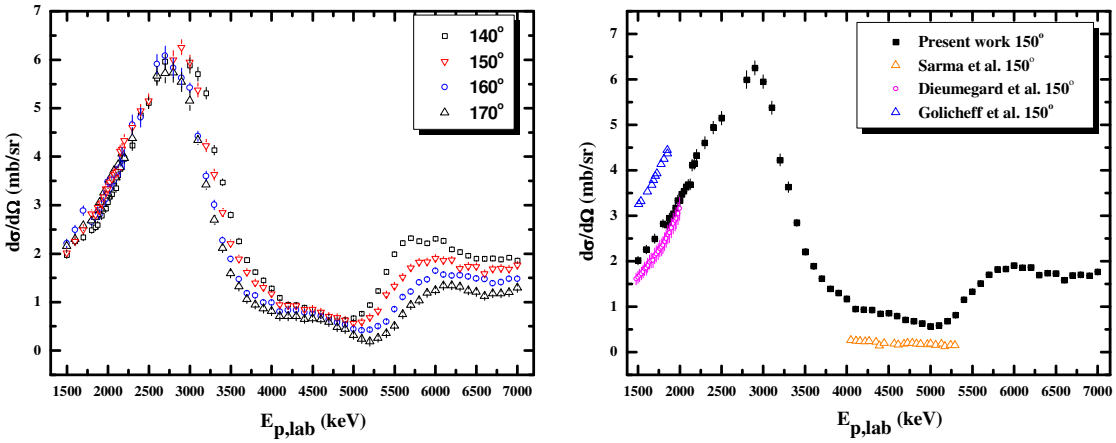

Σχήμα 2.4: Διαφορικές ενεργές διατομές για την αντίδραση ^{7}Li(p,α_0)^{4}He στις 140°, 150°, 160° και 170° μαζί με τα διαθέσιμα δεδομένα απο τη βιβλιογραφία.

Ενδεικτικά αποτελέσματα από τις διαφορικές ενεργές διατομές που προσδιορίστηκαν στην παρούσα εργασία για τις αντιδράσεις ^{19}F(p,p_0)^{19}F, ^{19}F(p,α_0)^{16}O και ^{19}F(p,$\alpha_{1,2}$)^{16}O παρουσιάζονται στα Σχήματα 2.5, μαζί με τα αντίστοιχα δεδομένα της βιβλιογραφίας, όπου αυτά υπάρχουν. Έντονη συντονιστική συμπεριφορά παρατηρείται σε όλες τις αντιδράσεις και ιδιαίτερα στην ελαστική σκέδαση, όπου η διαφορική ενεργός διατομή παρουσιάζει πολύπλοκη δομή με αλληλεπικαλύψεις συντονισμών των αντίστοιχων ενεργειακών σταθμών του σύνθετου πυρήνα ^{20}Ne. Όπως φαίνεται από τη δομή αυτή, το ενεργειακό βήμα των μετρήσεων μας αποδεικνύεται σχετικά ανεπαρκές (μεγάλο) για μια λεπτομερή και αναλυτική περιγραφή της ελαστικής σκέδασης. Να σημειωθεί εδώ ότι ο αρχικός σχεδιασμός του συγκεκριμένου πειράματος αφορούσε τη μελέτη του συστήματος p+^{7}Li. Η χρήση του LiF στόχου όμως επέτρεψε τελικά και την παράλληλη μελέτη του p+^{19}F σε αρκετά ικανοποιητικό βαθμό (ως προς το ενεργειακό εύρος μελέτης και το ενεργειακό βήμα). Η σύγκριση με τα διαθέσιμα πειραματικά δεδομένα της βιβλιογραφίας, αλλά και με τις θεωρητικές-evaluated τιμές μέσω του SigmaCalc [25] (έως 1730 keV), δίνει γενικά ενεργειακές περιοχές με αρκετά καλή συμφωνία (στις μεγαλύτερες κυρίως ενέργειες πρωτονίων), αλλά και περιοχές που τα δεδομένα διαφέρουν σημαντικά, καθιστώντας τον έλεγχο της αξιοπιστίας τους πολύ σημαντικό.

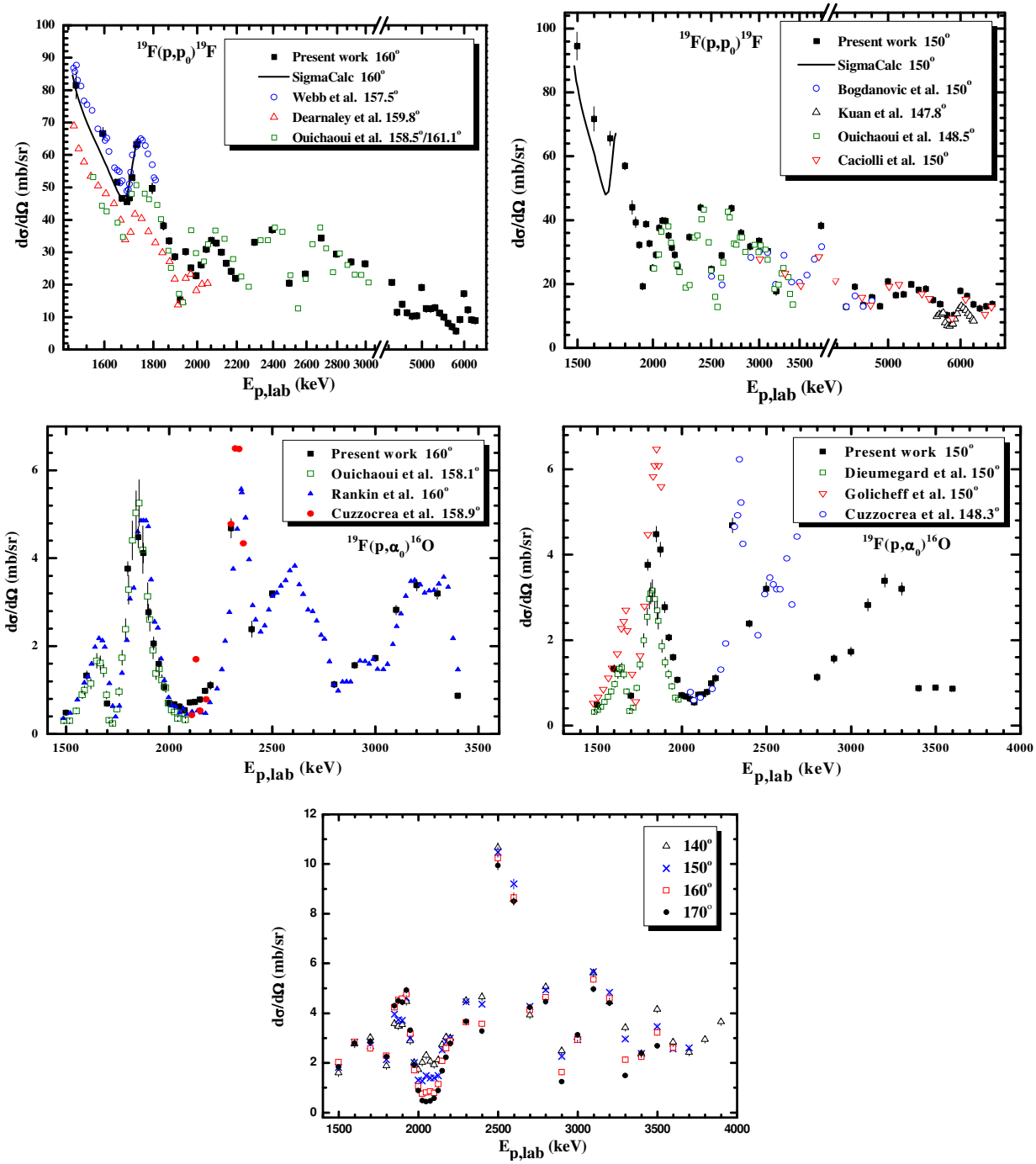

Σχήματα 2.5: Διαφορικές ενεργές διατομές για τις αντιδράσεις $^{19}F(p,p_0)^{19}F$, $^{19}F(p,\alpha_0)^{16}O$ και $^{19}F(p,\alpha_{1,2})^{16}O$, μαζί με τα διαθέσιμα δεδομένα απο τη βιβλιογραφία.

Να σημειωθεί εδώ ότι στην επόμενη ενότητα (3), παρουσιάζεται η πειραματική επαλήθευση των προσδιορισμένων διαφορικών ενεργών διατομών της παρούσας εργασίας για τα συστήματα p+^{7}Li και p+^{19}F.

2.2 Μελέτη d+^{nat}Mg

Οι μετρήσεις για τον προσδιορισμό των διαφορικών ενεργών διατομών για τις αντιδράσεις $^{nat}Mg(d,d_0)^{nat}Mg$ και $^{24}Mg(d,p_0,p_1,p_2)^{25}Mg$ έγιναν σε δύο φάσεις. Πρώτα έγινε η μελέτη στο ενεργειακό εύρος 1.3-2.1 MeV με βήμα 25-50 keV και γωνίες ανίχνευσης 140°, 150°, 160° και 170°, χρησιμοποιώντας ένα λεπτό στόχο μαγνησίου (μείγμα φυσικού μαγνησίου και $MgCl_2$) εξαχνωμένο πάνω σε ένα φύλλο άνθρακα. Πάνω από το στρώμα μαγνησίου, εξαχνώθηκε ένα λεπτό στρώμα Ta, για λόγους κανονικοποίησης του παράγοντα QΩ. Τα αποτελέσματα της μελέτης αυτής φανέρωσαν μια έντονα συντονιστική δομή για ενέργειες δευτερίων γύρω από τα 1800 keV και έτσι το πείραμα επαναλήφθηκε για ενέργειες 1.66 – 2 MeV με πολύ μικρότερο βήμα (2-5 keV) και περισσότερες γωνίες ανίχνευσης (συνολικά στις 55°, 70°, 90°, 125°, 140°, 150°, 160° and 170°), ώστε να περιγραφεί με λεπτομέρεια η περιοχή αυτή. Να σημειωθεί εδώ ότι τα δεδομένα στη βιβλιογραφία για αυτές τις ενέργειες διέγερσης του σύνθετου πυρήνα ^{26}Al είναι πολύ περιορισμένα, αλλά και αντιφατικά, καθώς παρουσιάζουν την περιοχή με Ericson διακυμάνσεις, με τις ενεργειακές στάθμες να μην παρουσιάζουν όμως συστηματική αύξηση της πυκνότητάς τους, ενώ μια διακριτή στάθμη (με συντονιστική συμπεριφορά) έχει επίσης αναφερθεί-παρατηρηθεί σε μεγαλύτερη ενέργεια διέγερσης.

Ο χαρακτηρισμός του στόχου βασίστηκε στην επιπλέον ακτινοβόλησή του με δέσμη πρωτονίων στα 1700, 2200 και 2500 keV στις 150˚ και 170˚, όπου υπάρχουν evaluated δεδομένα για την διαφορική ενεργό διατομή της ^{nat}Mg(p,p) (SigmaCalc) που έχουν ελεγχθεί (με ~5% αβεβαιότητα). Το στρώμα Ta προσδιορίστηκε με την τεχνική XRF και τελικά ο λόγος των παχών που χρησιμοποιήθηκε στην αντίστοιχη σχέση 2.2 για τις διαφορικές ενεργές διατομές βρέθηκε ίσος με:

$$\frac{N_{t,Ta}}{N_{t,^{nat}Mg}} = 0.038 \pm 0.002$$

Η συνολική στατιστική αβεβαιότητα των διαφορικών ενεργών διατομών που προσδιορίστηκαν για την ελαστική σκέδαση υπολογίστηκε στο ~5%, προερχόμενη κυρίως από τον χαρακτηρισμό του στόχου, ενώ η αβεβαιότητα για τις τιμές που προσδιορίστηκαν για τις υπόλοιπες (d,p) αντιδράσεις κυμάνθηκε στο ~10%, λόγω της μικρότερης στατιστικής των αντίστοιχων κορυφών στα φάσματα. Ενδεικτικά αποτελέσματα για τις διαφορικές ενεργές διατομές που προσδιορίστηκαν στην παρούσα εργασία παρουσιάζονται στα Σχήματα 2.6 μαζί με τα μόνα διαθέσιμα αντίστοιχα δεδομένα της βιβλιογραφίας (των Omar et al. [51]). Ικανοποιητική συμφωνία παρατηρείται σε κάθε τέτοια σύγκριση, ενώ από τα δεδομένα της παρούσας εργασίας συνολικά γίνεται φανερή η ισχυρή γωνιακή (και συσχετισμένη στα διάφορα κανάλια εξόδου) εξάρτηση των ενεργών διατομών που υποδηλώνει την ύπαρξη διακριτών σταθμών του σύνθετου πυρήνα.

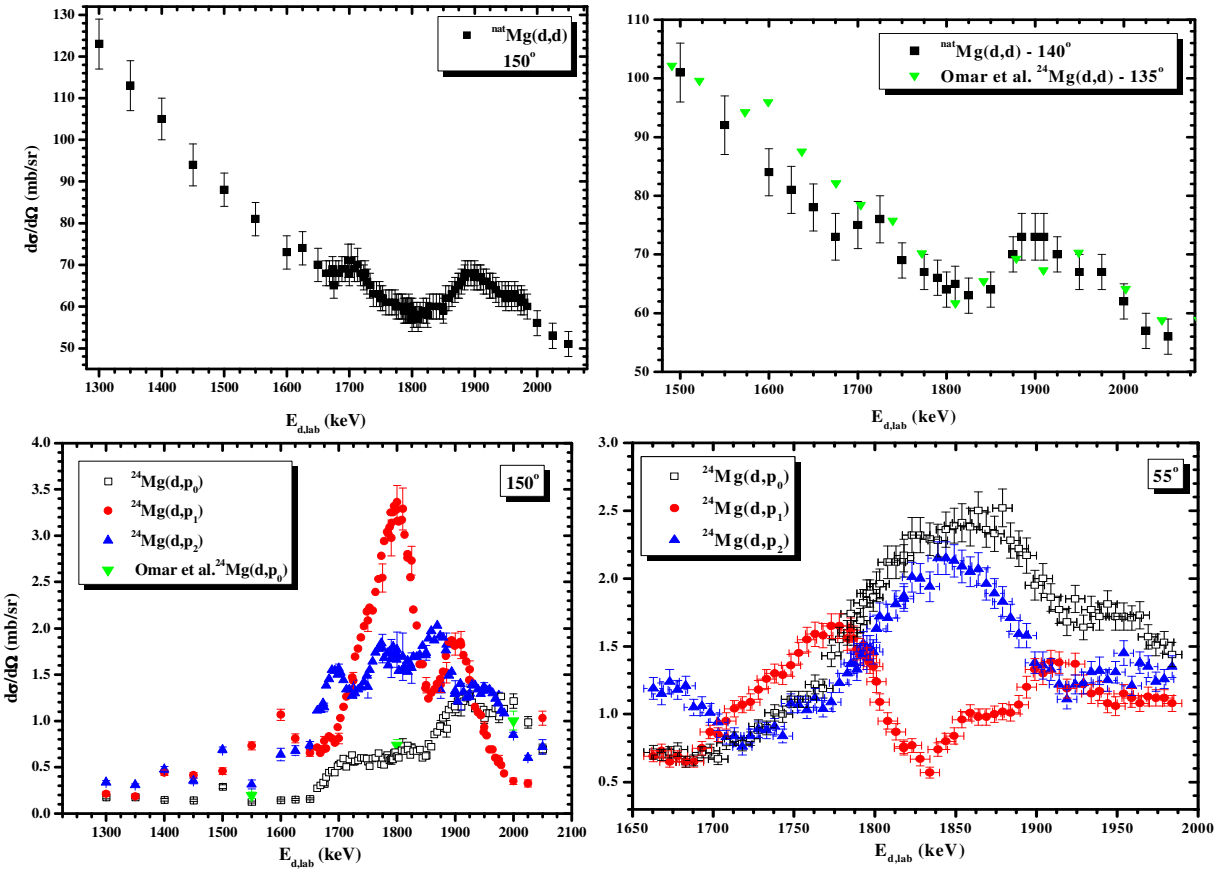

Σχήματα 2.6: Διαφορικές ενεργές διατομές για τις αντιδράσεις ^{nat}Mg(d,d$_0$)^{nat}Mg και ^{24}Mg(d,p$_0$,p$_1$,p$_2$)^{25}Mg, μαζί με τα διαθέσιμα δεδομένα από τη βιβλιογραφία.

3. Έλεγχος αξιοπιστίας – benchmarking

Ο έλεγχος αξιοπιστίας (benchmarking) των ενεργών διατομών ελαστικής σκέδασης αφορά τη μελέτη της συγκεκριμένης σκέδασης χρησιμοποιώντας παχύ ομοιόμορφο στόχο του υπό μελέτη στοιχείου. Η διαδικασία που ακολουθείται βασίζεται στην σύγκριση του πειραματικού φάσματος με την αντίστοιχη προσομοίωση. Η μεθοδολογία αυτή απαιτεί την ακριβή προσομοίωση των πειραματικών συνθηκών, προσδιορίζοντας και υπολογίζοντας όλους τους παράγοντες που επηρεάζουν το αντίστοιχο φάσμα, ώστε οι πιθανές διαφορές στην τελική σύγκριση των φασμάτων, από την προσομοίωση και το πείραμα, να μπορούν να αποδοθούν στην διαφορική ενεργό διατομή που χρησιμοποιήθηκε στην προσομοίωση. Το φάσμα από παχύ στόχο αντιστοιχεί στις αλληλεπιδράσεις της δέσμης με το υλικό του στόχου σε όλο το πάχος του, από τα επιφανειακά στρώματα (μέγιστη ενέργεια ανίχνευσης) έως αυτά που αντιστοιχούν στα σωματίδια που ανιχνεύονται με μηδαμινή ενέργεια. Η μορφή του αποκαλύπτει επομένως την αντίστοιχη διαφορική ενεργό διατομή, μετά από συνέλιξη με την απώλεια ενέργειας και τον ενεργειακό διασκεδασμό στο στόχο και την διακριτική ικανότητα, όπως φαίνεται και στη σχέση 1.2. Η προτεινόμενη μεθοδολογία για το benchmarking αφορά επίσης και άλλες παραμέτρους

που σχετίζονται με το χρησιμοποιούμενο στόχο και επηρεάζουν την διαδικασία αξιολόγησης των ενεργών διατομών.

Πιο συγκεκριμένα τα προτεινόμενα βήματα που αναπτύχθηκαν στα πλαίσια της παρούσας διατριβής αφορούν τα εξής:

1) την ακριβή βαθμονόμηση της ενέργειας από τον επιταχυντή, η οποία μπορεί να προσδιοριστεί χρησιμοποιώντας τους λεπτούς συντονισμούς της αντίδρασης ^{27}Al(p,γ) στα 992 keV (Γ=110eV), της ^{13}C(p,γ) στα 1745 keV (Γ=340eV) και της ^{32}S(p,pγ) στα 3379 keV (Γ=1keV), καλύπτοντας έτσι μεγάλο εύρος ενεργειών, χρησιμοποιώντας τους αντίστοιχους στόχους (μετρήσεις PIGE – γ ακτινοβολίας).

2) την εύρεση της διακριτικής ικανότητας των ανιχνευτών αναλύοντας τα φάσματα (edges σήματος) από λείο στόχο σε χαμηλές ενέργειες.

3) τη χρήση των πιο αξιόπιστων διαθέσιμων μοντέλων για τον υπολογισμό του stopping power και straggling μέσα στο στόχο (Ziegler-Biersack-Littmark [6] και Chu & Yang [20,11] αντίστοιχα). Διερευνώντας την ακρίβεια των μοντέλων αυτών, διαπιστώθηκε ότι στις χαμηλές ενέργειες, υπάρχουν σημαντικές αποκλίσεις μεταξύ των παραγόμενων (προσομοιωμένων) και των πειραματικών φασμάτων (ανάλογα το στόχο). Η διαδικασία benchmarking πρέπει λοιπόν να περιορίζεται στο επιφανειακό σήμα εύρους ~250 keV (παράθυρο ανάλυσης). Συνεπώς τα βήματα για τις μετρήσεις με παχύ στόχο θα πρέπει να είναι μικρά και ανάλογα της δομής της αντίστοιχης ενεργού διατομής.

4) τις πολλαπλές σκεδάσεις μέσα στο στόχο. Στην ίδια ανάγκη για περιορισμό της ανάλυσης κοντά στην επιφάνεια του στόχου και για μικρά ενεργειακά βήματα στο πείραμα μας οδηγεί και η ανίχνευση σωματιδίων που έχουν υποστεί πολλαπλές σκεδάσεις (αναφερόμενοι κυρίως στις διπλές κυρίως σκεδάσεις της δέσμης σε μεγάλες γωνίες) μέσα στο στόχο. Το φαινόμενο αυτό εντοπίζεται στις χαμηλές ενέργειες και είναι εντονότερο για τα πιο βαριά στοιχεία (από τα οποία μπορεί να αποτελείται ο υπό μελέτη στόχος).

5) τη φύση του στόχου. Το φαινόμενο του διαυλισμού (channeling) για τους κρυσταλλικούς στόχους θα πρέπει να αποφεύγεται κατά την πειραματική διαδικασία, τοποθετώντας το στόχο υπό την κατάλληλη κλίση (ή ιδανικά υπό συνεχή περιστροφή). Η τραχύτητα των χρησιμοποιούμενων παστίλιων θα πρέπει ανάλογα να αντιμετωπιστεί και αυτό μπορεί να γίνει διορθώνοντας *a posteriori* τα φάσματα βασιζόμενοι στο μοντέλο των S.L. Molodtsov et al. [84], το οποίο παραμετροποιεί την επιφανειακή τραχύτητα και «διορθώνει-συμπληρώνειι» το αντίστοιχο προσομοιωμένο φάσμα, ώστε να είναι άμεση η σύγκρισή του με το αντίστοιχο πειραματικό. Στα πλαίσια της παρούσας εργασίας αναπτύχθηκε αλγόριθμος βασιζόμενος στο μοντέλο αυτό, ο οποίος χρησιμοποιήθηκε σε όλες τις περιπτώσεις benchmarking με στόχο παστίλια.

6) τον προσδιορισμό του φορτίου στο στόχο. Ο πιο ακριβής τρόπος για τον προσδιορισμό του παράγοντα QΩ είναι η κανονικοποίηση της κάθε μέτρησης στη σκέδαση Rutherford στο βαρύ στοιχείο του στόχου. Αν ο παχύς χρησιμοποιούμενος στόχος (ως χημική ένωση) δεν

περιλαμβάνει ένα τέτοιο στοιχείο, τότε η εξάχνωση ενός λεπτού στρώματος χρυσού για παράδειγμα κρίνεται απαραίτητη για την κανονικοποίηση.
7) και την αποφυγή του pile-up, κρατώντας το ρεύμα στο στόχο χαμηλό (στα ~5nA).
8) Τέλος, πιθανές σημαντικές προσμίξεις/contaminants αλλά και γεγονότα (συνεισφορά) υποβάθρου από άλλες αντιδράσεις θα πρέπει να διερευνώνται σε κάθε περίπτωση.

Οι κύριες πηγές αβεβαιότητας ακολουθώντας τα βήματα αυτά προέρχονται από τη στατιστική των πειραματικών φασμάτων και τον προσδιορισμό του φορτίου στο στόχο. Αυτοί οι παράγοντες σχετίζονται κυρίως με το χρησιμοποιούμενο στόχο και στα περισσότερα benchmarking αποτελέσματα της παρούσας διατριβής η αβεβαιότητα της διαδικασίας δεν ξεπέρασε το ~4%.

3.1 Benchmarking στις μελέτες p+^{7}Li, p+^{19}F και d+^{nat}Mg

Με την παραπάνω διαδικασία ελέγχου των ενεργών διατομών, επαληθεύτηκαν οι τιμές που προσδιορίστηκαν πειραματικά στα πλαίσια της παρούσας εργασίας για τα συστήματα p+^{7}Li, p+^{19}F και d+^{nat}Mg. Η χρήση του στόχου LiF και ο τρόπος προσδιορισμού των ενεργών διατομών (σχετικές μετρήσεις με τη σκέδαση Rutherford από τους πυρήνες Au του στόχου, σχέση 2.2), οδηγεί σε συσχετισμένα αποτελέσματα για όλες τις αντιδράσεις (p+^{7}Li, p+^{19}F) και γωνίες ανίχνευσης που μελετήθηκαν, αφού μόνο ο αριθμός των ανιχνευόμενων γεγονότων αλλάζει. Έτσι, ελέγχοντας την ορθότητα ενός σετ δεδομένων, ελέγχονται όλα ταυτόχρονα. Στο Σχήμα 3.1 φαίνεται αριστερά ο έλεγχος της ^{19}F(p,α_0) αντίδρασης χρησιμοποιώντας έναν παχύ στόχο BaF_2 με ενέργεια πρωτονίων στα 2300 keV, όπου το φορτίο (παράγοντας QΩ) προσδιορίστηκε αναπαράγοντας το σήμα ^{nat}Ba(p,p) που ακολουθεί τη σχέση Rutherford, ενώ δεξιά φαίνεται το benchmarking και της αντίδρασης ^{7}Li(p,α_0) με ακτινοβόληση παχύ στόχου LiF. Οι προσομοιώσεις έγιναν χρησιμοποιώντας τον κώδικα SIMNRA [70] και τις πειραματικές τιμές διαφορικών ενεργών διατομών της παρούσας μελέτης, ενώ οι πειραματικές μετρήσεις με τους παχείς στόχους διεξήχθησαν στο εργαστήριο του Ινστιτούτου Πυρηνικής και Σωματιδιακής Φυσικής στο ΕΚΕΦΕ «Δημόκριτος». Τα παραγόμενα φάσματα από τις προσομοιώσεις αναπαράγουν πολύ καλά τα πειραματικά φάσματα, αποδεικνύοντας έτσι την ορθότητα των αντίστοιχων διαφορικών ενεργών διατομών, άρα και όλων των δεδομένων για τις αντιδράσεις p+^{7}Li και p+^{19}F που μελετήθηκαν.

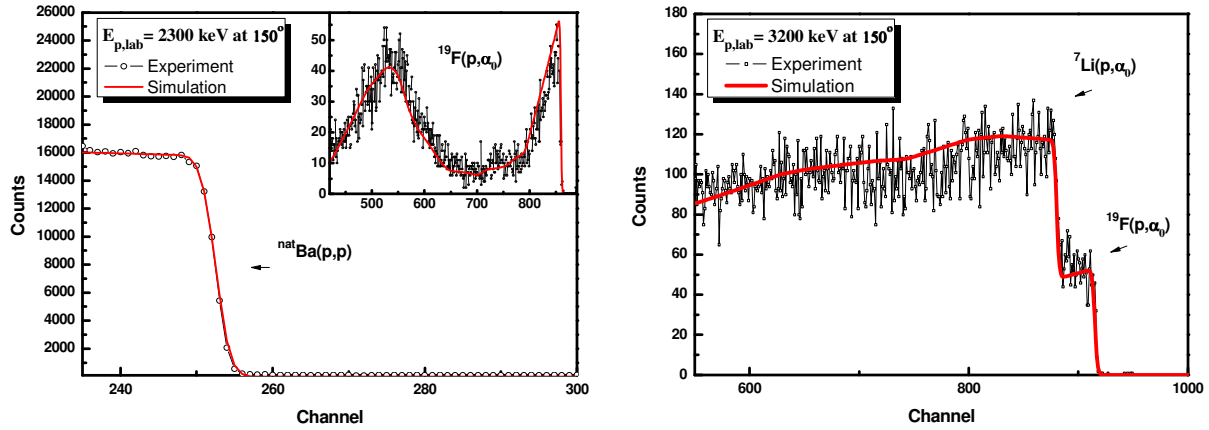

Σχήμα 3.1: Πειραματικά φάσματα στις 150°, ακτινοβολώντας παχύ και λείο BaF_2 (αριστερά) και LiF (δεξιά) στόχο με πρωτόνια ενέργειας 2300 και 3200 keV αντίστοιχα, μαζί με τα παραγόμενα φάσματα χρησιμοποιώντας τον κώδικα SIMNRA.

Ανάλογα επαληθεύτηκαν και οι (επίσης συσχετισμένες) διαφορικές ενεργές διατομές που προσδιορίστηκαν πειραματικά στην παρούσα εργασία για τις αντιδράσεις $^{nat}Mg(d,d_0)$ και $^{24}Mg(d,p_0,p_1,p_2)$, όπως φαίνεται στο Σχήμα 3.2, χρησιμοποιώντας παστίλια MgO με ένα λεπτό στρώμα χρυσού στην επιφάνεια (για τον προσδιορισμό QΩ) στα 1700 και 2000 keV, επικεντρώνοντας την ανάλυση στις (d,p) αντιδράσεις.

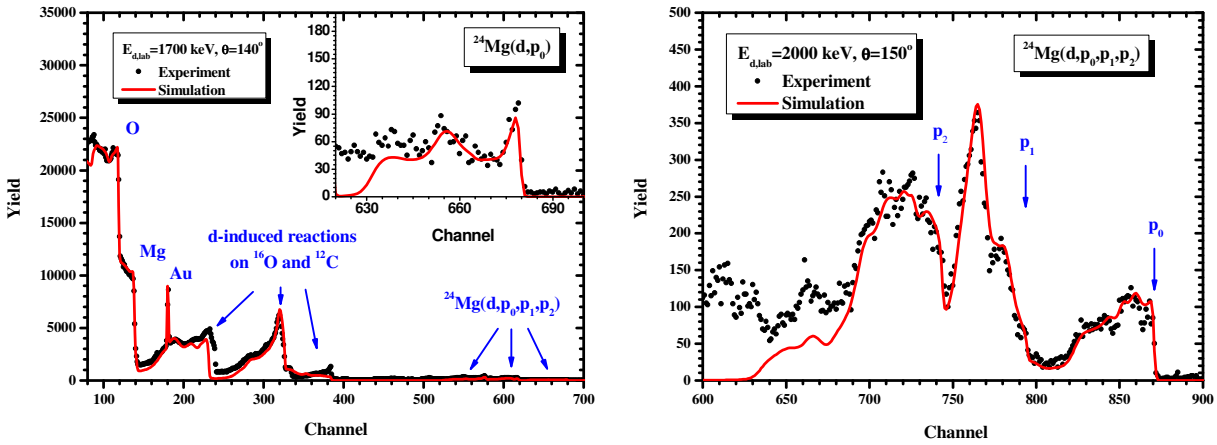

Σχήμα 3.2: Πειραματικά φάσματα στις 140° και 150°, ακτινοβολώντας την παστίλια MgO με δευτέρια ενέργειας 1700 και 2000 keV, μαζί με τα παραγόμενα φάσματα χρησιμοποιώντας τον κώδικα SIMNRA.

3.2 Benchmarking στα δεδομένα για (p,p) σε ^{23}Na, ^{31}P, ^{nat}S και ^{nat}Si

Επιπλέον benchmarking μετρήσεις πραγματοποιήθηκαν στα πλαίσια της παρούσας εργασίας, σύμφωνα με την παραπάνω μεθοδολογία, για τον έλεγχο των διαφορικών ενεργών διατομών που αφορούν τις αντιδράσεις (p,p) σε ^{23}Na, ^{31}P, ^{nat}S και ^{nat}Si**.** Πιο συγκεκριμένα, οι αντίστοιχες evaluated διαφορικές ενεργές διατομές (SigmaCalc [25]), αξιολογήθηκαν με benchmarking

φάσματα πάνω σε κατάλληλους στόχους, λείους, κρυσταλλικούς (πλακίδιο Si και GaP) ή παστίλιες (NaBr και MoS_2) με ένα λεπτό στρώμα Au στην επιφάνεια, σε γωνίες ανίχνευσης στις 121°, 149° και 173° για ενέργειες δέσμης πρωτονίων 1.2 - 3.5 MeV με βήμα 250 keV. Οι μετρήσεις πραγματοποιήθηκαν στο Πανεπιστήμιο του Surrey (Ion Beam Centre, University of Surrey, United Kingdom) στον επιταχυντή 2 MV Tandetron, ενώ ο κώδικας WiNDF [82] χρησιμοποιήθηκε για τις αντίστοιχες προσομοιώσεις, όπου η κορυφή του Au σε συνδυασμό με το σήμα από το βαρύ στοιχείο του κάθε στόχου (στις χαμηλές ενέργειες η σκέδαση πρωτονίων ακολουθεί τη σκέδαση Rutherford) χρησιμοποιήθηκαν για τον προσδιορισμό του φορτίου της κάθε μέτρησης.

^{nat}Si(p,p) και ^{nat}S(p,p)

Οι θεωρητικές τιμές (evaluated) από το SigmaCalc της διαφορικής ενεργού διατομής για την σκέδαση ^{nat}Si(p,p) φτάνουν την ενέργεια των 3 MeV (ενέργεια δέσμης), ενώ για την ^{nat}S(p,p) τα 3.5 MeV. Με τα φάσματα της παρούσας μελέτης επαληθεύτηκαν οι τιμές για την ^{nat}Si(p,p) μέχρι τα 2.3 MeV και για την ^{nat}S(p,p) μέχρι τα 3.2 MeV, αναπαράγοντας τα πειραματικά φάσματα εντός 1-8%, όπως ενδεικτικά απεικονίζεται στο Σχήμα 3.3 για την ^{nat}Si(p,p) στα 1782 keV (αριστερά) και δεξιά για την ^{nat}S(p,p) στα 2284 keV (η ανάλυση περιορίζεται πάντα στο επιφανειακό σήμα των ~250 keV και αφού έχει αφαιρεθεί το σήμα από το βαρύτερο στοιχείο του στόχου (MoS_2) - εικονιζόμενο πλαίσιο). Σε μεγαλύτερες ενέργειες και συγκεκριμένα στα ~3.5 MeV που παρουσιάζεται σημαντική αύξηση της ενεργού διατομής, παρατηρήθηκαν σημαντικές διαφορές ανάμεσα στα πειραματικά και στα προσομοιωμένα φάσματα, όπως φαίνεται στο Σχήμα 3.4 αριστερά. Τα φάσματα της παρούσας εργασίας συνέβαλαν στην αντίστοιχη διόρθωση των παραμέτρων των θεωρητικών υπολογισμών (που πραγματοποίησε ο Δρ. A.F. Gurbich) δίνοντας διορθωμένες τιμές στη νέα έκδοση SigmaCalc 2.0 που αναπαράγουν τέλεια τα αντίστοιχα φάσματα (Σχήμα 3.4 δεξιά).

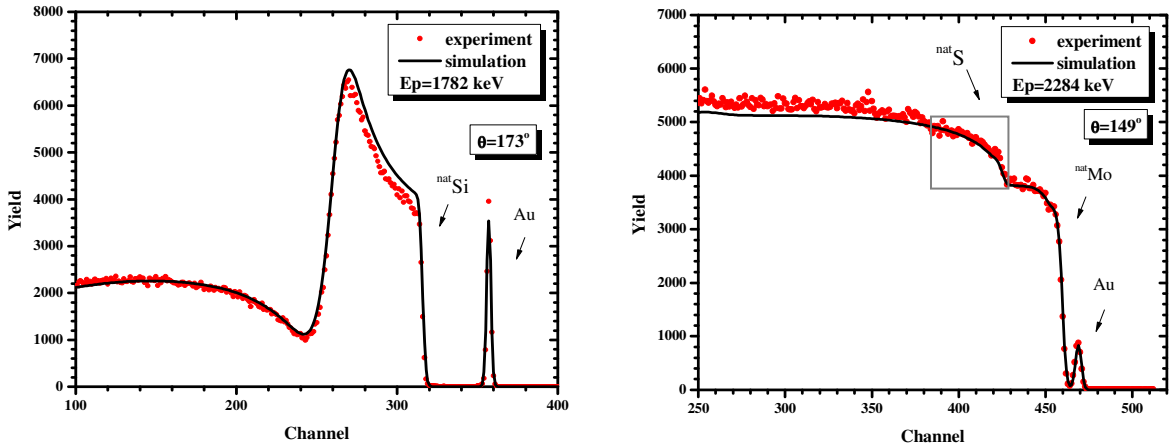

Σχήματα 3.3: Πειραματικά φάσματα ακτινοβολώντας το στόχο Si (αριστερά) και το στόχο MoS_2 (δεξιά), μαζί με τα παραγόμενα φάσματα χρησιμοποιώντας τον κώδικα WiNDF και τις evaluated

διαφορικές ενεργές διατομές από το SigmaCalc. Στο πλαίσιο δεξιά απεικονίζεται το ‘‘παράθυρο’’ της ανάλυσης στην επιφάνεια του σήματος ^{nat}S(p,p) μετά την αφαίρεση του ^{nat}Mo(p,p) σήματος.

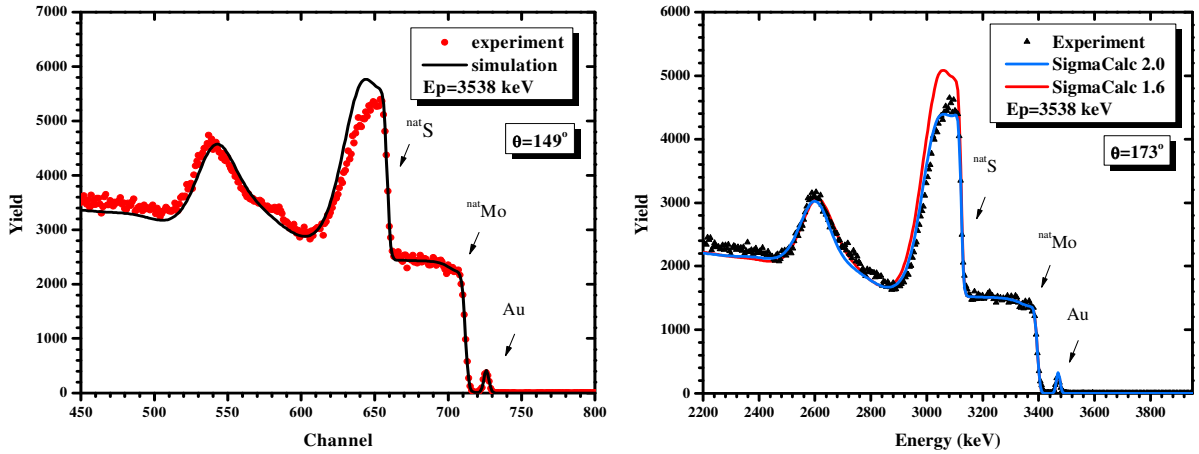

Σχήμα 3.4: Πειραματικά φάσματα στις 149° και 173° ακτινοβολώντας την παστίλια MoS_2 με πρωτόνια στα 3538 keV, μαζί με τα αντίστιχα προσομοιωμένα φάσματα χρησιμοποιώντας τις evaluated διαφορικές ενεργές διατομές από το SigmaCalc.

Η παρούσα μελέτη benchmarking για την ^{nat}S(p,p) είναι διαθέσιμη online στην επιστημονική κοινότητα στην ιστοσελίδα του SigmaCalc [25]. Εκεί υπάρχουν όλα τα πειραματικά φάσματα από τον παχύ στόχο MoS_2 μαζί με τα χαρακτηριστικά τους και ο χρήστης μπορεί άμεσα να κάνει τις αντίστοιχες προσομοιώσεις επιλέγοντας τις διαφορικές ενεργές διατομές που θέλει να ελέγξει. Με αυτόν τον τρόπο δίνεται άμεσα πληροφορία για την αξιοπιστία των δεδομένων πριν τη χρήση τους.

^{23}Na(p,p) και ^{31}P(p,p)

Στις περιπτώσεις αυτές οι evaluated τιμές για τη διαφορική ενεργό διατομή από το SigmaCalc αφορούν σχετικά μικρό ενεργειακό εύρος, οπότε μελετήθηκαν ως προς την αξιοπιστία τους και τα αντίστοιχα πειραματικά δεδομένα. Πιο συγκεκριμένα, οι evaluated τιμές της σκέδασης ^{23}Na(p,p) φτάνουν την ενέργεια των 1.5 MeV (ενέργεια δέσμης), ενώ για την ^{31}P(p,p) τα 2 MeV. Η αναπαραγωγή των πειραματικών φασμάτων από την παστίλια NaBr από τις αντίστοιχες προσομοιώσεις, χρησιμοποιώντας τις τιμές του SigmaCalc για την ^{23}Na(p,p), ήταν αρκετά καλή, όπως φαίνεται στο Σχήμα 3.5 αριστερά. Εξαιτίας όμως της χαμηλής στατιστικής (μετά την αφαίρεση του μεγάλου υποβάθρου από την Br(p,p) αντίδραση), τα αποτελέσματα είναι μόνο ποιοτικά-ενδεικτικά. Σε μεγαλύτερες ενέργειες δέσμης, όπου τα φάσματα μπορούν να αναλυθούν κανονικά, υπάρχουν μόνο τα πειραματικά δεδομένα από τη μελέτη των A. Caciolli et al. [89] στο εύρος 2.21-5.2 MeV, τα οποία οδηγούν σε πολύ καλή αναπαραγωγή των αντίστοιχων πειραματικών φασμάτων από την παστίλια NaBr (ως τα 3.5 MeV), όπως φαίνεται στο Σχήμα 3.5 δεξιά, για παράδειγμα. Τα δεδομένα αυτά μπορούν άρα να χρησιμοποιηθούν με

ασφάλεια στους θεωρητικούς υπολογισμούς για την επέκταση του evaluation σε μεγαλύτερες ενέργειες.

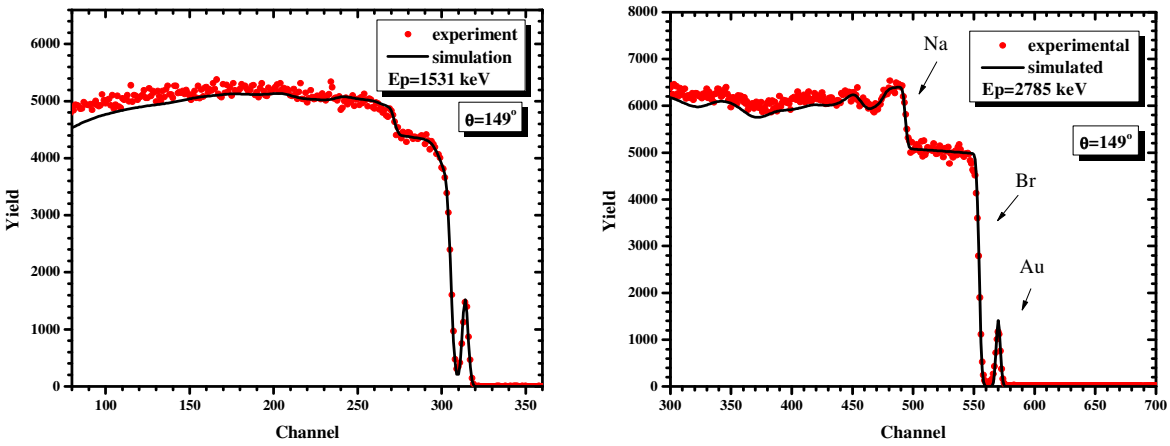

Σχήμα 3.5: Πειραματικά φάσματα στις 149° ακτινοβολώντας την παστίλια NaBr με πρωτόνια στα 1531 και 2785 keV, μαζί με τα αντίστιχα προσομοιωμένα φάσματα χρησιμοποιώντας τις evaluated διαφορικές ενεργές διατομές από το SigmaCalc (αριστερά) και τα δεδομένα των A. Caciolli et al. (δεξιά).

Η μελέτη της ^{31}P(p,p) με τον στόχο GaP, οδήγησε σε πολύ καλή αναπαραγωγή των πειραματικών φασμάτων από τις αντίστοιχες προσομοιώσεις για τα evaluated δεδομένα μέχρι τα 1.8 MeV, όπως φαίνεται στο Σχήμα 3.6 αριστερά. Τα φάσματα της παρούσας εργασίας συνέβαλαν στη διόρθωση των παραμέτρων των θεωρητικών υπολογισμών (που πραγματοποίησε ο Δρ. A.F. Gurbich) δίνοντας διορθωμένες τιμές έως τα ~2 MeV, στη νεότερη έκδοση SigmaCalc 2.0 που αναπαράγουν τέλεια τα αντίστοιχα φάσματα (Σχήμα 3.6 δεξιά). Στις μεγαλύτερες ενέργειες όμως, χρησιμοποιώντας τα μόνα διαθέσιμα πειραματικά δεδομένα των K.V. Karadzhev et al. [90] που φτάνουν ως τα 3.5 MeV, υπάρχουν σημαντικές αποκλίσεις των φασμάτων, όπως φαίνεται στο Σχήμα 3.6 κάτω, για παράδειγμα. Γίνεται σαφές από τα αποτελέσματα αυτά ότι στην περίπτωση της ^{31}P(p,p), χρειάζεται περαιτέρω πειραματική μελέτη για την επέκταση του αντίστοιχου evaluation σε υψηλότερες ενέργειες δέσμης πρωτονίων.

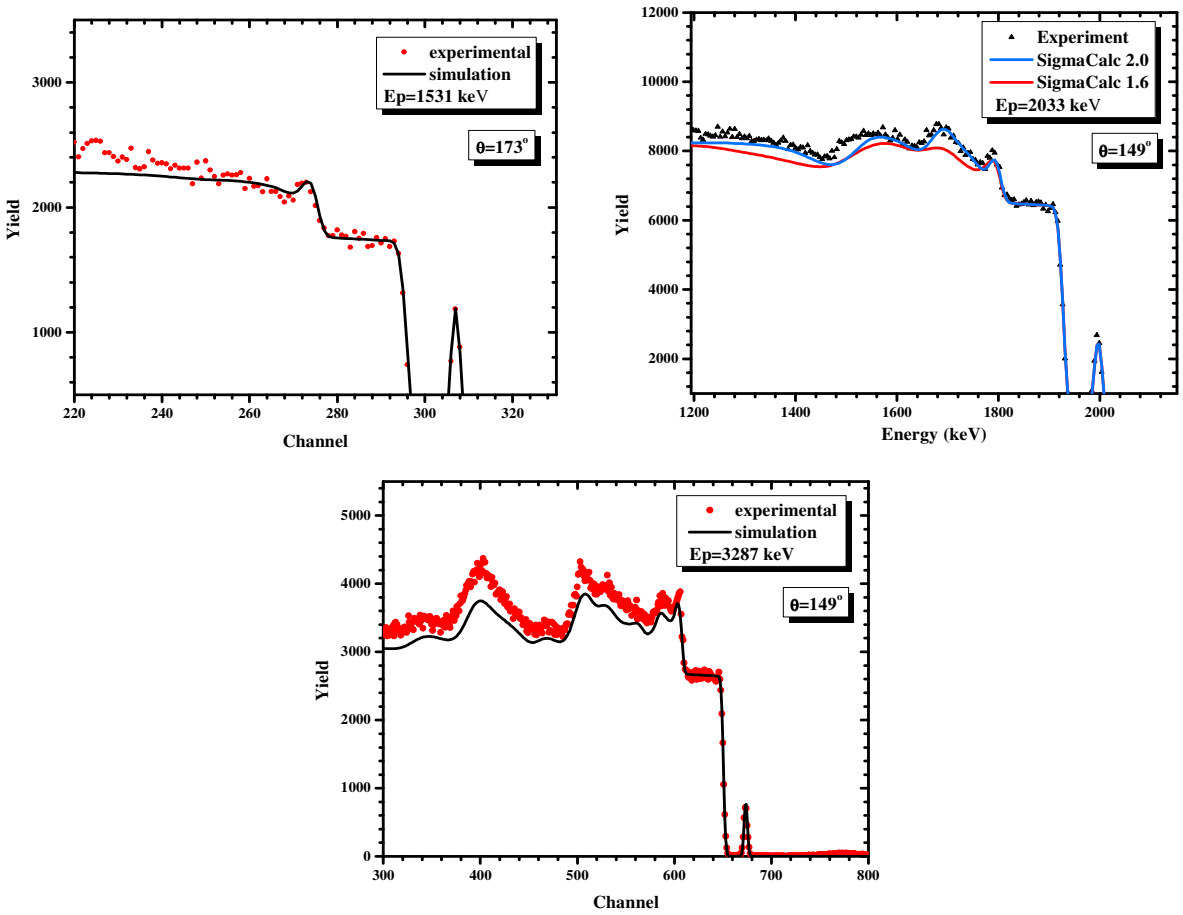

Σχήμα 3.6: Πειραματικά φάσματα ακτινοβολώντας το στόχο GaP με πρωτόνια στα 1531 και 2033 keV (πάνω) και 3287 keV (κάτω), μαζί με τα αντίστοιχα προσομοιωμένα φάσματα χρησιμοποιώντας τις evaluated διαφορικές ενεργές διατομές από το SigmaCalc για τις χαμηλές ενέργειες (πάνω) και τα δεδομένα των K.V. Karadzhev et al. (κάτω).

4. Θεωρητικός – φαινομενολογικός υπολογισμός ενεργών διατομών

Ο θεωρητικός υπολογισμός ενεργών διατομών, με έναν αριθμό παραμέτρων να προσδιορίζονται από τα αντίστοιχα πειραματικά δεδομένα (φαινομενολογική προσέγγιση – evaluation) για τις συντονιστικές αντιδράσεις (σύνθετου πυρήνα) βασίζεται στην R-matrix θεωρία [93] και είναι απαραίτητος για τους εξής λόγους: Η πιθανή έντονη γωνιακή εξάρτηση αλλά και ιδιαίτερα στενοί συντονισμοί μπορεί να παραβλεφθούν σε ένα πείραμα μέτρησης διαφορικών ενεργών διατομών (λόγω του πάχους του στόχου ή του ενεργειακού βήματος για παράδειγμα). Επίσης τα υπάρχοντα πειραματικά δεδομένα παρουσιάζουν σε πολλές περιπτώσεις αρκετές αποκλίσεις και καλύπτουν περιορισμένο εύρος σε ενέργειες και κυρίως γωνίες ανίχνευσης. Η κριτική ενσωμάτωση των διαθέσιμων πειραματικών δεδομένων σε ένα ενιαίο θεωρητικό πλαίσιο οδηγεί στα πιο ακριβή δεδομένα διαφορικών ενεργών διατομών, τα οποία μπορούν να υπολογιστούν για κάθε γωνία ανίχνευσης, στοιχειοθετώντας έτσι τα προτεινόμενα θεωρητικά (recommended-evaluated) δεδομένα.

Σύμφωνα με τη θεωρία σκέδασης, η επιταχυνόμενη δέσμη περιγράφεται ως ένα εισερχόμενο επίπεδο κύμα που αλληλεπιδρά με το πυρηνικό δυναμικό του στόχου-πυρήνα εμφανίζοντας ένα σφαιρικό εξερχόμενο κύμα (ανάπτυξη σε μερικά κύματα). Η ενεργός διατομή σύμφωνα με αυτή τη θεώρηση εκφράζεται τελικά από την μετατόπιση φάσης δ_ℓ μέσω της συνάρτησης σκέδασης U_ℓ, η οποία μπορεί να υπολογιστεί χρησιμοποιώντας τη θεωρία R-matrix. Η βασική αρχή της θεωρίας αυτής αποτελείται από το διαχωρισμό του χώρου σε δύο μέρη, ένα εξωτερικό και ένα εσωτερικό σε σχέση με την πυρηνική ακτίνα. Στο εξωτερικό μέρος περιγράφονται τα κανάλια αντίδρασης (εισόδου και εξόδου), η συνάρτηση σκέδασης και η ενεργός διατομή, ενώ το εσωτερικό μέρος αφορά τον σύνθετο πυρήνα και τις ιδιότητες του. Συνδέοντας τα δύο αυτά μέρη με τις κατάλληλες συνοριακές συνθήκες των αντίστοιχων κυματοσυναρτήσεων, η συνάρτηση (πίνακας) σκέδασης, άρα και η ενεργός διατομή, υπολογίζεται μέσω των ιδιοτήτων του σύνθετου πυρήνα που εκφράζονται στη συνάρτηση (πίνακα) R και αφορούν τις ενεργειακές στάθμες του, οι οποίες προκύπτουν και χαρακτηρίζονται πειραματικά (φαινομενολογία).

Υπολογισμοί για την σκέδαση ^{19}F(p,p)

Η διαδικασία αυτή υλοποιήθηκε στην παρούσα εργασία, χρησιμοποιώντας τον κώδικα AZURE [98], για την ελαστική σκέδαση πρωτονίων από φθόριο επεκτείνοντας τα ήδη υπάρχοντα evaluated δεδομένα, που φτάνουν μέχρι τα 1730 keV, μέχρι τα 2250 keV (ενέργεια της δέσμης).

Τα βήματα των υπολογισμών περιλαμβάνουν αρχικά τη βιβλιογραφική εξέταση των διαθέσιμων πειραματικών διαφορικών ενεργών διατομών και της φασματοσκοπίας του σύνθετου πυρήνα ^{20}Ne. Δεδομένου ότι τα διαθέσιμα πειραματικά δεδομένα σε μεγαλύτερες ενέργειες από τα 1700 keV παρουσιάζουν ιδιαίτερα πολύπλοκη δομή με επικαλύψεις συντονισμών, αλλά και με διαφορές στις απόλυτες τιμές διαφορικών ενεργών διατομών, οι

υπολογισμοί βασίστηκαν κυρίως στα πειραματικά δεδομένα της παρούσας εργασίας που έχουν ελεγχθεί για την ορθότητά τους (προηγούμενη ενότητα), τα οποία περιγράφουν με ικανοποιητικό βήμα την ενεργό διατομή ελαστικής σκέδασης μέχρι τα ~2250 keV (Σχήμα 2.5). Σημαντική πληροφορία αντλήθηκε παρ' όλα αυτά από δεδομένα της βιβλιογραφίας για συγκεκριμένες ενεργειακές περιοχές όπως γύρω από τα 1750 keV και τα διαθέσιμα benchmarking φάσματα, με στόχο μια παστίλια ZnF_2 pellet για ενέργειες πρωτονίων μέχρι τα 2250 keV και γωνίες ανίχνευσης στις 140°, 150°, 160° και 170°, που υποβοήθησαν τη διαδικασία των θεωρητικών υπολογισμών (feedback) αλλά και τον έλεγχο των αποτελεσμάτων, όπως περιγράφεται στην επόμενη παράγραφο. Να σημειωθεί εδώ ότι τα φάσματα στα 2000 keV με την παστίλια ZnF_2 δε χρησιμοποιήθηκαν, καθώς η συνεισφορά από την $^{19}F(p,\alpha_4)$ αντίδραση ήταν σημαντική, λόγω της συγκρίσιμης ενεργού διατομής της με αυτή της ελαστικής κοντά στα 1900 keV. Στην περίπτωση αυτή, οι θεωρητικοί υπολογισμοί βασίστηκαν μόνο στα επιλεγμένα πειραματικά δεδομένα χρησιμοποιώντας λεπτό στόχο που κατέδειξαν την ιδιαίτερα ισχυρή λεπτή δομή της διαφορικής ενεργού διατομής στην ενεργειακή περιοχή ~1850-1950 keV.

Χρησιμοποιώντας τα δεδομένα του Tilley et al. [102] για τις 15 αντίστοιχες στάθμες του ^{20}Ne με μικρές ενεργειακές μετατοπίσεις και αλλαγές στα εύρη Γ και προσθέτοντας μια στάθμη στα 14.669 MeV (2^-) με Γ_p=6.4 keV και Γ=16 keV δίπλα στην αμφίβολη στάθμη μεγάλου εύρους η οποία έχει αναφερθεί στα 14.693 MeV (1^+) για την αναπαραγωγή της συντονιστικής δομής γύρω από την ενέργεια δέσμης ~1.92 MeV (και αντίστοιχη ενέργεια διέγερσης ~14.67 MeV του ^{20}Ne), οι υπολογισμοί με τον κώδικα AZURE έδωσαν τα αποτελέσματα που φαίνονται στα Σχήματα 4.1. Τα αποτελέσματα στα άνω γραφήματα 4.1 συγκρίνονται με τα υπάρχοντα θεωρητικά αποτελέσματα (SigmaCalc [25]), όπου η αναπαραγωγή των δεδομένων είναι πολύ καλή ως τα ~1.5 MeV, ενώ για μεγαλύτερες ενέργειες οι υπολογισμοί δίνουν υψηλότερες τιμές, συμφωνώντας με τα επιλεγμένα πειραματικά δεδομένα, όπως φαίνεται και στα κάτω γραφήματα 4.1.

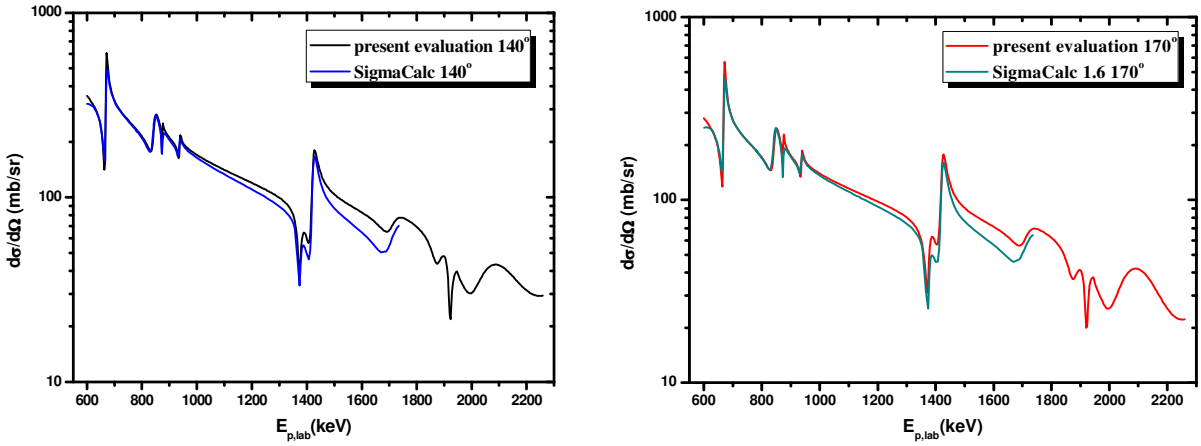

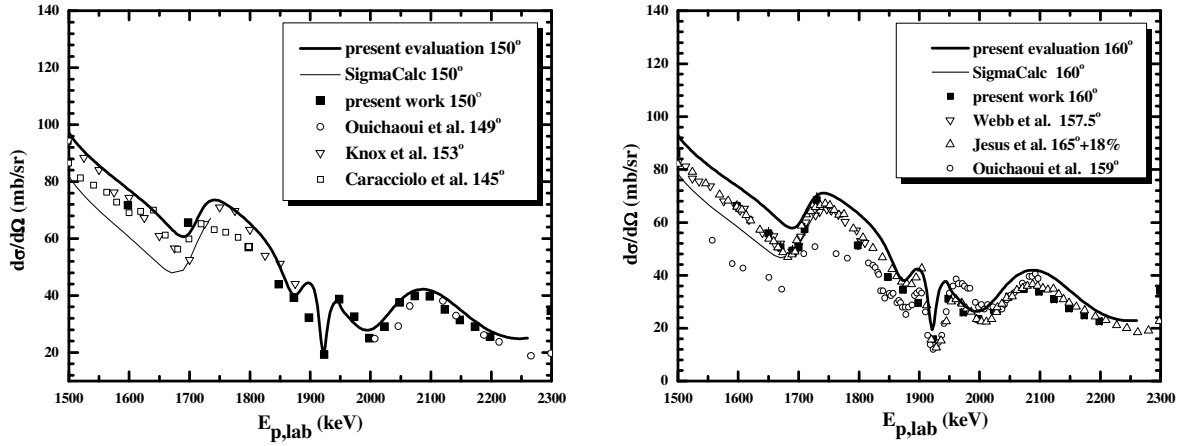

Σχήματα 4.1: Τα αποτελέσματα της παρούσας μελέτης (evaluation) μαζί με τα υπάρχοντα evaluated δεδομένα από το SigmaCalc (έως τα 1730 keV) στις 140° και 170° (πάνω) και στις 150° και 160° μαζί με επιλεγμένα δεδομένα της βιβλιογραφίας (κάτω).

Τα διαθέσιμα benchmarking φάσματα χρησιμοποιώντας παστίλια ZnF_2 pellet στα 1730 και 2250 keV, χρησιμοποιήθηκαν τέλος και για τον έλεγχο της ορθότητας των θεωρητικών αποτελεσμάτων της παρούσας εργασίας για την $^{19}F(p,p)$ σκέδαση, όπως φαίνεται στα Σχήματα 2.2. Η συνεισφορά υποβάθρου στα φάσματα αυτά, προερχόμενη από γεγονότα μετά τις $^{19}F(p,\alpha_3)$ and $^{19}F(p,\alpha_4)$ ήταν αμελητέα, όπως αναμενόταν, αλλά φάνηκε και στα ίδια τα φάσματα. Τα προσομοιωμένα φάσματα (με τον κώδικα SIMNRA [70]) αναπαράγουν εντός ~3-7% τα πειραματικά φάσματα, επαληθεύοντας τις evaluated τιμές διαφορικών ενεργών διατομών της παρούσας εργασίας που χρησιμοποιήθηκαν στις προσομοιώσεις.

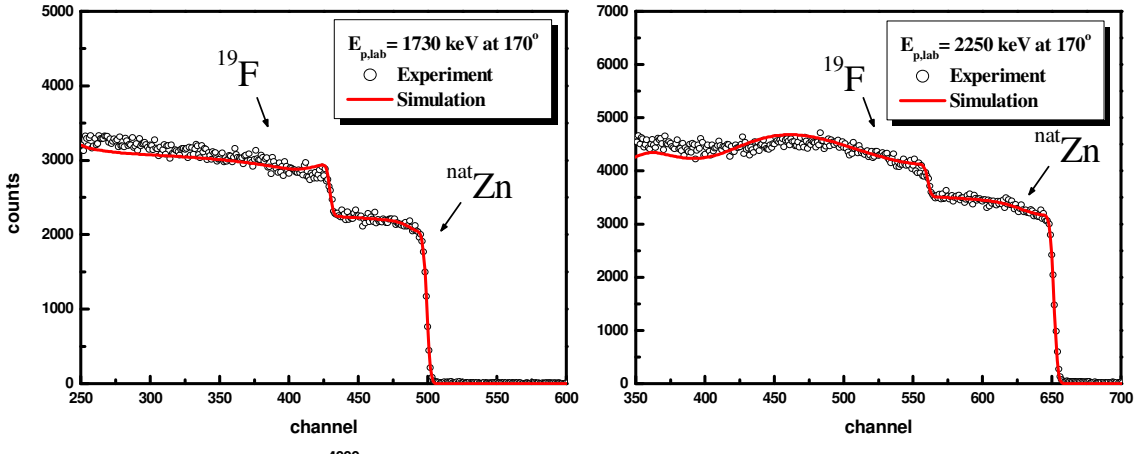

Σχήματα 4.2: Πειραματικά φάσματα ακτινοβολώντας την παστίλια ZnF_2 στις 170°, μαζί με τα αντίστοιχα προσομοιωμένα φάσματα χρησιμοποιώντας τις evaluated διαφορικές ενεργές διατομές της παρούσας μελέτης.

5. Προοπτικές

Η εφαρμογή και η αξιοπιστία των EBS και NRA αναλυτικών τεχνικών βασίζονται σε μεγάλο βαθμό στις χρησιμοποιούμενες διαφορικές ενεργές διατομές. Κρίνεται λοιπόν απαραίτητη η περαιτέρω μελέτη και ο προσδιορισμός διαφορικών ενεργών διατομών με μεγάλη ακρίβεια στις περιπτώσεις που τα δεδομένα της βιβλιογραφίας παρουσιάζουν μεγάλες αποκλίσεις και ειδικά στις περιπτώσεις εκείνες που η βιβλιογραφία παρουσιάζει ελλείψεις, όπως η ελαστική σκέδαση δευτερίων από ελαφρείς πυρήνες. Ο έλεγχος της αξιοπιστίας των διαφορικών ενεργών διατομών (benchmarking) μπορεί τελικά να οδηγήσει στα πιο ακριβή αναλυτικά αποτελέσματα και για αυτό είναι πολύ σημαντικό να ελεγχθούν όλες οι τιμές και ειδικά τα evaluated δεδομένα που θεωρούνται τα πιο αξιόπιστα, αφού παράγονται ενσωματώνοντας τα αντίστοιχα πειραματικά δεδομένα σε ένα ενιαίο θεωρητικό πλαίσιο. Η διαδικασία benchmarking αναμένεται λοιπόν να αποτελέσει ένα σημαντικό πεδίο έρευνας τα επόμενα χρόνια (τρέχων τεχνικό πρόγραμμα της IAEA), επεκτείνοντας τη μελέτη σε ανεξάρτητα εργαστήρια, χρησιμοποιώντας διαφορετικούς στόχους αλλά και ενσωματώνοντας διαφορετικές πειραματικές τεχνικές όπως ΔΕ/Ε ανίχνευση, ώστε να ελεγχθούν/μελετηθούν οι διαφορικές ενεργές διατομές και για προβληματικές περιπτώσεις όπως η σκέδαση ^{nat}B(p,p). Νέες αξιόπιστες μετρήσεις διαφορικών ενεργών διατομών, μαζί με τα αντίστοιχα πειράματα benchmarking μπορούν να οδηγήσουν στην επέκταση των evaluations σε υψηλότερες ενέργειες για χρήση των IBA τεχνικών σε μεγαλύτερα βάθη, αλλά και να χρησιμοποιηθούν στους θεωρητικούς υπολογισμούς για δύσκολες περιπτώσεις, όπως η σκέδαση ^{nat}B(p,p), που δεν υπάρχουν evaluated δεδομένα ενώ είναι απαραίτητα στην IBA κοινότητα.

Επιπλέον, benchmarking μελέτη με διαχωρισμό πρωτονίων-άλφα σωματιδίων (π.χ. με τη ΔΕ/Ε τεχνική) συγκεκριμένα για τη σκέδαση ^{19}F(p,p) στην προβληματική περιοχή γύρω από τα 1900 keV θα συμβάλλει στον ακριβέστερο καθορισμό των αντίστοιχων παραμέτρων των θεωρητικών υπολογισμών της παρούσας εργασίας. Ταυτόχρονοι θεωρητικοί υπολογισμοί για τα (p,α) κανάλια θα προσφέρουν επίσης ιδιαίτερα σημαντικές πληροφορίες για το σύστημα p+^{19}F και τις παραμέτρους του μοντέλου (αφού θα πρέπει να τονιστεί ότι οι θεωρητικοί υπολογισμοί-evaluation είναι μια δυναμική διαδικασία βασιζόμενη στα πειραματικά δεδομένα).

Τέλος, τα αποτελέσματα της παρούσας εργασίας από τη μελέτη του συστήματος d+^{nat}Mg καλύπτουν μεγάλο εύρος γωνιών ανίχνευσης και καναλιών εξόδου και μπορούν να συνεισφέρουν σε μελλοντική μελέτη για το χαρακτηρισμό των αντίστοιχων ενεργειακών σταθμών του σύνθετου πυρήνα ^{26}Al.

ABSTRACT

The Ion Beam Analysis (IBA) techniques are a powerful tool to investigate in a non-invasive way the near-surface composition of a material. To this purpose, the object to be analyzed is used as a target for a beam of accelerated charged particles. The interactions of the beam particles with the atoms (or the nuclei) of the target material induce from the latter the emission of secondary radiation (X-rays, gamma rays, particles), having an energy characteristic of the emitting atom or nucleus. Suitable detectors are then used to collect and discriminate in energy the emitted radiation. In the case of emitted particles their energy also depends on the energy losses both of projectiles and registered particles on the paths traversing by them in the sample before and after the interaction respectively. This makes it possible not only to detect an element but also to determine the depth profile of its concentration in a single measurement. Ion Beam Analysis techniques are thus implemented on a wide variety of applications, ranging from environmental studies, cultural heritage and geology to semiconductor, metallurgy and chemistry.

Among the IBA techniques, EBS (Elastic Backscattering Spectroscopy) and NRA (Nuclear Reaction Analysis), depending on the interaction occurring in the target between the accelerated particles and the atomic nuclei, are especially suited for light element detection, which generally constitutes a great challenge in the field. The application of these methods requires the determination of the differential cross sections used in the concentration calculations, over a wide range of energies and detection angles with the highest possible accuracy. The theoretically evaluated cross-section data are the most reliable ones to be used in such analytical studies, since they involve a critical assessment of the available experimentally determined cross sections, followed by a proper tuning of the corresponding nuclear model parameters. The existing experimental data are quite scarce and discrepant in many cases, hindering both their direct use in implementing the aforementioned IBA techniques and the corresponding evaluation process, thus limiting the applicability of both EBS and NRA.

My dissertation's contribution in this field mainly involves the measurement of selected reactions critical for EBS and NRA purposes. Using these reactions, natural magnesium, fluorine and lithium can be accurately determined in near surface layers of materials. Part of my research also involves the development of an experimental procedure, called benchmarking, for the validation of charged particle differential cross section datasets, which is indeed of great importance for all analytical applications. Benchmarking is an integral experiment that needs to

be very carefully designed and performed, since a great number of parameters need to be investigated and accurately determined. Benchmarking is actually in many ways critical for the implementation of EBS and NRA techniques in material analysis, besides the validation of differential cross-section data, since it also provides feedback for the adjustment of the parameters of the nuclear model used in the evaluation procedure. Moreover, it can facilitate the extension of the existing evaluations to higher energies, it can help in assigning realistic uncertainties to the cross sections, and it can also indicate recommended experimental datasets to be used in analysis in the absence of theoretically evaluated ones.

The theoretical approach of the elastic scattering and particularly the scattering theory, along with the subsequent theoretical models used in the evaluation procedure of the cross section data, is also presented in this dissertation. Namely, the case of the $^{19}F(p,p_0)$ elastic scattering was studied, performing R-matrix calculations with the use of the AZURE code.

CHAPTER 1

ION BEAM ANALYSIS

The aim of this chapter is to present an overview of the Ion Beam Analysis (IBA) fundamentals. Starting from an overview of the corresponding theory, not only concerning the related nuclear physics concepts and models, but also concerning the experimental features present in the corresponding spectrometry, this chapter presents the important aspects of Ion Beam Analysis. All the nuclear techniques used in this field are briefly described here, while the basic ones are throughout analyzed. The implementation of these techniques is investigated in all aspects, proving the importance and the critical role of the differential cross sections of the studied nuclear reactions. The subsequent motivation of the present thesis in this field is eventually presented in the end of this chapter.

Ion Beam Analysis is a powerful tool in the general field of applied nuclear physics, to study the near-surface composition of a material in a non-destructive way, with the use of an accelerated ion beam impinging on the sample of interest (target). The quantification and the depth profiling of an element in a sample is achieved by detecting the emitted radiation (particles, gamma-rays, X-rays) after the interaction between the charged particles of the beam and the nuclei or the atoms of the target, as sketched in Figure 1.1. The energy of the emitted radiation is characteristic for each interaction, enabling the determination of elemental or isotopic concentration in depth. IBA techniques are therefore implemented on a wide variety of applications, ranging from environmental studies, cultural heritage, geology, to semiconductor, metallurgy and chemistry.

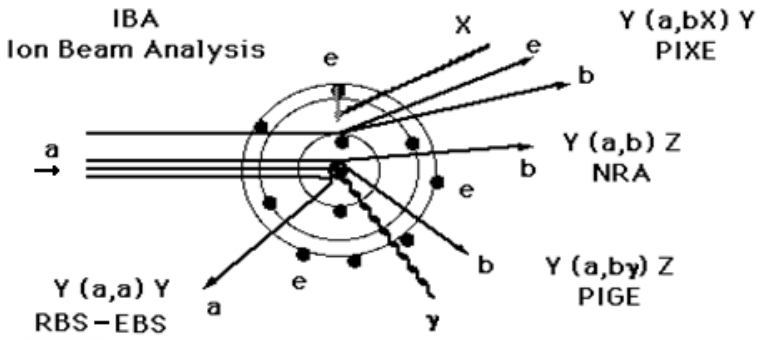

Figure 1.1: Schematics of the processes exploited by Ion Beam Analysis indicating the most commonly used techniques, detecting the corresponding outgoing particle or radiation.

1.1 General features of theory

An overview of the interaction between the projectiles and the nuclei of the target is described in this section, in order to present the main features of the underlying nuclear physics. Among all the reaction mechanisms, that are mentioned here, the elastic scattering theory is in more detail analyzed, in order to reveal the differences between the potential scattering and the compound nucleus scattering, as illustrated in section 1.1.2, characterizing the corresponding IBA techniques. The application of these techniques, determined by the corresponding spectrometry, is totally related to phenomena occurring during the experimental procedure. The theoretical assessment of these spectrometry features plays a key role in the implementation of the techniques and is therefore also presented below.

1.1.1 Reaction mechanisms

The contributing reaction mechanisms for the projectile–nucleus interaction are sketched in the following figure 1.2 in chronological series of occurrence, showing the connection between all processes. Only the main categorization of the reactions is, however, briefly described here, concerning a light charged–particle beam, which is the case study in this dissertation.

As sketched in Figure 1.2, after the first interaction, the projectile may leave the nucleus immediately by a direct reaction or interact with a nucleon and start a cascade of nucleon-nucleon interactions from which pre-equilibrium emission may occur. During this cascade, the energy is shared among an increasing number of nucleons until the eventual formation of the compound nucleus, which may decay into the elastic or any of the reaction channels that are allowed energetically.

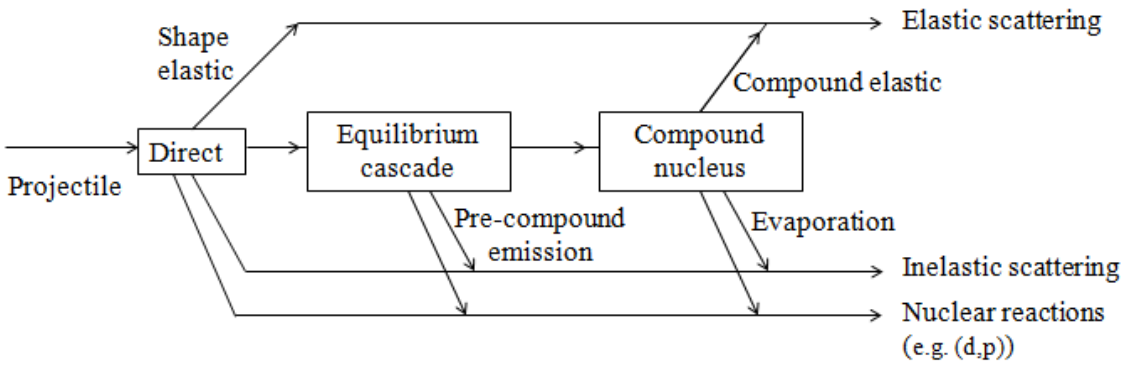

Figure 1.2 Direct, pre-compound and compound nucleus contributions to a nuclear reaction [based on 1].

The combination of the shape and the compound elastic processes gives the measured elastic scattering cross section, while the direct, pre-equilibrium and compound nucleus inelastic processes combine to give the inelastic cross sections concerning all the other non elastic reactions.

It should be noted here that the contribution of each mechanism depends mainly on the beam energy and on the projectile-target combination and is actually a subject of investigation most of the times, as analyzed in the following section (1.1.2).

a) Direct reactions

The direct reactions take place in the time the projectile takes to traverse the target nucleus, typically around 10^{-22} s. In these processes the projectile may interact with a nucleon or a group of nucleons or the whole nucleus (potential scattering) and emission takes place immediately. Exactly because of the momentum transfer to a small amount of nucleons or due to the form of Coulomb potential (scattering), there is a strong forward angular dependence for this kind of reactions. The simplest direct reaction is elastic scattering, which leaves the target nucleus in the ground state. It is also called potential or shape elastic scattering, because it proceeds through the direct interaction of a single bombarding particle with a potential well, representing the nucleus. Protons at very low energies for example, are repelled by the electrostatic field of the nucleus (Coulomb) and are scattered elastically with a cross section given by the Rutherford formula, which is described in the following section concerning the scattering theory (1.1.2). Inelastic scattering predominantly excites collective states, one nucleon transfer reactions excite single-particle states and multinucleon transfer excites cluster states.

Most of our knowledge of nuclear structure comes from direct reaction studies (for example the (d,p) ones), measuring the absolute cross section for exciting each state, the angular distribution of the emitted particles and if possible their polarization.

b) Compound nucleus reactions

In these reactions the projectile is captured (absorbed) by the target nucleus producing an intermediate compound nucleus, while its energy is shared and re-shared among all the nucleons of the compound nucleus until it reaches a state of statistical (thermal) equilibrium. After a time much longer than the time required by the projectile to cross the nucleus (to pass through the region occupied by the potential well of the nucleus), a nucleon or a group of nucleons near the

surface may receive enough energy to escape. This required time depends on the projectile energy and at low incident energies may be 10^6-10^7 times greater than the transit time (the time of direct interaction) and at high incident energies it may be only about 10-100 times greater [1]. A typical lifetime for a compound nucleus, which is always highly excited because the absorbed particle brings both its kinetic and bond energy, is ~10^{-14} s. This statistical process, leads eventually to the decay of the compound nucleus with the emission of some particle, favoring the evaporation of particles with energy near the smallest possible energy to any direction (with front–back symmetry). If the excitation energy of the compound nucleus is high enough, several particles may be evaporated in sequence and the process continues until the energy of the nucleus is below the threshold for particle emission and then the energy emits γ-rays until it reaches the ground state. The compound elastic scattering case is the one of emitting the same particle as the absorbed one (projectile), after forming the compound nucleus, and leaving the residual nucleus (the re-formed original one) in ground state. This scattering is strongly affected by the structure of the compound nucleus, mainly concerning its energy levels, as further described in the following 1.1.2 section. The nucleus may however decay in a variety of other ways, for example heavy compound nuclei may fission into two fragments of comparable mass.

Information gained from the study of compound nucleus processes includes the properties of the states of the compound nucleus, the mechanism of nuclear deexcitation including the role of the angular momentum and the nuclear deformation in affecting particle evaporation.

c) Pre-equilibrium reactions

It is also possible that a particle is emitted neither immediately after a direct reaction, nor after a long time by the statistical decay of the compound nucleus. The projectile may share its energy among a small number of nucleons, which may further interact with other nucleons and during this cascade of nucleon–nucleon interactions through which the energy of the incident particle is progressively shared among the target nucleons, a particle may be emitted again to any direction long before the attainment of statistical equilibrium. These processes constitute the pre-compound or pre-equilibrium reaction mechanism. The study of these reactions is of great importance to investigate the mechanism of thermalization of the nucleus, i.e. the reaching of the statistical equilibrium state.

1.1.2 Scattering theory – cross section

The elastic scattering of the beam charged particles from the target nuclei depends on the interference of the Coulomb and the nuclear forces, as analyzed in this section. The penetration of the projectile in the nuclear-force short range depends mainly on the projectile energy and the target nucleus itself. This range leads actually to a strict demarcation between the regions where only long-range Coulomb forces or only nuclear forces operate, as the latter are at least 100 times greater than Coulomb forces at short distances of about 1 fm.

An atomic nucleus is a strongly bound system of nucleons located in a small domain with a typical radius $R=R_0A^{1/3}$ (fm) with R_0=1.1-1.5 [2 – chapter 3] with a typical value of R_0=1.25 fm [3], where A is the mass number. Considering the nucleus as a uniformly charged sphere of radius R, the dependence of the electrostatic potential energy on the distance r for the projectile–nucleus system, with charge z and Z respectively, is the following [2 – chapter 3]:

$$V_C(r) = \begin{cases} \dfrac{Zze^2}{r} & for\ r \geq R \\ \dfrac{Zze^2}{2R}\left(3 - \dfrac{r^2}{R^2}\right) & for\ r \leq R \end{cases} \qquad 1.1$$

The transition from repulsion to attraction for the combined Coulomb and nuclear potential, sketched in Figure 1.3 [2 – chapter 3], proceeds in a narrow region in the vicinity of the boundary of the nucleus (r_1 and r_2 are the classical turning points). A charged particle should have sufficient kinetic energy T to overcome the Coulomb potential barrier of height $B_C = \frac{Zze^2}{R}$, in order to reach the range of nuclear forces. According to quantum mechanics, however, the particle can still penetrate through the barrier even in the case of having kinetic energy below the potential barrier, with its **transparency** D being given by the following equation. Therefore, nuclear reactions with low energetic charged particles are indeed feasible at energies below the potential barrier. The two regions of both forces, the long ranged Coulomb and the short ranged nuclear ones, are thereby interfering, thus mixing the corresponding two kinds of scattering, as further explained below.

$$D \approx exp\left[-\frac{2}{\hbar}\int_{r_1}^{r_2}\sqrt{2\mu(V_C - T)}\,\mathrm{dr}\right] \qquad 1.2$$

where $\mu = Mm/(M+m)$ is the reduced mass.

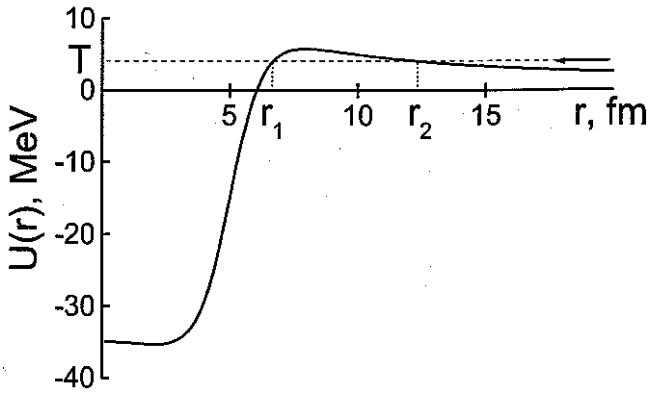

Figure 1.3: The combined Coulomb and nuclear potential of a nucleus. The classical turning points for a particle with kinetic energy T are located at r_1 and r_2 [2 – chapter 3].

If the projectile-nucleus interaction is conditioned **solely** by the long range electric (Coulomb) forces, then the **differential cross section** $\frac{d\sigma}{d\Omega}$ of an elastic scattering event, generally defined as the probability of a reaction to occur, can be analytically calculated using the **Rutherford formula**, derived from the conservation of energy and angular momentum and defining the impact parameter b as the perpendicular distance to the closest approach to the target nucleus (if the projectile were undeflected).

The differential cross section for the so-called Rutherford scattering $\frac{d\sigma_R}{d\Omega}$, which denotes the probability of a particle (Z_1, M_1) with energy E to be scattered from a nucleus (Z_2, M_2) to an angle θ per steradian (Ω), in the laboratory system, is given by:

$$\frac{d\sigma_R}{d\Omega}(E,\theta)=\left(\frac{Z_1 Z_2 e^2}{4E}\right)^2 \frac{\left[(M_2^2-M_1^2\sin^2\theta)^{1/2}+M_2\cos\theta\right]^2}{M_2\sin^4\theta\left(M_2^2-M_1^2\sin^2\theta\right)^{1/2}} \qquad 1.3$$

At **short distances** though, of the order of the range of the nuclear forces, simultaneous knowledge of the momentum and the impact parameter (distance-position) of the scattering particle is impossible according to Heisenberg's uncertainty principle. Consequently, no theory can in principle incorporate the nuclear forces for the determination of the particle trajectory. In this framework, **quantum mechanics** must be used instead of classical physics. In this region, elastic scattering differential cross sections deviate [3] from the Rutherford ones, exactly

because of the interference between the nuclear and Coulomb scattering, as mentioned above (see barrier transparency D). These phenomena can be studied and analyzed in the framework of quantum mechanics with the help of suitable models, as described in the next paragraphs.

The elastic scattering of two nuclei (projectile m_1 with a target nucleus m_2) can be described by the Schrödinger equation with a potential V, generally depending on the distance between the two particles, their spin and relative velocity [3]. Considering the coordinates of the two particles with vectors r_1 and r_2 relative to an arbitrary origin fixed in the laboratory frame of reference, the separation vector $\boldsymbol{r} = r_1 - r_2$ is independent of the origin choice, while the vector $R_{CM} = (m_1 r_1 + m_2 r_2)/(m_1 + m_2)$ describes the motion of the center of mass system (CM) of the two particles in the laboratory one (LAB). By writing: $\boldsymbol{\psi(r_1, r_2) = \psi(r)\chi(R_{CM})}$, the Schrödinger equation for the total motion in the LAB system can be separated into two equations: one for the relative motion in the CM system and one for the motion of the centre of mass in the LAB system respectively, as follows [3]:

$$\nabla^2\psi(r) + \frac{2\mu}{\hbar^2}(E_{ch} - V)\psi(r) = 0 \qquad 1.4$$

$$\nabla^2\chi(R_{CM}) + \frac{2M}{\hbar^2}(E_{LAB} - E_{ch})\chi(R_{CM}) = 0 \qquad 1.5$$

where $M = m_1 + m_2$, $\mu = m_1 m_2/(m_1 + m_2)$ is the reduced mass of the two particles with the projectile (m_1) having kinetic energy E_{LAB}. Then the channel energy is $E_{ch} = \frac{m_2}{m_1+m_2}E_{LAB}$, being the only available energy to initiate reactions. The interaction potential V denotes the combined nuclear and Coulomb potential.

The **second equation** describes the uniform motion of the centre of mass in the LAB system. Taking the z-axis for this direction of motion of the center of mass (beam direction), the equation has the plane wave solution:

$$\chi(z) = \exp\left\{iz\left[\frac{2M}{\hbar^2}(E_{LAB} - E_{ch})\right]^{\frac{1}{2}}\right\} \qquad 1.6$$

It should be noted here that all the above calculations are non-relativistic, which is usually adequate for low energy nuclear reactions used in IBA. At higher energies, namely above 100 MeV, the corresponding relativistic equations must be used. These cases are beyond the scope of the present dissertation and are thus not included here.

The **first equation**, describing the interaction of two particles through a potential V(r), actually contains all the physics of the interaction. It indeed shows that the Schrödinger equation describing the motion of two interacting particles is equivalent to that of one particle with the reduced mass μ in one-body potential. The solution of this equation gives the elastic scattering cross section as a function of the incident energy, but an analytical solution is not possible to be obtained. Only **approximate** numerical solutions can be applied, as briefly shown in the subsequent analysis that follows.

An approximate solution when $\boldsymbol{E_{ch} \gg |V(r)|}$ is the following (first order Born approximation) [3]. For quantitative analysis the equation is considered in spherical coordinates giving a general solution ψ of the following form, with the Legendre polynomial denoted as $P_l(cos\theta)$, the radial wave function as R_{kl} and a coefficient A_l, explained below. It is evident that each partial wave corresponds to particles moving with a given orbital momentum l and is characterized by the $P_l(cos\theta)$ angular distribution *(partial wave expansion*).

$$\psi = \sum_{l=0}^{\infty} A_l \, P_l(cos\theta) R_{kl}(r) \qquad 1.7$$

Prior to scattering, the wave function ψ for a particle with a given momentum p has the form of a plane wave $\boldsymbol{e^{ikz}}$, expressed in spherical coordinates, considering that far from the center of scattering (at large distance r) the radial function for each component l can be represented in the form of two partial spherical waves, one convergent $e^{-i\left(kr-l\frac{\pi}{2}\right)}$ and one divergent $e^{i\left(kr-l\frac{\pi}{2}\right)}$ from the center of the interaction. The plane wave describing this initial stage of scattering is thus depicted with these spherical waves having equal amplitudes, as follows:

$$\boldsymbol{\psi = e^{ikz} = \sum_{l=0}^{\infty} \frac{(2l+1)i^l}{2ikr} P_l(cos\theta) \left[e^{i\left(kr-l\frac{\pi}{2}\right)} - e^{-i\left(kr-l\frac{\pi}{2}\right)}\right]} \qquad 1.8$$

where k is a propagation vector $k = \frac{p}{\hbar} = \frac{1}{\lambda}$ or $k^2 = \frac{2\mu}{\hbar}(E_{ch} - V) \approx \frac{2\mu}{\hbar}E_{ch}$

with $\lambda\!\!\!^{-}$ the reduced de Broglie wavelength ($\lambda\!\!\!^{-} = \frac{\lambda}{2\pi}$)

In the course of scattering, the plane wave interacts with the field of the nucleus V(r), giving rise to a spherical wave divergent from the center of the interaction to the (θ,φ) direction. In the case of azimuthal asymmetry around the z axis, as in the case of unpolarized particles and targets (considered spinless), it gets the form of:

$$\boldsymbol{f(\theta)\frac{e^{ikr}}{r}} \qquad 1.9$$

The 1/r factor represents the decreasing of the flux in inverse proportionality to the square of distance ($\psi\psi^* \sim \frac{1}{r^2}$), while $f(\theta)$ is the amplitude of the wave and θ the scattering angle.

In spherical coordinates, the additional divergent wave induces the $\boldsymbol{S_l}$ coefficient at the divergent wave to the radial part R_{kl} , since the ratio between the two spherical partial waves changes. It has therefore the form of:

$$R_{kl} \sim S_l e^{i\left(kr - l\frac{\pi}{2}\right)} - e^{-i\left(kr - l\frac{\pi}{2}\right)} \qquad 1.10$$

In the case of elastic scattering though, the fluxes for the convergent and divergent should be equal, meaning that $|S_l|^2 = 1$. This factor can thus be written as follows:

$$\boldsymbol{S_l = e^{2i\delta_l}} \qquad 1.11$$

$\boldsymbol{\delta_l}$ is called phase shift of the $\boldsymbol{l}$th partial wave and it physically denotes the difference in the wave velocity in the presence of the nuclear force field inside the nucleus as illustrated in Figure 1.4 [2 – chapter 3]. In the elastic scattering they are real numbers, while in the case of inelastic ones they become complex, decreasing the amplitude of the divergent waves ($|S_l|^2 < 1$).

After the scattering, the superposition of the plane wave e^{ikz} and the $\frac{e^{ikr}}{r}f(\theta)$ one, depicts the interaction problem, which can thereby be treated with the wavefunction ψ given by the following relation, expressed also in spherical coordinates:

$$\boldsymbol{\psi \approx e^{ikz} + \frac{e^{ikr}}{r} f(\theta) = \sum_{l=0}^{\infty} \frac{(2l+1)i^l}{2ikr} P_l(cos\theta) \left[e^{2i\delta_l} e^{i\left(kr - l\frac{\pi}{2}\right)} - e^{-i\left(kr - l\frac{\pi}{2}\right)} \right]} \qquad 1.12$$

$$\boldsymbol{f(\theta) = \frac{1}{2ik} \sum_{l=0}^{\infty} (2l+1)\left(e^{2i\delta_l} - 1\right) P_l(cos\theta)} \qquad 1.13$$

In the case that the projectile has a nonzero spin, the equations become more complicated because the radial wave equation splits into 2s+1 equations, but the entire described scheme remains valid. Moreover, taking into account the known Coulomb potential for charged projectiles, an additional term in the scattering amplitude is needed, with $\boldsymbol{\sigma_l}$ the phase shifts for Coulomb scattering respectively. Then the scattering amplitude is given by the following relation.

$$\boldsymbol{f(\theta) = f_C(\theta) + \frac{1}{2ik} \sum_{l=0}^{\infty} (2l+1)\left(e^{2i\delta_l} - 1\right) e^{2i\sigma_l} P_l(cos\theta)} \qquad 1.14$$

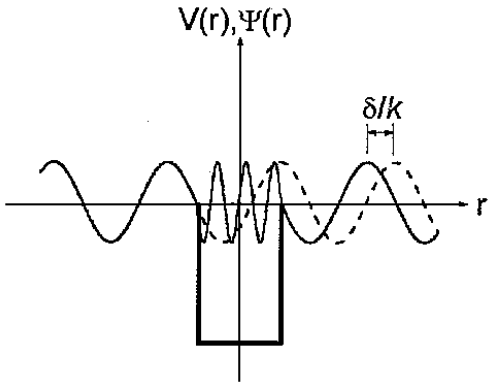

Figure 1.4: Formation of the wave phase shift [2 – chapter 3]. After the scattering the partial wave has the form of $R_{kl} \approx e^{i\left(kr - l\frac{\pi}{2} + 2\delta_l\right)} - e^{-i\left(kr - l\frac{\pi}{2}\right)}$.

By definition, the differential cross section $\frac{d\sigma}{d\Omega}$ is equal to the fraction dN/N of projectiles scattered into the given solid angle, as sketched in Figure 1.5. The number of particles dN traversing the surface element dS per unit time is determined by the probability of finding particles in the elementary volume $dV=vr^2\sin\theta d\theta d\varphi$, with v the particle velocity. Since $d\Omega=\sin\theta d\theta d\varphi$, one can immediately derive the following relation concerning the differential cross section [2 – chapter 3], showing that the angular distribution of the scattered particles is defined by the scattering amplitude f(θ).

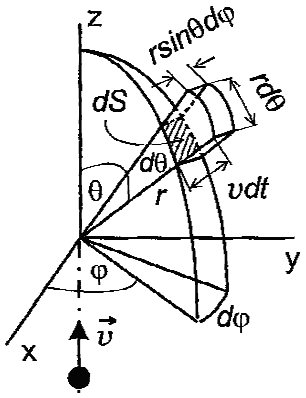

Figure 1.5: Illustration of the definition of the differential cross section [2 – chapter 3].

$$\frac{d\sigma}{d\Omega} = |f(\theta)|^2 \qquad 1.15$$

Differential cross section for elastic scattering can therefore be calculated from the above equation with the f(θ) function, being expressed through phase shifts δ_l. The exact knowledge of the phase shifts δ_l themselves is actually sufficient for the cross section determination, while the experimental determination of differential cross sections with detectors placed at suitable scattering angles enables in reverse the phase shifts assessment.

The phase shifts being functions of k and l, do not depend on the scattering angle and are calculated by solving the Schrödinger equation (eq. 1.4) with an **assumed potential V(r)** and boundary conditions concerning the continuity of the solution and its first derivative at the nucleus surface at radius R.

The consideration made so far concerning the energy of the projectile and the potential, namely that $\boldsymbol{E_{ch} \gg |V(r)|}$ is actually not very realistic in most cases. As has already been pointed out, the interference of the absorptive effects (see 1.1.1 and transparency D, equation 1.2) needs also to be taken into account, since all the other channels, namely the direct non-

elastic processes, the pre-equilibrium and the compound nuclear reactions can also occur, affecting the elastic scattering cross-section [1]. The **optical model** [3,1], which is described in more detail in chapter 5 (section 5.1.33), is a relatively simple model used to account for elastic scattering in a general way, also incorporating these effects, by proposing a one-body complex potential V(r) to represent the scattering. The interaction is considered to be determined by the bulk features of the nucleus, meaning that the used potential depends mainly on the nuclear dimension and nuclear shape (without detailed structure). This potential consists of two parts, as seen in the following relation to describe a proper radial dependence.

$$\boldsymbol{V(r) = U(r) + iW(r)} \qquad 1.16$$

The real part, U(r), is responsible for the elastic scattering between the projectile and target and the imaginary part, W(r), for the absorption. The real part U(r) is similar to the shell-model potential and is thus described, with some energy dependent modifications, by the Woods-Saxon analytical expression [1], considering a diffuse nuclear surface, namely a smooth edge of the potential, around the mean nuclear radius R. On the contrary, a more complicated approach needs to be applied for the imaginary part, depending on the projectile energy. The full optical potential, including the Coulomb potential and a spin-orbit term has the following terms:

$$V(r) = V_C(r) + Uf_U(r) + iWf_W(r) + V_{SO}(r) \qquad 1.17$$

The smooth variations of the cross section, with broad minima and maxima can be in principle very well described with the optical model, while the strong resonant structure originating from the compound elastic scattering cannot. As has already been pointed out, compound elastic scattering is strongly affected by the structure of the compound nucleus. In particular, the energy at the maximum cross section corresponds to that one of the excited state of the compound nucleus and its width Γ gives the lifetime $\tau = \hbar/\Gamma$ of the state [1]. As seen in Figure 1.6 [2 – chapter 3], light nuclei present discrete energy levels and the cross section has thereby a resonant structure, while in the case of the high level density of heavy nuclei, smoother cross section dependence on energy is observed, because of the overlapping levels (Γ>D, where D is the energy spacing between sequential levels). In the intermediate case (Γ~D), where the level width Γ is comparable to the level spacing D, the cross section exhibits a strongly fluctuating structure, the so-called Ericson fluctuations [2 – chapter 3].

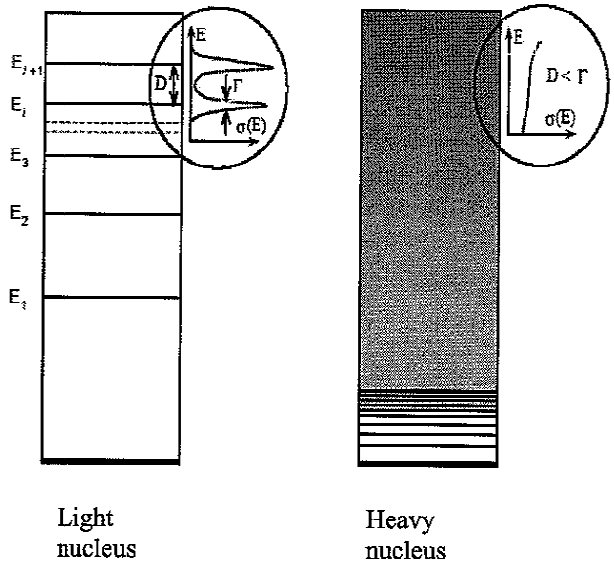

Figure 1.6: Diagrams of the energy levels for light and heavy nuclei and the corresponding cross section behavior [2 – chapter 3].

The strong resonant mechanism of light nuclei can be represented by the Breit-Wigner function (Lorentz type), which is the following formula, concerning the compound nucleus (CN) elastic cross section of a single isolated resonance (around the resonance energy E_R) for the orbital angular momentum l wave, considering all other channels closed [1].

$$\sigma_{E,CN,R}^{l} = \int |f(\theta)|^2 d\Omega = \frac{\pi}{k^2}(2l+1)\frac{\Gamma^2}{(E_R - E)^2 + \Gamma^2/4} \qquad 1.18$$

The cross section is of course composed of Coulomb, potential (optical model) and resonance terms, which amplitudes are added coherently. As a result of this interference, the excitation function (cross section) presents a typical structure with resonances pictured as dips and bumps, as shown in the Figure 1.7 [2 – chapter 3].

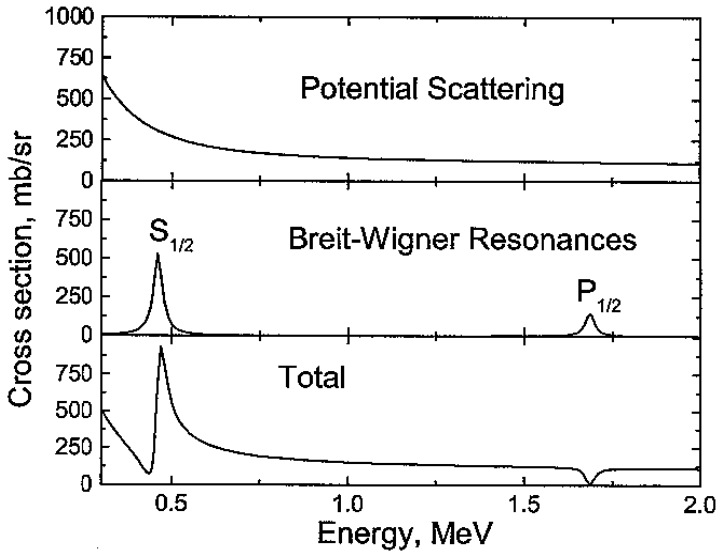

Figure 1.7: Interference of the potential and resonance scattering for $^{12}C(p,p_0)^{12}C$. Note that the resonance dramatically affects the cross section at energies much below the Coulomb barrier [2 – chapter 3].

1.1.3 Spectrometry

The theoretical aspects of studying the projectile-nucleus interaction with the use of an ion beam on a target are briefly described here, while the corresponding experimental part is thoroughly analyzed in chapter 2 and 3 (section 3.1). This procedure, which constitutes the foundation of Ion Beam Analysis, involves the detection of the outgoing particles, whereas the generated electrical signals get suitably processed, giving to the acquired data the form of a spectrum (hence the name spectrometry).

Starting from the exact point where the beam hits the target, one should consider four physical concepts entering into spectrometry, corresponding to specific physical phenomena [4]. Initially, the beam particles lose energy crossing the target material, before the point of interacting with its nuclei. This process leads to the concept of **stopping power** and to the capability of depth perception. Subsequently, there are statistical fluctuations in this energy loss of the beam particles moving through the dense medium (target), leading to the concept of **energy straggling** and to limitations in the achieved mass and depth resolution. Reaching eventually the projectile-nucleus interaction point, one should take into account the likelihood of occurrence of the specific nuclear reaction of interest. This leads to the third concept, the one of the **cross section** and of course to the capability of quantitative analysis. The last phenomenon

(fourth) certainly concerns the energy of the ejectile of the reaction, which is to be detected, and more specifically **the kinematic factor K** for the elastic scattering and the **Q-value** of the nuclear reaction. After the reaction, the emitted particles lose an additional amount of energy crossing back the material towards the detector. Consequently the energy of the detected particles depends on the depth at which the scattering occurred. Except for the case of the cross section concept, which has already been discussed above (1.1.2), all the other aspects will be analyzed in the following paragraphs.

1.1.3.1. Energy loss, stopping power

The physics of energy loss phenomena is very complex, involving many kinds of interactions among the projectile ion, the target electrons and nuclei. These phenomena have been the subject of intense studies since the beginning of the 20th century, because of their significant importance in many fields of physics. Concerning the Ion Beam Analysis field in the framework of this thesis, the situation will be simplified and limited to the basic concepts [2 – chapter 2] and models widely used.

The relative importance of the different interaction processes between the ion and the medium depends mostly on the ion velocity and on the atomic numbers of the ion and target atoms. The energy loss (ΔE) of the projectiles is defined as the average kinetic energy loss of point-like particles traversing matter, while the stopping power of a material for a particular ion is defined as the energy loss per distance travelled in the material, denoted as

$$S = \frac{dE}{dx} \qquad 1.19$$

This quantity depends on the ion type and the material traversed, as well as on the energy of the ion, and is usually considered in three velocity regimes, namely, low, intermediate and high velocities, as shown in Figure 1.8 [2 – chapter 2] for lithium ions in iron. The classification of the regimes is based on the ion velocity in comparison to the orbital velocity of the atomic electrons.

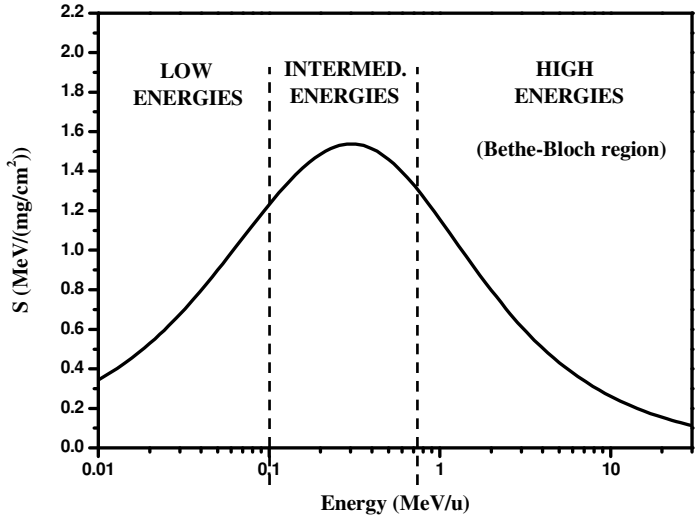

Figure 1.8: Regimes of ion stopping illustrated by ^{7}Li ions in iron.

At ion velocities v that are significantly lower than the Bohr velocity of the atomic electrons v_o the ion carries its electrons and tends to neutralize by electron capture. At very low velocities, elastic collisions with the target nuclei prevail and the so-called nuclear energy loss dominates. As the ion velocity increases, the nuclear energy loss diminishes as 1/E, as plotted in Figure 1.9 for silicon ions in silicon. Simultaneously, inelastic collisions with the atomic electrons become the main interaction, leading to significant increase of the so-called electronic energy loss. The total energy loss is in any case taken as the sum of the nuclear and electronic contributions. However, for most applications of Ion Beam Analysis, the nuclear contribution is small, typically below 1% of the electronic one (for energies above 200keV/amu).

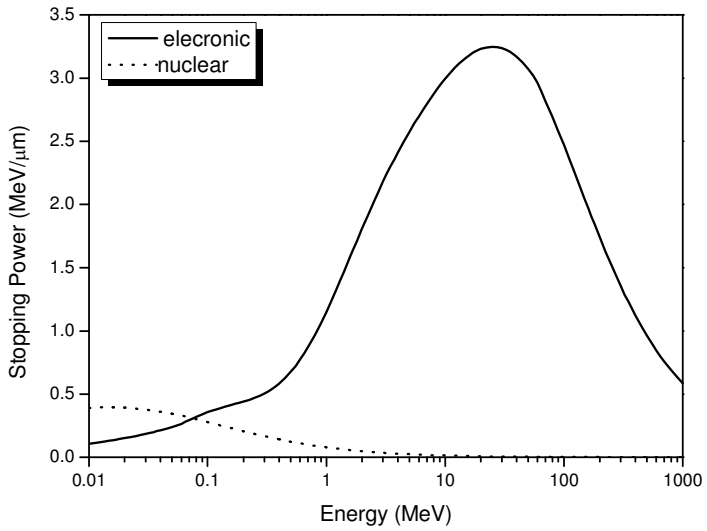

Figure 1.9: Electronic and nuclear stopping power for silicon ions in silicon, with the characteristic stopping maximum.

The theoretical framework for the energy loss was initially carried out by Bohr [4] and it is generally depicted through the well known **Bethe-Bloch formula** [3] that follows, concerning its relativistic form.

$$-\frac{dE}{dx} = \frac{4\pi}{m_e c^2}\frac{nz^2}{\beta^2}\left(\frac{e^2}{4\pi\varepsilon_0}\right)^2\left[ln\left(\frac{2m_e c^2\beta^2}{I(1-\beta^2)}\right)-\beta^2\right] \quad 1.20$$

The parameter I in this equation represents the mean excitation energy of the atomic electrons, which could in principle be computed by averaging over all ionization and excitation processes, but is rather regarded as an empirical constant with a value of the order of 10Z in eV. The electron density (electrons/cm^3) of the stopping target is denoted as $n=ZN_A\rho/A$.
Bethe Bloch equation is a good approximation at high energies, as shown in Figures 1.8 and 1.9, **beyond the maximum** in the stopping cross section, where the projectile is fully ionized [4].

The stopping cross section ε, is defined as the energy loss per atom per unit area (areal density) of material traversed. The relation between the two quantities is given by:

$$S \equiv \frac{dE}{dx} = N\varepsilon \quad 1.21$$

where N is the atomic density (atoms/cm^3).

Values of ion stopping cross sections in all elements are available from an extensive study based on semiempirical fitting of experimental data, while recent (up-to-date) data can be found in SRIM [5].

It should be noted here, that in cases of **compound** targets or **mixtures** of different elements, the Brag's rule approximation is used to calculate the stopping cross sections of the ions [4]. According to this approximation, each target atom acts independently in the energy loss process, ignoring any effects of chemical bonding in the material. This leads to the principle of linear additivity of stopping cross sections, postulated first by Bragg and Kleeman [2 – chapter 4], according to which the energy loss in the medium composed of various atomic species is the sum of the losses in the constituent elements, weighted proportionately to their abundance in the compound. The compound stopping cross section ε^{AmBn} of a molecule A_mB_n (or a mixture with equivalent composition) is given by the following relation, in terms of energy loss per molecule per unit are traversed:

$$\varepsilon^{A_m B_n} = m\varepsilon^A + n\varepsilon^B \quad 1.22$$

where ε^A and ε^B are the stopping cross sections of the atomic constituents A and B.
The corresponding stopping power is thus given by:

$$\left(\frac{dE}{dx}\right)^{AB} = N^{AB}\varepsilon^{AB} = N_A^{AB}\varepsilon^A + N_B^{AB}\varepsilon^B \quad 1.23$$

where N^{AB} is the molecular density (molecules/cm^3) and N_A^{AB} and N_B^{AB} are the atomic densities of A and B respectively (the subscripts m and n are suppressed in this notation). Deviations on the Bragg rule have been reported and a correction factor can be applied but further analysis is out of the scope of this thesis.

Model used

The compilation by Ziegler, Biersack and Littmark [6] based on electronic stopping power data consists the most frequently used model for the stopping power calculations of incident protons, deuterons and tritons in all elements. The electronic stopping power *Se* in eV/(10^{15} atoms/cm^2) for an incident hydrogen ion with energy/mass E in keV/amu, in the energy range of 10 keV/amu $\leq E <$ 10 MeV/amu, is given by:

$$S_e = \frac{S_{Low}S_{High}}{S_{Low} + S_{High}} \quad 1.24$$

with

$$S_{Low} = C_1E^{C_2} + C_3E^{C_4} \quad \text{and} \quad S_{High} = \frac{C_5}{E^{C_6}}\ln\left(\frac{C_7}{E} + C_8E\right) \quad 1.25$$

where $C_1 - C_8$ are fitting coefficients, partly tabulated in [7].

Calculations at higher energies or for heavier ions are irrelevant to the IBA studies and are therefore not included in the present work.

1.1.3.2. Energy straggling, resolution

The slowing of the beam particles, while crossing the material, is accompanied by a gradual spreading of their energy distribution, as shown in Figure 1.10. This phenomenon is called energy straggling and occurs due to statistical fluctuations in the number of collision processes [2 – chapter 2]. At the point (depth) where the very low energy ions eventually reach the energy that corresponds to the maximum stopping, their energy loss decreases with depth leading to the "energy bunching" of the straggling distribution [2 – chapter 2]. In Ion Beam Analysis, straggling broadens the measured energy distributions and impairs depth resolution by placing a finite limit for the precision with which energy losses and hence depths can be resolved by backscattering spectrometry. Except for atoms located at the surface of the target, the ability to identify masses is also impaired, since the beam energy E before the collision with a mass M_2 is no longer monoenergetic at some depth and thus the ratio E_1/E_0 and hence the identification of M_2 (see equation 1.34 below) becomes uncertain. It is therefore important to take into account and quantify the magnitude of energy straggling for any given combination of energy, projectile, target material and target thickness [4].

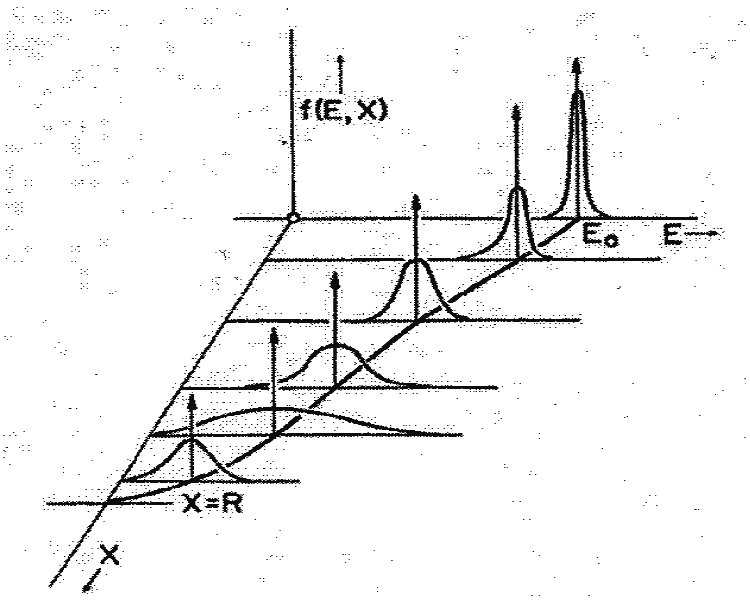

Figure 1.10: The evolution of the energy distribution as a function of depth as the ion traverses through a medium. The energy spread due to straggling increases with depth until the lowest-energy ions reach the energy of maximum stopping. Below this energy level, the energy loss of the ions decreases with decreasing energy leading to the "energy bunching" of the straggling distribution [2 – chapter 2].

Actually, the energy resolution in a spectrum arises from several different contributions [8, 2 – chapter 2]:

1. Electronic energy loss straggling due to statistical fluctuations in the transfer of energy to electrons. This is actually the main contribution of straggling and it is therefore analytically described below.
2. Nuclear energy loss straggling due to statistical fluctuations in the nuclear energy loss. Nuclear energy loss straggling is small compared to electronic energy-loss straggling for light ions (protons or helium ions), and can be neglected. For heavy ions the total straggling distribution is only somewhat larger than electronic energy loss straggling alone, but with a long tail towards low energies. However, the tail contains only a small fraction of all particles, and the width of the total energy distribution (electronic plus nuclear straggling) is still dominated by electronic energy-loss straggling [9]. The nuclear straggling is therefore neglected for all ion species.
3. Geometrical straggling due to finite detector solid angle and finite beam spot size, resulting in a distribution of scattering angles and different pathlengths for outgoing particles.
4. Straggling due to multiple small angle scattering, resulting in angular and energy spread on the ingoing and outgoing paths.
5. Straggling due to surface and interlayer roughness and thickness inhomogeneities of absorber foils and correlation effects in the energy loss [10, 11].
6. An additional contribution to the energy broadening, which is visible in the acquired experimental spectra, is the energy resolution of the detector, described also by a Gaussian distribution.
7. The beam energy profile itself, prior to the target impinging, contributes to the broadening of the energy as well, being also Gaussian, but this is in most cases neglected being very small comparing to the other factors.

The different Gaussian distributions to energy fluctuation in a spectrum can be added quadratically. Taking into account for example the detector resolution, the energy straggling and beam profile, respectively, the total variance of the energy loss fluctuations Ω_{TOT}^2 is given by:

$$\Omega_{TOT}^2 = \Omega_{DET}^2 + \Omega_{STR}^2 + \Omega_{BEAM}^2 + \ldots \qquad 1.26$$

Concerning the dominant contribution, which is in most cases the electronic energy loss straggling, there are four main theories describing it [12-14], each one applicable in a different regime of energy loss. With ΔE being the mean energy loss of the beam, and *E* the energy of the incident beam, the regimes can be distinguished as follows [8]:

$\Delta E/E$ < 10% **Vavilov's theory** [15, 13]: For thin layers and small energy losses the energy distribution is non-Gaussian and asymmetrical. However, in this case, the contribution of straggling to the total energy broadening is much smaller than the contribution of the finite energy resolution of the detector.

10-20% **Bohr's theory** [16, 17]: As the number of collisions becomes large, the distribution of particle energies becomes Gaussian, as described in detail below.

20-50% **Symon's theory** [12]: This theory includes non-statistical broadening caused by the change in stopping power over the particle energy distribution. If the mean energy of the beam is higher than the energy of the stopping power maximum, then particles with a lower energy have a higher stopping power, and particles with higher energy have a smaller stopping power. This results in a nonstatistical broadening of the energy distribution. The width of the particles energy distribution in Symon's theory is significantly higher than predicted by Bohr's theory. The distribution of particle energies is still Gaussian.

50-90% **Payne's and Tschalärs Theory** [18, 19]: When the energy losses become very large and the mean energy of the beam decreases below the energy of the stopping power maximum, the particle energy distribution again become skewed, because now particles with lower energy have a lower stopping power than particles with higher energy. The distribution is also approximately Gaussian.

The existing models used for the calculation of the energy straggling are based on the theory of Bohr, which is therefore the only one described here in detail. According to Bohr's theory, when the energy transferred to target electrons in the individual collisions is small compared to the width of the energy loss distribution, the energy distribution of the beam that has traversed a medium is approximately Gaussian, as a consequence of the assumption that the number of collisions is large and follows a Poisson distribution [2 – chapter 2]. The condition of a Gaussian distribution can actually be formulated as follows [2 – chapter 2]:

$$N_t[atoms/cm^2] \geq 2 \times 10^{20} \frac{1}{Z_2} \left(\frac{E[MeV/amu]}{Z_1} \right)^2 \qquad 1.27$$

where N_t is the areal density of the target material Z_2 for projectile of Z_1 with energy E.

In the limit of high energy velocity, beyond the stopping maximum (see Figure 1.8, 1.9), the energy loss is dominated by electronic excitations, as has been mentioned in the previous paragraph. In this region straggling is almost independent of projectile velocity. In this Gaussian region, Bohr derived the value for the standard deviation of the average energy loss fluctuation (Bohr value Ω_B), as follows [2 – chapter 2]:

$$\Omega_B^2[keV^2] = 0.26 Z_1^2 Z_2 N_t[10^{18} atoms/cm^2] \qquad 1.28$$

The FWHM of a Gaussian distribution (12-88% range of the error function) is wider that the standard deviation Ω (also denoted as σ[1]) of an energy distribution (range of 16-84%) by a factor of $2(2\ln 2)^{1/2}$=2.355 [4].

For thick targets, where the energy loss inside the target exceeds 25%, the Gaussian distribution fails [2 – chapter 2]. The applicability of Bohr's treatment has been extended to lower energies of light ions ($Z_1<Z_2$), in the vicinity of the maximum of the dE/dx curve and below, by Lindhard and Shaff, by proposing a simple correction for ion velocities below E[keV/amu]=$75Z_2$, as follows [2 – chapter 2]:

$$\frac{\Omega^2}{{\Omega_B}^2} = \begin{cases} 0.5L(x), for\ E[keV/amu] < 75Z_2 \\ 1, \qquad for\ E[keV/amu] \geq 75Z_2 \end{cases} \qquad 1.29$$

$$\text{with} \quad L(x) = 1.36x^{1/2} - 0.016x^{3/2}$$

$$x = \frac{E[keV/amu]}{25Z_2}$$

Further studies and calculations have been performed for lower energies, in the non-Gaussian region, concerning heavy ions and thick targets (a review of the corresponding references is found in [2 – chapter 2]). These corrections are in general incorporated in the existing models for straggling calculations, briefly described in the next paragraph together with the models themselves.

[1] σ^2 is the variance of the energy distribution, the full width at half maximum (FWHM) is $2(2\ln 2)^{1/2}\sigma = 2.355\sigma$

Concerning the straggling in **mixtures** and **compounds**, a similar treatment to that for energy loss, with a linear additivity approach, was proposed by Chu [20] according to the Bohr model. For a compound (or mixture) A_mB_n with atom density N^{AB}[atoms/cm^3] and corresponding elemental values N_A and N_B and also Ω^A and Ω^B for the assumed straggling values in a layer of thickness t, the straggling Ω^{AB} in this compound (or mixture) layer can be obtained from the expression:

$$\frac{(\Omega^{AB})^2}{N^{AB}t} = \frac{m(\Omega^A)^2}{N_A t} + \frac{n(\Omega^B)^2}{N_B t} \qquad 1.30$$

In the case of atomic concentrations: $m + n = 1$, then $N^A = mN^{AB}$ and $N^B = nN^{AB}$, the assumption of additivity bears out, by obtaining the following:

$$(\Omega^{AB})^2 = (\Omega^A)^2 + (\Omega^B)^2 \qquad 1.31$$

Models used

Qualitative agreement for light ion experimental data with the predictions of Bohr [16], Lindhard and Sharff [21], Bonderup and Hvelplund [22] and Chu [20] is generally observed [2 – chapter 2]. The Chu + Yang's theory, which is briefly described below, is actually considered to be the most complete and is thus recommended to be used in the computer codes simulating spectra. On the other hand [2 – chapter 2], binary collision approximation (BCA) calculations involving Monte Carlo calculations, has developed into many well-established computer codes such as SRIM [5] for the simulation of ion range distributions in material, based on transport theory (motion of the ions inside the target during their slowing down to zero energy).

Chu's theory takes deviations from Bohr straggling caused by the electron binding in the target atoms into account, and Yang's theory additionally incorporates charge state fluctuations of the ions. More specifically, in Chu's theory the Bohr straggling is modified by a correction factor *H* [20, 17]:

$$\sigma_{Chu}^2 = H(E/M_1, Z_2)\ \sigma_{Bohr}^2 \qquad 1.32$$

For lower ion energies the Bohr straggling is multiplied by the Chu correction factor $H(E/M_1, Z_2)$, which depends only on E/M_1 and the nuclear charge of the target atoms Z_2. Chu [20, 17] has calculated H by using the Hartree-Fock-Slater charge distribution. This calculation gives straggling values which are considerably lower than those given by Bohr's theory. The Chu

correction is mainly necessary for high Z_2 and low energies. For high energies H approaches 1 and becomes independent of Z_2 and energy. Charge state fluctuations of the ions result in an additional straggling contribution, taken into account empirically by Yang et al [11]. Using the effective charge and scaling approach for energy straggling and the Chu model and also considering correlation effects and charge change effects, an empirical formula was obtained by Yang fitting the data for heavier ion straggling. The total straggling, in Yang's theory is thereby expressed by [8]:

$$\frac{\sigma_{Yang}^2}{\sigma_{Bohr}^2} = \gamma^2(Z_1, Z_2, \nu)\frac{\sigma_{Chu}^2}{\sigma_{Bohr}^2} + \frac{\Delta\sigma^2}{\sigma_{Bohr}^2} \qquad 1.33$$

where $\gamma^2(Z_1, Z_2, v)$ is the effective charge factor for ions in matter, v the ion velocity, and $\Delta\sigma^2$ is the additional straggling due to correlation effects.

1.1.3.3. Kinematic factor, Q-value

The stopping power and straggling in the target till the interaction depth define only the corresponding projectile energy loss and beam energy spreading in the target up to the point of the interaction and the same applies to the particles escaping from the target along the outward path to the detector. Exactly at the interaction point though, the energy of the emitted particle E_1 depends of course on the occurred reaction, as shown below.

When the beam particle of mass M_1 collides **elastically** with the target nucleus mass M_2 with $M_1<M_2$, its energy decreases from E_0 to E_1, depending on the scattering angle θ and the masses, as seen in Figure 1.11. The energy E_1 is thus designated to their ratio, the kinematic factor K, according to the relation 1.34, originating from the kinematics of the reaction (conservation of kinetic energy and momentum) [4].

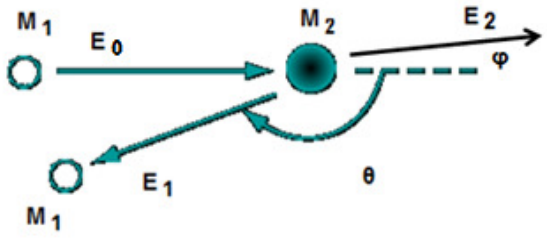

Figure 1.11: Kinematics of the elastic scattering schematically.

$$E_1 = K * E_0 \quad \text{with} \quad K = \left\{ \frac{\left[1-(M_1/M_2)^2 \sin^2\theta\right]^{1/2} + (M_1/M_2)\cos\theta}{1+(M_1/M_2)} \right\}^2 \qquad 1.34$$

In addition to the elastic scattering, which is characterized by the same types of particles in the entrance and the exit channels of the occurred interaction and the conservation of kinetic energy, other nuclear reactions can also take place when an accelerated beam impinges on the target, as discussed above (1.1.1). The possibility for the reactions to occur is governed also by conservations laws, the conservation of the number of nucleons, the electric charge, the energy, the angular momentum and the conservation of parity. The energy released (in the form of kinetic energy of the reaction products) in a **nuclear reaction** is called **Q-value**, originating from the conservation of energy. It is exactly the difference between the rest mass energy of the interacting particles (mass M_1 of the projectile and M_2 of the target nucleus) and the rest mass energy of the particles produced in the reaction (mass M_3 of the ejectile and M_4 of the residual nucleus), as given by the following equation:

$$Q = (M_1 + M_2)c^2 - (M_3 + M_4)c^2 \qquad 1.35$$

1.1.3.4. Mass and depth scale and resolution

As has already been pointed out, the purpose of spectrometry is to extract quantitative information in depth on the elemental composition of the sample of interest and this can be done by interpreting the acquired spectrum in terms of distributions of atoms in depth below the surface. The particle energy loss in the target, the energy straggling, the cross section and the kinematic factor consist mainly all the theoretical part of the analytical procedure, which immediately leads to practical features in the process, namely the mass and depth scale and resolution and the acquired yield. Focusing on the elastic scattering case of the possible projectile-target nucleus interaction, these features can be easily described as follows in the next paragraphs. In all other cases the situation is partly similar.

The kinematic factor K of the scattering, described in equation 1.34, depends only on the ratio of the projectile to the target masses and on the scattering angle θ. The plot of K versus M_2/M_1 and θ can be seen in Figure 1.12 [4] that follows. The equation for the kinematic factor contains exactly the essence of how spectroscopy acquires its ability to sense the mass of a

target atom, especially through the plot in Figure 1.12. Concerning multielemental targets, which is mostly the case, the mass separation depends exactly on the signal separation in the spectra, namely the detected particle energy separation. In the case that the target contains two types of atoms that differ in their masses by a small amount ΔM_2, it is important that this difference produces as large change ΔE_1 as possible in the measured energy E_1 of the projectile after the collision. As Figure 1.12 shows, a change of ΔM_2 (for fixed M_1) gives the largest change of K when $\theta=180°$ for all but the smallest values of M_2. Therefore, $\theta=180°$ is the preferred location for the detector to be placed. This is of course not possible, because the detector would obstruct the path of the incident particles. The detector is thus preferably positioned at some steep backward angle, such as at 170°. This arrangement is actually exactly the reason for the particular method to be named **backscattering spectrometry**. The nuclear techniques implementing backscattering spectrometry are analytically discussed in the following section.

For a fixed scattering angle θ, the energy separation ΔE_1 is given by:

$$\Delta E_1 = E_0 \left(\frac{dK}{dM_2}\right) \Delta M_2 \qquad 1.36$$

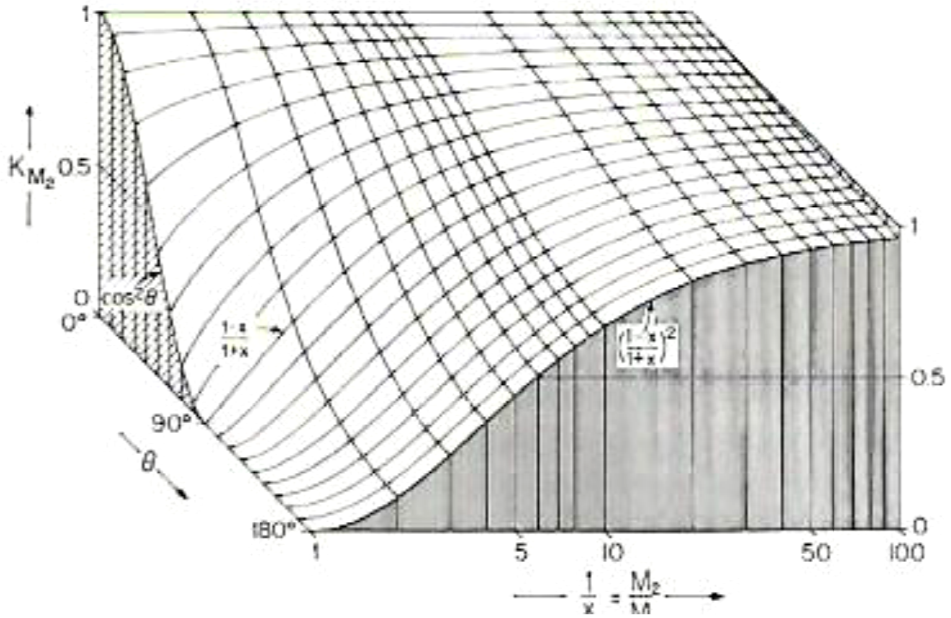

Figure 1.12: The kinematic factor K plotted as a function of the scattering angle θ and the mass ratio $x^{-1} = M_2/M_1$ [4].

For $M_2 \gg M_1$, which is most often the case, this reduces to the following equation, in the vicinity of $\theta = 180°$, i.e. $\theta = \pi - \delta$ [4]:

$$\Delta E_1 = E_0(4 - \delta^2)(M_1/M_2^2)\Delta M_2 \qquad 1.37$$

If ΔE_1 is set equal to δE, the minimum energy separation that can be experimentally resolved, then the **mass resolution** of the system δM_2 is [2 – chapter 4]:

$$\delta M_2 = \frac{\delta E}{E_0\left(\frac{dK}{dM_2}\right)} \qquad 1.38$$

The quantity δE depends on the energy spread in the spectrum, as discussed above; it is a matter of the detector resolution, the straggling, the beam energy profile (spread) and various geometric effects [2 – chapter 2]. At the sample surface, the mass resolution is primarily determined by the detector resolution, while for layers deep in the target straggling dominates. For fixed $\delta E/E_0$, as indicated in Figure 1.13 [2 – chapter 4], δM_2 improves with increasing beam mass (M_1). This can however be deceptive, since δE frequently depends on the beam mass, mainly because of the detector resolution for different ion species, which is in general worsening with increasing beam mass. The critical choice of beam mass and beam energy plays therefore an important role in the analytical procedure, as discussed further, along with other key factors, in the section 1.3.

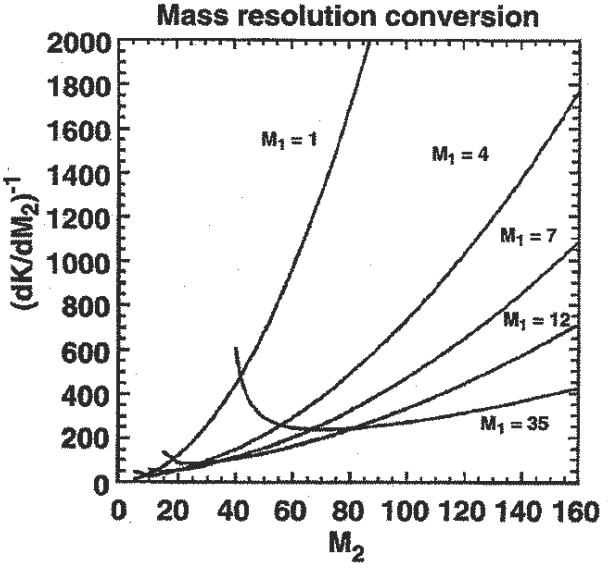

Figure 1.13: Plots of $(dK/dM_2)^{-1}$ versus target mass M_2 for several analysis beams (ion mass M_1) for specified $\delta E/E_0$ and backscattering angle at 180° [2 – chapter 4].

Concerning the relation of the energy of the scattered particle to the **depth** x in the sample where the scattering occurred, one obtains the following expressions [4] for the inward and the outward paths of the particles, respectively, as sketched and explained in Figure 1.14.

$$\frac{x}{cos\theta_1} = -\int_{E_0}^{E} \frac{dE}{dE/dx} \quad \text{and} \quad \frac{x}{cos\theta_2} = -\int_{KE}^{E_1} \frac{dE}{dE/dx} \qquad 1.39$$

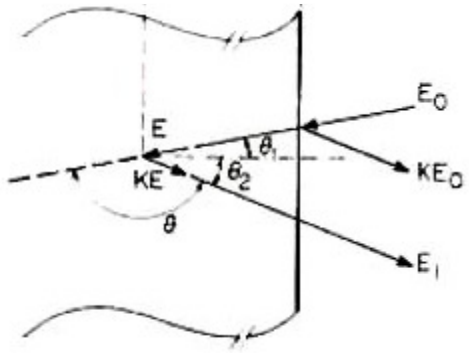

Figure 1.14: Backscattering events in in a sample (target) consisting of a monoisotopic element. The angels θ_1 and θ_2 are positive regardless of the side they lie with respect to the normal of the sample. The incident beam, the direction of detection and the sample normal are coplanar [4].

Assuming a constant value for dE/dx along the inward and outward path, one can calculate the difference in energy ΔE at a detector of a particle scattered at the surface and one scattered at a depth x, measured perpendicular to the sample surface for the inward and outward path. This quantity, concerning a monoelemental target, is given as a function of x and the energy loss factor [S] or the stopping cross section factor [ε], defined as follows [2 – chapter 4]:

$$\Delta E = [S]x \quad \text{or} \quad \Delta E = [\varepsilon]Nx \qquad 1.40$$

$$[S] = \left[K\left(\frac{dE}{dx}\right)_{in}\frac{1}{cos\theta_1} + \left(\frac{dE}{dx}\right)_{out}\frac{1}{cos\theta_2}\right] \qquad 1.41$$

$$[\varepsilon] = \left[\frac{K}{cos\theta_1}\varepsilon_{in} + \frac{1}{cos\theta_2}\varepsilon_{out}\right] \qquad 1.42$$

where K is the kinematic factor and θ_1 and θ_2 angles are defined by the experimental geometry, shown in Figure 1.13.

For **multielemental** samples the depth-energy relation must be calculated for each element separately. In the case of a compound A_mB_n target with molecular density N^{AB} (molecules/cm^3) and corresponding K and ε values, the total stopping cross section ε_0 is calculated using the equation (1.22), where the following equation provides the relation for each element (the A for example). The lower index refers to the scattering element and the upper one to the stopping material.

It should be noted here that for the evaluation of the ε values (eq. 1.42), the surface-energy approximation is usually used for the incident scattering energy E_0 (or the mean-energy approximation, corresponding to the energy in the middle of the thickness of the target), at which the ε_{in} is evaluated for all elements, while for the ε_{out} values, one needs to take into account the different energies after the scattering for each element (different K values) and evaluate the ε_{out} values at each KE_0 energy.

$$\Delta E_A = [\varepsilon]_A^{AB} N^{AB} x \tag{1.43}$$

$$[\varepsilon]_A^{AB} = \left[K_A \varepsilon_{in}^{AB} \frac{1}{cos\theta_1} + \varepsilon_{out,A}^{AB} \frac{1}{cos\theta_2} \right] \tag{1.44}$$

An **integral** over the relevant energy values needs in any case to be determined for the evaluation of either the energy loss or the stopping cross section factor, because of the existence of energy-dependent parameters, as seen in the previous note.

The minimum detectable depth difference δx, is of course related to minimum particle energy difference δE and leading to the **depth resolution** concept, as follows:

$$\delta x = \frac{\delta E}{[S]} \tag{1.45}$$

The minimum δE value is already described above, concerning its effect to mass resolution. Actually, there are significant similarities between depth and mass resolution, exactly because of the huge effect of the energy spread of the particles in both cases. In the particular case of depth, the depth resolution degrades with depth, since straggling simultaneously increases and therefore a common practice is to quote depth resolution at the surface. A convenient approximation is also to assume that all sources contributing to the energy spread are Gaussian

and adding them in quadrature. Depth resolution can actually be improved by increasing the energy loss [S], by tilting the sample normal relative to the incoming beam (increasing thus θ_1 and/or θ_2), thus increasing the path length to reach a given depth (measured perpendicular to the surface). However, large tilts introduce additional energy broadening placing a limit to the optimization of the resolution.

1.1.3.5. Yield

The yield of the particles emitted from a given depth in the sample corresponds to the number of detected particles (counts) in the acquired spectrum with respect to their energy (energy interval – channel). The conversion of the detector signals into the spectrum is described in detail in the next chapter (2.4).

The essence of depth profiling is exactly to relate the spectrum height H (or yield Y) to a slab of material with thickness t and number of atoms per unit area Nt at depth x, that produces particles detected in the energy interval δE, the energy width of a channel. Considering that the produced elemental peaks are much wider than the energy resolution of the detecting system, **the height (counts/channel)** for a single element peak near the surface of the target, corresponding to detected particles with energy E_1, is given by equation 1.46 [4], illustrated schematically in the Figure 1.15:

$$H(E_1) = \frac{d\sigma}{d\Omega}(E,\theta)Q\Omega\frac{\delta E}{[\varepsilon(E)]cos\theta_1} \qquad 1.46$$

where $\frac{\delta E}{[\varepsilon(E)]}$ is the areal density Nt contributing to one channel of the spectrum near the surface and E is the energy of the incident particle immediately before scattering. The stopping cross section factor [ε(E)] is defined in equation 1.42 in the previous paragraph, concerning the inward and outward paths. For the outward path, ε_{out} is evaluated at energy KE, taking into account the kinematic factor K of the scattering.

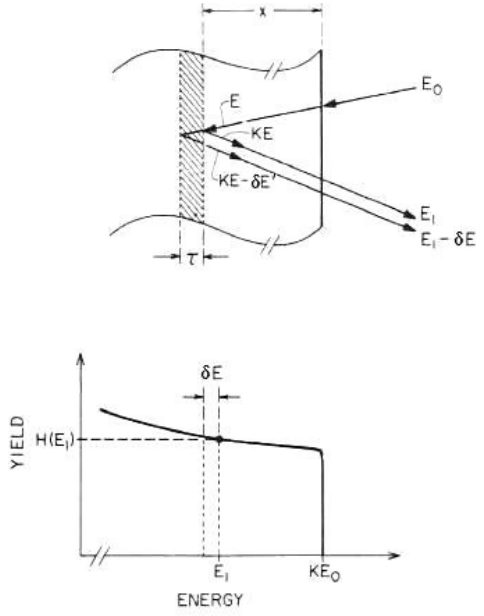

Figure 1.15: Backscattering on a monoelemental target at a depth x and the resulting spectrum [4].

The height of the two elemental peaks in a **compound** A_mB_n are given correspondingly by the following relation concerning each element (the A for example), with the corresponding stopping cross section factors described in equation 1.44:

$$H(E_1) = \frac{d\sigma_A}{d\Omega}(E,\theta)Q\Omega\frac{m\delta E}{[\varepsilon(E)]_A^{AB}cos\theta_1} \quad 1.47$$

It should be noted here that the calculations for the spectrum height for scattering at deeper layers of the target get more complicated, mainly because of the enhanced/increased energy loss and straggling effects, or even because of geometrical reasons (broadening).

1.2 Nuclear techniques

The nuclear techniques implementing Ion Beam Analysis (hence called IBA techniques), used for the quantification and/or the depth profiling of elements in a sample, are based on the already described interaction, occurring in the studied sample between the atoms or the nuclei of its comprising elements and the accelerated ions (beam) bombarding it. While crossing the material, the ions interact mostly with the electrons and rarely with the nuclei of the atoms of the sample, resulting to their energy loss and possibly to changes in their direction and particle and/or radiation emission (X-rays, γ- rays). Every possible interaction of the incident beam (projectile) with a nucleus in a sample (target), as sketched in Figure 1.16 that follows, leads to a specific result which is characteristic of the procedure. Detecting the characteristic emitted particle (ejectile), for example, one can identify the occurred interaction and then, following the specific methodology based on the principles described in the previous sections, one can eventually determine and quantify in depth the elements of interest in the sample. The identification of the particles in all Ion Beam Analysis techniques is based on their characteristic energy, which can in all cases be calculated, as described in 1.1.3.3.

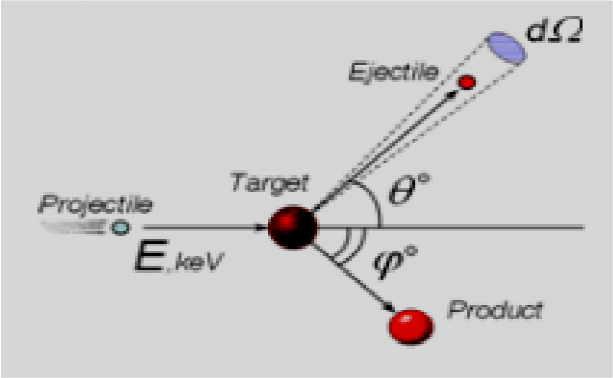

Figure 1.16: The interaction of the beam particles (projectile) with a target nuclei schematically.

The IBA techniques are divided in categories, depending on the studied interaction, namely on the detection system used, as seen schematically in Figure 1.17. The choice of the method to be used depends of course on the specific case study. A brief description of all the existing techniques is given below for reasons of completeness, whereas a detailed analysis of the methods used in the present dissertation (namely the RBS, EBS and NRA techniques) is subsequently presented.

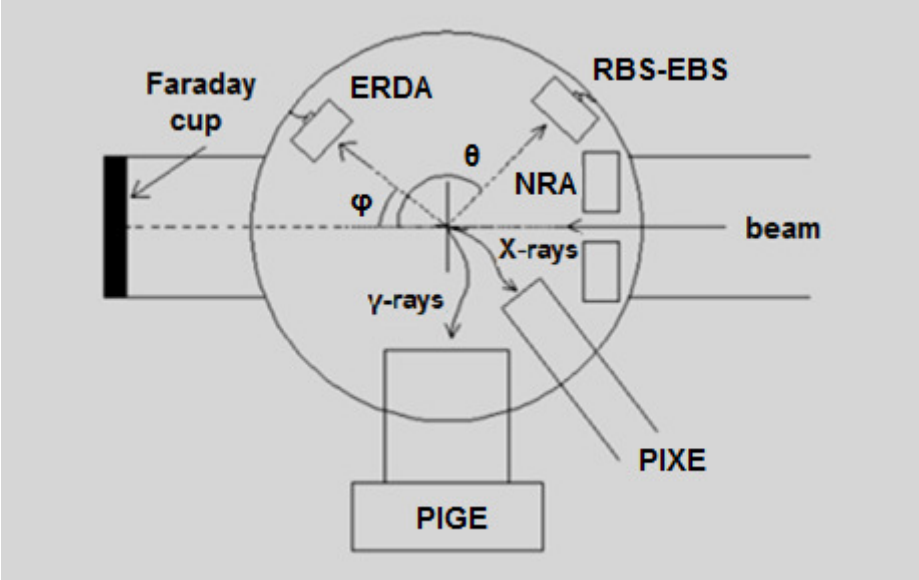

Figure 1.17: Schematic representation of the IBA nuclear techniques and the used setup, depending on the studied interaction and the detected product.

Rutherford Backscattering Spectroscopy – RBS: Detecting the particles that have been elastically scattered by the Coulomb potential of a nucleus of the target, meaning that the Rutherford formula can be applied for this interaction, the technique is called Rutherford Backscattering Spectroscopy. RBS is one of the mainly used techniques in Ion Beam Analysis and is thus described in detail in the following section.

Elastic Backscattering Spectroscopy – EBS: In the case that the detected particles originate from their elastic backscattering on the target nuclei, which does not follow the Rutherford's formula (depending on the energy of the projectile and the specific projectile/target combination), the technique is called Elastic Backscattering Spectroscopy. This technique is very similar to the RBS one; the one and only difference between the two techniques is that in EBS, because of the additional interference of the nuclear potential and other mechanisms, the elastic cross section of the scattering cannot be analytically calculated by any formula and needs to be determined experimentally.

Nuclear Reaction Analysis – NRA: This technique involves the detection of the particles (b) emitted via the nuclear reaction A(a,b)B occurring between the beam particles (a) and the nucleus of interest (A). The main important feature of this method is the high energy of the

detected particles in most cases, resulting from the Q-value of each nuclear reaction. This characteristic high energy of the particles enables the study of light isotopes, which may not be feasible with the use of other techniques.

Elastic Recoil Detection Analysis – ERDA: This technique is based on the A(a,a)A elastic scattering, like the RBS technique, but detecting the recoil A nucleus at forward angles instead of the scattered particle (ejectile a) at backward ones, as shown in Figure 1.17. It is mainly implemented for the detection of light elements like ^{1}H or ^{4}He, usually with a heavy ion beam on the target.

Particle Induced Gamma Emission – PIGE: The method of detecting γ – rays is based on the deexcitation of the compound or the residual excited nucleus through the emission of γ – rays (e.g. (p,γ) and (p,p'γ) reactions respectively), which are usually recorded with the use of High-purity Germanium (HPGe) detectors. The energy of the γ-radiation corresponds to transitions of the energy levels of the excited nucleus which are characteristic for every nucleus, thus enabling its analysis. When strong and narrow resonances exist in a system, PIGE can be used for accurate depth profiling by gradually changing the beam energy, thus "moving" the resonant interaction deeper inside the target. It has to be noted here, that γ – rays crossing the material can only be absorbed, meaning that there is no energy loss while interacting with matter if no absorption takes place. Their intensity is thus reduced and not their energy, which is always the case when particles interact with matter.

Particle Induced X-Ray Emission – PIXE: This technique involves the detection of the X-rays emitted from the target atoms, when outer shell electrons drop down to fill the inner shell vacancies caused by the ionization of the atoms, when being bombarded with an ion beam. However, only certain transitions are allowed. More specifically, each element has a unique X-Ray "fingerprint", a unique pattern consisting of a combination of K, L, and M X-Rays, due to the variation in the atomic structure. No information can though be provided concerning the depth profiling of the elemental distributions in the target, defining PIXE as the only non profiling technique in Ion Beam Analysis. It is widely used however, usually along with RBS, for the elemental analysis of samples.

1.2.1 Rutherford Backscattering Spectroscopy (RBS)

The spectroscopy based on the elastic scattering of the beam particles (RBS and EBS methods) is the most commonly used for the sample analysis. RBS' detailed description is indeed mandatory, since the EBS technique, being an extension of the RBS one, constitutes the main part of this dissertation.

As has already been described in 1.1.2, Rutherford scattering occurs when the beam particles are scattered by the Coulomb potential of the nuclei of the target, as seen schematically in Figure 1.18 for an alpha particle impinging on the atom of interest.

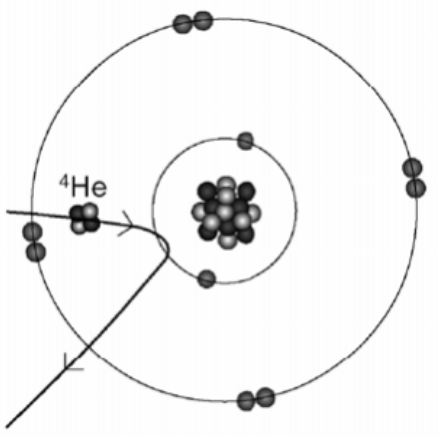

Figure 1.18: Rutherford scattering of an alpha particle from the nucleus of interest.

The RBS method, applied in such scattering cases, typically concerns the analysis of heavy nuclei (A>60), given that the ion beam by an accelerator is typically of a few MeV. Its application is thus advantageous for the study of heavy elements on light substrates. With this technique one can determine the stoichiometry and the profile of elements in depth, ranging from a few nm to several μm below the surface. The term backscattering corresponds to the fact that for standard applications the studied samples are thick and the incident particles have typically not enough energy to run through the sample, enabling only backward scattering to be studied. Moreover, backscattering at steep backward angles anyway enhances the mass resolution, as described in 1.1.3.4.

All the physical concepts and phenomena entering into spectroscopy are described in the previous section (1.1.3), concerning the calculations for the analysis, whereas the Rutherford formula for the cross-section determination in RBS is described in the scattering theory in section 1.1.2. More specifically, the implementation of the RBS technique lies mainly in the

exact study of the **acquired yield**, which is the result of all the processes occurring in the target before, during and after the scattering, including the energy loss and the straggling phenomena. The identification of the scattered particles in the acquired spectrum is rather trivial in most cases, because of their characteristic energy, which is *a priori* known and expected owing to the kinematic factor K, with minor corrections, concerning the target composition and the energy loss before and after the scattering heading towards the detector. The depth profiling of an element of interest lies exactly in the study of the energy distribution of the detected particles, translating their energy to the scattering depth. The energy of the detected particles at an angle θ (where the detector is placed) have actually a range of ΔE owing to the distribution of the nuclei causing the studied scattering, namely to the distribution of the element of interest, as shown in Figure 1.19 for the particular example.

As represented in this Figure, the particles reaching the detector induce signals which are electronically processed (as described in section 2.4) and are finally recorded in a spectrum (last image in the figure) according to their energy. The particles that are scattered from the heavy nuclei on the surface of the target (1´) do not lose energy before being scattered, since they do not travel through the material at all. Their energy gets consequently the maximum possible value, as calculated from the kinematics and these particles are thus recorded in the right part of the spectrum (at the highest energy values). When the scattering takes place deeper inside the target with terminal point the end of it (2 and 2´), the detected particles lose different amounts of energy, while crossing the material, depending on the depth of the interaction.

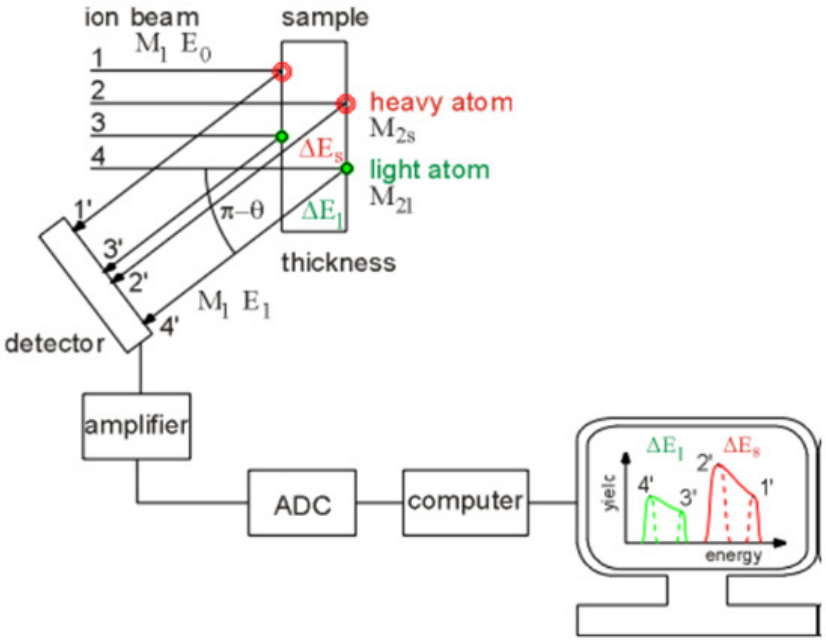

Figure 1.19: Schematics of the detection of the scattered beam particles from a heavy (in red) and a light (in green) element of the same thickness, constituting the target (sample).

Therefore, one gets a distribution of particles (counts) in the acquired spectrum within the energy range ΔE_s, depending on the total thickness of the target (assuming in this particular case, as shown in the sketch, that the target contains both of its comprising elements across its whole thickness (not in layers) and that the target thickness is such, that the particles can cross it and head backwards to the detector). The same illustration applies to the scattering from the lighter element (3´and 4´ in Figure 1.19), from which the particles are scattered with less energy, owing to the kinematics. The energy after the scattering is decreasing with decreasing mass number M_2.

It should be noted here that in the case of thicker heavy element or of smaller difference in masses (smaller ΔM) of the elements in the mentioned example, there would be an overlap in the curves in the spectra forming steps, depending also on the beam energy (see equations in 1.1.3 (4) section). This, however, would hinder the analysis only in extreme cases.

It has already been pointed out that the calculations for the RBS analysis (and actually for all IBA studies) are based exactly on the acquired yield. Its description is seen in the following relation, as has already been defined in section 1.1.3 along with the corresponding principles concerning all the involved physical phenomena.

$$H(E_1) = \frac{d\sigma_R}{d\Omega}(E,\theta)Q\Omega\frac{\delta E}{[\varepsilon(E)]cos\theta_1} \qquad 1.48$$

This equation shows that the acquired spectrum, excluding the special low energetic part for reasons that are about to be clear in the next paragraphs, mainly represents the product of the differential cross section variation with energy, along with the stopping power. The contribution of the energy straggling effect, the resolution of the detector and the ripple of the machine to the spectrum height is not depicted in this particular basic relation but is certainly taken into account in the models used for the numerical analysis (see 1.1.3.2).

In the special case of a very thin element of interest (thin film on a substrate for example), namely with thickness of a few keV (in terms of the energy loss of the incident particles), the following simpler equation can be used instead, depending however on the desired accuracy. This procedure gives satisfactory results for the studied atomic areal density N_t, but its reliability depends of course on the thickness of the film, in terms of the energy E used for the calculation.

The energy of the incident particles before the scattering can be assumed to have either the surface energy value, where no energy loss is taken into account, or an intermediate value in the film (surface energy approximation or mean energy approximation, respectively [4]).

$$H(E_1) = \frac{d\sigma_R}{d\Omega}(E,\theta)Q\Omega\frac{N_t}{cos\theta_1} \quad 1.49$$

In the opposite case of a target of infinite thickness (e.g. on substrate), meaning that the beam particles lose all their energy and stop inside it, the spectrum would be extended from the maximum energy after the scattering , corresponding to scattering on the surface of the targets, down to zero energy. This corresponds to the particles travelling the longest possible path in the sample before scattering, having though the needed amount of energy to cross it back (double energy loss) to reach the detector with minimal energy. For instance, if one has a uniform and infinitely thick target of gold and a proton beam of 2 MeV on it, which is a case of purely Rutherford scattering, the acquired spectrum would have a shape similar to the one illustrated in Figure 1.20.

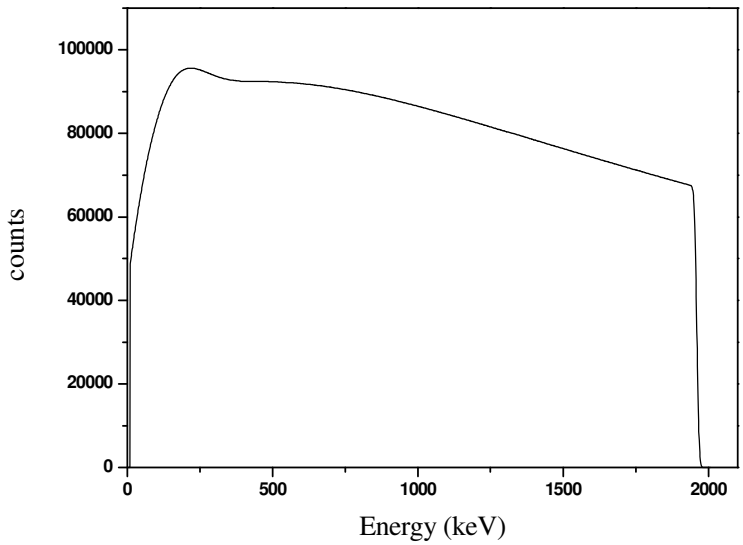

Figure 1.20: Spectrum of protons scattered from a uniform Au target at 170° for beam charge QΩ of 10^{12}(particles*sr).

The spectrum reveals the characteristic increase of the differential cross section with the decreasing energy of protons being scattered on the surface and deeper in the target (looking at the spectrum from the right to the left side). One can also notice the additional increase of the

scattered protons with very low energy, originating not only by the straggling effect, but also by the plural scattering in the target, denoting events which originate from multiple (usually double) large-angle scattering, resulting to low energy signals registered by the detector. At energies close to zero a decrease is observed in the yield owing to the same effect of plural scattering, combined with lateral straggling, which yields to a reduction in the number of backscattered beam particles that fall within the solid angle subtended by the detector.

An **application of the RBS technique** to thin film analysis is illustrated in the following Figure 1.21 [2 – chapter 4] for the general and ideal case of Rutherford scattering on a two-element A_mB_n thin film of uniform composition on a lower-mass substrate showing all the previously mentioned features of the acquired spectra.

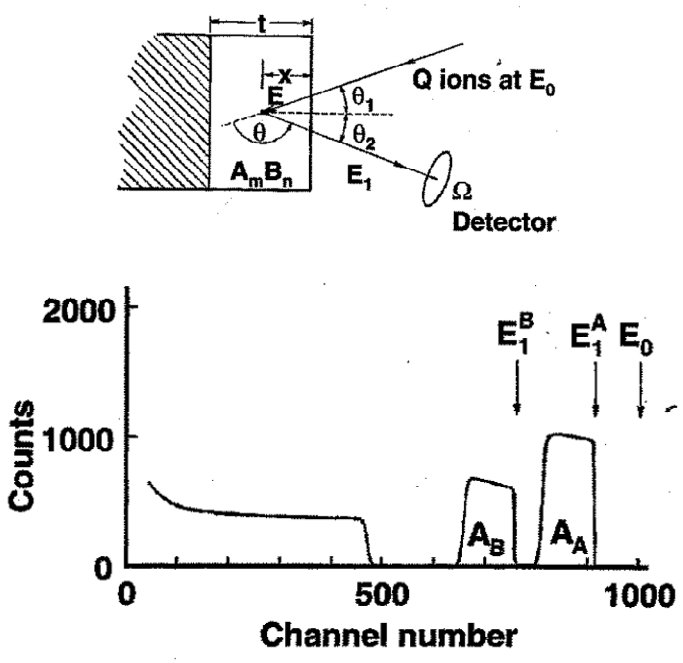

Figure 1.21: Experimental geometry (top) and the backscattering spectrum (bottom) for a two-element A_mB_n thin film of uniform composition on a lower-mass substrate [2 – chapter 4].

1.2.2 Elastic Backscattering Spectroscopy (EBS)

When the scattering of the ion beam from the target nuclei is not purely Rutherford, as analyzed in scattering theory (section 1.1.2), the situation gets more complicated. It became however evident that the interference of the Coulomb potential with the nuclear one and the occurred compound reaction mechanism strongly affect the elastic differential cross section, depending mostly on the beam energy and the target composition (light or heavy nuclei).

In such cases, the methodology is called Elastic Backscattering Spectroscopy in general and is actually very similar to the RBS one. The only difference between the two is that, since the scattering is not described by the Rutherford formula, the differential cross sections, being composed of the Coulomb, the potential and the resonant scattering, as described in 1.1.2, need to be experimentally determined for every projectile-nucleus system. This has already been done for many reactions in the past (and this procedure is still in progress) and in specific cases, cross sections can be theoretically calculated (evaluated), given that there has been a thorough (as possible) experimental study of the specific reaction. The applicability of EBS is thus limited by the experimental studies and the theoretical evaluations based on them, as described in detail in the following sections. The existing determined differential cross sections are available to the scientific community through the IBANDL database [23], which is part of the EXFOR [24] general one and SigmaCalc [25].

The EBS analytical calculations for the quantification and/or depth profile of the element of interest in a sample are correspondingly based on the same relation (1.48) describing the scattering through the spectrum height H, as follows:

$$H(E_1) = \frac{d\sigma}{d\Omega}(E,\theta)Q\Omega\frac{\delta E}{[\varepsilon(E)]cos\theta_1}$$

An example of RBS and EBS spectra for the same accumulated charge on the target, is illustrated in the following Figures 1.22, concerning the backscattering of alphas from a Fe_3O_4 film on a Fe substrate, clearly presenting the resonant structure of the alpha scattering on oxygen. The enhanced O peak in the right spectrum is due to the strong resonance in the $^{16}O(p,p)$ cross section at ~3.04 MeV.

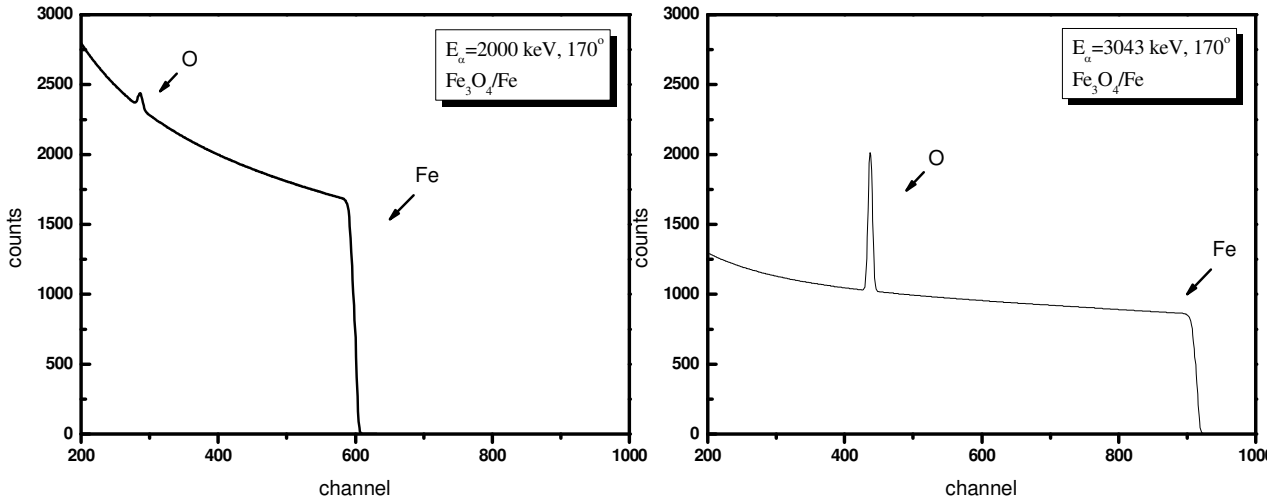

Figure 1.22: The 2 MeV Rutherford backscattering of alphas from a Fe_3O_4 film on a Fe substrate, along with the 3.043 MeV non Rutherford backscattering spectrum for the same accumulated charge (simulations).

The Elastic Backscattering Spectroscopy (EBS), being an extension of the RBS one, is generally preferable in most applications for the determination of the concentration profile of light elements, due to its superior depth resolution resulting from the enhanced stopping power of the outgoing particles, for the same analyzing depth. Moreover, it is usually performed in the same experimental setup (as the RBS one), with minimal changes in the experimental conditions. Actually, among all IBA techniques, EBS and NRA (as discussed below) are the most widely used methods, due to their high analytical power for accurate and also simultaneous determination of several light element concentrations in complex samples.

EBS is often used along with RBS for the parallel study of an element from which the scattering is purely Rutherford (e.g. on heavy element). The aim of this simultaneously study, as seen in the following section, is the determination of the ($Q\Omega$) factor. This technique of relative measurements, with respect to the Rutherford scattering on a heavy element, is widely used in the present work in the cross section determination and the benchmarking procedure, as seen in the following chapters.

1.2.3 Nuclear Reaction Analysis (NRA)

In the case of complex matrices or of isotope study, the Nuclear Reaction Analysis is usually implemented due to the favorable (positive) Q-value of a selected nuclear reaction A(a,b)B occurring when the ion beam hits the target. The detection of the ejectile b at the expected high energy is usually almost background free, meaning that no interference of the spectra peaks is usually present. The determination however of the corresponding reaction differential cross section is again a challenging task, requiring experimental studies. This method, as all IBA methods, is based on the relation describing the spectrum height (1.48), where the energy loss in the material enables again the depth profiling of the isotope of interest as previously described.

The most important NRA advantages are its high isotopic selectivity, its enhanced sensitivity for many abundant stable nuclides, the capability of least-destructive depth profiling, and the possibility of simultaneous analysis of more than one light element in near-surface layers of materials. Moreover, when deuterium is used as probing beam, important advantages for d-NRA studies emerge, due to: (a) the simultaneous excitation of most light elements (e.g. B, O, N, C, F, Al, Mg and S) usually co-existing in complex matrices, either in high concentrations or as impurities (which can unfortunately also cause some background interferences in certain cases due to peak overlaps), and (b) the enhanced sensitivity and accuracy, mainly due to the generally large differential cross-sections of the deuteron-induced nuclear reactions. It has to be noted though, that when d-NRA is implemented, radiation safety precautions are mandatory due to the emitted neutrons originating from (d,n) reactions on the target elements and the structural materials in the path of deuterons, and from the deuteron breakup (for deuteron beam energies higher than 2.2 MeV). This problem, however, is not critical, for low energies and beam currents of the order of nA typically used in NRA studies. The main problem that has actually hindered the wide implementation of NRA in depth profiling studies in the past is the fact that existing NRA differential cross-section datasets in literature (IBANDL [23] and EXFOR [24] databases) are usually not abundant, being also often quite discrepant.

An example of the successful NRA implementation over the EBS one is presented in Figure 1.24, concerning a gold sample with carbon traces on top, comparing the spectrum using the resonant $^{12}C(p,p)$ elastic scattering at 1750 keV on the left and the one using the $^{12}C(d,p_0)$ reaction at 1200 keV (right figure).

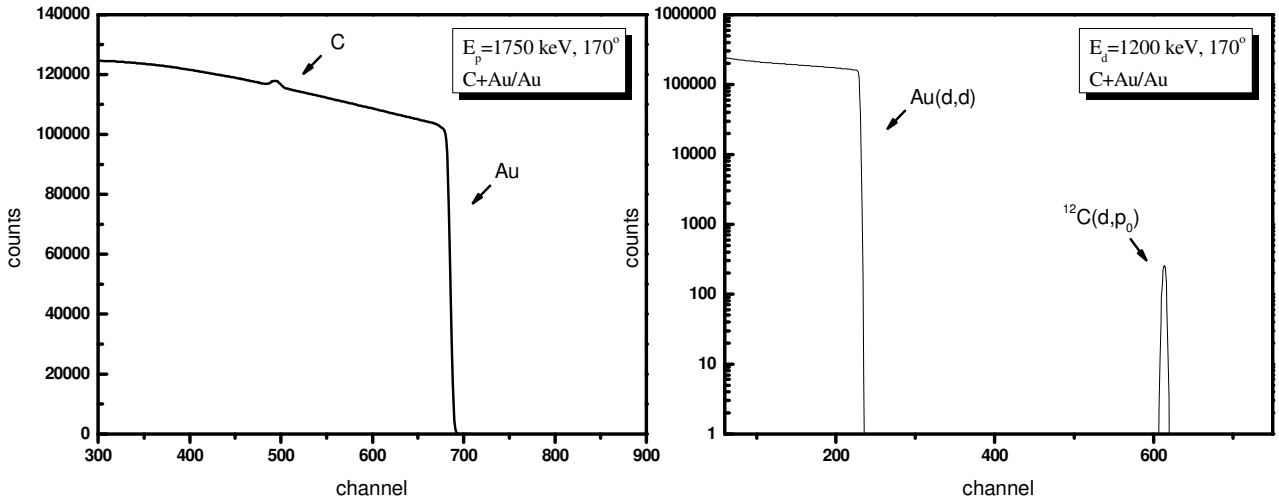

Figure 1.24: EBS spectrum in the resonant region of the $^{12}C(p,p)$ elastic scattering (left) comparing to the NRA spectrum of the $^{12}C(d,p)$ reaction (right) on a gold target with carbon traces on top for the same accumulated charge.

It should be mentioned here that the NRA method is often implemented along with the EBS and/or the RBS one, in order to obtain the most accurate results by combining the advantages of these techniques and/or by decreasing the uncertainties by the simultaneous combined analysis.

1.3 Implementation of the techniques

The implementation of the IBA techniques relies on the study and the analysis of the specific nuclear reaction(s) occurring in the sample of interest, while being bombarded with an ion beam, depending on the technique used. It certainly requires the use of the appropriate accelerated beam to impinge on the sample-target and the suitable experimental set up, consisting of the detector placed at the selected scattering angle and the corresponding electronics, as described in the following chapter. It has already been pointed out that, provided that the beam interaction with the target can in principle be monitored and studied in terms of the acquired spectrum, one can quantify and/or depth profile (depending on the technique used) the element or isotope of interest contained in the target. The latter can be achieved by analyzing the acquired data based on the principles of the nuclear reaction studied (mainly its cross section) and the detecting system used. As general requirement to the followed method, one should have all the parameters involved in the procedure accurately determined, namely the beam energy, the detector position-angle with respect to the beam direction, the solid angle of detection, the beam current (specifically the accumulated charge in the sample) and the characteristics of the detector and the electronics used, such as the detection efficiency and resolution and the amplification (in terms of spectrum calibration).

The actual implementation though of the IBA methods in material study, starts way before the final setting up of the detector(s) and the measurement itself (or the final analysis), since it is totally based on the exact selection of the appropriate technique to be used, depending on the specific case. The technique to be used depends primarily on the sample to be analyzed and its comprising element(s) or isotope(s) one wants to quantify and/or depth profile. The depth analysis together with the possible coexistence of near Z elements or of very heavy ones, plays a very important role to the analytical procedure and thereby to the methodology to be followed. Depending on the case, the appropriate ion beam at the specific energy is selected along with the emitted ejectile, originating from the reaction that suits the study, to obtain the most accurate results. The higher the energy of the projectiles, the deeper the probed analysis would be, but providing worse depth resolution because of the lower stopping power in the material with increasing energy. For each case, all the involved parameters are taken into account and the best compromise would lead to the most suitable technique to be used. For instance, for the profile of a heavy element, the RBS technique should be applied, while for the analysis of a very light element, ERDA or EBS is preferable. If the sample is thick, one would need highly energetic

beam particles, whereas for a thin sample a heavy ion beam is needed to provide better depth resolution. In the case of a specific isotope study, or of a complicated matrix, the NRA technique would in principle resolve the situation.

However, the choice of the IBA technique, the ion beam, the beam energy and the detector angle depends not only on the sample and its comprising elements, but also on the availability of the corresponding cross section data for the selected studied reaction to be used in the final concentration calculations. The whole analytical procedure of quantifying an element or isotope is actually based on the cross section concept, as described in detail in the previous sections. Except for the case of Rutherford backscattering spectrometry (RBS), where the cross section can be analytically derived from the corresponding formula (see 1.1.2), the implementation of all the depth profiling IBA techniques critically relies on the existing data (experimentally determined and/or evaluated ones) and their reliability. For a specific analysis, the most suitable method cannot be applied unless the corresponding differential cross section data exist. In addition to this constraint, the most precise, in all aspects, procedure could also be hindered by the accuracy of the used cross sections. A validation procedure of the data is, therefore, also very important for the proper implementation of the techniques.

There has been a tremendous progress accomplished during the last decade, through the creation of the IBANDL database [23], which contains differential cross sections suitable for IBA that can be directly incorporated in widely used analytical programs, as well as the existence of evaluated differential cross–section datasets that are available to the scientific community through the on–line calculator SigmaCalc [25] and through IBANDL as well. However, in the case of EBS and NRA (and d–NRA in particular), the present situation still leaves much to be studied, since the existing experimental data are quite scarce and discrepant in many cases, hindering both their direct use in implementing the aforementioned IBA techniques and the corresponding evaluation process, thus limiting the applicability of both techniques (EBS and NRA). Therefore, the measurement and evaluation of differential cross sections at steep backscattering angles suitable for IBA, constitutes an open field of ongoing research.

Moreover, the accuracy of the cross section data used in IBA analytical studies certainly plays a critical role in the final results and conclusions, since the whole procedure is completely based on these values. The experimental procedure to measure cross sections, as described in chapter 3 for such measurements in the framework of the present dissertation, includes a variety of uncertainty factors that could affect the calculations. Therefore, the obtained cross-section data, either derived from an experimental procedure, or within the evaluation process, which is

also based on experimental data (as described in chapter 5), need to be validated prior to their use, in order to check their reliability and accuracy. The benchmarking process denotes the validation procedure of cross section values, by acquiring thick target spectra containing the reaction of interest, followed by the detailed simulation of these spectra using the cross section data to be checked. The main concept of the benchmarking is based on the fact that the thick target spectrum reveals the true cross section of the corresponding reaction, convoluted of course with all the aforementioned other parameters. The whole procedure is described in detail in chapter 4. The fact that there are significant discrepancies in many cases in the existing data in IBANDL and EXFOR, concerning resonances or even plateaus of a cross section and moreover, the possible fine structure that cannot be depicted in the discrete experimental points of measured cross sections, make the benchmarking procedure more than useful and valuable. As described in detail in chapter 4, the benchmarking of the evaluated data plays a crucial role, not only in the validation of the data, but also in the evaluation procedure itself (feedback).

1.4 Motivation

The main contribution of the present doctoral thesis in the field of Ion Beam Analysis involves the measurement of the cross sections of selected reactions critical for EBS and NRA purposes. More specifically, the **p + ^{7}Li, ^{19}F** and the **d + ^{nat}Mg** systems were thoroughly studied, as described in chapter 3.

It should be pointed out that lithium and fluorine are very common elements in nature with huge technological interest. In particular, the quantitative determination of lithium is important for the characterization of various materials, including aluminum and magnesium alloys, ceramics, glasses, lubricants, greases, and rechargeable batteries. The quantitative determination of fluorine in various samples, on the other hand, is of great importance for material science, as well as, for medical, biological and environmental studies. The main problem concerning the depth profiling of lithium and fluorine is that since both elements are highly reactive, they are usually present in relatively complex matrices along with several medium- or high-Z elements. Thus, due to their low atomic number and their coexistence in heavy matrices, the determination of their profile concentrations presents strong analytical challenges for all IBA techniques. Among these techniques, Elastic Backscattering Spectroscopy (EBS) and Nuclear Reaction Analysis (NRA) are preferably used, due to their high analytical power for accurate and

simultaneous determination of several light element concentrations in complex samples. The existing differential cross-section datasets in the literature, necessary for the implementation of these techniques, are unfortunately inadequate and discrepant in many cases. More specifically, for the study of lithium concentration depth profiles, $^{7}Li(^{3}He,\alpha_0)^{6}Li$, $^{7}Li(^{3}He,d)^{8}Be$, $^{7}Li(^{3}He,p)^{9}Be$, $^{7}Li(p,p_0)^{7}Li$ and $^{7}Li(p,\alpha_0)^{4}He$ reactions have been proposed in the past [26–33,108-109]. The most promising one though, seems to be the $^{7}Li(p,\alpha_0)^{4}He$ reaction, because of its relatively high cross-section values and high Q-value, providing isolated peaks with practically no background. There is however a lack of corresponding data in the literature over a wide range of energies and detector angles.

The present study aims at contributing in this field through the differential cross-section study of the **$^{7}Li(p,p_0)^{7}Li$, $^{7}Li(p,p_1)^{7}Li$, and $^{7}Li(p,\alpha_0)^{4}He$ reactions**, as sketched in Figure 1.24, in the energy range of 1.5–7 MeV using a variable energy step and for detection angles between 140° and 170° in steps of 10°.

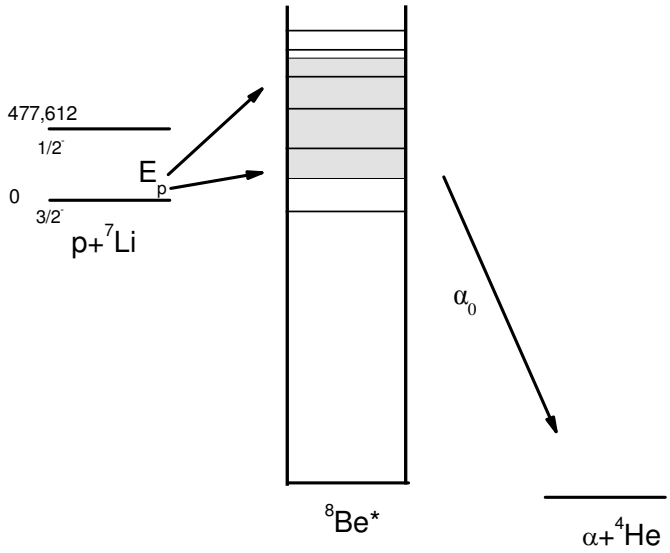

Figure 1.24: Level scheme of the p+Li system in C.M..

As far as fluorine is concerned, Proton Induced γ-ray Emission (PIGE) is mainly used for the determination of its profile concentrations, due to the existence of several, narrow and strong resonances in the $p+^{19}F$ system (e.g. the relatively narrow, Γ = 4.5 keV resonance at Ep = 872.11 keV of the $^{19}F(p,\alpha\gamma)^{16}O$ reaction). Alternatively, $^{19}F(d,\alpha_0)^{17}O$, $^{19}F(d,p_0)^{20}F$, $^{19}F(d,p_1)^{20}F$,

$^{19}F(p,p_0)^{19}F$, and $^{19}F(p,\alpha_0)^{16}O$ reactions have been proposed in the past [34–48]. However, several differential cross-section datasets in the literature concerning various p+^{19}F reaction channels are discrepant in many cases, mainly because of the complicated resonance structures involved. There has also been a tentative evaluation for proton elastic backscattering from ^{19}F for a limited energy range (550–1750 keV) retrieved from SigmaCalc [25]. It is important to note here, that this work aimed primarily at studying the p+^{7}Li system but due to the implemented LiF target though, selected differential cross-section values have also been determined for the **$^{19}F(p,p_0)^{19}F$, $^{19}F(p,\alpha_0)^{16}O$ and $^{19}F(p,\alpha_{1,2})^{16}O$ reactions**, sketched in the following Figure 1.25, in the same energy range (1.5–7 MeV) and scattering angles between 140° and 170° in steps of 10°. The alpha groups α_1, and α_2, belonging to the 6049 keV and 6130 keV excitation levels of the ^{16}O nucleus respectively, could not be analyzed separately, because of the coincidence of the corresponding peaks in the spectra for the proton energy range studied (due to the kinematics). It has to be pointed out however, that the adopted energy step was inadequate for a complete study of the strong and narrow resonances existing in the p+^{19}F system. Nevertheless, the determined, coherent differential cross-section datasets from the present work proved to be valuable for further evaluation purposes, presented in chapter 5.
This work, concerning both studies of p+^{7}Li and the p+^{19}F system, is analytically presented in chapter 3 (3.2 section).

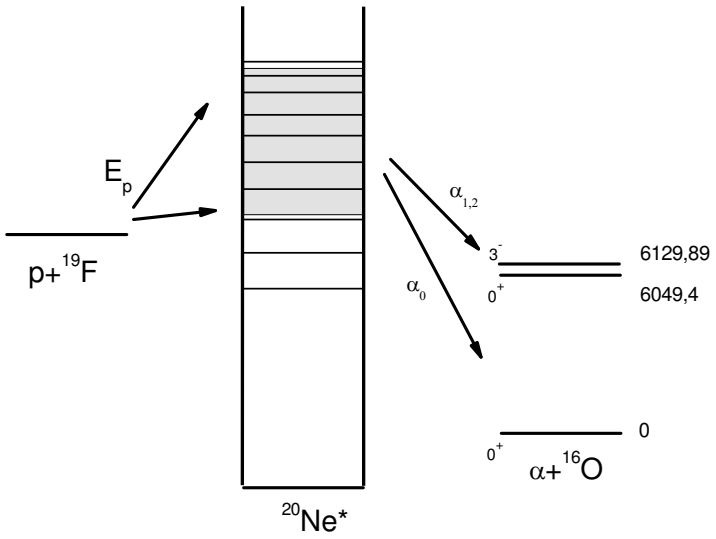

Figure 1.25: Level scheme of the p+F system in C.M.

Concerning the **magnesium study**, it should be noted that magnesium is the third most commonly used structural metal, following iron and aluminum. It is widely implemented in electronic devices and in front–end technology, mainly in the form of magnesium alloys. It is extensively used in the industry for the production of several high-volume parts, for the fabrication of numerous electronic devices, as well as, in the field of research of superconducting materials and applications [49]. Accordingly, magnesium depth profiling is of prime importance to characterize the produced alloys. Due to its low Z, however, and the fact that it is highly reactive and thus forms complex compounds, like lithium and fluorine, the accurate determination of its depth profiling presents a strong analytical challenge for the elastic backscattering spectroscopy (EBS) technique, despite the existence of multiple strong and narrow resonances [50]. Indeed, EBS measurements (involving mainly resonances in proton elastic scattering) can efficiently solve the problem of magnesium depth profiling in the cases where: i) the Mg concentration is not very low, especially in the presence of a high–Z matrix, ii) there is no signal interference from other light elements (usually in the form of overlapping resonances) e.g. as in the cases where Si and/or Al co–exist in a magnesium alloy. When these conditions cannot be met, nuclear reaction analysis (NRA) seems to be the most suitable technique for magnesium depth profiling studies, through the implementation of the $^{24}Mg(d,p_{0,1,2})^{25}Mg$ reactions, given that ^{24}Mg constitutes ~79% of natural magnesium.

In the particular case of d+^{nat}Mg system, sketched in Figure 1.26, it should be noted that there exists only one dataset [51] in literature, suitable for EBS and NRA studies, thus limiting the implementation of the corresponding techniques for Mg depth profiling studies. The dataset of Gallman et al. [52] concerns the study of $^{24}Mg(d,p)$ reactions at 120° and 80° in the high energy range of 2790-6100keV with a sparse energy step, while the study of Lee et al. [53] concerns one detection angle at 90° in a range of about 2000-4000 keV. Both datasets are thereby considered inadequate for Mg analytical studies.

The contribution of this dissertation in this field concerns the analytical cross section study of the $^{nat}Mg(d,d_0)$ elastic scattering and the $^{24}Mg(d,p_0,p_1,p_2)^{25}Mg$ reactions as well, at 55°, 70°, 90°, 125°, 150° and 170°. The deuteron energy ranged from 1300–2050 keV in the laboratory system, with a variable energy step, as discussed further in 3.3 section presenting also the results of this work.

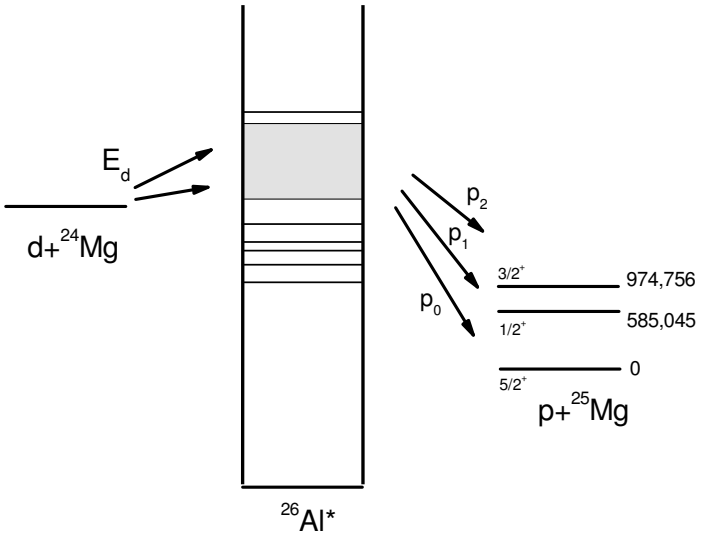

Figure 1.26: Level scheme of the d+Mg system in C.M.

Part of my research also involves the development of an experimental procedure for the validation of differential cross section datasets for charged-particle reactions on light isotopes, called **benchmarking**. The validity of the data used is of course of critical importance for all analytical applications. Benchmarking is actually an integral experiment that needs to be very carefully designed and performed, since a great number of parameters need to be investigated and accurately determined. The whole procedure is analytically described in this dissertation in chapter 4, presenting the benchmarking experiments performed for the validation of the measured differential cross sections mentioned above, namely the data concerning the studied p + ^{7}Li, ^{19}F and d + ^{nat}Mg systems. Moreover, in the general absence of cross-section validation in literature, benchmarking experiments were also preformed for the proton elastic scattering on ^{23}Na, ^{31}P, ^{nat}S and ^{nat}Si, being critical for analytical purposes. A different approach in the experimental procedure was applied for the validation of ^{nat}B(p,p) data, because of the nuclear reaction background, as described in section 4.7.

Besides the validation of differential cross-section data, benchmarking is actually in more ways critical for the implementation of EBS and NRA techniques in material analysis, since it also provides feedback for the adjustment of the parameters of the nuclear model used in the evaluation procedure, which eventually leads to the most reliable data to be used. Moreover, it can facilitate the extension of the existing evaluations to higher energies, it can help in assigning

realistic uncertainties to the cross sections, and it can also indicate recommended experimental datasets to be used in analysis in the absence of theoretically evaluated ones.

The last part of this dissertation concerns the theoretical cross-section investigation itself along with the subsequent theoretical models and phenomenology describing the occurred reaction processes. An example of the evaluation procedure of cross-section data, is alongside illustrated, concerning the case of the ^{19}F(p,p) reaction, in an attempt to extend the evaluation to higher energies.

CHAPTER 2
EXPERIMENTAL SET UP

The two experimental setups used for the cross section and the benchmarking measurements of the present thesis are described in this chapter. The production of the ion beam from both accelerators is briefly presented, while the scattering chambers, the used detectors and electronics, as well as the preparation of the targets are thoroughly described.

2.1 Accelerators

All the experiments for the cross section measurements were performed at the 5.5 MV Tandem accelerator located at the Tandem accelerator laboratory of the Institute of Nuclear and Particle Physics of the National Center for Scientific Research "Demokritos" in Athens, Greece. The benchmarking experiments for the (p,p) scattering on LiF, ^{nat}B and ^{19}F, as well as the (d,d) on ^{nat}Mg, were also performed at NCSR "Demokritos", while the benchmarking measurements concerning the elastic proton backscattering from ^{nat}Si, ^{23}Na, ^{31}P and ^{nat}S were performed at the 2 MV Tandetron accelerator of the Ion Beam Centre of the University of Surrey, England.

5.5 MV TN11 Tandem accelerator

The electrostatic accelerator at NCSR "Demokritos" is based on the Van de Graaf generator operation. The basic parts of the accelerator, sketched in Figure 2.1 along with the optical components, are the ion sources in the beginning of the line, the Van de Graaf generator in the center, inside the tank, responsible for accelerating the ions and finally the experimental beam lines. The high voltage structure of the accelerator is isolated by SF_6 gas at high pressure, whereas high vacuum of the order of 10^{-6} – 10^{-7} Torr is maintained in the accelerating tube and beam lines. At the end of the experimental beam lines there is usually a carefully designed chamber, where the beam hits the target of interest, and the detection system. Each line has a different geometry with specific layout and capabilities, serving specific experimental purposes.

The choice and the configuration of a beam line are based on the purpose and the needs of each experiment.

Starting from the ion sources, it should be mentioned that there are two kinds of sources, the duoplasmatron for light ions (protons and deuterons) and the sputtering source for heavy ones (^{12}C, ^{16}O etc). The produced ions from the source used, depending on the desired ion for each case, are negative. They get pre-accelerated (60kV) entering the pre-acceleration tube to the central transfer line, where they gain energy being attracted by the positive voltage of the generator (up to 5.5 MV). This voltage is provided with the use of a rotating belt (insulator) system, depositing positive charge on the terminal (metallic sphere), thus charging it, while a corona feedback system is used for the stabilization of the voltage. In the center of the terminal, the ions pass through a thin carbon foil (~10 μg/cm^2), which strips their electrons turning them from negative to positive ions. The positively charged particles are subsequently repulsed from the applied (positive) voltage of the terminal resulting to a second stage of acceleration (additional) of the particles (hence the name 'tandem' accelerator). Afterwards, the beam is focused entering the first electromagnetic quadrupole and is guided to the 90° bending analyzing magnet, which selects the ions with the desired energy (central value E, depending on the field) and a well-specified q/m ratio. The magnetic field strength is accurately measured and tuned through a feedback system through a Nuclear Magnetic Resonance (NMR) system. However, the exact determination of the beam energy, namely the accurate calibration of the magnetic field (and related fringe fields) in terms of energy is actually a very challenging task and is described in more details in a following section (3.1.2.1).

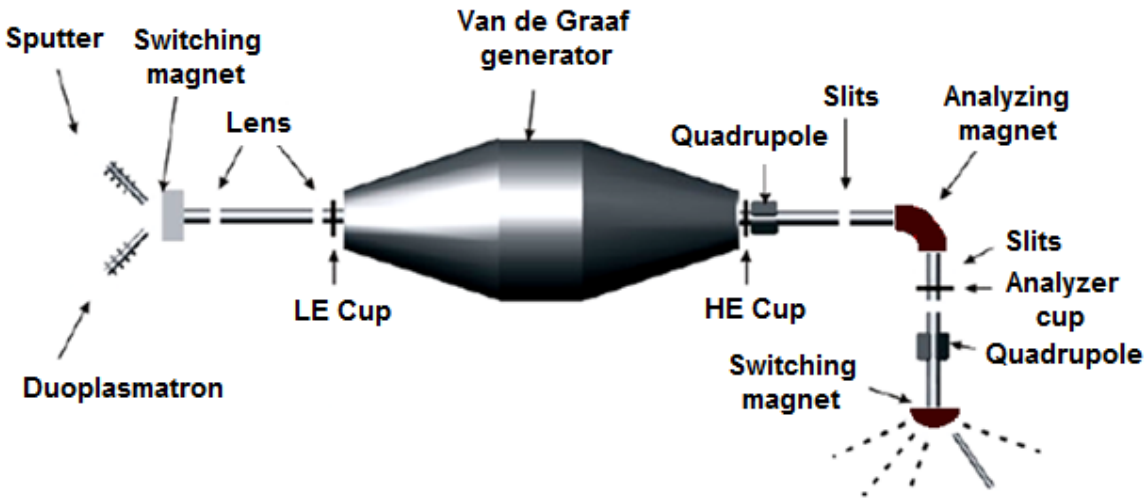

Figure 2.1: Schematics of the 5.5 MV HV Tandem accelerator at NCSR "Demokritos".

2 MV Tandetron Accelerator [54,55]

The fully computer controlled 2MV Tandetron accelerator at the Ion Beam Center of the University of Surrey resembles, in its main principle, the one at NCSR "Demokritos" described above, since it is also of tandem type. The Tandetron high voltage power supply is based on the Cockcroft-Walton system, with Radio Frequency power (at 14 KHz) fed to all stages together, making it extremely responsive and more controllable compared to the use of a belt-driven machine with a corona feedback system. The terminal potential is stabilized by a feedback system which uses a generating voltmeter (GVM) and capacitive pickoff monitors. The duoplasmatron source allows for a H^- beam to be extracted, while a lithium charge exchange channel can provide a negatively charged He beam. A cesium-sputter source is used to produce heavy ion beams. The accelerator is equipped with a compact dual source injection system, as sketched in the following Figure 2.2 [55], while the source selection and the mass analysis of the injected ion beam are accomplished by the 90° switching/analyzing magnet. Before the ion beam enters the accelerator tubes, the Q-snout [US patent #5.247.263.] accelerates the ions up to 80 keV. This serves for the matching of the ion energy to the focusing power of the acceleration tube entrance, whereby a beam waist is created at the center of the stripping channel. The double acceleration is achieved with the stripping gas in the terminal, turning the negative ions to positive, while a quadrupole doublet is used for the final focusing of the beam and a switching magnet is of course used for the beam line selection (see Figure 2.3 [54]).

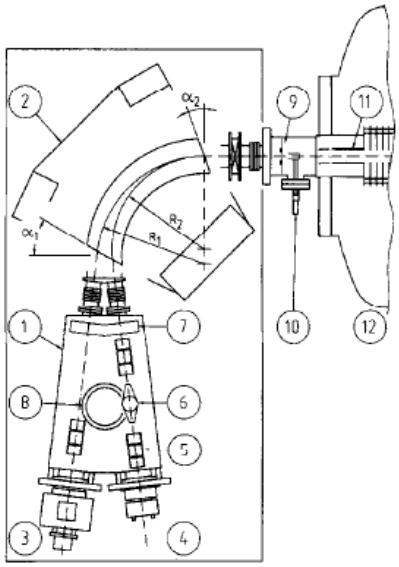

Figure 2.2: Layout of the dual source injector. (1) Injector block, (2) 90" magnet, (3) Cs sputter source, (4) duoplasmatron, (5) einzel lens, (6) lithium charge exchange channel, (7) steerers, (8) turbomolecular pump, (9) defining aperture. (10) Faraday cup, (11) Q-snout, (12) tank [55]

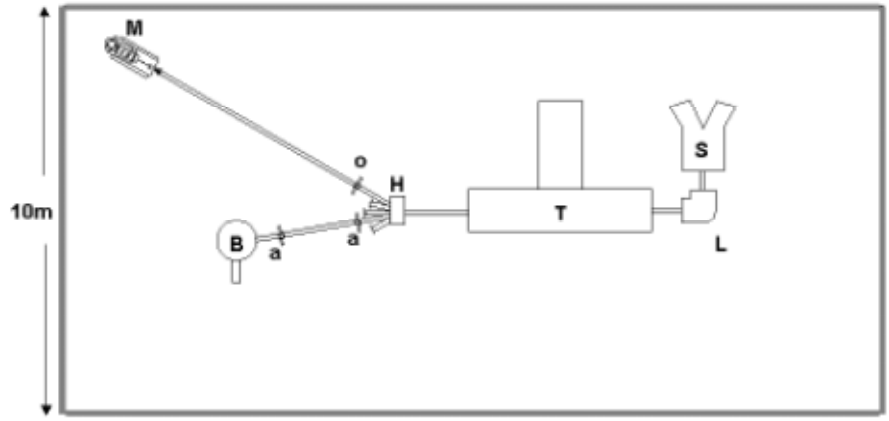

Figure 2.3: Schematic of the building with 2MV Tandetron installation (approximately to scale). S = double source assembly, L = low energy magnet, T = 2MV Tandetron accelerator, H = high energy magnet, M = microbeam line with object aperture ("o"), B = broadbeam (millibeam) line with apertures ("a") [54].

2.2 Scattering chamber

At the Tandem laboratory of NCSR "**Demokritos**" we used the beam line at the end of which there is a 70cm in diameter scattering chamber. This chamber is always in high vacuum, of the order of 10^{-6} Torr, during the measurements, with the use of a rotary and a turbo pump. A collimator of 2mm in diameter and an anti-scatterer of 2.5mm in diameter are placed at the entrance of the chamber (with a distance of ~3cm between them) resulting to a beam size of ~2mm in diameter onto the target. As seen in Figure 2.4, the target is placed in the center of the chamber on a special support and the detectors at the scattering angles of interest on both goniometric tables. In general, four targets on holders of certain specifications can be mounted on this support in the center of the chamber and only a vertical movement (and rotational if necessary) is necessary for the exact placement of each target on the course of the beam. The detectors are mounted on special holders on the goniometer, as described below. The signals of the detectors are guided out of the chamber using BNC vacuum feedthroughs, as seen in Figure 2.4. These connectors provide also the means for the power supply of the detectors.

The 60cm in diameter scattering chamber used in **Surrey** was quite similar to the described one at "Demokritos", being mostly dedicated to such studies, where multiple detectors and targets can be mounted. The proton beam can be focused down to ~1mm in diameter on the target, but various sets of collimation can also be used. A six axis goniometer [54] with a sample stage with dimensions of 105x153mm (able of holding many and/or large samples) sliding into the mechanism, enables the micrometric movement and, when needed, the tilt of the targets. Their correct positioning along the z-axis (beam axis), according to their thickness (up to ~6 mm for the used targets), is also allowed. The targets are mounted all together on the sample holder (depending on their size of course), enabling the automatic switch from one target to another for each energy step, during the measurements. The sample exchange mechanism acts through an vacuum tight system, allowing for the fast exchange of the targets. The scattering angles, where the detectors are placed, as described below, can be directly measured with high accuracy (of 0.1°), using a beam-line laser and the motors for the alignment.

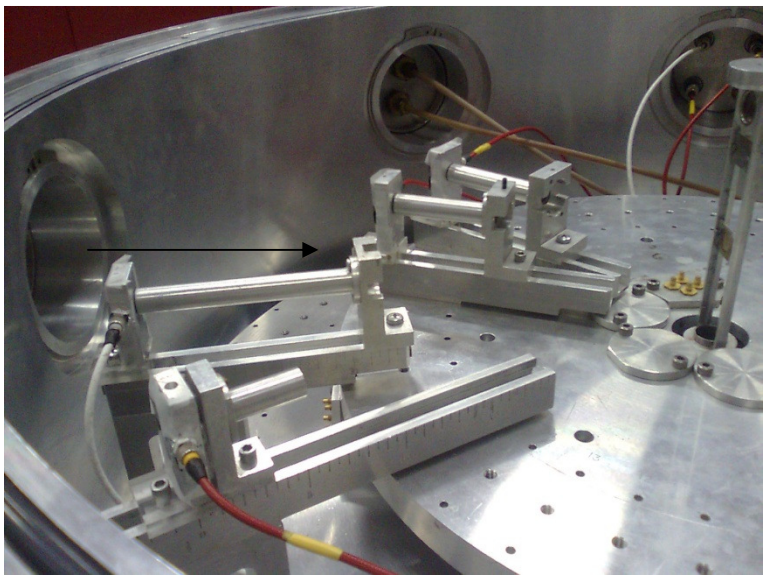

Figure 2.4: The scattering chamber at NCSR "Demokritos" with four detectors already in their final position. The arrow shows the direction of the beam onto the target (in the center of the goniometric table).

2.3 Detector setup

For the detection of the scattered particles, Silicon Surface Barrier (SSB) detectors were used for all the measurements. Except from the case of the ΔE/E experiment, described thoroughly in 4.7, the setup consisted of either 2 or 6 detectors, depending on the case, with 15-20 keV energy resolution and thicknesses that varied from 300 μm up to 1000μm. This thickness was in all cases sufficient for the deposition of the full energy of the particles of interest, thus enabling their correct detection. The detectors were placed at the desired scattering angles in each case, with the use of special calibrated rails inside the goniometric chamber, while small aluminum tubes ~1cm in diameter and of various lengths (~4-7cm) were placed in front of them, as seen in Figure 2.4. These tubes hinder the detection of scattered particles on the walls of the chamber itself and/or the Faraday cup at the end of the beam line (which is not included in Figure 2.4). Exactly in front of the active surface of each detector, orthogonal slits of ~4 x 8 mm^2, as seen in Figure 2.5, are placed in order to define the active area of detection to a small but sufficient enough opening (solid angle Ω) exploiting the phi invariance. The distance of the detectors from the target varied from 12 up to 25 cm, so that each detector had an angular acceptance of about ±1° or smaller.

Figure 2.5: Photo of a silicon (SSB) detector in place in the scattering chamber, without the aluminum tubes, in order to make the orthogonal slits visible.

For the benchmarking measurements that were performed at the Ion Beam Center, at the University of **Surrey**, two detectors were installed in the plane of the beam incidence (IBM geometry) at 120.6° and 148.8°, while a third one in Cornell geometry at 173.5°. The scattering angles were directly measured with high accuracy (of 0.1°), using a beam-line laser and the motors for the alignment, as already mentioned. The detectors at 120.6°, 148.8° and 173.5° were placed at a distance of ~14, 12 and 19 cm from the target, with orthogonal slits having a width

of ~ 2, 2 and 5 mm in front of them, in order to reduce the effective angular uncertainty to ~1°, 1.4° and 2.3° respectively.

2.4 Electronics

The detection system used at both laboratories, at "Demokritos" and at the University of Surrey, consisted of Silicon Surface Barrier (SSB) detectors, placed at the corresponding angles of interest, as already mentioned. In both cases the detectors were used along with the standard NIM electronics for spectroscopy, described as follows, besides the case of using ΔE/E telescopes described in detail in section 4.7.

Generally each detector produces an electrical signal, proportional to the energy of the detected particle. The detector functions normally, giving the best possible signal, when it is fully biased. The produced signal though, gets modulated electronically, as sketched in Figure 2.6 to take its final form, which is the form of a spectrum (described in detail in the following section).

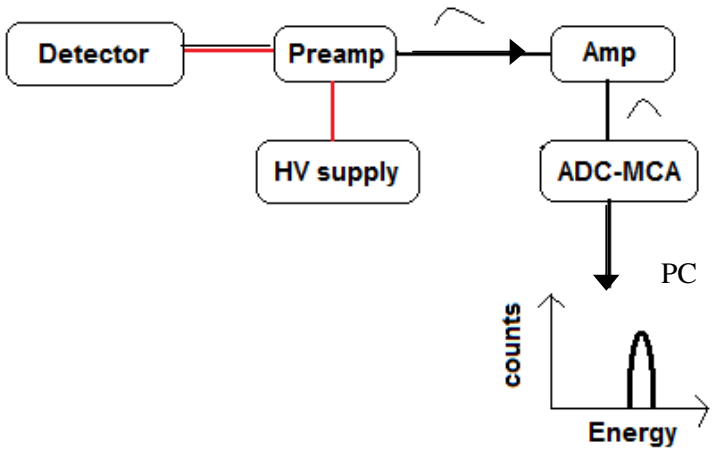

Figure 2.6: Schematic of the used electronics to obtain the spectrum on the computer.

Initially, it gains a small amplification by the preamplifier which is directly connected to it, in order to convert charge into voltage and to match the impedance for the transmission of the signal through a long cable. Through the preamplifier the detector gets biased using a high voltage power supply unit. Then the signal gets modulated and amplified by a spectroscopic amplifier. This step involves the adjustment of various parameters, namely the shaping time and

pole to zero level of the pulse, the polarity, the output (unipolar or bipolar) and possibly the DC level restorer. Besides the amplification (gain) that depends on the energy of the studied particles, which can widely vary from case to case (EBS comparing to NRA analysis for example), the rest of the parameters are tuned only in the beginning of an experiment, since they mostly depend on the functionality of each detector and the counting rate, which is always kept low in the order of ~1-5 kHz (full spectrum rate) when working with protons or deuterons. Afterwards, the signal is digitized with the use of an ADC (Analog to Digital Converter) and is then registered to a channel depending on its height (its voltage corresponding to the deposited particle energy) with the use of a multi channel analyzer (MCA). Due to the low resolution of the detectors used compared to the HPGe ones, 1024 channels are sufficient for the recording of the pulses to a spectrum. One typical spectrum is presented in Figure 2.7 representing the number of detected particles (counts) at each specific energy (channel). The channel to energy relation, i.e. the ADC-MCA energy calibration, enables the peak identification and is described in detail in the following chapter (section 3.1.1.1).

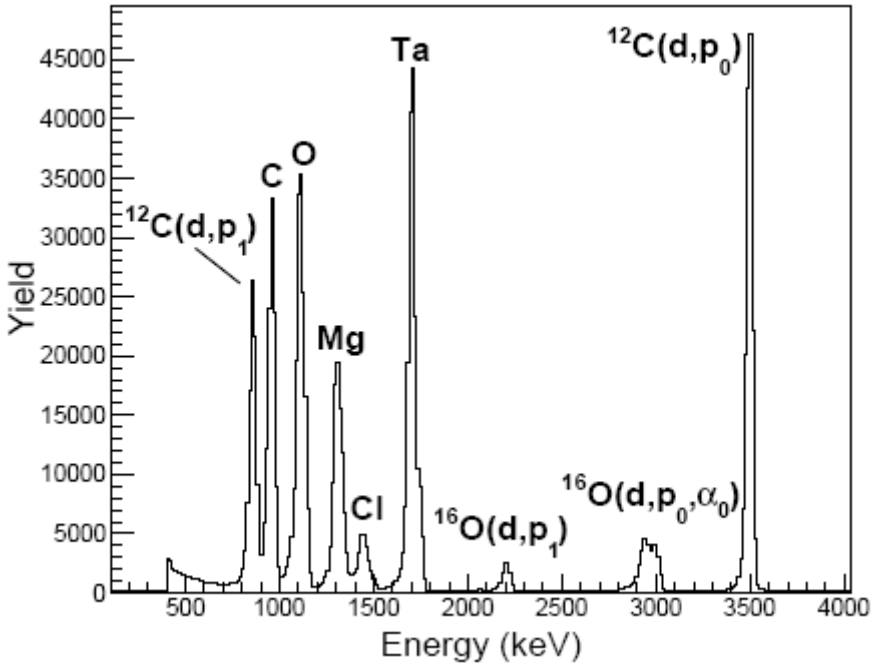

Figure 2.7: Typical experimental spectrum taken with a thin target consisting of Ta/Mg/$MgCl_2$ evaporated on a carbon foil, at 150° for $E_{d,lab}$ =1785 keV along with the corresponding peak identification.

2.5 Target preparation

The targets used for the differential cross-section measurements and all the benchmarking experiments, were all made at the Tandem laboratory at NCSR "Demokritos", using the evaporator and the high pressure system for manufacturing pellets. The evaporator, as seen in Figure 2.8, is mainly a chamber in high vacuum, where two different techniques can be applied for the evaporation of a material. Depending only on the material (melting point, chemical behavior etc) one can either use thermal evaporation, or use the electron-gun technique. The latter is a sputtering method in a very close geometry with electrons produced by a heating resistor and directed onto the material with the use of a proper magnetic field. The material for evaporation is placed at the central part of the chamber onto a special but simple construction according to the evaporation method to be used. Above it and at a variable distance between 10-20cm, a mechanical support for the substrate (supporting material of the target) is placed, as can be seen in the right photo in Figure 2.8.

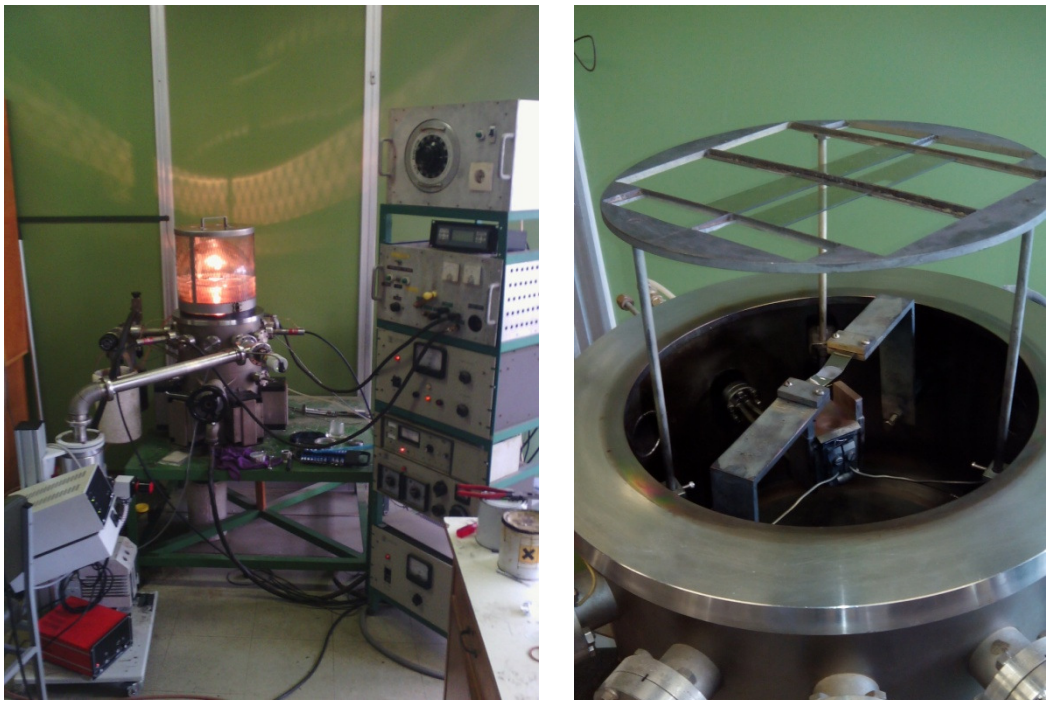

Figure 2.8: The evaporator of the Tandem laboratory in the Institute of Nuclear and Particle Physics of NCSR "Demokritos"

As an example of the procedure, the preparation of the target for the p+LiF cross-section measurements will be described as both techniques of evaporation were used. It consisted of a carbon foil of 52 ± 2 μg/cm^2 thickness, with a LiF layer of (960 ± 38)x10^{15} at/cm^2 that was evaporated onto the carbon foil. A thin gold layer of 4.4 ± 0.3 μg/cm^2 was additionally evaporated onto the LiF layer. The actual thickness calculation of all the layers is described in detail in section 3.2.1. In the beginning the carbon foil was made using the electron-gun method, where a small piece of graphite was bombarded with electrons resulting in the sputtering of carbon atoms. At a distance of ~20cm over the graphite, several glass slides (~2 x 7 cm), with a thin film of soap mixture (10% betaine and 90% sugar water) which has previously been applied on, were placed on a special support at the evaporator, as seen in Figure 2.8 (right photo). After several hours of electron sputtering the evaporation was stopped and a thin layer of carbon was formed onto the soap film of the glass slides. The carbon layer was afterwards removed from the glass by slowly dissolving the soap mixture in water. As the mixture dissolves the carbon layer floats on the water and can be easily placed on a target holder.

This procedure leads to the production of several carbon foils depending on the number of glass slides placed in the chamber during the evaporation. It should be noted here that this is the same procedure followed for producing the carbon stripping foils of the accelerator, as described in the previous section (2.1). These foils need of course to be thinner, about 10μg/cm^2.

For the evaporation of the LiF layer onto the carbon foil, the needed quantity (m) of LiF powder was placed on a metallic sheet (boat), made of Ta, and the carbon foil (on a target holder) was placed above it, at a distance (r) of ~15cm. As high current passed through the Ta boat, LiF melted and then evaporated, resulting at a deposition onto the carbon foil with an areal density d. The calculation for the isotropic evaporation in this geometry (in the upper 2π part of the evaporator) is actually trivial, as shown in the following equation.

$$m = d * (2\pi r^2)$$

For the gold layer of the target, the same procedure was followed. Instead of the LiF powder a small piece of gold (~40mg) on a new Ta boat was placed. On top of it the carbon foil with the LiF layer was placed downwards for the gold to be evaporated on the LiF layer, for wear protection and charge/solid angle normalization purposes (as explained in section 3.1).

For the d+^{nat}Mg differential cross-section measurements the thin target used was made in a very similar way. That is, by evaporating a mixture of natural magnesium and magnesium chloride powder (in a Ta boat) on a ~10 μg/cm^2 carbon stripping foil and by evaporating afterwards a thin Au layer on top of it. Alternatively, a thin Ta layer can be evaporated on top of the magnesium target, by increasing the current in the tantalum boat containing the mixture (immediately after the evaporation of the magnesium mixture) till the evaporation point of the tantalum itself is reached. The thicknesses of all the layers were determined accurately as described in the corresponding section 3.3.1.

The pellets that were used for the benchmarking measurements, were produced by highly pressing the desired powder. The NaBr, MoS_2, ZnF_2 and B pellets were made by implementing a 6 ton pressure on the corresponding powder for 10 min, in 2 ton gradual steps. Along with the other thick targets used for these measurements, namely the Silicon [111] and GaP wafers and the Mg tape, all the pellets were covered with a thin layer of gold following. Thus, all targets used had a thin layer of Au on top, for wear protection and charge/solid angle normalization purposes (as already mentioned above).

2.6 Target characterization

The chosen target is of critical importance for the reliability of all the experiments performed, concerning both the differential cross-section measurements and the benchmarking ones. It is therefore evident that, prior to their use, all targets need to be characterized in the most accurate way. It should be noted here that the procedure of the target preparation itself is unavoidably responsible for some secondary effects, namely the eventual presence of impurities in the target. Depending on the case, this can involve surface oxidization and the presence of small amounts of nitrogen and possibly chlorine, due to the involved water in the evaporation procedure concerning the thin targets (when making the carbon backing foil). Moreover, carbon molecules may also be deposited onto the target beam spot, being drifted by the beam particles during the target irradiation (carbon build up). However, under the typical experimental conditions, in terms of beam current and irradiation time, the carbon build up effect is negligible. All the above parameters are studied and are taken into account in the analysis depending on their scale and the case study.

For the quantification of mid-heavy and heavy elements and, in particular, for the thin layer of gold deposited on top of the targets, the X-ray Fluorescence (XRF) technique is used. This technique has generally a typical detection limit for elements lighter than magnesium (Z>12) and is also of limited accuracy (as low as 10%), pending on the target composition, the thickness (e.g absorption effects in the pellets) and/or the target's homogeneity [56]. For light element quantification, where this method (XRF) cannot be applied, other complementary IBA techniques are implemented in such a way, that the cross section is precisely known and preferably following the Rutherford formula (RBS technique), choosing low energetic or heavy beam particles for instance, thus allowing for the determination of the studied thickness, with a better accuracy than typical XRF measurements. Combined techniques can also be used in some cases in order to minimize the induced uncertainties in the target composition.

Each target needs therefore to be characterized using the appropriate technique according to its composition. The characterization of the targets used for the cross-section measurements of the present studies, is analytically described in sections 3.2.1 and 3.3.1 respectively. On the other hand, the pellets used for the benchmarking runs (excluding the boron case in section 4.7) did not really need any special treatment for the determination of the thin gold layer thickness, since the obtained spectra at low energies were sufficient to determine this value. This was indeed feasible by using the Rutherford scattering of the heavier element of each thick compound target used at these energies, as thoroughly described in the relevant sections in chapter 4 (4.5-4.8).

CHAPTER 3

DIFFERENTIAL CROSS – SECTION MEASUREMENTS

The main contribution of the present dissertation in the field of Ion Beam Analysis is to provide differential cross sections to the scientific community, thus facilitating the implementation of the EBS and NRA techniques. More specifically, the p+Li, p+F and d+Mg systems were studied at NCSR "Demokritos" and the obtained cross-section data for the $^{7}Li(p,p_0)^{7}Li$, $^{7}Li(p,p_1)^{7}Li$, $^{7}Li(p,\alpha_0)^{4}He$, $^{19}F(p,p_0)^{19}F$, $^{19}F(p,\alpha_0)^{16}O$ and $^{19}F(p,\alpha_{1,2})^{16}O$ reactions, as well as for the $^{nat}Mg(d,d)$ and $^{24}Mg(d,p_i)$ reactions, are presented in this chapter. It is essential, however, to describe the experimental and analytical procedure for the cross-section determination in detail prior to the measurements themselves (presented in sections 3.2 and 3.3). Therefore, the methodology used, all the steps needed for the spectral analysis and the corresponding calculations are in detail presented in the first sections of this chapter.

3.1 Determination of the differential cross section

The determination of the differential cross section ($d\sigma/d\Omega$) of a reaction is based exactly on its definition in the case of an ultra thin target, as discussed in section 1.2.1 and also seen in the simplified equation 3.1 below. The differential cross section represents the probability of the beam particles with energy E (in the laboratory system) to be scattered from the target nuclei to an angle θ (EBS case) or to react with the nuclei emitting an ejectile at an angle θ (NRA case), depending on the studied reaction. Using an ultra thin target containing the element of interest, the detected particles (yield) at θ, within the detector solid angle Ω, originating from the occurred reaction, are thus measured with respect to the number of the beam particles (charge Q) reaching the target and the solid angle of the detector, normalized also to the number of the target nuclei N_t.

$$\left(\frac{d\sigma}{d\Omega}\right)_{E,\theta} = \frac{Y}{N_t(Q\Omega)} \qquad 3.1$$

The thickness N_t corresponds to the thickness of the target element/isotope involved in the studied reaction, measured in surface density units (at/cm^2), while the Ω factor represents the solid angle covered by the detector and is given in sr. The resulting cross section is therefore measured in mb/sr.

It should be noted here, that equation 3.1 is valid only in ultra thin target cases, namely with minimal beam energy loss inside the target and only when the cross section does not present strong variation within this energy interval. Concerning however the latter special cases (with Breit-Wigner resonances, seen in 1.1.2), the analysis is significantly limited due to the beam energy uncertainty (ripple), as it will be described in 3.1.2.1. The effect of the energy loss in the cross section determination is analytically described in 3.1.2.2.

All the terms in the above equation can be experimentally measured, thus calculating directly the unknown cross section. More specifically, the detected particles $\boldsymbol{Y}$ are easily counted analyzing the spectra, as described in detail in the following section. The determination of the target thickness $\boldsymbol{N_t}$, on the other hand, is usually quite challenging and each target needs to be characterized in a different way, depending on its consisting elements, as described in section 2.6. The accumulated charge $\boldsymbol{Q}$ in such experiments can be measured by integrating the induced current on the target and the Faraday cup behind it, using a current integrator. Due to secondary effects in the irradiated target though (like electron emission from the target elements), some kind of suppressing voltage needs to be applied in the circuit. Alternatively, the use of a close geometry of the target-chamber-Faraday cup setup (the chamber being the Faraday cup) would lead to a better counting of the charge, but this is never the case in such studies, where the chamber is of relatively large dimensions to fit the detectors at some cm distance from the target and is always prone to small parasitic currents which impede its use as a Faraday cup. Actually the Faraday cup in these studies is inefficient, usually being far from the target (at a distance of ~125 cm in our case), and thus covering only the really straight forward particles, making the charge measurement inaccurate. Actually, it has been proven in the past, that the suppressed accumulated charge in the scattering chamber used at Demokritos, where the cross sections of the present work were measured, is collected with errors ranging from 3 to 15%, depending not only on the ion species and energy, but also on the target thickness, thus presenting a strong challenge in the minimization of the measured charge uncertainties. Another issue that needs to be treated carefully is the determination of the solid angle $\boldsymbol{\Omega}$ for each detector. It can indeed be

measured with the use of an isotropic alpha source (2π) of known activity placed exactly in the position of the target. This measurement though is also not precise enough, mostly because of the different dimensions of the source and the beam spot. Summarizing, the QΩ factor is overall hard to be absolutely measured at the desired accuracy of a few percent and for its determination in the present study we used the scattering on the thin layer of gold on the targets, which is purely Rutherford at the studied energies. This methodology leads to the use of formulas for relative measurements of the cross sections, namely compared to the ones on gold, described as follows below. The scattering on thin gold is of course also described by equation 3.1, where the cross section $(\frac{d\sigma}{d\Omega})_{Au}$ is in this case analytically calculated using the Rutherford formula (see section 1.2.1).

For example, in order to measure the differential cross sections of the proton scattering on the x element, using a thin target containing the x element with an ultra thin layer of gold on top, one would need to use formulas 3.2 and 3.3, respectively, for one measurement (E_p ,θ). The detected particles at the scattering angle θ, originating from the scattering on x and Au nuclei are now written as Y_x and Y_{Au} respectively. The cross sections and the thicknesses of the two elements are also denoted in a similar way.

$$(\frac{d\sigma}{d\Omega})_x = \frac{Y_x}{N_{t,x}(Q\Omega)} \qquad 3.2 \qquad\qquad (\frac{d\sigma}{d\Omega})_{Au} = \frac{Y_{Au}}{N_{t,Au}(Q\Omega)} \qquad 3.3$$

During one measurement, at one proton energy that is, the accelerated protons react with both x and Au nuclei, for the same accumulated charge Q (given that the number of the scattered particles in the first Au layer, that obviously do not reach the deeper layer, are negligible (below 0.1%) compared to the beam particles impinging on the target) and the scattered protons from both elements are recorded by the detector set at θ within the same solid angle Ω.

Dividing these two equations, we get the desired cross-section values relatively to the Rutherford ones from the scattering on gold without the QΩ product, as seen in the final equation 3.4. These two major sources of big uncertainty are in this way eliminated, making this method far more accurate than absolute measurements (calculating cross sections directly using equation 3.1 and measuring Q and Ω independently). The ratio of the thicknesses of the two

layers $\frac{N_{t,Au}}{N_{t,x}}$ is usually determined coherently to further reduce the uncertainty. A detailed assessment of the uncertainties in the present measurements of cross sections is discussed in the corresponding sections (3.2.2 and 3.3.2).

$$(\frac{d\sigma}{d\Omega})_x = (\frac{d\sigma}{d\Omega})_{Au} \frac{Y_x}{Y_{Au}} \frac{N_{t,Au}}{N_{t,x}} \qquad 3.4$$

The procedure that follows the performed experiment and the acquisition of the data is throughout described in the following sections. This procedure is necessary for the determination of the cross sections and it practically consists of three steps. Initially, the acquired spectra recorded by the detectors, along with the corresponding electronics that have already been described above, need to be analyzed and the target thickness to be determined. Calibrating the energy of the accelerator and knowing the composition of the target, the final energy of the beam particles can be calculated and therefore the unknown cross sections can eventually be determined at each energy step.

3.1.1 Spectrum analysis

A typical spectrum is seen in Figure 3.1 for the proton beam at $E_{p,lab}$=4780 keV at 150° hitting a carbon target with a thin layer of Au on top. This experimental spectrum shows the number of protons scattered to 150° after interacting with the thin target, with respect to the channels of the ADC (with incorporated MCA –multi channel analyzer). After calibrating the ADC, i.e. finding the relation between the channel and the particle's energy, as described in the following section, one can identify the peaks in a spectrum of the specific reaction that yielded the detected particles. Afterwards, the peak(s) corresponding to the reaction(s) of interest should be integrated to give the yield Y needed in the equation for the determination of the cross section (Y_x and Y_{Au} in the above equation 3.4).

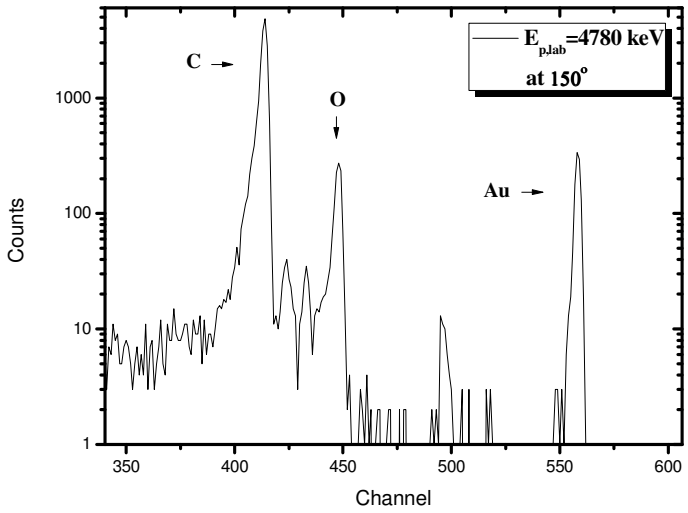

Figure 3.1: Typical spectrum of the detector at 150° for proton beam on a thin carbon target with a thin Au layer on top.

3.1.1.1 Peak identification

The acquired spectra using thin targets usually exhibit several peaks corresponding to groups of detected particles at several energies (channels). Since the targets often contain more elements than the studied one(s), (see section 2.5 for the ones used in the present work) the detected particles have specific energies, depending on the nuclei they have interacted with and the type of the occurred reaction. As has already been analyzed in 1.1.3.3, the elastic scattering follows the kinematics of the reaction, while for a nuclear reaction its Q-value and the exciting level of the residual nucleus should be taken into consideration. In all cases the energy of the detected particles is characteristic of the reaction and can be *a priori* calculated. After calculating the expected groups of energies of the particles, with the use of LARELKIN [57] or catkin [58], for instance, originating from all the possible reaction channels regarding all the elements of the target, one can identify the peaks in a spectrum, by **calibrating the ADC**, as described in the following paragraph. With the ADC energy calibration one determines the linear correlation between the channels of the spectrum and the energy of the corresponding detected particles, namely the **gain** (in keV/channel) and the **offset** (in keV). Afterwards, possible unknown peaks in a spectrum must be attributed to reactions with small (unconsidered) contaminations of the target or unaccounted reaction channels of one or more isotopes, which can in reverse be identified since their energy (group of channels) is known (in the spectrum). The origin of all detected particles (always in groups forming peaks) can thereby be determined. It has to be

noted here that the ADC calibration is very important in cases where there are lots of peaks in the spectra. This can be the case, when the target consists of many elements/isotopes and/or when lots of different reactions occur between the beam particles and the nuclei in the target (as in the case of highly energetic beam particles). In such cases, spectra can occur with overlapping peaks or with peaks that "suddenly" appear (at the onset of an additional reaction channel). Such experiments need to be treated in a very careful and systematic way in the analytical procedure, in order to study the reactions (peaks) of interest and not some other parasitic ones in the spectra, rendering the calibration procedure and thus the peak identification very important.

A quite precise ADC calibration can be performed during the first steps of an experiment. With the use of a triple alpha source (^{239}Pu, ^{241}Am, ^{244}Cm), from which the emitted alpha particles have characteristic and well known energy (with the highest intensities at 5156.6, 5485.6, 5804.8 keV respectively), prior to the target irradiation, one can not only fix the gain of the amplification used and check the electronics, but also roughly calibrate the ADC. Using the three (main) peaks of the detected alpha particles, one relates their energy to the corresponding ADC channels (position in the spectrum), thus enabling the calibration of the spectrum (with extrapolation), by determining the gain and the offset factors of the linear relation between the detection energy and the channel. With this calibration, one can identify some characteristic peaks in a spectrum during the experiment, like the elastic scattering peaks and especially the one corresponding to the elastic scattering on the heaviest element (which will be the one on the right of the group of the elastic ones) or on the thickest element (wider peak). In Figure 3.1 for example, we can see three peaks corresponding to the elastic scattering of protons on carbon, oxygen and gold at 150°. The final and most accurate calibration of the spectra for the analysis is actually performed after the measurements, using the acquired spectra themselves in the whole range of studied energies. The calibration is indeed more accurate this way, because no extrapolation is needed. Generally, even two known (identified) peaks that are far from each other in one spectrum can be used for its calibration (when for example the experiment involves only a few measurements at close beam energies) giving satisfactory results.

It should be noted here that there are various parameters being involved in the peak identification and the accurate ADC calibration procedure [2 – chapter 15]. These include the accelerator calibration (described in detail in the following section 3.1.2.1), the energy loss of the projectile and the ejectile in the target, the effects of the detector entrance window and dead layer (the so-called pulse height defect -PHD) and the detector resolution. The accuracy of the obtained energy calibration relies on the precise determination of these parameters that affect the

position of edges and peaks in a spectrum. However, the significance of these effects in the whole procedure generally depends on the case study and the desired accuracy. It should also be mentioned here that fractional channel numbers could be used in the calibration procedure and special attention should also be drawn in the strong correlation of the gain and offset factors, as described in [2 – chapter 15].

Regarding the exact energy value of the detected particles relative to their energy loss in the target, one can use in general the surface signals to eliminate the corresponding uncertainties. The use of standard samples for the energy calibration is in any case preferable [2 – chapter 15]. The PHD effect, which results in a slightly different (non linear) response of the detector for different ion species passing the detector entrance window and dead layer needs to be taken into account (e.g implement PHD correction in the analytical codes) especially in NRA studies, or when working at significantly different beam energies (or of wide energy range). However, in the case studies of the present thesis, which concerned proton and deuteron beams, this effect was indeed negligible.

At **NCSR "Demokritos",** where all the cross-section measurements were performed, the standard procedure of the ADC calibration involves the use of a thick gold target at several beam energies for the gain adjustment and determination. A pure polished silicon wafer is always used as target, preferably measured at the lowest beam energies, for the subsequent determination of the resolution of the detectors. In the present studies, the final calibration was obtained using the peak of gold (top layer of the targets used) in the acquired spectra over the whole energy range studied. Such is the case shown in Figure 3.2, for proton energies ranging between 2.7-7 MeV, which presents excellent linearity. An increase in the number of experimental points in the least square fit method results of course in the reduction of the corresponding statistical errors in the determination of the gain (slope in keV/ch) and offset (keV) parameters. It should be noted here that the detected energies used for the scattered particles from gold were corrected to their final values, in terms of the accelerator calibration and the thickness of gold layer, as described in detail in the next section. Moreover, the position (channel) of each detected particle (group) depends on the corresponding pulse height of the recorded signal, which is of course not the same for all the detectors used in one experiment being placed at different scattering angles, depositing different energy in them and having different cable set and amplification, even using the same ADC type. Therefore, each detector spectrum, corresponding to one ADC, needs to be calibrated separately. The calibration factors

concern of course the measurements where no change in the amplification occurs. If the gain needs to be changed, for example, one needs to recalibrate the ADC afterwards. Therefore any kind of changes in the electronics is highly avoided during the measurements.

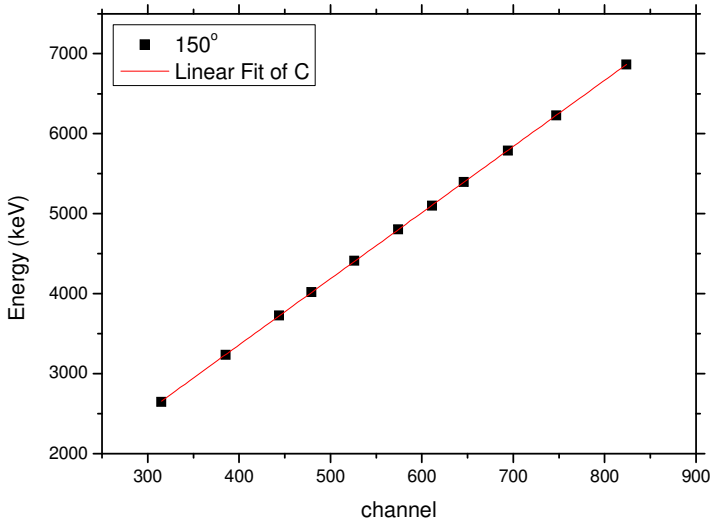

Figure 3.2: ADC calibration using the surface signal originating from the elastic scattering on gold.

3.1.1.2 Peak integration

Having identified the peaks of interest in all the acquired spectra, one needs to integrate them to obtain the yield for the calculation of the corresponding cross section. If the studied peak is not overlapping with another one in the spectrum, it is trivial to integrate it by initially subtracting any possible background counts using any kind of spectrum analysis program. In the case that the peak is not isolated, double fit with asymmetric Gaussian-type functions is needed for the determination of the integral of the studied peak. Triple fit may also be needed in the case of peak overlapping in both the left and right side of the peak of interest. This fitting procedure might be very sensitive to the program used and usually leads to larger statistical errors in the result. In the extreme case that there is a total overlap between two peaks, no accurate result can be obtained. One can and should spot such a case, by examining the nearby peaks to the studied one at each measurement sequentially, since the kinematics and thus the distance between the peaks differ for different beam energies (at least one peak of the two would correspond to a

nuclear reaction in a nuclei of the target elements). Actually, these cases can be predicted just by knowing the kinematics of all the occurring reactions in advance (using the LARELKIN code [57], for example), namely the expected energies of all the peaks in the spectra prior to the analysis procedure. Peaks originating from elastic scattering would never totally overlap except in the case of very bad resolution of the detector and/or in the case of bad mass resolution, depending on the masses of the target elements and the beam energy, as described in section 1.1.3.4, (e.g. in the case of isotope study at low energies). In these cases, it is evident that elastic scattering cross sections cannot be measured at all.

In the studied cases of the present dissertation, most of the peaks of interest were isolated, as described in detail in sections 3.2 and 3.3, but there were still a few cases where double fit was needed especially at the lowest energies, where the elastic peaks of the light nuclei were very close to each other. All experimental spectra for the cross section measurements were analyzed using the TV program [59], enabling the user to subtract any kind of background (linear or polynomial), to fit with fixed or different FWHM or asymmetries, when necessary, and also to obtain the yield with its statistical uncertainty.

3.1.2 Energy determination

The last step for the calculation of the differential cross sections $\frac{d\sigma}{d\Omega}(E,\theta)$ of a reaction, at the specific energy E and at the detection angle θ, is the determination of the exact energy of each measurement E (projectile energy step) corresponding to each analyzed spectrum. The needed accuracy in the energy calibration, though, depends of course on each case study. In the present dissertation, where resonant structures are generally investigated, the accuracy of the beam energy plays indeed a critical role on the obtained results, as further discussed in the following sections.

As described in section 2.1 (for the Tandem accelerator at NCSR “Demokritos”), the energy of the beam particles entering the scattering chamber depends on the applied accelerating voltage but only the field strength of the analyzing magnet can be accurately measured (with the NMR technique), as described in section 2.1. Therefore by calibrating this field in terms of energy (offset of the magnet), one determines the energy of the beam, with an uncertainty (ripple) which depends on the opening of the analyzing slits. In the case of the used Tandetron accelerator of the Ion Beam Centre of the University of Surrey, it is not the field of the magnet

that is accurately determined, but the applied voltage itself, with the GVM. One needs therefore to calibrate directly the voltage to energy terms, taking into account all the effects occurring in the accelerating procedure affecting the beam energy, such as the extraction voltage and the stopping power in the stripping gas.

Finally, in order to calculate the exact energy E of the beam particles reacting with the nuclei of the target, one needs not only to calibrate the accelerator beam energy, but also to take into account the energy loss crossing the target till the interaction occurs (deeper in the target), generally using the standard convention of attributing the cross section to the half of the target's thickness (mean value approximation), as seen below.

3.1.2.1 Accelerator energy calibration

There are several ways to calibrate an accelerator, including resonances in elastic scattering, threshold reactions with neutrons in the exit channel etc [2 – chapter 15]. However, the most accurate procedure would involve the study of very narrow resonances (a few eV) with γ-ray emission, over a wide energy range, ideally over the whole energy range studied. The gamma emission is preferable, since the detection of γ-rays is achieved with a better resolution compared to charged particle detection. The existence, however, of only a few such reactions (known) at a limited energy range, having in most cases some uncertainty (small but still evident) in the exact energy and width of the resonance, inhibits the ideal accelerator calibration.

The standard reaction generally implemented is the $^{27}Al(p,\gamma)^{28}Si$ one, which presents a very narrow resonance (Γ=110 eV) for $E_{p,lab}$ = 991.9 keV [60], as shown in Figure 3.3. The use of two more resonances at higher proton energies, namely the (1747.6±0.9) keV of the $^{13}C(p,\gamma)^{14}N$ reaction (Γ=122 eV) [61] and the (3379±1) keV of the $^{32}S(p,p\gamma)^{32}S$ reaction (Γ=700 eV) [62] is described in section 4.2.1, revealing the high accuracy of the procedure up to ~3.4 MeV proton beam energy [63]. The use of the $^{14}N(p,p'\gamma)^{14}N$ reaction with resonances in the range of 4-6 MeV has also been reported recently [64], but the procedure provides limited accuracy, because of the width of the resonances (17-106 keV) and the 3 keV uncertainty in all resonance positions.

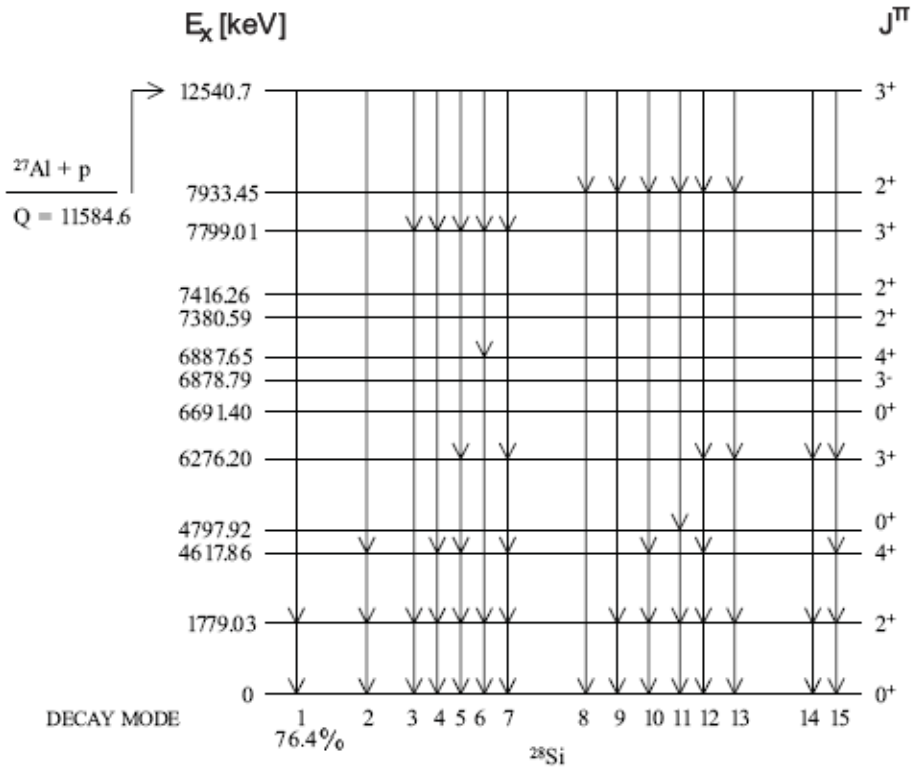

Figure 3.3: Decay modes of the 991.9 keV resonance [60].

The implementation of the $^{27}Al(p,\gamma)^{28}Si$ reaction, was carried out in the beginning and/or in the end of all the measurements performed at the Tandem accelerator at NCSR "Demokritos" to calibrate its energy. A thick aluminum foil was placed at the end of the beamline in close geometry with a 50% relative efficiency high purity germanium detector (HPGe) facilitating the detection of the emitted γ-rays at 1779 keV. A step of 1 keV in the beam energy (nominal E_p) was used from 1002 down to 985 keV to scan the resonance, while an equal number of protons (charge Q) impinged on the target each time. Counting the γ-rays emitted at 1779 keV in each measurement, as plotted in Figure 3.4, one can determine the energy of the accelerator and its uncertainty (ripple), as follows. The mid-point of the sigmoidal-like rise of the observed counting rate corresponds to the resonance energy (991.9 keV). According to the NMR frequency however, it was found to be at 995 keV (nominal energy), yielding a "shift" (offset) of approximately 3 keV in this case. The width α from 25% up to 75% of the maximum yield [65] corresponds to the energy ripple and it was found to be 1.5 keV (~0.15% of the impinging beam energy).

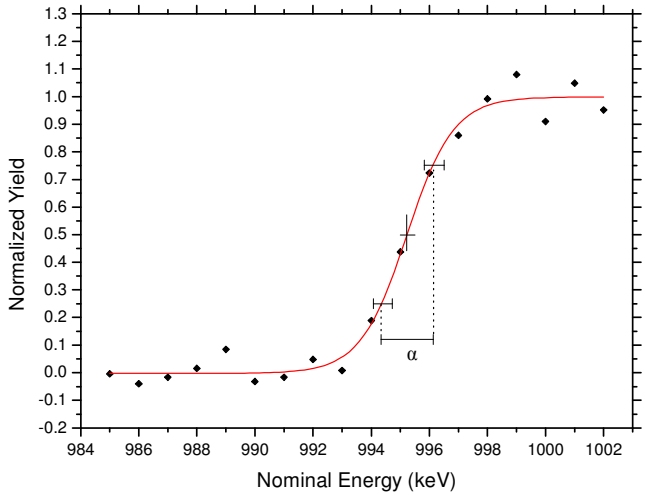

Figure 3.4: Normalized thick target yield of the $^{27}Al(p,\gamma)^{28}Si$ reaction in the energy range of 985-1002 keV calculated using the corresponding NMR frequency.

3.1.2.2 Energy loss in the target

After the calibration of the accelerator energy, as described in the previous section, the only additional correction to be applied to the projectile energy, in order to obtain the exact energy value E before the interaction, is the beam energy loss in the target till the actual interaction with its nuclei. This energy should then be related to the corresponding interaction and thus to the corresponding studied cross section values, as described in equation 3.1.

The phenomenon of the beam energy loss in material has actually been thoroughly analyzed in section 1.1.3, along with other important theoretical aspects of spectrometry. It became evident along those lines that the projectile energy loss in the target depends both on its energy and on the specific material crossed. The study of the energy loss in all the elements of the target separately is therefore mandatory. The fact that the targets used for the cross section measurements consist of different elements or compounds in layers, and that the energy of the detected particles is characteristic of the element (or isotope) involved in the reaction (and the type of it), indeed enables the correction for the energy loss to be applied in layers. The used targets are ultra thin, meaning that the energy loss in each layer is minimal and can be approximated to be constant over its whole thickness. The use of ultra thin targets plays nevertheless a crucial role in the whole cross-section calculation procedure, as has already been

pointed out in the beginning of this chapter, in terms of the energy variation of the cross sections themselves.

The usual treatment when using ultra thin targets is to assume that all reactions occurred in the middle of the corresponding layer (mean energy approximation [4]). This assumption is actually very close to reality since the energy loss in the target itself is very small (usually below 3 keV even at low energies) and thus the studied cross sections can be considered to correspond to this "mean" value of energy. More specifically, for the first layer element interactions, the projectiles are considered to have crossed a path till the middle of its thickness and their energy is accordingly corrected. Likewise, the energy loss crossing the first layer and half of the second layer is calculated for the second layer interacting projectiles etc. The uncertainty originating from this approximation is in all cases well below the ripple value of the beam energy and can thus be omitted in the error calculations.

As has already been mentioned, all the used targets for the cross-section measurements consisted of a thin gold layer on top (first layer) and of a thin layer of carbon foil on the back side (backing), while the layer in between was comprised of the studied element (see section 2.5). The proton energy loss in these two elements (gold and carbon), as an example, is plotted in the following Figure 3.5, calculated using the SRIM 2011 [5] code, showing its energy and Z dependence. For all the studied cases which follow, the targets are in detail described in the corresponding sections (3.2.1 and 3.3.1) along with the subsequent energy loss calculations. It has to be noted here, however, that possible diffusion of gold in the next layer or the presence of other elements on the surface of the target, such as oxygen from the environment or due to the manufacturing of the targets (like nitrogen from the used soap in the evaporating procedure), is indeed negligible compared to the main composition of the target and is thus not included in any energy calculations except for the case of the magnesium study. As analytically presented in the corresponding following section 3.3.1, such contaminants were present over the whole thickness of the used magnesium target and therefore their energy loss was carefully analyzed.

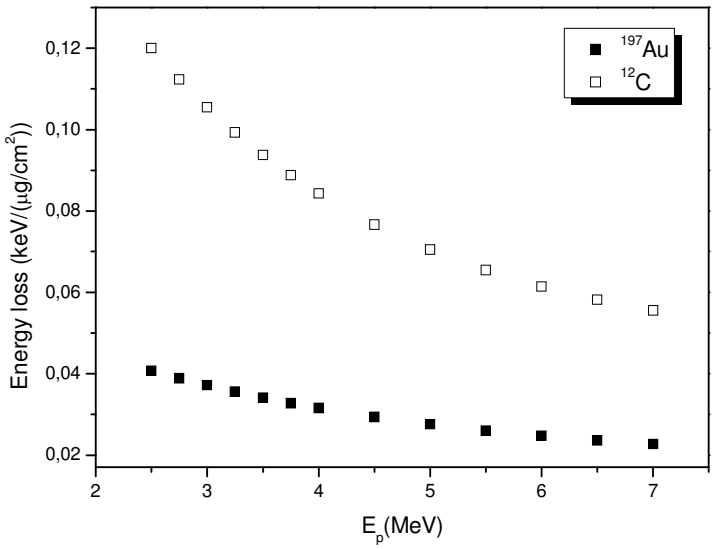

Figure 3.5: Proton energy loss in the layers of gold and carbon respectively.

To summarize, the final energy of the projectiles is always calculated according to the energy calibration of the accelerator (offset) and the energy loss in the target itself. The energy uncertainty certainly involves the ripple of the accelerator (beam profile) and the energy straggling in the target, as described in section 1.1.3, as well as the energy loss calculation and approximation, with the ripple being of course the predominant factor when using ultra thin targets. The subsequent cross section uncertainty is evidently pronounced in the cases of resonant structure, depending however on the width of the studied resonances and the ripple. In the special cases of strong resonant structures, cross sections cannot be calculated using the equation 3.1 at all, as has already been pointed out in the beginning of this chapter. In all cases though, when using ultra thin targets, the limit of the analysis is indeed set by the thickness of the target and the ripple of the accelerator.

3.2 Cross-section measurement for $^{7}Li(p,p_0)^{7}Li$, $^{7}Li(p,p_1)^{7}Li$, $^{7}Li(p,\alpha_0)^{4}He$, $^{19}F(p,p_0)^{19}F$, $^{19}F(p,\alpha_0)^{16}O$ and $^{19}F(p,\alpha_{1,2})^{16}O$ reactions

The differential cross sections measured at NCSR "Demokritos" concerning the p+Li and p+F systems are presented in this section, along with the detailed target characterization. The measurements concerned the $^{7}Li(p,p_0)^{7}Li$, $^{7}Li(p,p_1)^{7}Li$, $^{7}Li(p,\alpha_0)^{4}He$, $^{19}F(p,p_0)^{19}F$, $^{19}F(p,\alpha_0)^{16}O$ and $^{19}F(p,\alpha_{1,2})^{16}O$ reactions in the energy range of 1.5–7 MeV using a variable energy step and for detection angles between 140° and 170° in steps of 10°. The results obtained and the discrepancies found are also thoroughly discussed and analyzed. These measurements contribute in the field of lithium and fluorine depth profiling, as has already been presented in section 1.4, by implementing both the EBS and NRA techniques in each case. It is important to note here, that this work aimed primarily at studying the p+^{7}Li system but due to the implemented LiF target though, selected differential cross-section values have also been determined for the p+^{19}F system.

The determination of the differential cross-section values for ^{7}Li and ^{19}F reactions respectively, was carried out following the formulas for relative measurements, as described in the previous section, compared to the differential cross section of the $^{197}Au(p,p_0)$ reaction, as follows:

$$\left(\frac{d\sigma}{d\Omega}\right)_{Li} = \left(\frac{d\sigma}{d\Omega}\right)_{Au} \frac{Y_{Li}}{Y_{Au}} \frac{N_{t,Au}}{N_{t,Li}}$$

$$\left(\frac{d\sigma}{d\Omega}\right)_{F} = \left(\frac{d\sigma}{d\Omega}\right)_{Au} \frac{Y_{F}}{Y_{Au}} \frac{N_{t,Au}}{N_{t,F}} \qquad 3.5$$

where Y generally corresponds to the experimental yield (integrated peak counts), and N_t to the number of the corresponding target atoms per cm^2.

Due to the kinematics of the studied reactions, all peaks in the spectra were isolated, as shown in the typical spectrum in Figure 3.6, over the whole energy range studied, except for a very few cases, e.g. peaks that correspond to the $^{7}Li(p,\alpha_0)^{4}He$ and $^{19}F(p,\alpha_0)^{16}O$ reactions coincide for the proton energy range ~2550-2750 keV at 150^{o}, thus rendering their independent analysis impossible.

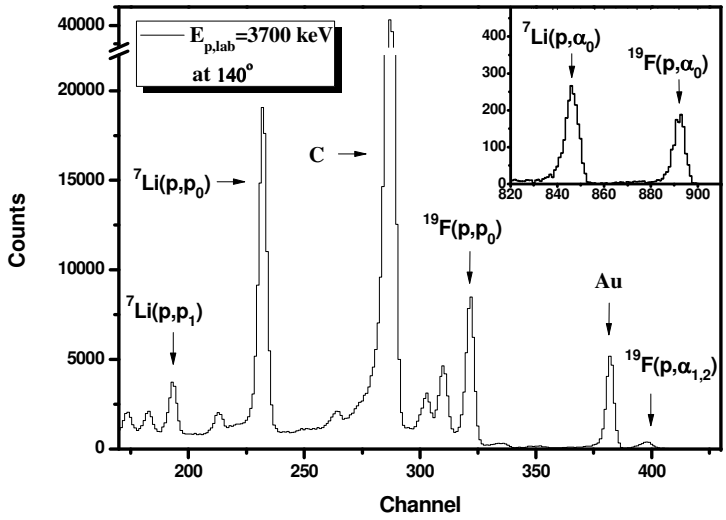

Figure 3.6: Typical experimental spectrum with a thin target consisting of Au/LiF evaporated on a carbon foil, taken at 140° and for $E_{p,lab}$= 3700 keV, along with the corresponding peak identification.

3.2.1. Target characterization

The LiF target implemented for the cross-section measurements consisted of a thin gold layer of (4.4 ± 0.3) μg/cm^2 evaporated onto a thin LiF layer of (960 ± 38)×10^{15} at/cm^2 on a carbon backing foil of 52 ± 2 μg/cm^2 and was manufactured in the Tandem Laboratory at NCSR "Demokritos", as presented in section 2.5. The thickness determination of the used target plays an important role for the accurate calculation of the studied cross sections, as has already been described above.

The thickness of the gold layer was determined by performing X–ray Fluorescence (XRF) analysis using the in-house developed portable XRF setup [66] of the Institute of Nuclear and Particle Physics of NCSR "Demokritos". The thickness, on the other hand, of the LiF layer was estimated using the evaluated differential cross sections from SigmaCalc calculations [25] for proton elastic scattering on ^{19}F at 1600 keV, where there are no strong variations in the cross section, at 160°. Prior to the determination of the LiF thickness in such a way, a validation experiment at 1600 keV was performed for the verification of the evaluated differential cross sections to be used. For this experiment a thick CaF_2 pellet and the SIMNRA code [70] were used for the simulation of this measurement. The simulated spectrum was produced using the evaluated differential cross-section dataset from SigmaCalc for the $^{19}F(p,p_0)^{19}F$ scattering, taking into account a very small energy step for the incoming and outgoing protons, the effect of

multiple scattering, the beam ripple, Ziegler–Biersack-Littmark [6] stopping power data, and Chu and Yang's straggling model, as implemented in the SIMNRA code. The elastic scattering on ^{12}C and ^{16}O (on the surface of the pellet) were also simulated using the corresponding evaluated data from SigmaCalc. The spectrum acquired by the detector at 160^{o} could be reproduced by the simulation, as shown in Figure 3.7, only with the evaluated cross sections being increased by 17%. This increase corresponds to the narrow energy window E_p~1575-1600 keV, as shown by the dotted lines in Figure 3.7, where the elastic scattering signal from fluorine is not contaminated. Using these corrected data for fluorine for E_p=1600keV at 160°, the thickness of the fluorine layer with respect to the gold one was then determined directly in the following way (equation 3.6), in order to minimize the uncertainty of the ratio to ~4%. The error of ~4% in the thicknesses originates only from the statistical uncertainty of the integrated yields (Y). It should be noted here that the inherent error in the evaluated data was not taken into account. The assessment of the uncertainties in the evaluated datasets has actually been the subject of recent studies [67, 68] being in general quite a challenging task.

$$\frac{N_{t,Au}}{N_{t,F}} = \frac{(\frac{d\sigma}{d\Omega})_F}{(\frac{d\sigma}{d\Omega})_{Au}} \frac{Y_{Au}}{Y_F} \quad \Rightarrow \quad \frac{N_{t,Au}}{N_{t,F}} = 0.028 \pm 0.001 \qquad 3.6$$

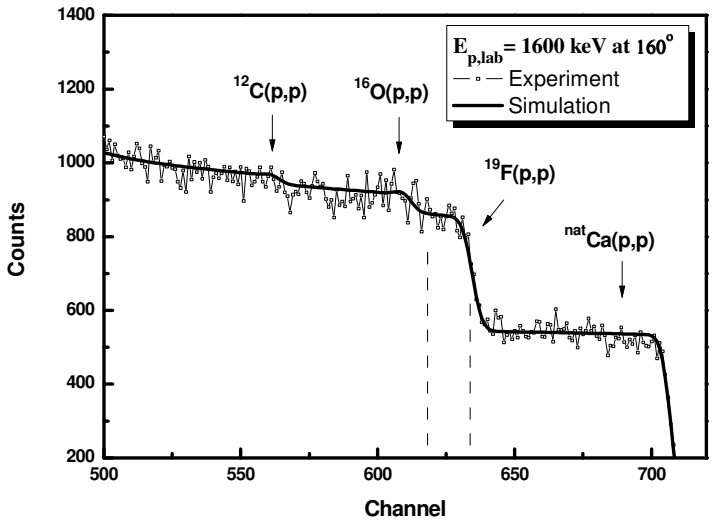

Figure 3.7: Experimental spectrum taken whilst irradiating the thick CaF_2 pellet at E_{lab}=1600 keV at 160° along with the simulated spectrum using the evaluated cross sections [25] increased by 17%, using the SIMNRA code [70].

In general, alkaline/halogen salts maintain their stoichiometry even under extreme conditions due to the strength of the involved chemical bond. The Li:F ratio of the target was however studied using transmission ERDA with 5.9 MeV ^{12}C ions and was found to closely approximate 1:1, but the analysis proved to be complicated and therefore inaccurate, because of the significant peak overlapping and background contribution. The 1:1 ratio was thus verified by the thick target spectra obtained for the validation procedure, described in detail in the following section 4.5. Such spectrum at 3200 keV, using a thick LiF target, can be seen in the following Figure 3.8, along with the corresponding simulation (using SIMNRA [70]). The thick LiF target was a highly pressurized pellet made of LiF powder, consisting thus of LiF in 1:1 ratio. The simulation was performed using the obtained cross sections of the present measurements for the (p,α_0) reactions on lithium and fluorine, assuming an equal concentration of these elements in the thin target used (1:1 LiF). Comparing the simulated thick target spectra to the experimental ones, one can check if this assumption is correct, just by comparing the relative heights of the two reaction yields (near the surface) in both spectra. It was thereby proved (see Figure 3.8), that the ratio of the two elements was correctly assumed to be 1:1 within 3%. Nevertheless, this procedure leads to a systematic uncertainty of the lithium thickness of ~3%. The absolute height of the simulated spectrum is further discussed in the benchmarking section in 4.5, yielding results for the validation of the cross sections themselves.

The thickness of the lithium layer of the target was thus determined to be equal with the fluorine one and it was actually also used in the calculations with respect to the gold layer directly, as follows:

$$\frac{N_{t,Au}}{N_{t,Li}} = \frac{N_{t,Au}}{N_{t,F}} = 0.028 \pm 0.001$$

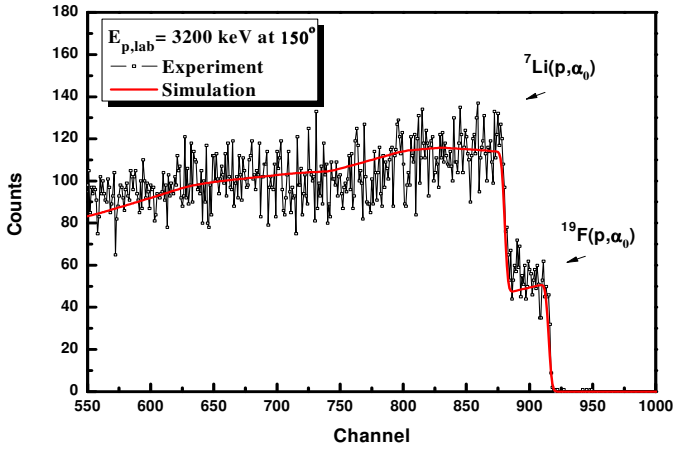

Figure 3.8: Thick LiF target spectra in the region of the (p,α_0) reactions for the study of the relative height between the two reaction yields in the surface region.

3.2.2. Assessment of the uncertainties

The combined statistical errors for the obtained differential cross sections for the $^{7}Li(p,p_0)^{7}Li$, $^{7}Li(p,p_1)^{7}Li$, $^{7}Li(p,\alpha_0)^{4}He$, $^{19}F(p,p_0)^{19}F$, $^{19}F(p,\alpha_0)^{16}O$ and $^{19}F(p,\alpha_{1,2})^{16}O$ reactions, varied between ~1-4% for the (p,p_0) elastic scattering and ~4-7% for the inelastic nuclear reactions, including the uncertainties in peak integration (including counting statistics and background subtraction). The overall target thickness' uncertainty of ~4%, is systematic, while an additional systematic uncertainty for the lithium case of ~3% originates from the LiF ratio in the target (see previous section). The reported proton energy values in the laboratory reference frame correspond to the half of the LiF layer's thickness, with negligible straggling, following SRIM calculations [5], after the proper correction according to the results of the accelerator calibration presented in the previous section, with an accuracy of 4-10 keV over the whole studied energy range.

3.2.3. Results and Discussion

The correlated differential cross-section values obtained for the $^{7}Li(p,p_0)^{7}Li$, $^{7}Li(p,\alpha_0)^{4}He$ and $^{7}Li(p,p_1)^{7}Li$ reactions are presented here in detail, along with their corresponding uncertainty, in Figures 3.9, Figures 3.10 and in Figure 3.11 respectively, for the laboratory detector angles 140°, 150°, 160° and 170°, along with data from literature, when available. The error bars shown in the following graphs for the obtained data are only the statistical experimental errors (excluding the uncertainty in the determination of the target's thickness), while the error bars along the x- axis (energy ripple of 0.16%) are not visible due to the adopted scale. The obtained cross sections [71] are also presented in tabular form in Appendix A.

Two resonances are clearly revealed in the region up to 2700 keV, namely at $E_{p,lab}$~2050 and ~2500 keV, as seen in Figures 3.9, corresponding to the excited levels of the compound nucleus ^{8}Be at 18910 and 19400 keV [http://www.nndc.bnl.gov/chart/] respectively. Comparing the present data at higher energies with those published by Caciolli et al. [26] in Figure 3.9 (left), one would notice that there is a discrepancy around the peak at ~4 MeV both in the shape of the curves and in absolute values. In Figure 3.9 (top), it is seen that there is an angular dependence of cross sections only close to that same peak. A very good agreement is nevertheless observed between the present data and the other existing data points. The corresponding reported uncertainty of Gleyvod et al. [109] and Fasoli et al. [27] ranges from ~10 to 15% and up to

1.5% respectively, while there is no error assignment for the data of Kilian et al. [108], and Malmberg et al. [28].

Angular dependence of the cross sections is also seen in Figure 3.10 (top) for the $^{7}Li(p,\alpha_0)^{4}He$ reaction and in Figure 3.11 for the $^{7}Li(p,p_1)^{7}Li$ reaction. It is also noticeable that in Figure 3.10 (bottom) there is no agreement in absolute values with the few available datasets in literature ([29] and [30]).

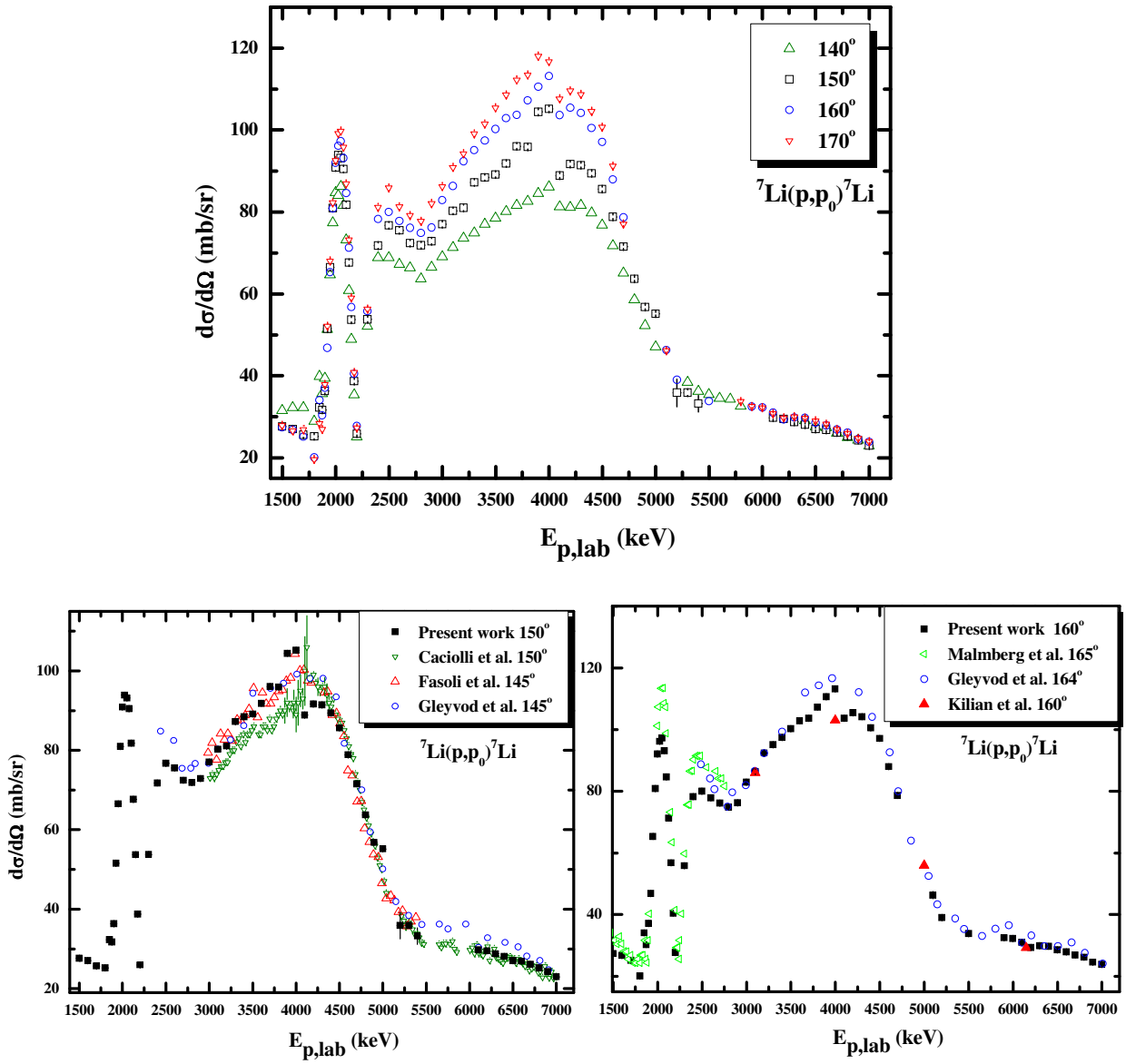

Figures 3.9: Differential cross section values (mb/sr) for the $^{7}Li(p,p_0)^{7}Li$ reaction at 140°, 150°, 160° and 170° for $E_{p,lab}$=1500-7000 keV along with data from literature, when available. Error bars are not shown in the graphs for clarity reasons, except for the case of 150° and 160°, where data from the present work can be directly compared to those of Caciolli et al. [26] (with a quoted uncertainty of ~8% around 4 MeV and ~4% elsewhere) and of Kilian et al. [108] (no reported uncertainty) respectively.

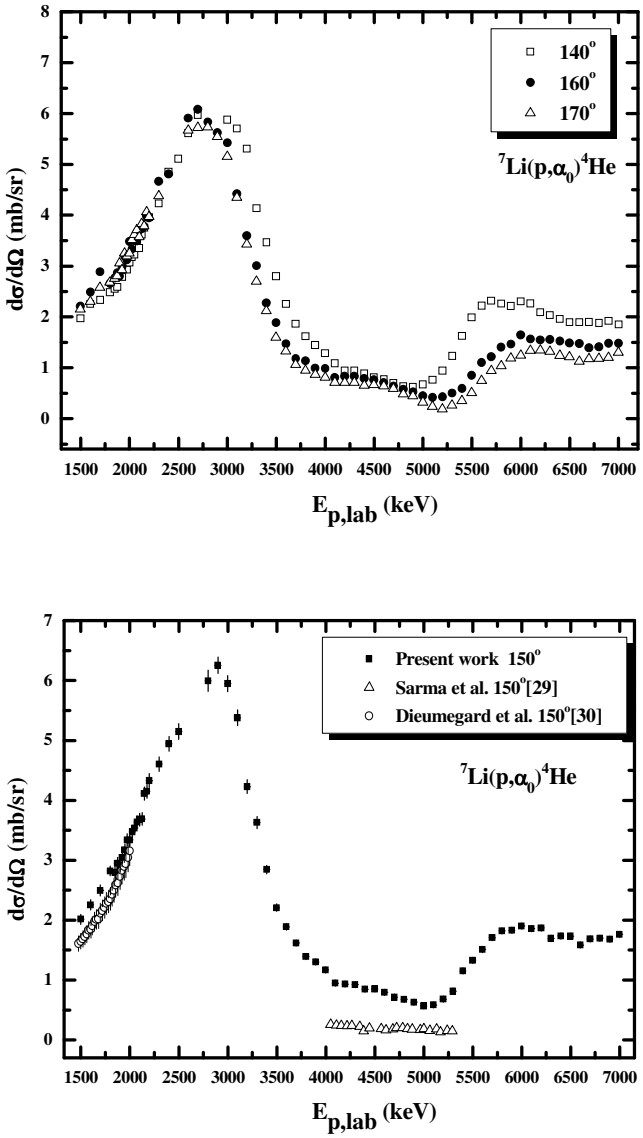

Figures 3.10: Differential cross-section values (mb/sr) for the ^{7}Li(p,α_0)^{4}He reaction at 140°, 150°, 160° and 170° for $E_{p,lab}$=1500-7000 keV. Error bars are not shown in the graphs for clarity reasons except for the case of 150°, where data from the present work can be directly compared to those of Sarma et al. [29] and Dieumegard et al. [30] (with quoted uncertainties of 3-8% and 8% respectively).

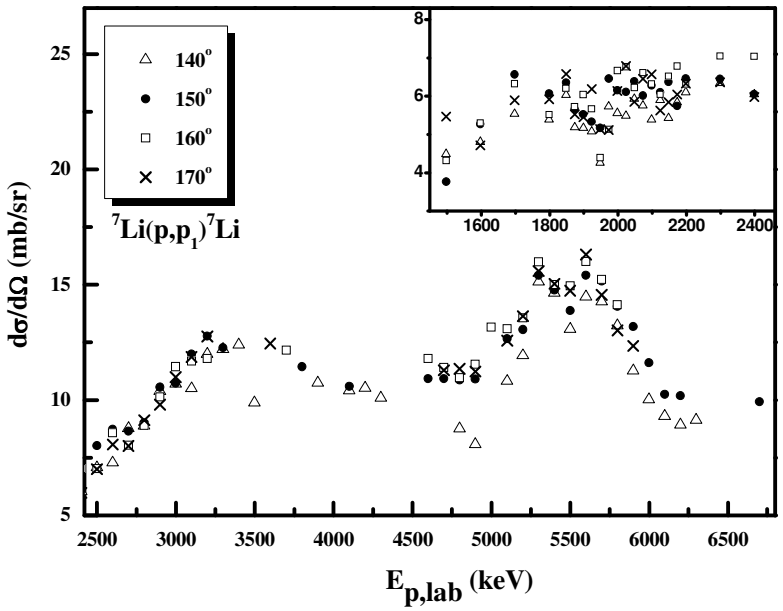

Figure 3.11: Differential cross-section angular dependence for the ^{7}Li(p,p$_1$)^{4}He reaction at 140°, 150°, 160° and 170° for $E_{p,lab}$=1500-7000 keV. Data are plotted without error bars for clarity reasons.

Differential cross sections obtained for the ^{19}F(p,p$_0$)^{19}F, ^{19}F(p,α$_0$)^{16}O and ^{19}F(p,α$_{1,2}$)^{16}O reactions, for the same energy range and laboratory detection angles 140°, 150°, 160° and 170°, are presented in detail [71], along with the corresponding uncertainty (excluding the uncertainty in the determination of the target's thickness) in tabular form in Appendix B and are also plotted in Figures 3.12a-d, Figures 3.13a-d and in Figure 3.14 respectively. The alpha groups α_1, and α_2, belonging to the 6049 keV and 6130 keV excitation levels of the ^{16}O nucleus respectively, could not be analyzed separately, because of the overlap of the corresponding peaks in the spectra for the proton energy range studied. Data are again reported in the graphs with the corresponding statistical experimental errors along with data from literature, when available, while the error bars along the x- axis (energy ripple of ~0.16%) are not visible due to the adopted scale. Differential cross sections for the ^{19}F(p,p$_0$)^{19}F reaction, plotted in Figures 3.12a-d, show their complicated structures with strong resonances. For a detailed study of the p+^{19}F system, smaller energy steps than the ones adopted in the present work (which was tuned for the lithium case in the first place, as has already been mentioned) were apparently needed. To clarify the situation near 1700 keV, after comparing the obtained results primarily to the evaluated ones, the study of the energy range between 1600-1800 keV was indeed repeated in smaller steps at 160° and

170°, seen in Figures 3.12c-d, showing excellent agreement in that region. Moreover, comparing overall the data from the present work to the evaluated ones (SigmaCalc [25]) and to other data from literature, as it is shown in Figures 3.12a-d, one would notice discrepancies in absolute values in some cases, whereas there are energy regions, where all data agree well in absolute values. In particular, in Figure 3.12c (160^o) data of Webb et al.[39] agree well with data from the present study at 1500-1800 keV and the same occurs, not only with the data of Cuzzocrea et al.[34] at 2120-2520 keV (Figure 3.12a), but with the data of Kuan et al.[38] as well (Figure 3.12d). In Figures 3.13a-d, concerning the $^{19}F(p,\alpha_0)^{16}O$ reaction, a good agreement both in shape and in absolute values between all datasets is observed, while the energy step of the present work seems to be again inadequate for a detailed study of the observed resonances.

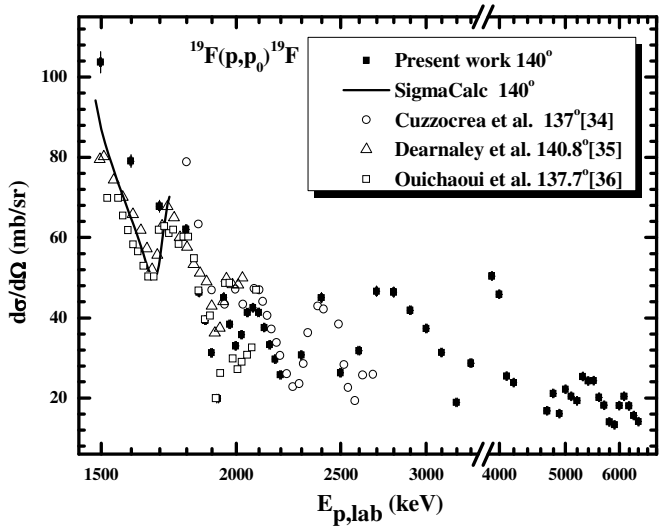

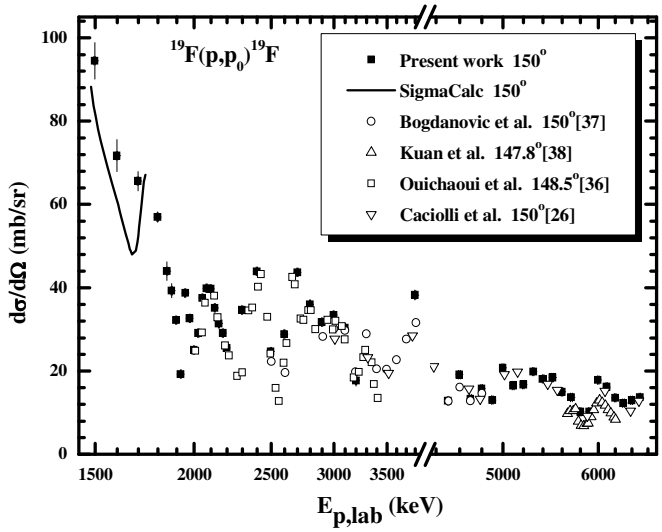

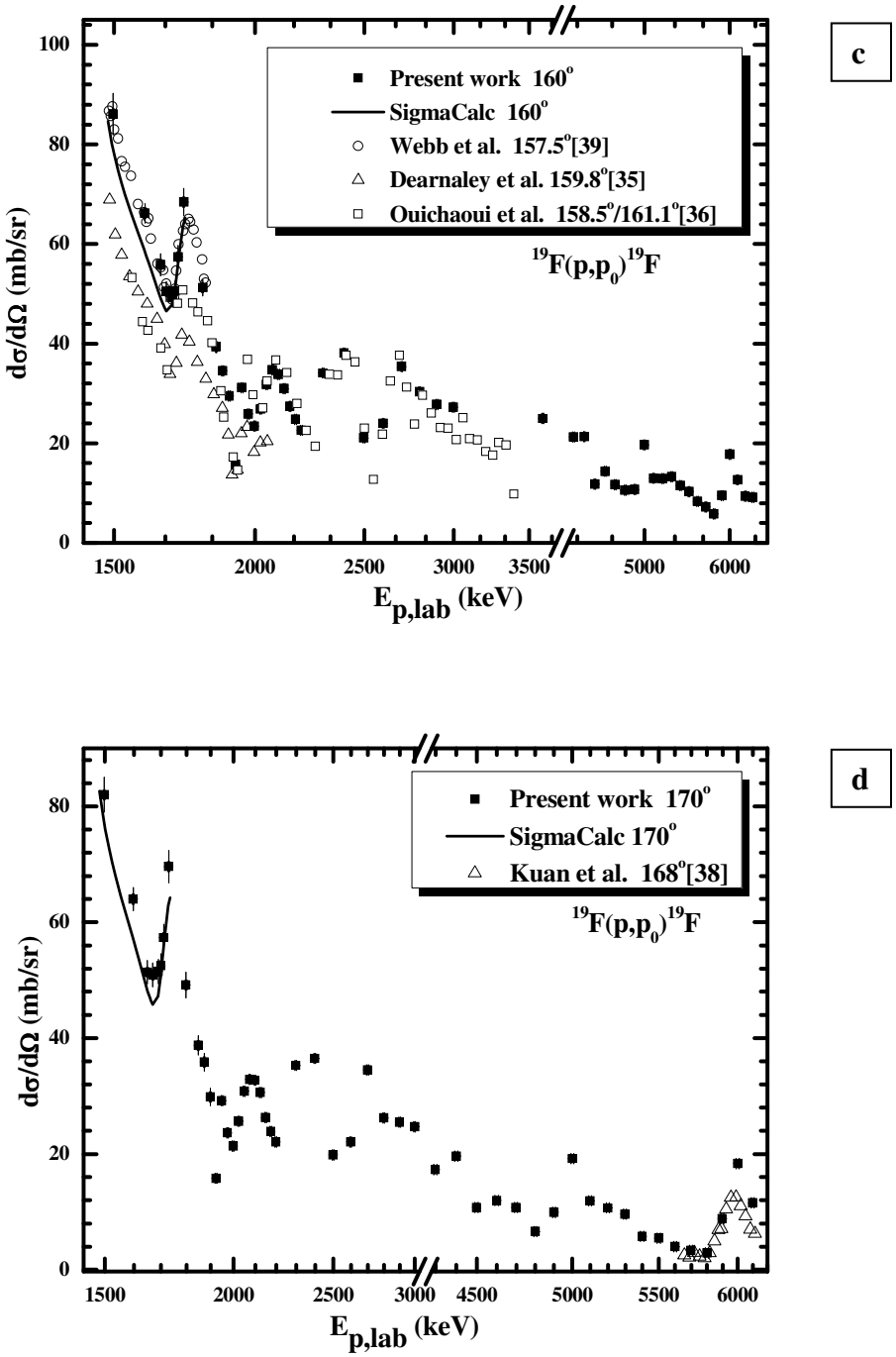

Figures 3.12 a-d: Differential cross-section values (mb/sr) for the $^{19}F(p,p_0)^{19}F$ reaction at 140°, 150°, 160° and 170° for $E_{p,lab}$=1500-7000 keV. The obtained data with the combined statistical experimental errors are plotted in the graphs along with the evaluated cross sections (SigmaCalc) [25] and data from literature, when available (with a quoted uncertainty of 2% for data by Cuzzocrea et al. [34] and Dearnaley et. al [35] as well) for comparison.

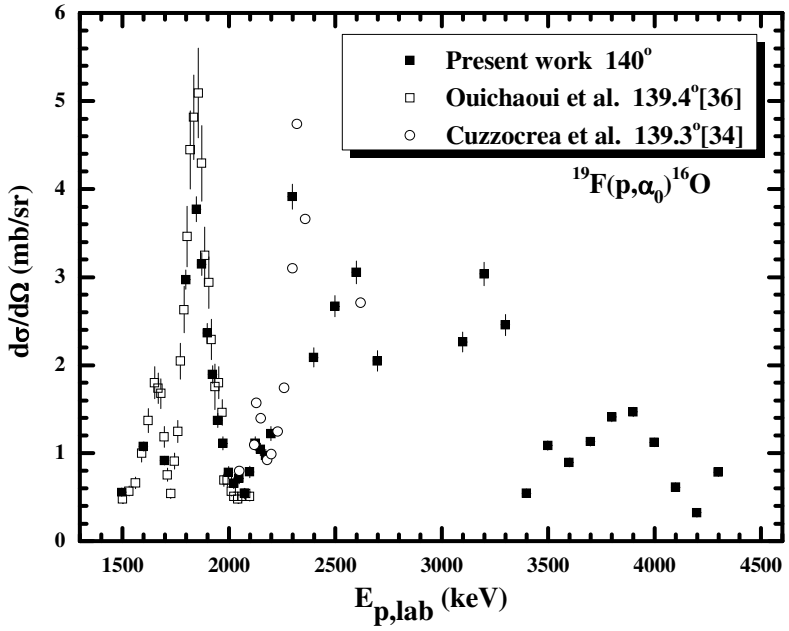
Present work 140°
Ouichaoui et al. 139.4°[36]
Cuzzocrea et al. 139.3°[34]
$^{19}F(p,\alpha_0)^{16}O$
dσ/dΩ (mb/sr)
$E_{p,lab}$ (keV)
0
1
2
3
4
5
6
1500
2000
2500
3000
3500
4000
4500

a

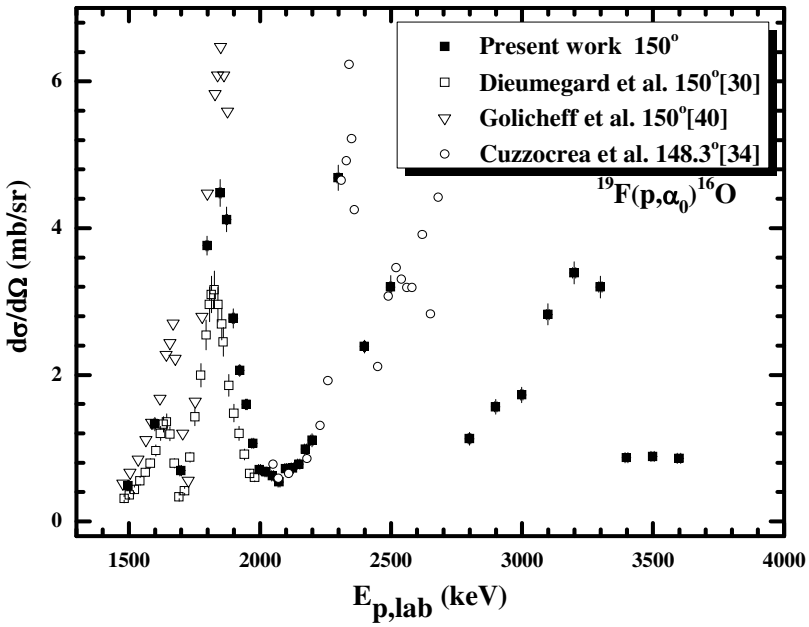
Present work 150°
Dieumegard et al. 150°[30]
Golicheff et al. 150°[40]
Cuzzocrea et al. 148.3°[34]
$^{19}F(p,\alpha_0)^{16}O$
dσ/dΩ (mb/sr)
$E_{p,lab}$ (keV)
0
2
4
6
1500
2000
2500
3000
3500
4000

b

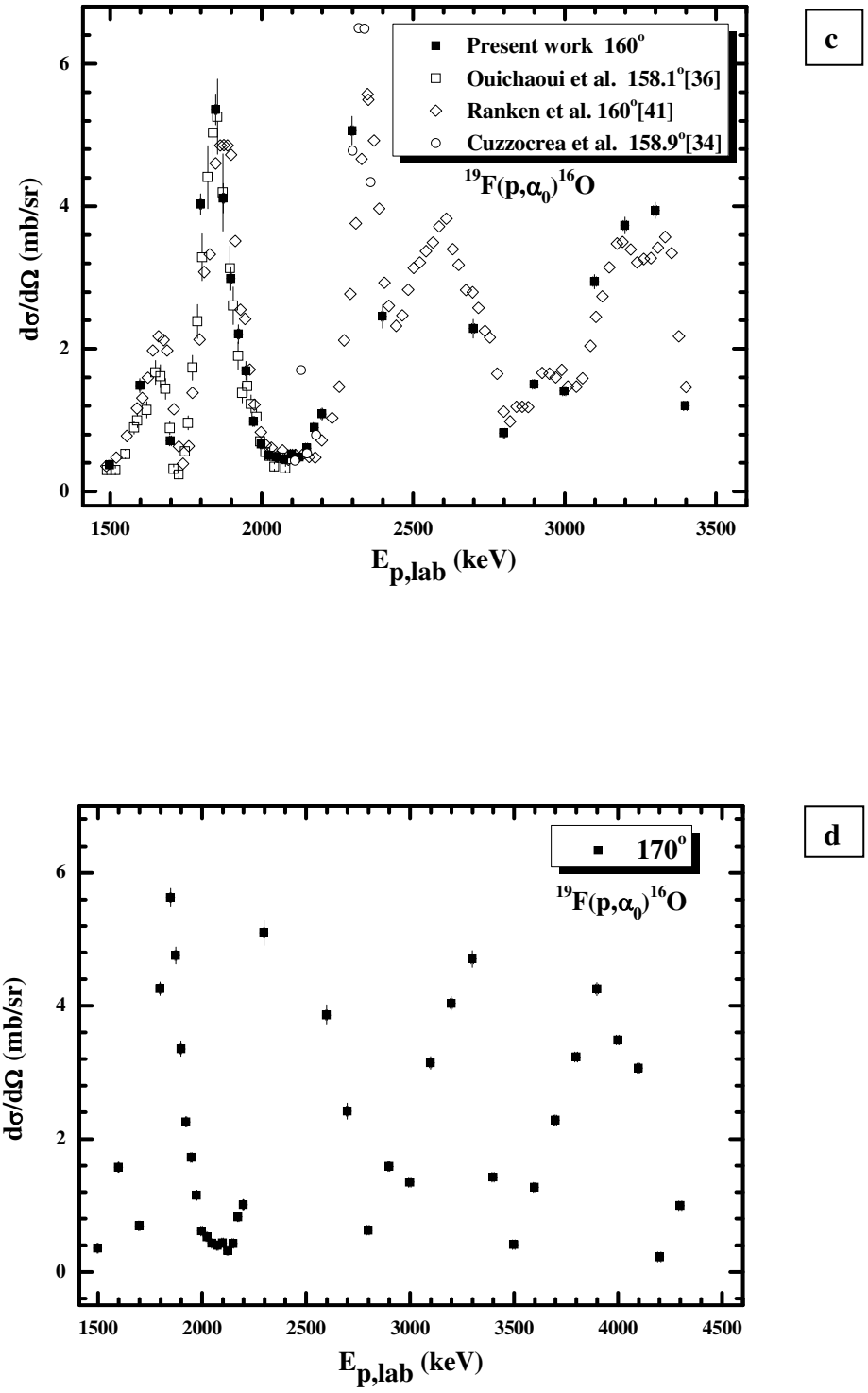

Figures 3.13a-d: Differential cross-section values (mb/sr) for the $^{19}F(p,\alpha_0)^{16}O$ reaction at 140°, 150°, 160° and 170° for $E_{p,lab}$=1500-4500 keV. The obtained data with the combined statistical experimental errors are plotted in the graphs along with data from literature, when available, for comparison.

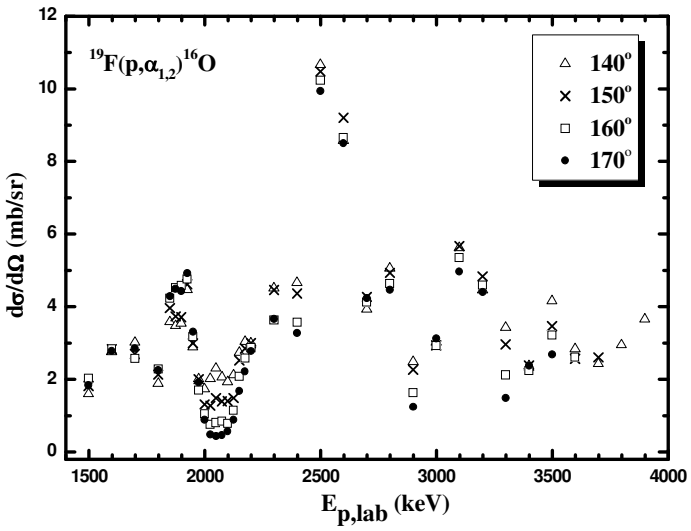

Figure 3.4: Differential cross-section values (mb/sr) for the $^{19}F(p,\alpha_{1,2})^{16}O$ reaction at 140°, 150°, 160° and 170° for $E_{p,lab}$=1500-4000 keV. Data are plotted without error bars for clarity reasons.

Due to the observed discrepancies among differential cross-section datasets from literature, a validation procedure using thick targets is critical in order to verify the obtained values. It is important to note however, that all datasets obtained in the present study are correlated. By validating a dataset of cross sections concerning one particular reaction channel for the p+^{7}Li system, as presented in detail in the following chapter (4.5 section), one simultaneously validates all the correlated datasets of the other exit channels, taking into account that only peak integration differs, while all the other parameters in the relative formula remain intact. The same naturally occurs in the p+^{19}F case as well (also described in 4.5).

3.3 Cross-section measurements for the ^{nat}Mg(d,d) and ^{24}Mg(d,p$_i$)^{25}Mg reactions

The cross-section measurements of the d+Mg system, which were also performed at NSCR "Demokritos", are presented in this section, along with the target characterization and the discussion about the obtained results in comparison to related data from literature. The present results contribute in the field of magnesium depth profiling, as has already been presented in section 1.4, by implementing the EBS and NRA techniques.

The cross-section measurements were carried out in two distinct phases, namely during two independent experimental runs. The primary object of the work was to measure the ^{24}Mg(d,p$_i$)^{25}Mg reactions at backward scattering angles, thus enabling the NRA method to be implemented in depth profiling studies of Mg. More specifically the first three proton levels (p_0, p_1, p_2) were studied at 140°, 150°, 160° and 170° at deuteron energies ranging from 1300–2050 keV in the laboratory system, with a variable energy step of ~50 down to ~10 keV (in apparent resonant regions), using the setup described in chapter 2. However, differential cross sections of the ^{nat}Mg(d,d$_0$) elastic scattering were alongside also calculated for the backscattering angles at 140^o and at 150^o, for the same deuteron beam energy range. This study revealed an unexpected resonant-like structure, with strong deviations from the Rutherford formula, due to the existence of several, possibly overlapping resonances. It became thereby evident, that further investigation of this phenomenon was necessary, taking into account that in all nuclear compilation reports in literature (e.g. in [69] or in http://www.nndc.bnl.gov/chart/) there is no reference to the corresponding excited states of the compound nucleus ^{26}Al for the center of mass energy range covered in the present work.

Within this framework, a second experimental run was performed in the energy range of interest, namely at 1660-1990 keV with dense energy steps of 2 and 5 keV for the detection angles at 150° and 170°, which are suitable for EBS depth profiling studies, and at 55°, 70°, 90° and 125°. A detailed study of the region of interest, mainly tuned for the elastic scattering (d,d) on Mg, was thereby enabled, aiming also to a possible future level characterization of the compound nucleus ^{26}Al with R-matrix calculations of the d+^{24}Mg system. The obtained results of this run are of course complementary datasets to the previously calculated ones, described above (first experiment).

The experimental setup and the followed procedure for both experiments were almost identical (placing extra detectors for the second detailed run), while the targets used in each run were manufactured and characterized in a similar way, described in the next paragraph. For reasons of clarity, however, the calculations and the target characterization of only the second run will be presented in this dissertation.

The differential cross sections for the $^{nat}Mg(d,d_0)$ and the $^{24}Mg(d,p_i)^{25}Mg$ reactions were determined, as described previously (section 3.1), relative to the elastic scattering on tantalum, which was evaporated on top of the target using the following equation for each measurement (energy step E) and scattering angle θ:

$$(\frac{d\sigma}{d\Omega})_{Mg} = (\frac{d\sigma}{d\Omega})_{Ta} \frac{Y_{Mg}}{Y_{Ta}} \frac{N_{t,Ta}}{N_{t,Mg}}$$

where Y generally corresponds to the experimental yield (integrated peak counts), and N_t to the number of corresponding target atoms per cm^2.

A typical experimental spectrum, showing mostly the elastic peaks, can be seen in Figure 3.15 for $E_{d,lab}$=1785 keV at 150°, along with the corresponding peak identification, while in Figure 3.16, one can see all the peaks in the acquired spectrum for $E_{d,lab}$=1300 keV at 140°. The high energetic part of the spectrum in the latter figure is also presented in the inset, containing the $^{24}Mg(d,p_i)$ peaks of interest. It should be noted that by using a natural magnesium target, the $^{24}Mg(d,p_1)$ peak could be contaminated by the $^{25}Mg(d,p_5)$ one over the whole energy range studied in the present work, due to reaction kinematics. However, the low abundance of ^{25}Mg in ^{nat}Mg, the absence of other $^{25}Mg(d,p_x)$ peak in the experimental spectra and the successful correlated benchmarking of all the studied ^{24}Mg proton levels, shown in section 4.6, render such a contamination insignificant.

The obtained calculated results of both runs (being merged), compared with the only existing dataset in literature in the same energy and angular range [51], are overall presented and analyzed in the following corresponding section (3.3.3). It has to be noted here that both measurements were thoroughly validated, using a thick Mg target with a thin Au layer evaporated on top, as described in the corresponding section (4.6) of the following chapter.

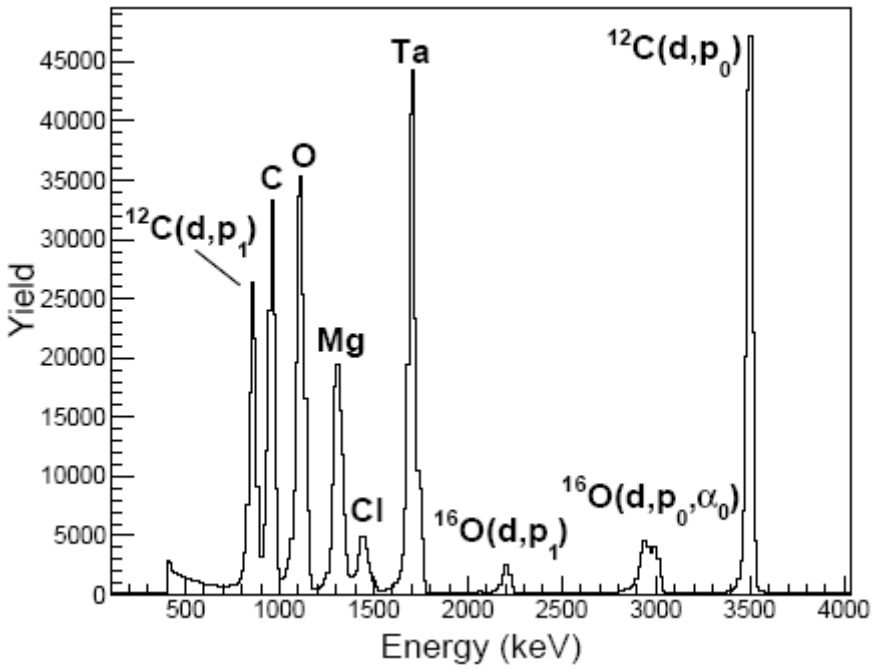

Figure 3.15: Typical experimental spectrum with a thin target consisting of Ta/Mg/$MgCl_2$ evaporated on a carbon foil, taken at 150° for $E_{d,lab}$ =1785 keV along with the corresponding peak identification (elastic scattering and nuclear reactions).

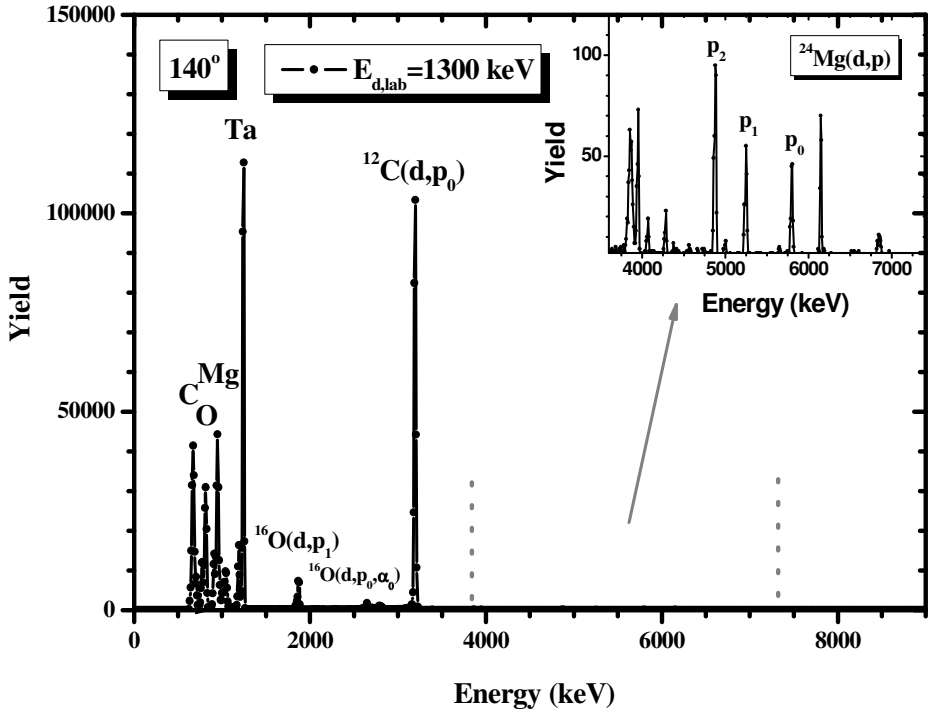

Figure 3.16: Typical experimental spectrum with a thin target consisting of Ta/Mg/$MgCl_2$ evaporated on a carbon foil, taken at 140° and $E_{d,lab}$=1300 keV, along with the corresponding peak identification.

3.3.1. Target characterization

The thin target used for the d+Mg differential cross-section measurements was made by evaporating a mixture of natural magnesium and magnesium chloride powder (in a Ta boat) on a ~10 μg/cm^2 carbon foil and by evaporating afterwards a thin Ta layer on top of it, as described in section 2.5.

In order to accurately define the ratio of the tantalum to magnesium atoms per surface unit ($N_{t,Ta}/N_{t,Mg}$), the elastic scattering data at three proton energies, namely at E_p= 1700, 2200 and 2500 keV were studied using the SIMNRA code [70]. The N_{Ta}/N_{Mg} ratio was used as a free parameter for the simulation and the evaluated differential cross section datasets for the $^{nat}Mg(p,p_0)$ reaction, which has been validated in the past [50] to an accuracy of the order of ~5%, were taken from the online calculator SigmaCalc [25]. As an illustration of the target characterization procedure, a typical experimental spectrum along with the simulated one can be seen in Figure 3.17. The strong carbon peak is attributed to the supporting foil, the presence of chlorine is related to the evaporation process, while the corresponding one of oxygen is connected with the unavoidable oxidization of magnesium and Ta. As far as these elements are concerned, evaluated cross-section data for proton elastic scattering on C and O were also taken from [25] to be used in the simulations. Possible deviations from Rutherford scattering concerning the $^{nat}Cl(p,p)$ reaction at relatively low proton beam energies (below 3 MeV) have not been thoroughly investigated, thus experimental data for $^{35}Cl(p,p)$ at 150^o were used from IBANDL [23], while for $^{37}Cl(p,p)$ no deviations were taken into account in the simulations.

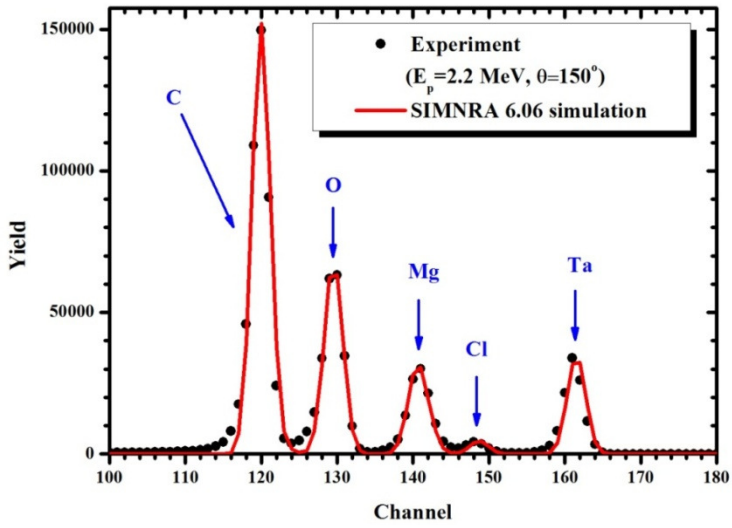

Figure 3.17: A typical proton elastic scattering energy spectrum that was used for the target characterization, along with the corresponding SIMNRA simulation.

The ratio N_{Ta}/N_{Mg} was then calculated as follows, by averaging the results for the three proton energies using the backscattering spectra at 150° and 170° due to their superior depth resolution, while the standard deviation corresponded to the statistical uncertainty of the average value.

$$\frac{N_{t,Ta}}{N_{t,^{nat}Mg}} = 0.038 \pm 0.002$$

3.3.2. Assessment of the uncertainties

Concerning the deuteron elastic scattering cross sections on ^{nat}Mg, the main source of the ~5% uncertainty originates from the target characterization. More specifically, the statistical uncertainty in the N_{Ta}/N_{Mg} ratio was estimated to be 5.3%. Taking into account that the elastic peaks in the proton backscattering spectra were isolated with practically no background, while, at the same time, all the systematic sources of error were eliminated in the determination of the ratio, this uncertainty reflects in practice the uncertainty of the evaluated data in the elastic scattering of protons from ^{nat}Mg, at different energies and angles. It should also be noted here that the proton beam energies implemented for the determination of the ratio were not in the vicinity of strong, narrow resonances. Other sources of uncertainty were neglected in this case, given that the statistical uncertainty from the yield ratio of the elastic peaks (Y_{Mg}/Y_{Ta}) was kept less than 1%, even in the case of the overlapping ^{nat}Mg and ^{nat}Cl peaks at forward angles.

On the other hand, concerning the ^{24}Mg(d,p$_i$) differential cross sections, the most important remaining uncertainty factor was undoubtedly related to the integrated number of counts of the proton peaks of the deuteron–induced reactions on ^{24}Mg, denoted as Y_{Mg}. This uncertainty, when the differential cross–section values were significantly low, reached values as high as ~10% and was the dominant factor of the overall uncertainty.

The energy loss of the deuteron projectiles across the target material was calculated using the SRIM Monte-Carlo simulation code [5] and by adopting the averaged results of the target characterization procedure described previously. The same procedure was followed for the determination of the energy straggling (~6 keV), which was the dominant factor in the uncertainty in energy with respect to the accelerator energy ripple.

3.3.3. Results and Discussion

Concerning the elastic scattering $^{nat}Mg(d,d_0)$, the obtained cross sections of the present work for the two forward angles and the ones at 90° and 125° are presented in Figure 3.18 and the corresponding results for the backward detection angles relative to EBS studies in Figures 3.19, along with the combined statistical experimental errors and data from literature when available. The obtained cross-section values [72, 73] are also presented in tabular form in Appendix C.
The included N_{Ta}/N_{Mg} ratio statistical ambiguity of 5.3% is the dominant uncertainty in these cases, as already noted in the previous section. The elastic scattering excitation functions were recorded in steps of 5 keV, while a 2 keV step was adopted in the energy region around 1800 keV.

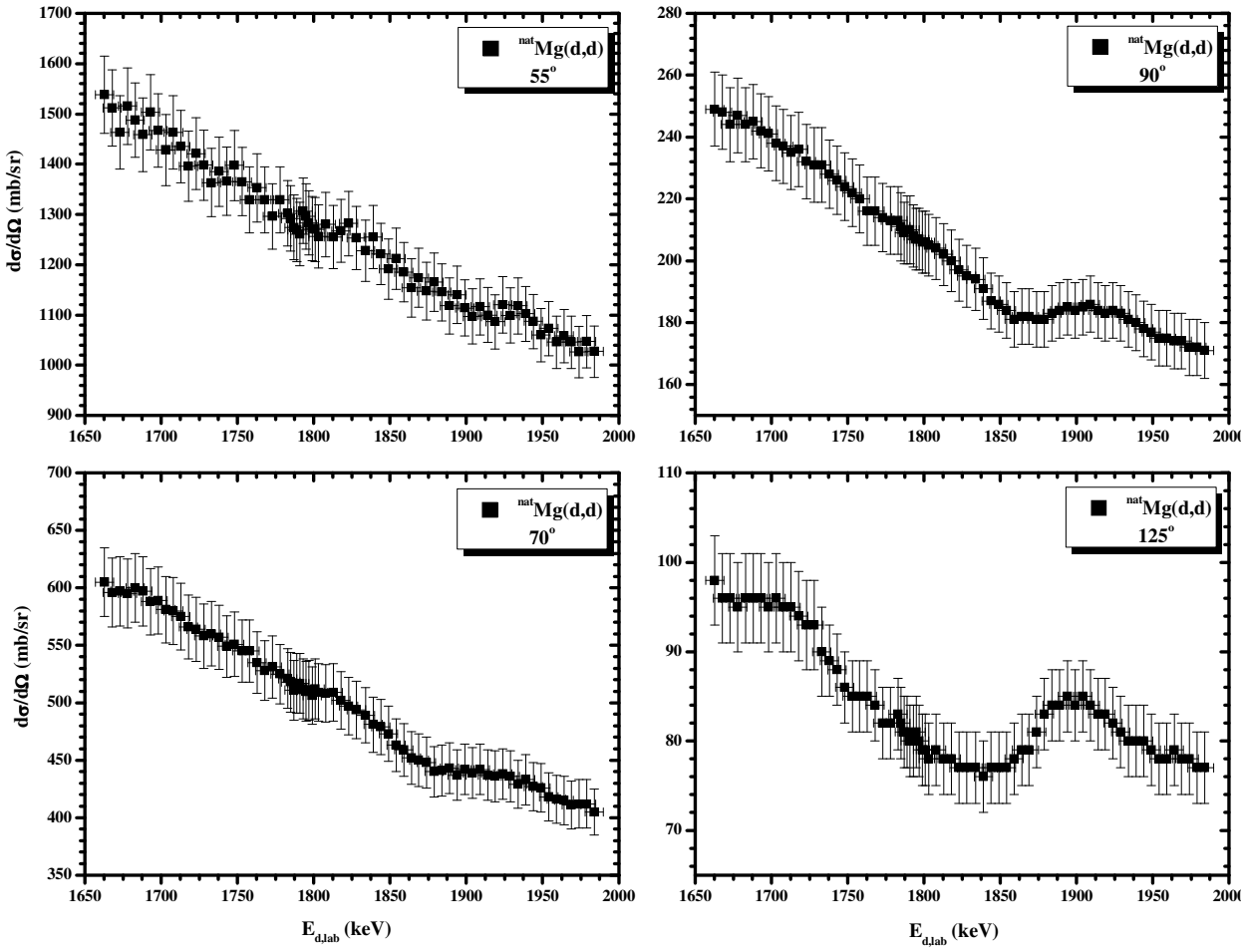

Figure 3.18: Differential cross-section values of the ^{nat} Mg(d,d0) reaction for the forward angles θ_{lab} =55°, 70°, as well as for 90° and 125° for $E_{d,lab}$ =1660-1990 keV.

The only dataset found in literature by Omar et al. [51] for elastic scattering at 135° is presented in arbitrary units (as stated) compared to the Rutherford values with no corresponding error assessment. The ratio to Rutherford values are stated in the corresponding figure of the article apparently in percentage form. Therefore, by converting the data by Omar et al. (taken from the IBANDL database having exactly the same form) to mb/sr and also dividing them by a factor of 100, one should be able to compare the cross sections between the two datasets. This comparison is seen in Figure 3.19 concerning the obtained data at 140°.

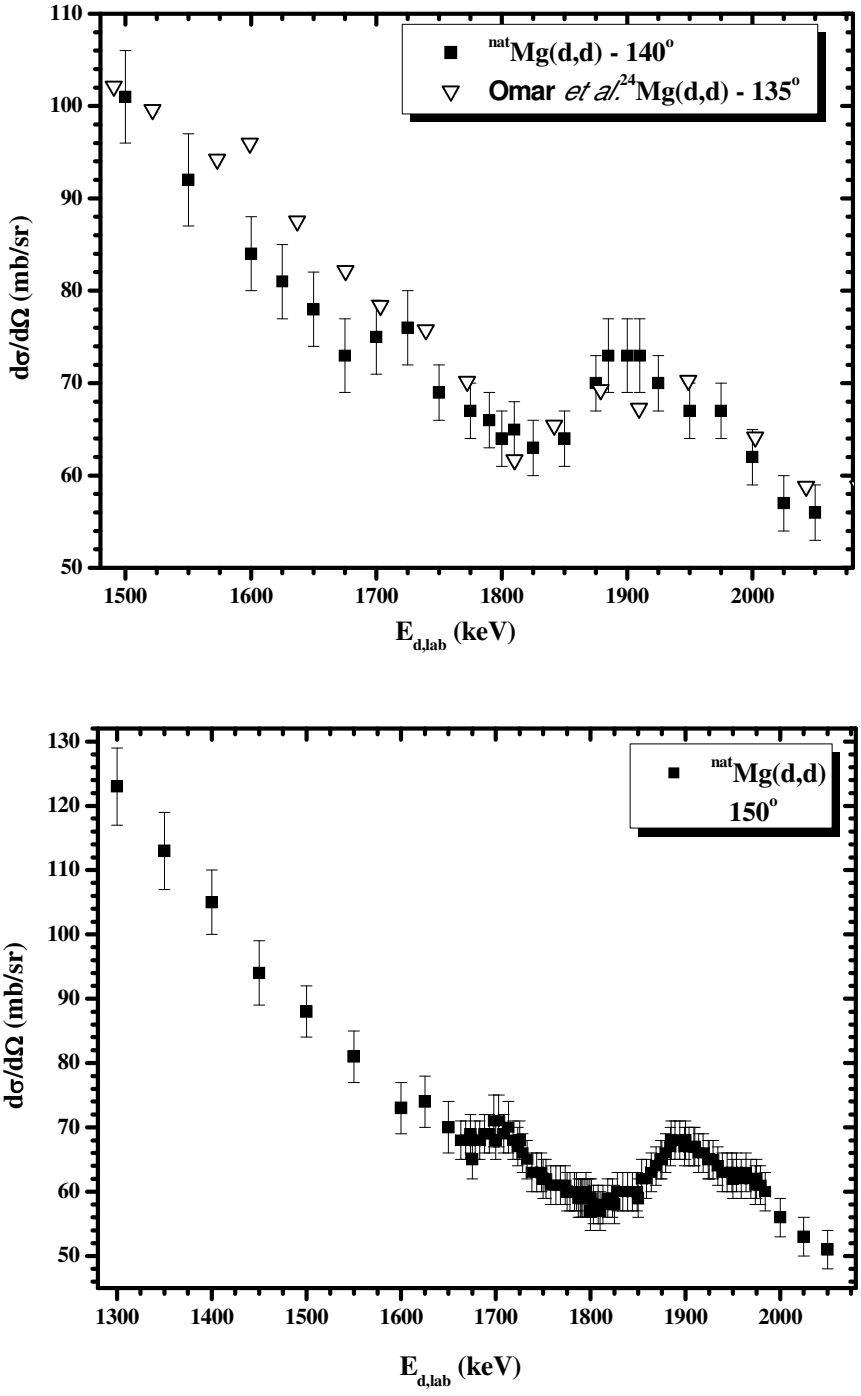

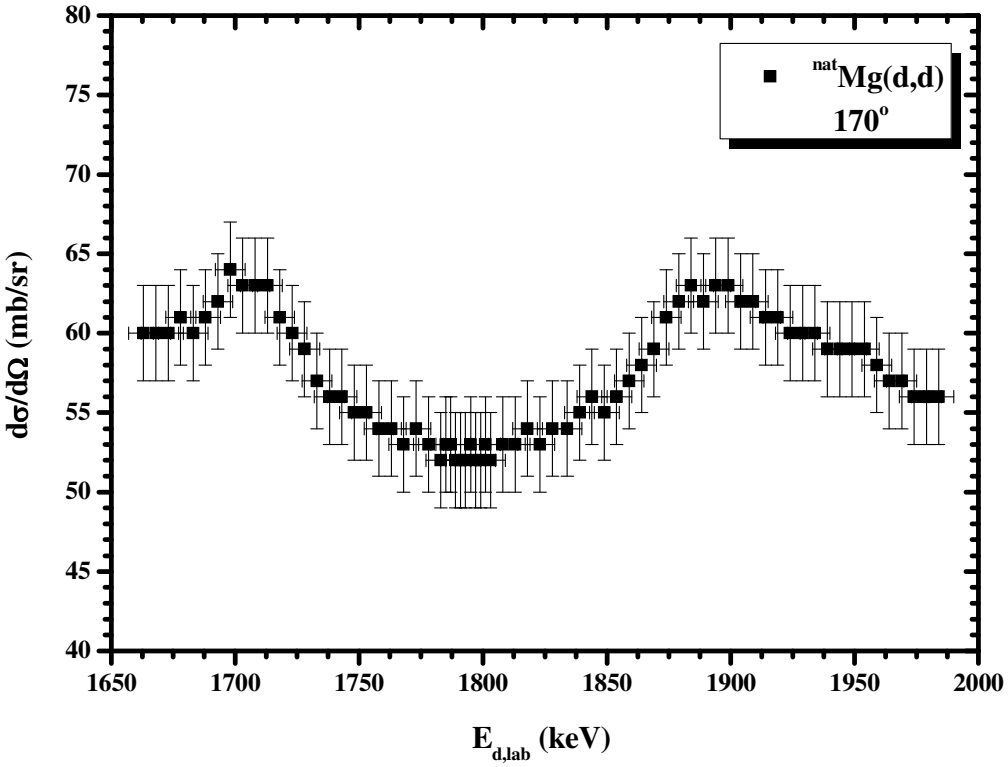

Figure 3.19: Differential cross-section values of the ^{nat} Mg(d,d$_0$) reaction between 140° and 170 for the corresponding energy range studied, along with the corresponding uncertainties. The dataset by Omar et al. [51] at 135° is also illustrated being divided by a factor of 100 for comparison.

The comparison of the obtained data with the only related available work in literature ([51]) shows the following. Concerning the elastic scattering ^{nat}Mg(d,d$_0$), the two datasets, plotted above in Figure 3.19, seem to be in very good agreement, given not only the non attributed uncertainty of the cross section-values by Omar et al., but also their uncertainty originating by the stated ambiguous units of the data themselves.

The obtained results for the differential cross–section values of the ^{24}Mg(d,p$_0$,p$_1$,p$_2$)^{25}Mg reactions [72, 73] are presented in tabular form in Appendix C and are plotted in Figures 3.20, for all detection angles between 55° and 170°, along with the only available data from literature [51] at 119° and 150° for comparison.

Concerning the ^{24}Mg(d,p$_0$) reaction, for all three points reported in [51] at 150° and the one at 119° in the studied energy range, the agreement with the results presented in this work is fair within 1–2 σ. The large errors reported in [51] in this case are attributed to the normalization procedure followed, relatively to the elastic scattering cross sections. However, it is not clearly

indicated in the text whether the $^{nat}Mg(d,d_0)$ reaction results at 135° were averaged relative to the Rutherford elastic scattering values, or a point–by–point comparison was adopted for the normalization

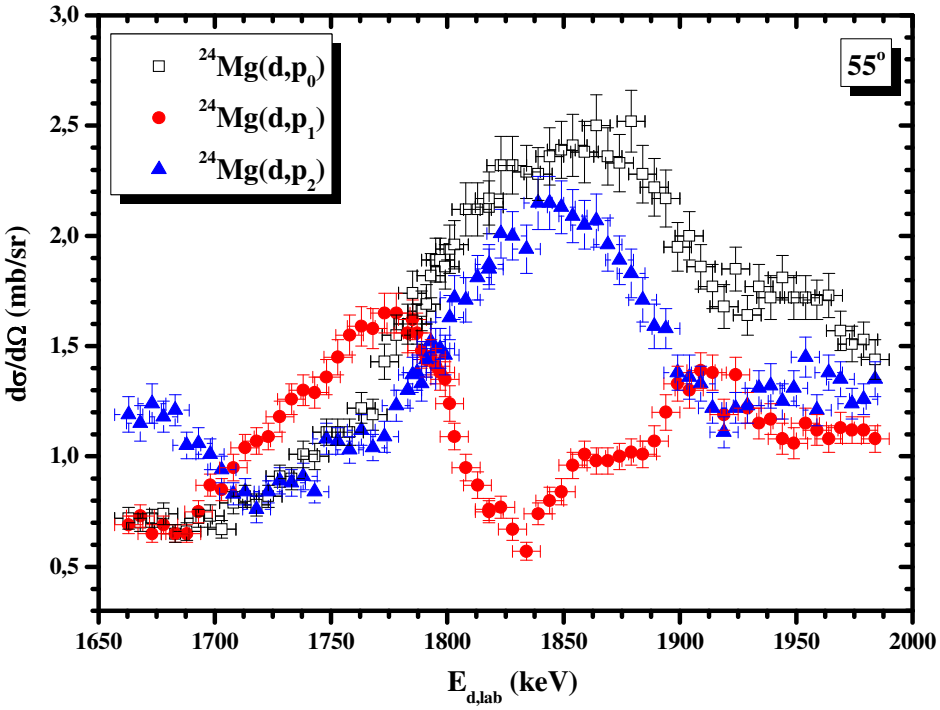

.

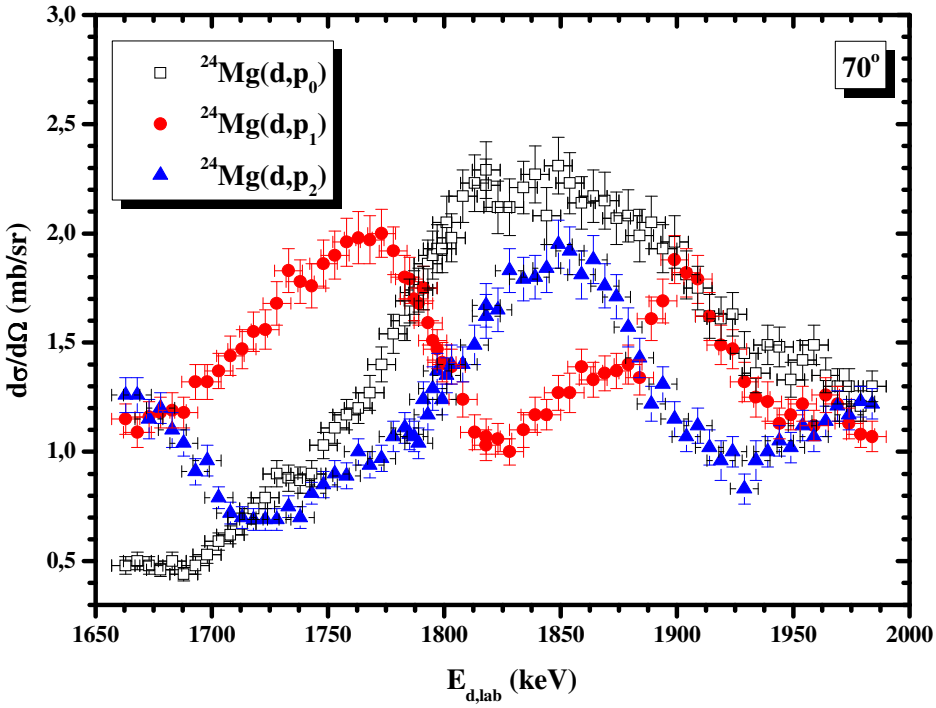

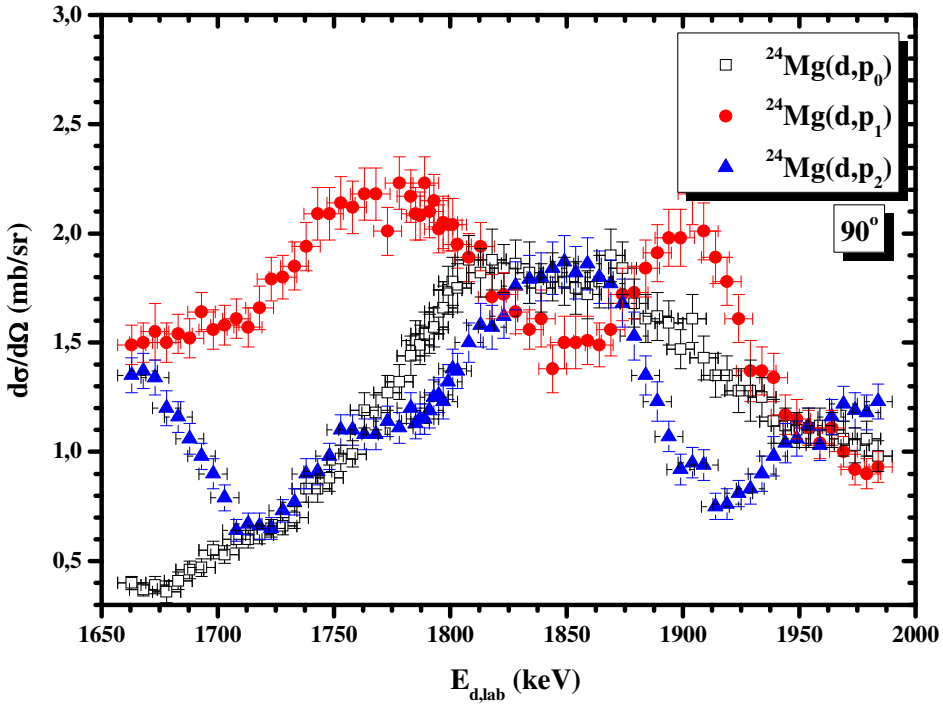
3,0
2,5
2,0
1,5
1,0
0,5
dσ/dΩ (mb/sr)
1650
1700
1750
1800
1850
1900
1950
2000
E d,lab (keV)
24Mg(d,p0)
24Mg(d,p1)
24Mg(d,p2)
90°

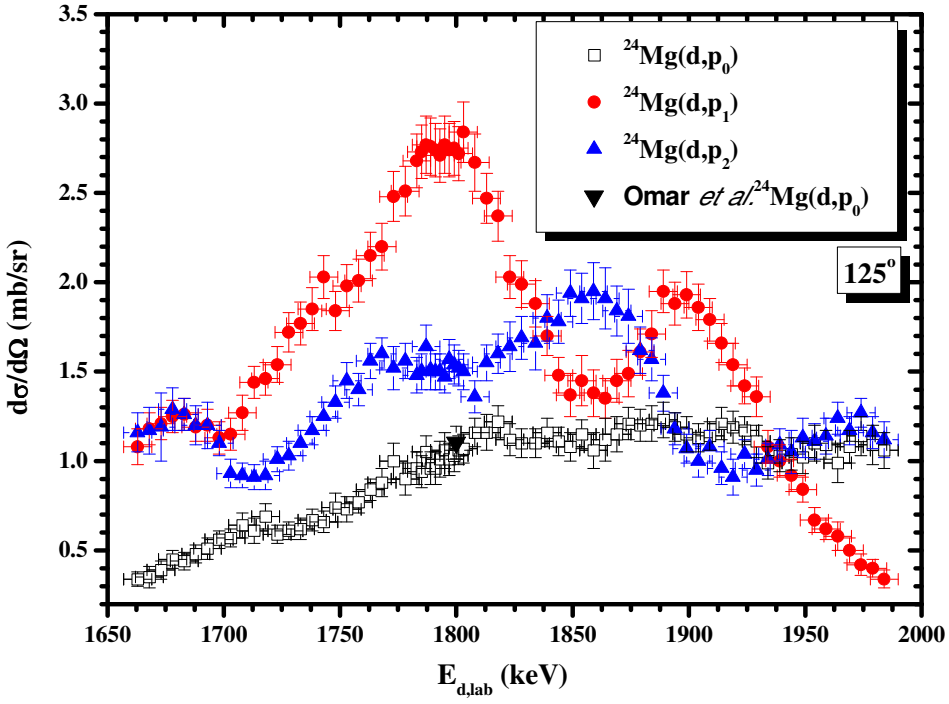
3.5
3.0
2.5
2.0
1.5
1.0
0.5
dσ/dΩ (mb/sr)
1650
1700
1750
1800
1850
1900
1950
2000
E d,lab (keV)
24Mg(d,p0)
24Mg(d,p1)
24Mg(d,p2)
Omar et al. 24Mg(d,p0)
125°

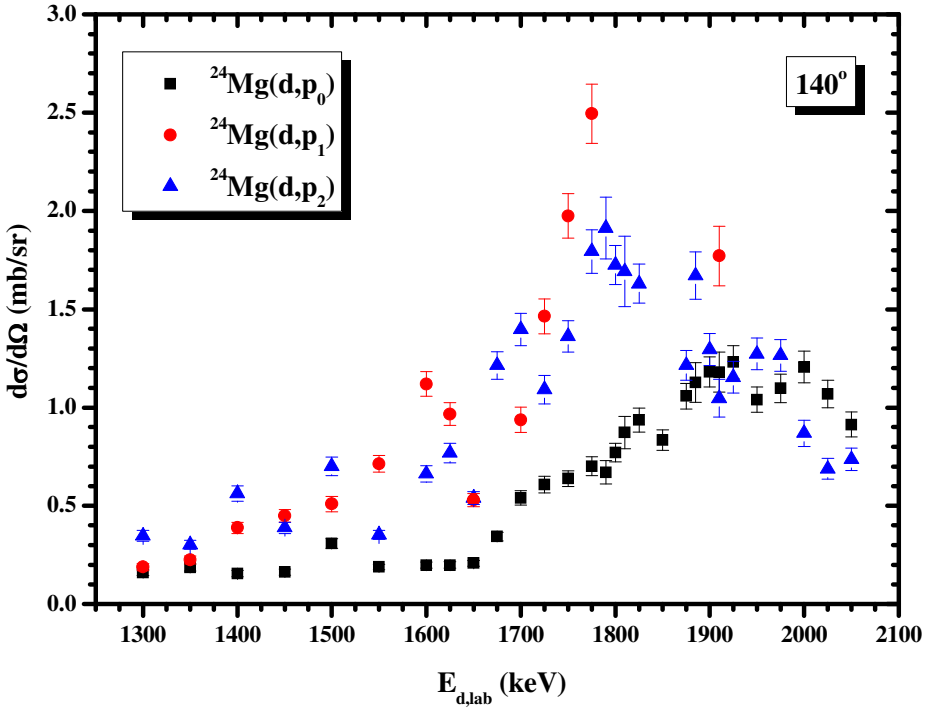
^{24}Mg(d,p$_0$)
^{24}Mg(d,p$_1$)
^{24}Mg(d,p$_2$)
140^o
dσ/dΩ (mb/sr)
E$_{d,lab}$ (keV)

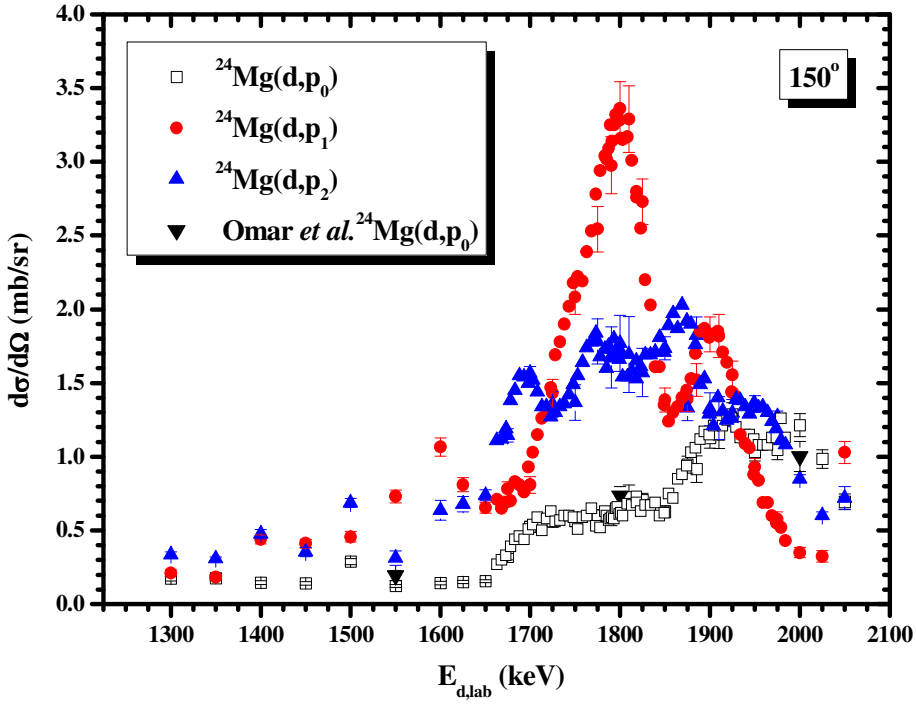
^{24}Mg(d,p$_0$)
^{24}Mg(d,p$_1$)
^{24}Mg(d,p$_2$)
Omar *et al.* ^{24}Mg(d,p$_0$)
150^o
dσ/dΩ (mb/sr)
E$_{d,lab}$ (keV)

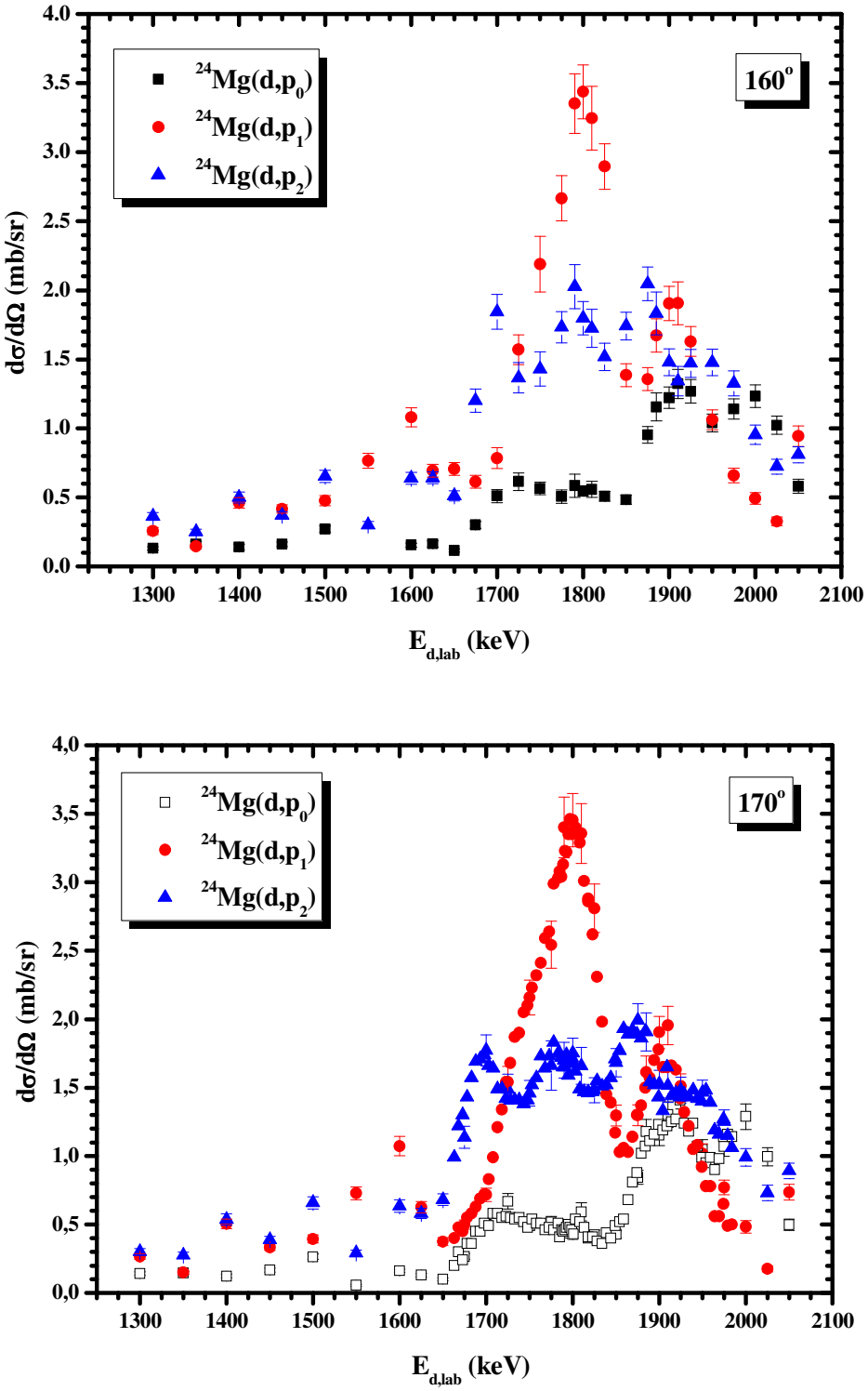

Figures 3.20: Differential cross–section values of the ^{24}Mg(d,p$_0$,p$_1$,p$_2$)^{25}Mg reactions at detection angles between 55° and 170°, for the corresponding energy range studied, along with the only available data from literature by Omar et al. [51] at 119° and 150° for comparison. The combined experimental errors are included in the graphs, as well as the ones along the y–axis of the older dataset [51]. For reasons of clarity, the errors along the x-axis have not been included.

The most significant result of this work, however, is that the obtained data clearly reveal the existence of several, possibly overlapping, resonances, corresponding to unknown levels of the compound nucleus ^{26}Al. In the region around 1800 keV, a strong, resonant-like behavior can be seen in the experimental data concerning all reaction channels. Especially the maximum in the yield around $E_{d,lab}$=1810 keV appears to be very pronounced in the (d,p_1) reaction over the whole angular range studied, less pronounced in the (d,p_0) and (d,p_2) reactions and as a minimum in the ^{nat}Mg(d,d_0) one, clearly indicating the possible existence of a level in the compound nucleus ^{26}Al. For beam energies of ~1800 keV, the excited states of the compound nucleus ^{26}Al with energies of the order of 13 MeV are populated. The spectroscopic information in this region of excitation energies is rather limited [74, 75] and contradictory, as Ericson fluctuations have also been reported in the past [76]. However, it should be noted that according to previous works [http://www.nndc.bnl.gov/chart/] the existence of a discrete level at 13910 keV of ^{26}Al, which is beyond the energy range probed in the resent work, as well as the non decreasing energy difference between the excited states of ^{26}Al at such excitation energies, contradict this argument. It has been shown in several works (e.g. [77]) that at such low deuteron energies the compound nucleus mechanism strongly prevails over the direct reaction one. It is thus surprising that in all nuclear compilation reports in literature (e.g. in [69] or in http://www.nndc.bnl.gov/chart/) there is no reference to the corresponding excited states of the compound nucleus ^{26}Al for the center–mass energy range covered in the present work, the characterization of which (determination of the J^{π} value) will be the subject of a future work.

It should also be pointed out here that the variation of the differential cross–section values of practically all proton levels studied was relatively smooth, over the whole covered energy and angular range, as shown in Figures 3.20a–h. This greatly facilitates NRA profiling studies also allowing for a correlated analysis of thick or deep–implanted magnesium layers, especially in the common case of compact experimental chambers with fixed detector settings, where the detector to target distance is relatively small (in order to increase statistics), and thus the angular uncertainty is usually large, or when the accelerator beam energy and its ripple are not known with high accuracy. Moreover, taking into account the superior mass resolution of deuterons over protons, the absence of strong, narrow resonances in the elastic scattering ^{nat}Mg(d,d) and the observed rather smooth angular variation of the differential cross sections, deuteron elastic scattering studies prove to be particularly convenient for Mg depth profiling for routine applications and a viable alternative to the proton elastic scattering ones. Within this framework,

the simultaneous implementation of both EBS and NRA techniques using a deuteron beam can evidently result in more detailed and accurate magnesium depth profiling studies.

CHAPTER 4

VALIDATION PROCEDURE – BENCHMARKING

It has already been pointed out that the implementation of all Ion Beam Analysis (IBA) depth profiling techniques critically depends on the accuracy of the existing differential cross-section datasets for the reactions involved (see section 1.3). The evaluated cross-section data, available through the online calculator SigmaCalc [25], are the most reliable data to be used in analytical studies, since they involve a critical assessment of the available experimental data, which are often scarce and/or discrepant, followed by a proper tuning of the corresponding nuclear model parameters [78]. However, most of the evaluated datasets are still not adequately validated. A carefully designed benchmarking experimental procedure, which regards the actual **validation of differential cross-section data** via the acquisition of thick target spectra followed by their simulation, is thus mandatory. Benchmarking can also provide **feedback** for the adjustment of the parameters of the nuclear model used in the evaluation process, and can help in assigning realistic uncertainties to the cross sections. Moreover in the absence of evaluated cross sections, it can indicate recommended experimental datasets. In the past, benchmarking results have usually been reported, related to the validity of specific experimentally determined differential cross-section datasets [e.g. 79-81]. However, such measurements have never been performed in a systematic and consistent way, taking into account all the fine steps and details of the benchmarking process.

The present dissertation contributes in this field exactly by developing a methodology for this process, concerning the detailed investigation of all the involved parameters, thus defining the **necessary steps** for the benchmarking process, described in the beginning of this chapter following a brief description of the general methodology and concept. Within this framework, benchmarking measurements were performed for the validation of the measured cross sections analytically presented in the previous chapter and the results obtained are presented and analyzed here in detail. Extra benchmarks concerning important cross sections relevant to IBA are also presented in this chapter, in sections 4.7 and 4.8. More specifically, a different approach is proposed in section 4.7, for studying the cases, where there is background contribution of alpha particles (originating from (p,α) reactions) inhibiting the benchmarking process of the proton elastic backscattering. The systematic and coherent benchmarking studies presented in

section 4.8 on the other hand, aim at validating the already existing evaluated cross sections, facilitating also their extension to higher energies.

4.1 Methodology

The benchmarking of the cross section of a specific elastic scattering reaction concerns the study of the scattering itself using a uniform thick target of the element of interest. The followed procedure is actually based on the comparison between the acquired thick target spectra and the corresponding simulation of the spectra. The scope and the challenge of this process is to perform simulations under the same conditions with those of the experiment and then after locking all the other parameters involved, affecting the obtained spectra, one can attribute any possible discrepancies between the simulations and the real experimental spectra exclusively to the differential cross-section data used in the simulations (over a restricted energy range, as discussed in the following section). Benchmarking is thereby a validation procedure concerning the corresponding cross-section values of the studied interaction.

More specifically, using a thick target, the acquired backscattering spectrum does not consist of thin peaks, but it depicts a yield in a "huge" energy range. It represents, namely, the scattering of the particles on the "total" thickness of the target, ranging from its surface, on the right edge of the spectrum, corresponding to the particles with the highest energy of detection, down to the very deep layer of it, which corresponds to the particles having energy close to zero reaching back the detector after being scattered deep inside the target. A similar situation has already been described in detail in section 1.1.1, concerning the RBS spectra. The only difference in the benchmarking spectra is that the cross sections under investigation do not follow the Rutherford formula, being thus categorized as EBS or NRA spectra (see also 1.1.2). Therefore the shape of each obtained spectrum reveals the corresponding cross section curve at the specific energy range, mainly convoluted with the detector resolution, the stopping power and the straggling function in the target, as analyzed in section 1.1.3. In that section, the simplified relation of the obtained thick target yield has been presented, which is also seen below, along with its complete description [65], including also the accelerator energy distribution (ripple) $g(E',E_0)$ for mean incident energy E_0, the energy loss in target Δ and the energy straggling $W(E,E',E'')$, as follows:

$$Y(E_1) = \frac{d\sigma}{d\Omega}(E,\theta)Q\Omega\frac{\delta E}{[\varepsilon(E)]cos\theta_1} \quad 4.1$$

$$Y(E_1) = \int_{E_0-\Delta}^{E_0}\int_0^{\infty}\int_0^{\infty}\frac{d\sigma}{d\Omega}(E'',\theta)Q\Omega\frac{\delta E}{[\varepsilon(E'')]cos\theta_1}g(E',E_0)W(E,E',E'')dE''dE'dE \quad 4.2$$

An example of the benchmarking procedure, namely of the actual comparison between the experimental obtained spectra and the simulated ones is given in the following figures, for the proton backscattering on a thick carbon target [79] (Figure 4.1) and the corresponding evaluated cross-section data [25] used for the simulation in Figure 4.2. In the square seen in this figure, one can see the similar in shape corresponding cross sections, which are this way validated, since the reproduction of the experimental spectrum is excellent, as shown in Figure 4.1.

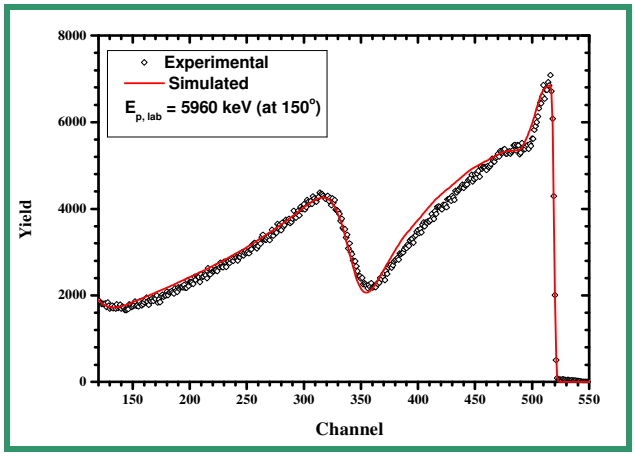

Figure 4.1: Thick target spectra acquired at 150° corresponding to elastic proton scattering on carbon at 5960 keV [79].

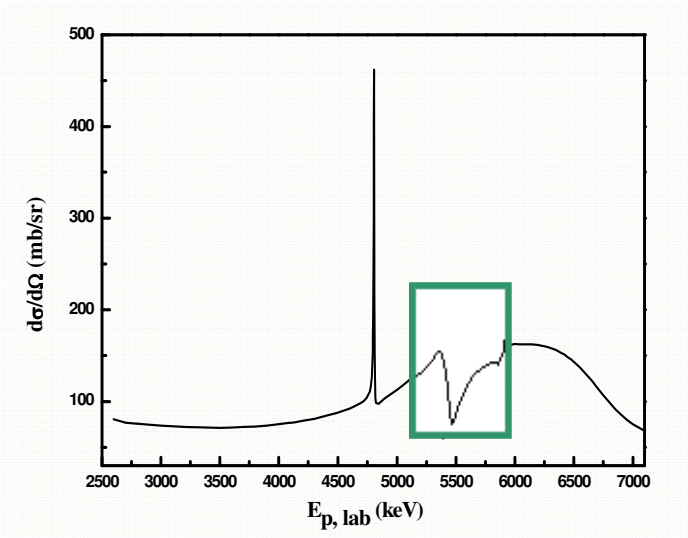

Figure 4.2: Evaluated differential cross section of the proton elastic scattering on carbon at 150° [25].

The whole **experimental procedure** for benchmarking the elastic scattering on the studied element involves several steps to allow for accurate simulations to be afterwards performed. These steps are thoroughly described in the following section and can be summarized here as follows: (i) the acquisition of EBS thick target spectra from uniform thick targets of known composition with good counting statistics, (ii) the accurate calibration of the accelerator over a broad energy range, (iii) the precise determination of the detector resolution and (iii) the minimization of target-related effects such as channeling, surface roughness, etc.

4.2 Benchmarking steps

Benchmarking is an experimental procedure that needs to be very carefully designed. In order to simulate the thick target spectra acquired, one must investigate and accurately determine all the parameters involved.

A thick target spectrum is essentially a convolution of the stopping power and the straggling function in the material, the resolution of the detector and the corresponding cross section, as analyzed in section 1.1.3, but several other parameters are also important for accurate simulations. These include the calibration of the accelerator energy and the ADC, the determination of the accumulated charge in the target and the treatment of possible background counts and/or pile-up effects. Special attention should also be drawn to the proper selection of the thick target used in benchmarking, in terms of its element composition and structure, for several reasons. These mainly concern the background contribution, the charge/solid angle normalization, the multiple scattering and the effect of surface/interlayer roughness or channeling. Each of these parameters affects the obtained spectra in a different way, but all of them need to be carefully treated for a proper and accurate validation procedure. In addition to the above, the code used for the simulation should be capable of taking into account any possible fine structure of the corresponding differential cross section (sharp narrow resonances).

For the present benchmarking measurements, all the mentioned parameters were treated in the most detailed way (as possible), as described in the following paragraphs, while the SIMNRA code [70] and the DataFurnace code [82], which is capable of taking into account the cross-section fine structure and self-consistently fitting multiple spectra, were used for the simulations. The simulated spectra were along these lines produced taking into account a very small energy step for the incoming and outgoing particles, the effect of multiple scattering, the

beam ripple, ZBL stopping power data [6], and Chu and Yang's straggling model [20, 11] as implemented in the codes used. It should be noted here that for the moment all popular analytical codes do not take the uncertainties in the experimental differential cross-section datasets into account, while the assessment of the uncertainties in the evaluated datasets has been the subject of recent studies [67, 68].

4.2.1 Energy calibration

The energy of the protons impinging on the target is certainly an essential parameter to be precisely known for accurate simulations in the validation procedure. Especially in the cases of resonant structures, the incident energy plays a crucial role in the process. The actual energy for all the benchmarking measurements performed in the present work was determined by calibrating the accelerators, as previously described in 3.1.2.1 section.

More specifically, for the calibration of the GVM Tandetron accelerator at the University of Surrey, where the proton backscattering cross sections on ^{nat}Si, ^{23}Na, ^{31}P and ^{nat}S were studied for validation up to 3.5 MeV (described in section 4.8), three narrow resonances were used, namely the (991.9±0.1) keV one of the ^{27}Al(p,γ)^{28}Si reaction (Γ=110eV) [60], the (1747.6±0.9) keV of the ^{13}C(p,γ)^{14}N reaction (Γ=122 eV) [61] and the (3379±1) keV of the ^{32}S(p,pγ)^{32}S reaction (Γ=700 eV) [62] using a 10% HPGe detector. The linearity of the energy with respect to the accelerating voltage, as shown in the following Figure 4.3, was found to be excellent over the whole energy range studied. The uncertainty of the proton energy was calculated to be less than 0.1%. All the other benchmarking measurements were performed at NCSR "Demokritos", where the accelerator was similarly calibrated with the use of the same resonances.

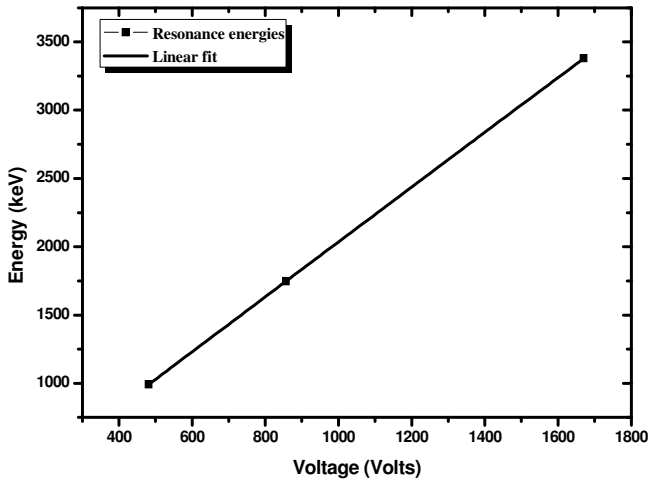

Figure 4.3. Tandetron accelerator calibration of the University of Surrey using the three mentioned narrow resonances.

4.2.2 Detector resolution and ADC calibration

Another parameter that needs to be taken into account for a proper benchmarking is the resolution of the detectors, which is, of course, also convoluted in the obtained spectra, affecting their shape in terms of energy spread (seen in chapter 1, section 1.1.3(2)). It is therefore necessary to determine it precisely, along with the calibration of the ADC, in order to simulate the spectra under the same conditions prior to the validation procedure, that is, prior to the comparison between the experimental and the corresponding simulated spectra.

In the present benchmarking measurements, the simulation of the backscattered protons from the polished targets (silicon and/or GaP wafer) at all studied angles, compared to the corresponding experimental spectra acquired, enabled simultaneously the calibration of the ADC using the Au peak over a wide beam energy range, as described in detail in the second paragraph of section 3.1.1.1, and the determination of the resolution of the detectors. In the following Figure 4.4, such comparison is shown for a proton backscattering spectrum from a silicon wafer with a thin Au layer on top. The resolution of the used detector is directly indicated by the slope of the silicon edge (since the target is polished) and thus one can easily determine it by simulating the slope adjusting the appropriate value for the resolution. The small peak on the right of the spectrum in Figure 4.4, corresponding to the scattering on the thin Au layer could also be used for the adjustment of the resolution by fitting/simulating its FWHM. However, this is not equally accurate as the silicon edge, because the FWHM of the peak is a convolution of both the detector resolution and the thickness of the Au layer, considering that the ripple of the accelerator is much smaller than the detector resolution, thus inducing the uncertainty of the Au thickness into the resolution determination, which is of course undesirable.

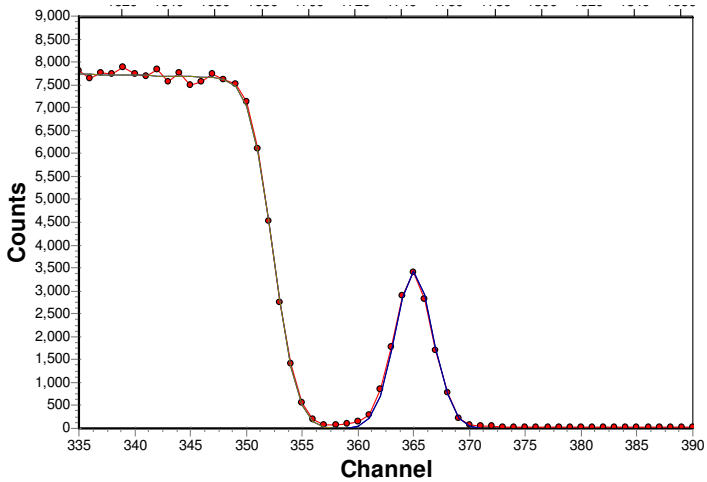

Figure 4.4: Simulation of the edge (slope) of a Si wafer to determine the resolution of the used detector.

4.2.3 Pile-up

Another important effect that could impede and/or mislead the validation procedure is the pile-up of the detected events in the acquired thick target spectra, occurring in cases with high counting rate.

Calculations of the corresponding spectral distortion and the pulse losses can in principle be applied with high accuracy, concerning both the tail pile-up and the leading edge overlap, as analyzed in Molodtsov et al. [83] by considering a Poisson probability distribution and proper response functions for the description of the phenomenon. It should be noted here, that the exclusive use of electronic pile-up rejection cannot resolve the problem, as discussed in [83].

In order to totally avoid the pile-up effect, the beam current needs to be low, at about 5nA, depending on the solid angle of the detector (distance from the target), the beam energy and the comprising elements of the target. Given that the distance of the detector is adjusted only once, in the beginning of an experiment, and then stays fixed, the beam current on the target should always be monitored with respect to the counting rate of the acquired spectra during all measurements (since pile-up effect is easily recognizable in the spectra from the characteristic tail formation-shape).

It should be pointed out here that this simple method of eliminating the pile-up effect, by keeping the beam current low, was in fact applied in all the measurements of the present work.

4.2.4 Stopping power, straggling and plural scattering

The benchmarking procedure totally relies on the acquired thick target spectrum, which is in turn the absolute result of the interaction between the beam particles and the target atoms described in chapter 1 (section 1.1). Concerning the stopping power and the straggling in the target, the models, which are considered to be the most accurate ones, need to be used in the code used for the simulations of the thick target spectra. These are the model of Ziegler–Biersack–Littmark [6] for the proton stopping power and the one of Chu & Yang [20, 11] for the straggling function. The effect though, of these two parameters, as well as the effect of plural scattering, especially when a heavy element is present in the target, were investigated in the present studies by comparing the simulated and the experimental spectra obtained at close energies (i.e. at resonances and then, in small energy steps above the resonances) and using different stopping power compilations. It was found that the effect of these three parameters

could not be simulated in a satisfactory way at lower energies (deeper in the targets), as it can be observed in Figure 4.5, for the plural scattering effect. Although each of these parameters has a different dependence on depth, all of them are more pronounced, with decreasing energy of the incoming particles. In order to diminish such problems in the simulations, the analysis was limited relatively close to the surface leaving a narrow window of opportunity for the validation of the cross-section data. The energy step for all the benchmarking runs was thus small, not larger than 250 keV, over the whole energy range studied (see section 4.8).

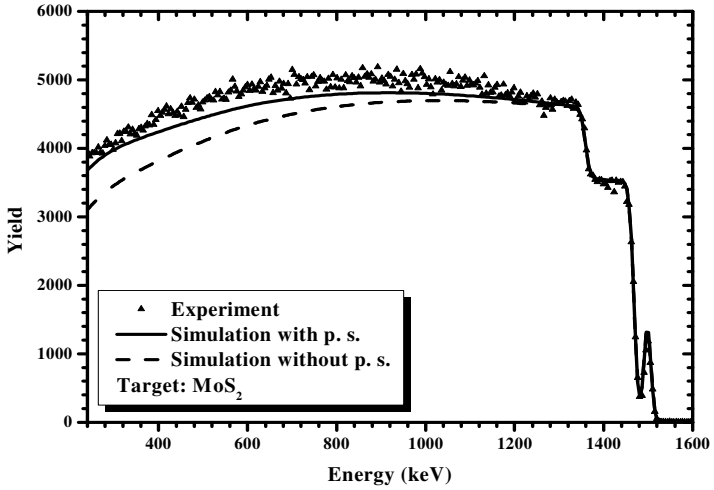

Figure 4.5. Thick target spectrum (MoS_2) simulated with and without plural scattering at 1531 keV at 148.8°, along with the corresponding experimental spectrum.

4.2.5 Accumulated charge – solid angle

The accumulated charge Q, along with the subtended solid angle of the detector Ω, evidently play a critical role in the obtained thick target yield, as depicted in the equations presented in the beginning of this chapter (4.1). The QΩ factor is preferably indirectly determined to achieve better accuracy, as mentioned in the previous chapter concerning cross-section measurements. The so called charge-solid angle normalization denotes the determination of the QΩ factor of a measurement relatively to the simulation of the Rutherford signal of a target element with known thickness (preferably of infinite thickness). A thin Au layer was therefore evaporated on top of all targets used in the present benchmarking runs.

This procedure leads to the determination of (QΩ) with an uncertainty depending on the determination of the Au thickness and the statistics of the corresponding signal. However, these are features that can in principle be very well controlled and determined, as further described in the following section 4.4 concerning the overall uncertainty assessment.

4.2.6 Background and channeling effect

Depending on the elements comprising the thick target and the beam energy, there may be several nuclear reactions occurring in the target, as analyzed in chapter 1 (section 1.1.1). This results in the detection of several outgoing particles/products, depositing different amounts of energy in the detector. The corresponding spectra consist therefore of several overlapping signals at some point at relatively low energies (in the case of thick targets). Considering that in the present work the studied part of the spectra concerns the elastic scattering cases, background contribution of counts originating from other reaction channels, inhibits the direct validation procedure. The treatment of such background is thus crucial and depends on each case study, in terms of the other possible reaction channels and the scale of the phenomenon, being revealed by the acquired spectra themselves. For example, a linear regression rule can be applied for the background subtraction in cases of smooth linear contributions, like the ones described in section 4.6. In cases of a very pronounced background contribution one can use ΔE/E telescopes to separate the different particle species and thus "clean" the spectra, as proposed in section 4.7 studying the ^{nat}B(p,p) backscattering. This method can of course be applied only when the contributing particles present a considerably different energy loss in the thin ΔE detector used.

Concerning the channeling effects when using crystalline targets, one can artificially misalign the target with respect to the beam axis, either by tilting it, or by randomly rotating it during the measurements. In the case of a constant tilt of the target, one should be certain of the misalignment by checking the obtained spectra and preferably by scanning it to determine a correct position (tilt) with random rotation, by measuring the obtained surface yield at each step. The latter method was in fact implemented in the following cases of crystal targets (see 4.8). It should be noted here, that in any case, when using crystalline targets, the imitation of a "random" spectrum cannot be better than 98%, as has been reported in the past [4].

4.2.7 Contaminations

Moreover, there may be some contaminants in the thick targets used for the benchmarking measurements, affecting the backscattering spectra with unwanted peaks. The existence of a small amount of carbon cannot be totally avoided (carbon buildup during the measurements) and the same applies in most of the cases to oxygen as well (oxidization on the surface). Moreover, both the procedure of the target preparation and the sealing afterwards can possibly induce only

slight contaminations in the target composition. The unwanted effect of these contaminants should always be taken into account if necessary, (e.g. the $^{12}C(p,p)$ elastic scattering has already been evaluated and validated [79] over a broad energy range), in cases for example where the unwanted peak is very close to the one of the element under study. In most cases though, these small contaminants appear at the low energy part of the spectra and do not really affect the validating results in the benchmarking procedure, as evidenced in the present studies described in the following sections (4.5 – 4.8).

4.3 Roughness of the targets

The surface roughness of the target can significantly affect the shape of the spectra, affecting the energy of the incoming and outgoing particles near the surface region, and thus, it is very important to treat it carefully, when present. An example of this effect is shown in Figure 4.6 comparing the experimental proton spectrum of a rough MoS_2 target to the simulated one with and without the roughness correction. The roughness of the pellets used in the present study was treated *a posteriori* using a built algorithm, implementing the mathematical model developed by Molodtsov *et al.* [84], which parametrizes and takes into account the possible secondary crossings of protons in the asperities of the target surface. The corrected spectrum of the example shown below, in Figure 4.6, is plotted in black solid line reproducing the experimental data.

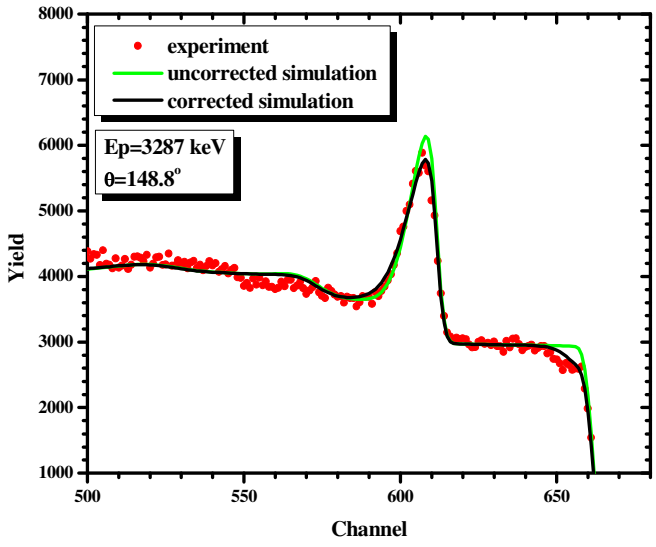

Figure 4.6: Backscattering proton spectra on a MoS_2 pellet, along with the corresponding simulations with and without roughness correction.

4.3.1 Model

The mathematical model for the roughness effect (Molodtsov et al. [84]) is based on the parameterization on the fraction **n** of the scattered particles, which cross one or more valleys in the material, depending on its sharpness **p** and the scattering angle **θ**, as shown in the following Figure 4.7, whereas a random height chosen from a Gaussian distribution of variance $\boldsymbol{\sigma^2}$ is assigned to a regular linear grid of reference points with separation d to model the rough surface. The dimensionless parameter p can range between [0.5-3] and the scattering angle is of course considered to vary between 90° and 180°.

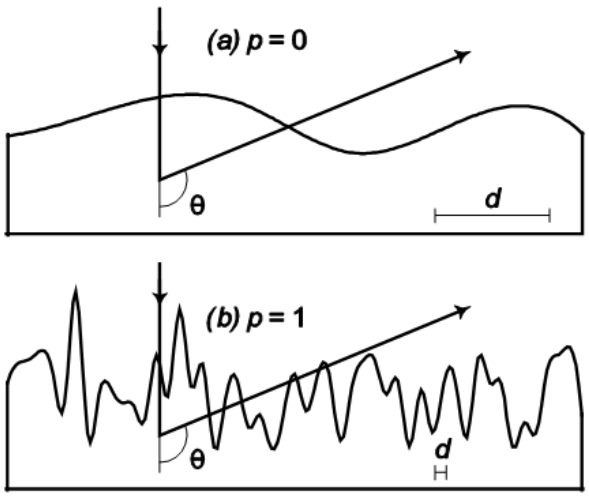

$$p = \log \frac{\sigma}{d}$$

Figure 4.7: Schematics of the surface roughness described in p,θ, σ and d parameters.

The additional exit path length **x** in these asperities, as calculated with Monte Carlo simulations, is parametrized through the function **f(x)** (equation 1). The induced α and b parameters, as well as the n fraction of the particles, depend on p and θ, as described in the following equations (4.3-4.6).

$$f(x) = \frac{b^{a+1}}{\Gamma(a+1)} x^a \exp(-bx), \tag{4.3}$$

$$n(\theta, p) = \frac{1 - \exp\left[k_4 (180 - \theta)^{k_5}\right]}{\left\{1 + \exp\left[k_6 z(\theta, p)\right]\right\}^{k_7}} \tag{4.4}$$

$$a(\theta,p)=k_4\{\cosh[k_5 z(\theta,p)]\}^{k_6}+k_7 \quad (4.5)$$

$$b(\theta,p)=\frac{(k_4+\theta)z(\theta,p)\exp[k_5 z^2(\theta,p)]+k_6+k_7\theta+k_8\theta^2}{1+\exp[k_9 z(\theta,p)+k_{10}]} \quad (4.6)$$

with different $\boldsymbol{k_i}$ for each parameter (n, a, b) and general functions z(θ) and φ(θ,p) as given below:

$$\varphi(\theta)=k_0\theta^2+k_1\theta+k_2$$
$$z(\theta,p)=\theta\sin[\varphi(\theta)]+p\cos[\varphi(\theta)]+k_3 \quad (4.7)$$

The uncorrected simulated spectrum $\mathbf{Y_0(E)}$ should be convoluted with the f(x) function in order to obtain the final spectrum **Y(E) corrected** for the roughness effect, as shown in the following equation (4.8), accounting for the secondary crossings in the material asperities of the fraction n particles.

$$Y(E)=n\int_0^{\infty}Y_0(E')\frac{f\left(\frac{(E,E')}{\sigma}\right)}{\sigma S(E')}dE'+(1-n)Y_0(E) \quad (4.8)$$

X(E,E') accounts for the distance in the material traveled by a particle with initial energy E' and final E, as calculated using the corresponding stopping power function S(E), seen in the following relation.

$$X(E,E')=\int_E^{E'}\frac{d\hat{E}}{S(\hat{E})} \quad (4.9)$$

4.3.2 Code

A programming code was developed using FORTRAN to calculate the corrected backscattering spectrum taking into account the roughness effect of a target, as is parametrized in the model of S.L. Molodtsov et al. [84], briefly described in the previous section.

SRIM calculations were used to calculate the stopping power in the targets, while a linear interpolation of the backscattering data was implemented between each two channel yields in order to convert the channel binning of the spectra to a continuous energy range. The sharpness **p** and the height **σ** of the Gaussian distribution of the model were determined with the MINUIT [85] routine for χ^2 minimization, accordingly incorporating the code as needed. The **input** concerns the energy of the incident protons, the scattering angle, the target, the ADC calibration and the corresponding file with the experimental and the uncorrected simulated spectrum, while the **output** file contains the final corrected spectrum.

4.4 Assessment of the uncertainty factors

The assessment of the uncertainties in the benchmarking procedure is very important and must be the result of the detailed study of all the parameters involved in the simulating and validating steps. The obtained simulated yield is directly related to the stopping power systematics. The effect though of different stopping power compilations (e.g. ZBL [6] and Andersen-Ziegler [86]) in the integrated yield corresponding to ~250 keV from the surface which were used in the validation procedure of the studied benchmarks (described in the following paragraphs), was always less than 1%. The pulse height defect, related to the energy loss in the dead layer of the detector, has also a negligible effect on the analysis for the proton energy range studied (1-4 MeV in most cases) and the ADC width (keV/channel) used. The important uncertainty factors in the present studies, apart from the special case of ^{nat}B(p,p), as described in 4.7 in detail, are thus related to the **counting statistics** and the accurate determination of the accumulated charge Q multiplied by the solid angle Ω subtended by each detector (**QΩ factor**). The effect of these parameters is strongly target dependent. Whenever the target consists of a compound with a high-Z element, for which the elastic cross section does not deviate from the Rutherford formula, the uncertainty in the determination of the QΩ factor is minimized, while the corresponding uncertainty in the statistics is maximized, because one has to subtract the large Rutherford signal of the high-Z element from the total experimental one, in order to validate the cross-section for the light element of interest. In order to minimize the uncertainty of the QΩ factor at high proton energies, where possible deviations from the Rutherford formula could in principle exist for Ga and Br (using GaP and NaBr targets for studying the cases of ^{31}P(p,p) and ^{23}Na(p,p) respectively), the data were normalized relative to the Rutherford backscattering on

the thin Au layer evaporated on top of all targets. The thickness of the deposited thin Au layers was calculated for each target, by fitting the simulated spectra at several low beam energies and detector angles, where the proton elastic backscattering on the element of interest or the heavy element in the case of compound targets follows the Rutherford formula and by taking afterwards the average value and/or with the XRF technique using the in-house developed portable XRF setup [66] of the Institute of Nuclear and Particle Physics of NCSR "Demokritos". This procedure yielded an estimated uncertainty of ~3% in all cases, and this was in fact the dominant uncertainty in the validation procedure, except for the case of the NaBr target and the complicated case of ^{nat}B(p,p), which are described in the following sections. On the other hand, at lower proton beam energies the uncertainty in the determination of the QΩ factor was minimized, since it was obtained directly from the Br, Mo and Ga signal, originating from the backscattering on the heavy element of each target (NaBr, MoS_2 and GaP respectively), following the roughness correction and the dominant uncertainty was thus the statistical error in the experimental yield. In all cases, however, with the exception of ^{23}Na(p,p) and ^{nat}B(p,p), the total combined uncertainty in the present work, including all statistical errors, did not exceed 4% (±1σ).

4.5 Benchmarking on the studied p+LiF cross sections

Due to the observed discrepancies among differential cross-section datasets from literature, a benchmarking procedure is critical in order to validate the obtained results for the $^{7}Li(p,p_0)^{7}Li$, $^{7}Li(p,p_1)^{7}Li$, $^{7}Li(p,\alpha_0)^{4}He$ and ^{19}F $(p,p_0)^{19}F$, $^{19}F(p,\alpha_0)^{16}O$ and $^{19}F(p,\alpha_{1,2})^{16}O$ reactions, presented in 3.2.3. It is important to note here, that all datasets obtained in the present study (3.2 section) are correlated. Therefore, by validating a dataset of cross sections concerning one particular reaction channel for the p+^{7}Li system, one simultaneously validates all the correlated datasets of the other exit channels, taking into account that only peak integration differs, while all the other parameters in the relative formula remain intact, as has already been discussed in 3.2.3. The same naturally occurs in the p+^{19}F case as well. The (p,α_0) reactions were considered to be the most favorable ones to be benchmarked, since the corresponding peaks in the thick target spectra are the only ones that present no interferences over a broad energy range, thus enabling the validation of the corresponding cross sections. Unlike the (p,α), the (p,p) spectra are affected by plural scattering in heavy elements present in the thick target used (BaF_2 case, see below). Additionally, as it has already been mentioned, the (p,p) cross section (especially in the ^{19}F case) presents a complicated structure with many narrow resonances, for the study of which, the energy step adopted in the present work is not appropriate.

More specifically, benchmarking measurements were performed at NCSR "Demokritos", using thick and mirror-polished BaF_2 and LiF targets to validate the obtained differential cross sections of the (p,α_0) reactions for both elements (^{7}Li and ^{19}F) using the SIMNRA code. Prior to their use, both targets were kept in sealed containers with silica gel, for protection against humidity wear and surface changes. The simulated spectra were produced using the obtained differential cross-section datasets and as described in the previous sections 4.1 and 4.2. The Rutherford differential cross sections for the scattered protons from Au and Ba were also used for the simulated spectra. The obtained spectra at 150° at 2300 and 3200 keV are presented in Figures 4.8a-b respectively, which show the excellent reproduction of the experimental spectra in the energy range corresponding to the studied $^{7}Li(p,\alpha_0)^{4}He$ and $^{19}F(p,\alpha_0)^{16}O$ reactions, thus validating the obtained cross-section datasets. It is important to note here, that in Figure 4.8b, the reproduction of the thick LiF target spectrum by the simulated one verifies not only the accuracy of the obtained differential cross sections involved, but also the validity of the Li:F ratio in the thin target being equal to 1:1, as discussed in section 3.2.1 (target characterization).

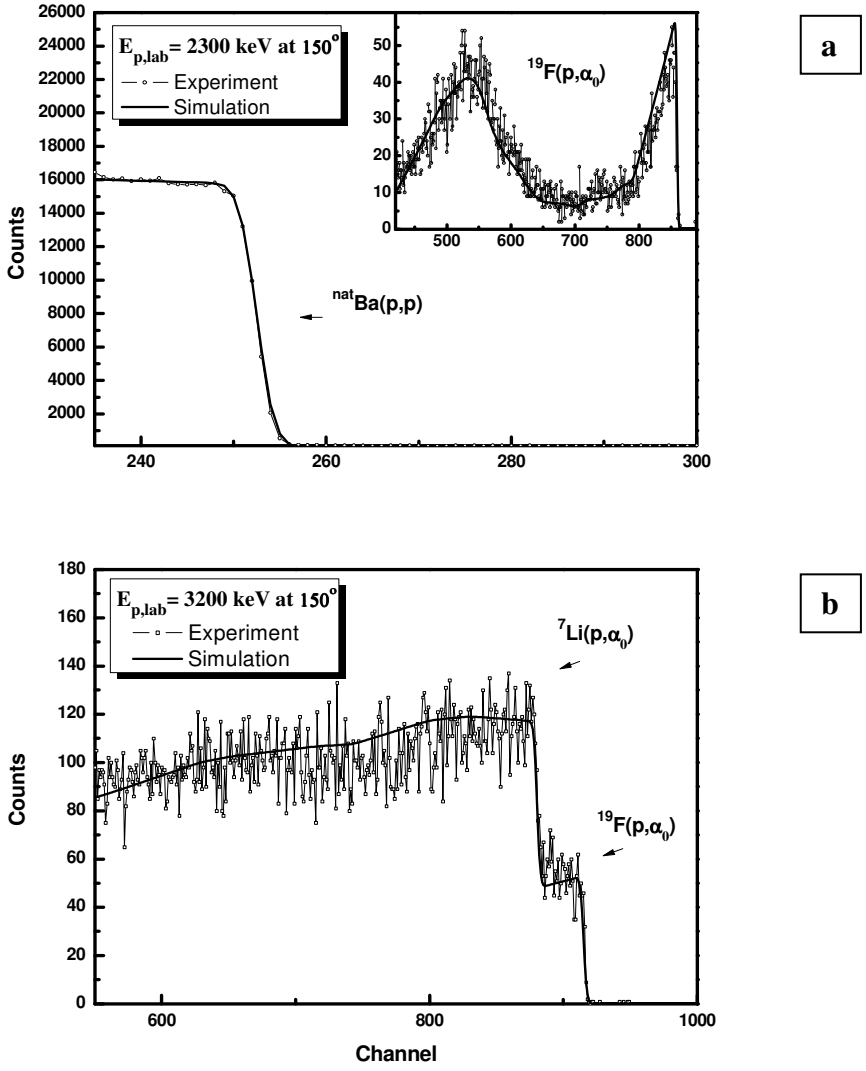

Figures 4.8a, b: Experimental spectra taken at 150°, whilst irradiating the thick and mirror-polished BaF_2 (a) and LiF (b) targets at 2300 and 3200 keV, respectively. The experimental spectra are presented along with the simulated ones using the SIMNRA code [70]. In the inset, spectra are presented in the range corresponding to the $^{19}F(p,\alpha_0)$ reaction.

4.6 Benchmarking on the studied d+Mg cross sections

The obtained cross-section values for the ^{nat}Mg(d,d) and ^{24}Mg(d,p$_i$) reactions, which are presented in section 3.3, have been validated with benchmarking measurements at two deuteron beam energies, namely at 1700keV and 2000keV. The used target consisted of a thick, high–purity, highly–pressed magnesium oxide pellet (a MgO crystal was not implemented in order to avoid channeling effects) with an ultra thin layer of Au evaporated on top of it for solid angle and beam current normalization purposes. The thickness of the gold layer was verified by the RBS measurements and simulations using SIMNRA. It should be noted here that since the obtained cross sections for the studied ^{nat}Mg(d,d) and ^{24}Mg(d,p$_i$) reactions are correlated, only the acquired spectra with the best resolution were used for the validation procedure, namely the ones acquired at 140° and 150°. Moreover, the validation was performed following the methodology presented in the previous sections (4.1- 4.3) using the SIMNRA code.

The final benchmarking results are shown in Figures 4.11a,b, for $E_{d,lab}$=1700 and 2000 keV, at 140^o and 150^o respectively, along with the proper peak identification. The solid line represents the simulations using the differential cross–section datasets obtained in the present work for ^{nat}Mg(d,d$_0$) and ^{24}Mg(d,p$_{0,1,2}$), along with evaluated datasets from SigmaCalc [25] for ^{16}O and ^{12}C (surface contamination). The agreement between the experimental spectra and the simulated results for the ^{24}Mg(d,p) reactions is quite satisfactory for both detection angles and over the whole energy range studied in the present work. More specifically, as shown in Figure 4.11b for the higher benchmarking energy, the experimental spectra are reproduced with an accuracy better than ~7–12% (comparing the integrated experimental and simulated yield of the ^{24}Mg(d,p) reactions).

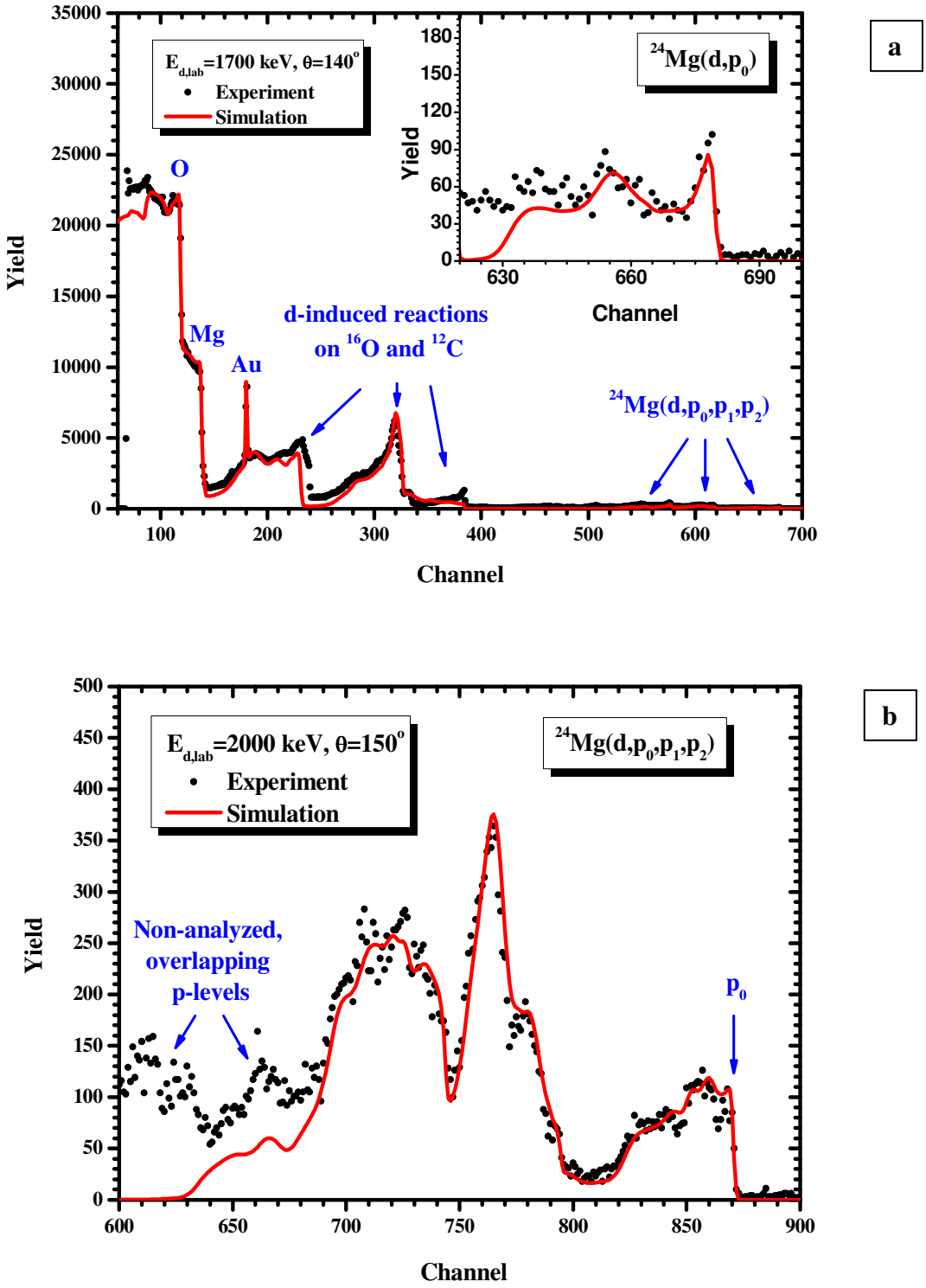

Figure 4.11a, b: Benchmarking results for $E_{d,lab}$=1700 keV and 2000 keV using a magnesium oxide pellet with a thin gold layer on top, along with the corresponding peak identification.

It is evident that in EBS benchmarking runs, a slightly better agreement between simulated and experimental spectra can in principle be achieved. Benchmarking d–NRA data is a rather complicated process, due to the present lack of evaluated differential cross–section datasets for all the 3 major stable light element isotopes (^{25}Mg and ^{26}Mg constitute 10% and 11% of ^{nat}Mg respectively), and the existence of background counts under the studied proton peaks. Consequently, and taking into account the structure and composition of the implemented thick target, the attained agreement is quite encouraging.

Within this framework, benchmarking measurements for the elastic scattering ^{nat}Mg(d,d) were repeated using a thick Mg metallic ribbon instead, also with an ultra thin layer of Au evaporated on top of it for protection against wear and for charge/solid angle normalization purposes. For additional protection against oxidization, the target was constantly kept in a closed container filled with Ar before the irradiation. Nonetheless, a thin oxidized layer, of the order of 1500×10^{15} at/cm^2 on the target's surface was unavoidably formed, leaving a rather narrow window of opportunity for validation purposes, between the surface energy signals of the elastic scattering on Mg and O. Thus, starting at E_d=1750 keV, benchmarking spectra were acquired with a small energy step of 50-100 keV at 150^o and 170^o, following the same methodology. It should be noted here that the amplification of the signals in these runs was chosen to be adequate for studying explicitly the elastic scattering case, resulting to relatively large gain values, thus the high energetic (d,p) peaks were not present in the spectra.

As shown in Figure 4.12 in semi-logarithmic scale for a typical acquired spectrum, the benchmarking process was impeded by a background contribution (as high as 5-7%) induced by protons originating from (d,p_x) reactions on all stable Mg isotopes. The usual ways of removing such a background, i.e. with the use of absorber foils or ΔE/E telescopes, are not applicable in this particular case, since they are based on the different stopping power of particle species. In the deuteron-proton case, there is only a small difference between the stopping power values, especially for the low scattering energies involved, thus requiring large thicknesses of the ΔE detector, which would further complicate the analysis by inducing large uncertainties, especially concerning the implemented straggling function. Moreover, an analytical calculation and subtraction of the corresponding yield from the experimental spectra is not possible, since there are no cross-section data in literature for these reactions at such low energies. This background contribution was eventually estimated, following a linear regression rule on the high energy part,

beyond the Mg elastic scattering edge, and was subsequently subtracted from all experimental spectra, prior to the simulation process, as demonstrated in Figure 4.12.

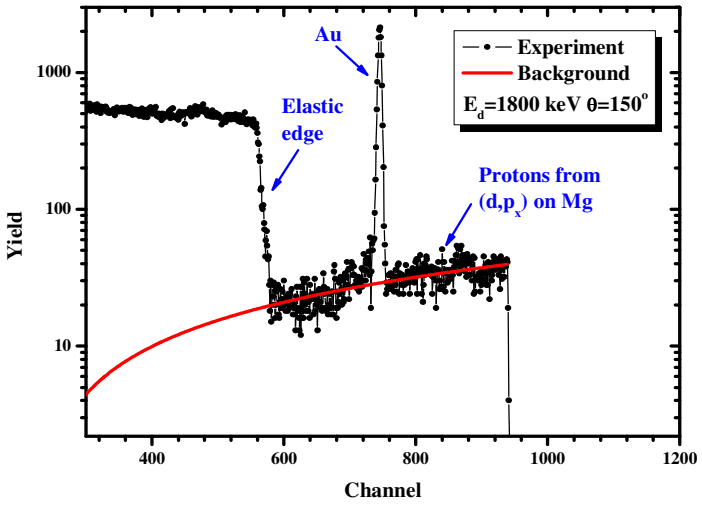

Figure 4.12: Typical background subtraction of the estimated background contribution induced by protons originating from (d,p_x) reactions on Mg isotopes prior to the benchmarking simulation process at E_d=1800 keV at 150°.

Following the background subtraction, the simulation was performed using again the SIMNRA code. The Au layer thickness was measured to be around 24μg/cm^2 using the *in situ* XRF spectrometer. The treatment of the target surface roughness was made following the methodology presented in [63]. As shown in Figure 4.13, for E_d=1750, 1850 and 1950 keV at 170°, the reproduction of the experimental spectra using the differential cross-section datasets determined in the present work was excellent and the observed deviations did not exceed 5% in all studied cases.

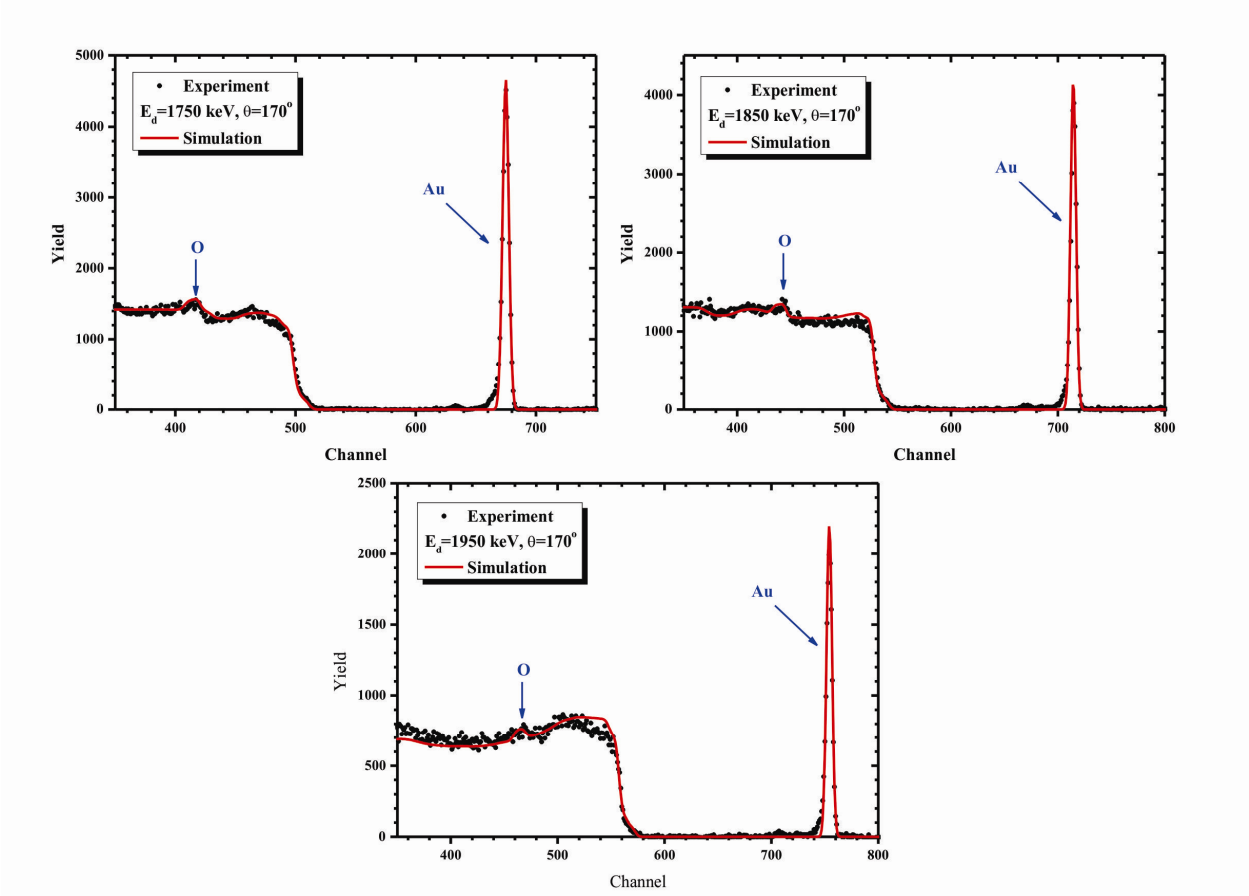

Figure 4.13: Benchmarking spectra for E_d=1750, 1850 and 1950 keV at 170° using a metallic magnesium target with a thin layer of gold, along with the corresponding simulations using the SIMNRA code [70].

4.7 Benchmarking on the ^{nat}B(p,p) cross section

Boron is widely used not only in the semiconductor industry as dopant/impurity in silicon and germanium substrates, but also in nuclear technology as the main reactor moderator. The quantification and depth profile of boron in all applications is thus critical but unfortunately the existing cross section data for the implementation of the IBA techniques in the field is rather discouraging, due to the significant discrepancies among the data.

The benchmarking of the ^{nat}B(p,p) reaction data is however impeded by the yield contribution of (p,α) reactions on boron isotopes, which lies under the thick target spectra acquired, as plotted in the following Figure 4.14 concerning the present case of a boron pellet with a thin gold layer on top used as target. This contaminant contribution ranges up to 15 % for beam energies reaching 3 MeV. The procedure of benchmarking becomes thereby more complicated, since one has to take into account the contribution of all the reactions to the obtained yield, in order to validate the used cross sections for the corresponding simulations. In the case of known reactions, such as the contribution of small contaminants like carbon or oxygen on the surface of the target (see section 4.2.7) the problem can easily be treated, but for yield contributions over the whole range of the spectra with unknown and/or unvalidated reaction channels, the process gets far more complicated. Trying to simulate the underlying contaminant spectra, namely the (p,α) channels in the case of boron, one would induce huge uncertainties to the validation procedure.

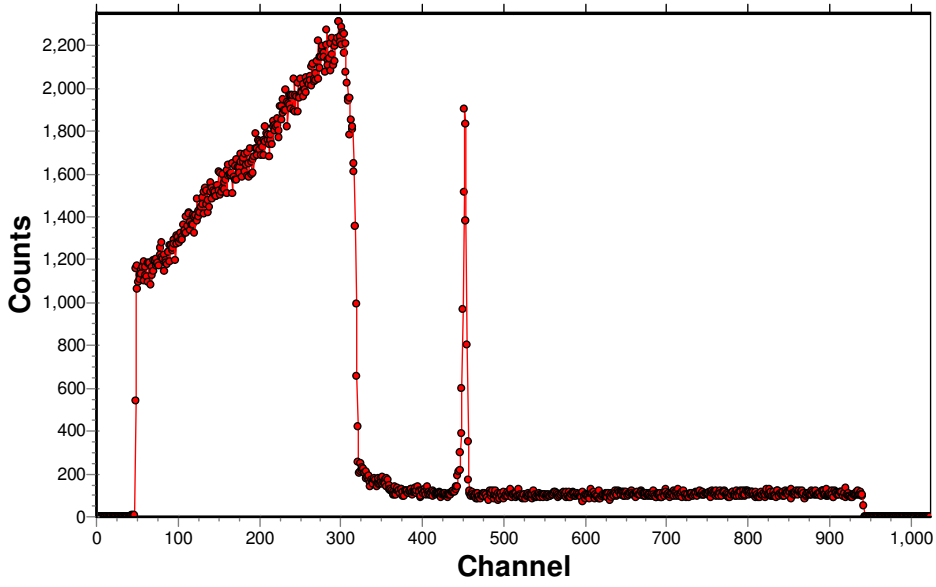

Figure 4.14: Experimental spectrum acquired at E_p=1500 keV at 170° using a boron pellet with a thin gold layer on top.

A different approach of benchmarking measurements is proposed here for such cases of background contribution by using ΔE/E telescopes, being implemented for the exact aforementioned case of the ^{nat}B(p,p) reaction. A brief description of the ΔE/E telescope technique (which has been widely used for other experimental purposes [87]), along with the corresponding electronics, is presented in the following paragraph. The attempt to systematically benchmark the elastic proton backscattering on ^{nat}B, using a ^{nat}B pellet with a thin layer of gold on top, in the energy range of 1500-3300 keV at 120° and 170° is subsequently discussed.

4.7.1 ΔE-E telescope

A ΔE/E telescope consists of two SSB detectors in a row, as seen in the following picture (Figure 4.15), that is of a very thin transmission one (ΔE) first, in which the detected particles do not deposit their full energy and a thick one (E) exactly behind it, in which they finally stop. The use of event by event acquisition implementing such telescopes, as briefly described below, can indeed help in resolving the complicated cases of benchmarking, such as ^{nat}B(p,p), where background contributions exist in the obtained spectra originating from (p,α) reactions. This can be achieved by separating the spectra of protons and alphas, exploiting the measurable different amount of the deposited energy in the thin (ΔE) detector of the two particles while crossing it. The used electronics for the event by event acquisition of 3 telescopes is schematically shown in Figure 4.16 that follows. The overall procedure involves the generation of a pulse gate in which all the signals are recorded, triggering on the E detectors, due to solid angle and noise reduction considerations.

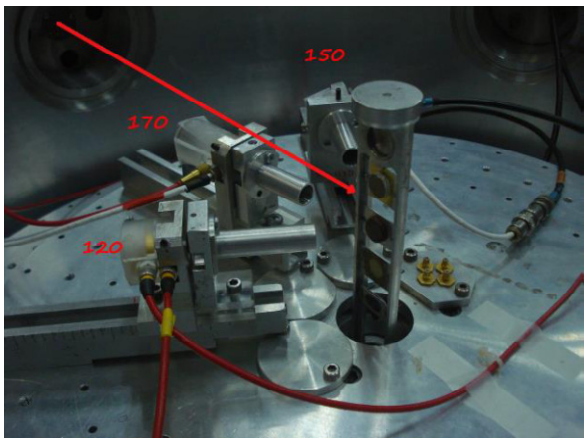

Figure 4.15: The scattering chamber containing 3 ΔE/E telescopes on the goniometric table. The arrow shows the course of the beam hitting the target.

Plotting the detected counts of a single telescope (ΔE and E), one gets the desired information, as seen in Figure 4.17, leading to the identification of the particles. One can afterwards treat the data as desired, namely project the studied particles (for example the lower "banana" shaped counts in Figure 4.17, corresponding to protons) to their energy in the E detector, or add the corresponding energies for all particles deposited in both detectors, obtaining eventually all the information, when both ΔE and E detectors can be accurately calibrated and noise issues (which are quite common for thin detectors) are resolved.

This method can be applied in all cases, where the energy loss of the different kind of particles crossing the ΔE detector is indeed significant. For example, the separation of low-energy deuterons and protons cannot be achieved with this method (since a quite thick ΔE detector is required).

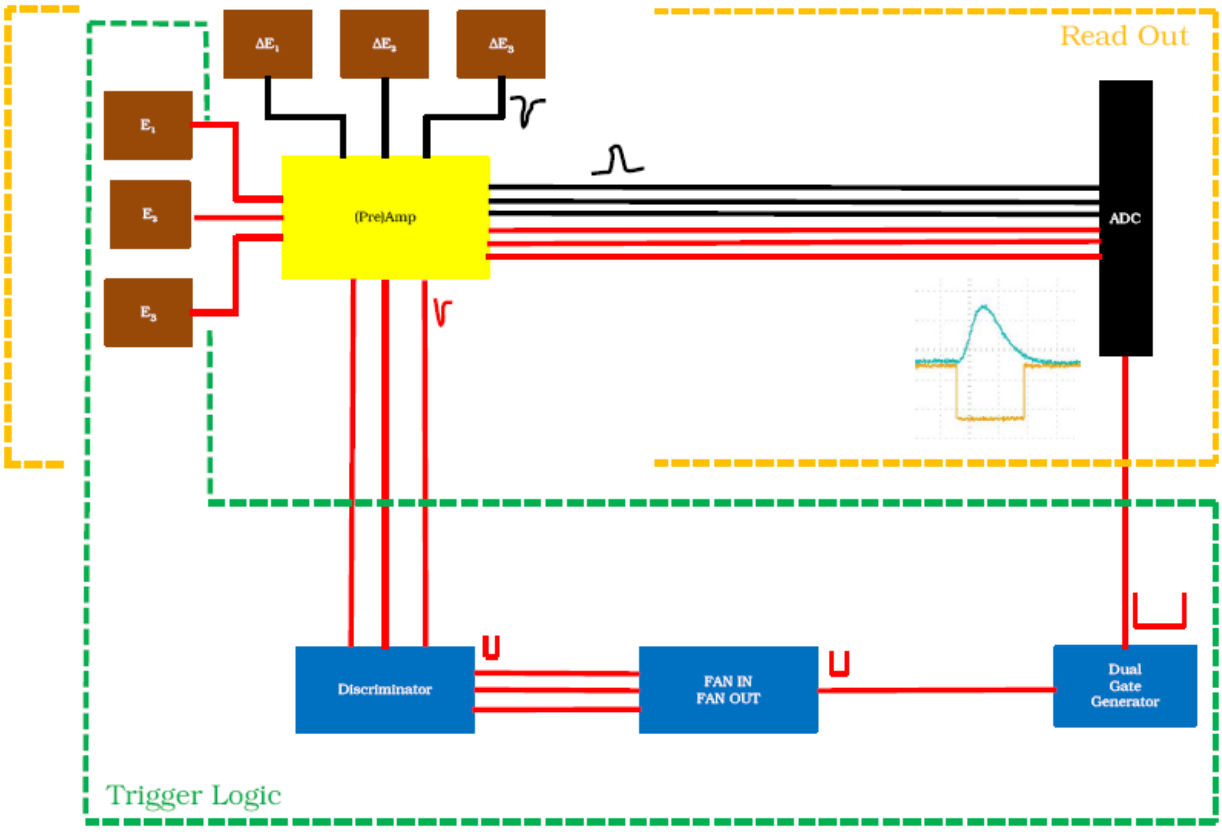

Figure 4.16: Schematics of the used electronics for the event by event acquisition.

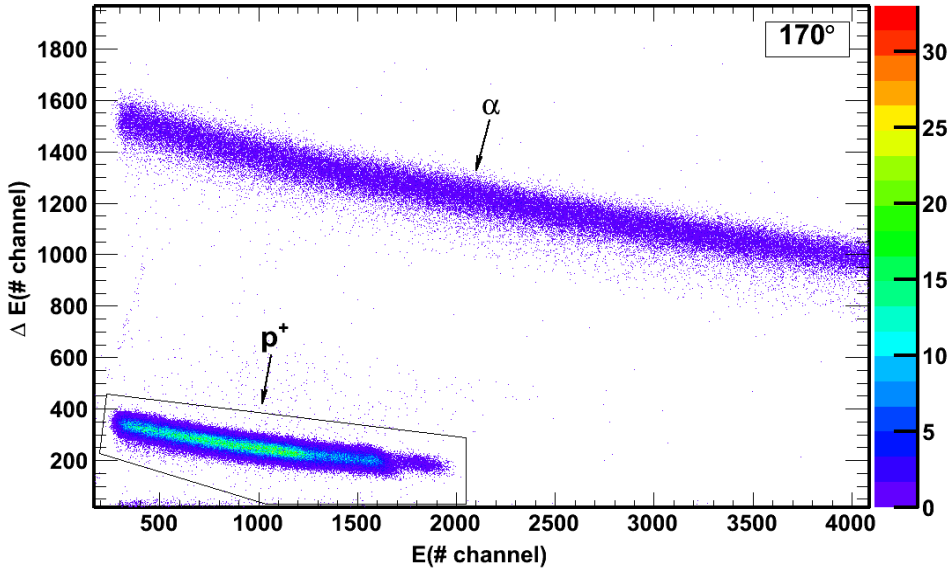

Figure 4.17: Particle identification plotting the detected counts with respect to the deposited energy in ΔE and E detector, presenting the so-called "bananas".

4.7.2 Results and Discussion

Boron backscattering was studied in the present work, both by using standard NIM electronics and by implementing the ΔE/E technique up to 3.3 MeV. With the use of a ΔE/E telescope, the detected protons and alphas are eventually separated as described above, thus enabling two different ways to further analyze the data. The first one is to directly perform simulations of the protons acquired by implementing the telescope and the second one to study the acquired alphas instead, which constitute the background contribution and continue from there, depending on the case. Both techniques were investigated in the present work, concerning the case of ^{nat}B(p,p) benchmarking as analyzed below.

Using the ΔE/E telescopes and after projecting the proton counts to the deposited energy in the thick E detector, the obtained proton yield was free of background alpha contributions. The subsequent validation step involved the actual simulation of the acquired proton spectra being evidently of different kind than the simulations described in the previous benchmarking experiments (4.5-4.6), due to the implemented thin ΔE detectors. Each simulation in this case depended on the energy loss and straggling in the corresponding thin ΔE detector. In order to reproduce these effects in the simulated spectra, a proper silicon foil, namely of the same thickness of the corresponding thin detector, was used as absorber foil in all simulations. The nominal thickness of the ΔE detectors used was checked experimentally and was eventually

determined using a triple alpha source. The procedure followed was rather simple and involved the detection of the emitted alpha particles in a thick detector with and without the unknown thin detector in front of it. This method led to its thickness determination with an accuracy of the order of 4% (uncertainty in the stopping power [5]).

The study on the other hand of the detected alphas, as shown in Figure 4.18, revealed a linear dependence with energy, which enabled a linear regression rule to be applied. Thereby their contribution to the obtained yield when using standard NIM electronics could be subtracted, as demonstrated in Figure 4.19, similarly to the magnesium case presented in the previous section (4.6). This way the simulation procedure and thereby the validation process is simplified, as it does not depend on any straggling function (other than the one in the studied material).

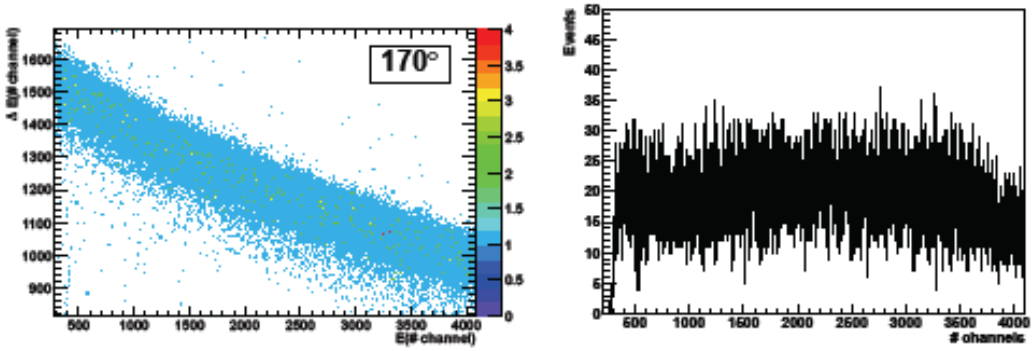

Figure 4.18: The alpha-particle identification (on the left) for proton beam energy at 1500 keV using the ΔE/E telescope at 170° and their projection to the deposited energy in the E detector (on the right).

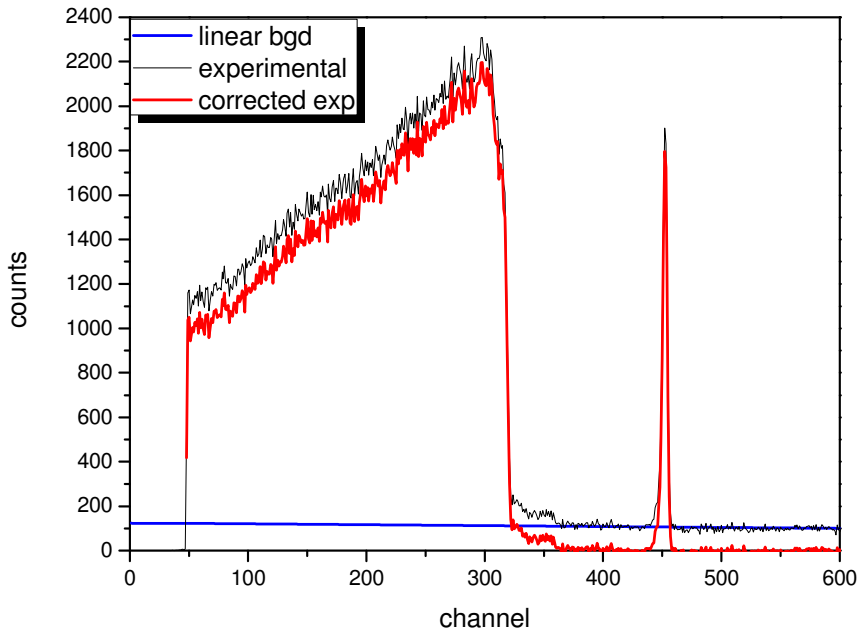

Figure 4.19: Linear background subtraction resulting to the corrected spectrum in red at 1500 keV at 170°.

Both techniques present distinct inherent disadvantages. The former strongly depends on the accuracy of the straggling function and the thickness of the ΔE detector which acts as an absorber foil, while the latter ignores any possible variations in the underlying alpha background. Providing also that there still seem to be discrepancies between both implemented techniques for the same energy window, the complete analysis will be the subject of a complementary future study.

Another problem which should be noted here is the determination of the actual thickness of the thin gold layer used for the normalization of the charge (QΩ factor). Using the XRF technique, one can obtain a very poor accuracy of ~15%, because of the light substrate (boron). Therefore the results of this technique were also tested implementing a MgB_2 pellet as target at a beam energy of 1500 keV at 170°, where the proton backscattering on magnesium can be considered as reliable (evaluated and validated [50, 25]), to give a reference point for Boron yield at that energy and angle.

4.8 Benchmarking on the proton backscattering on ^{23}Na, ^{31}P, ^{nat}S and ^{nat}Si

The measurements for the benchmarking on the proton backscattering on ^{23}Na, ^{31}P, ^{nat}S and ^{nat}Si were performed in one comprehensive run using the 2 MV Tandetron Accelerator at the Ion Beam Centre at the University of Surrey, described in 2.1 section. Spectra of elastically backscattered protons from ^{23}Na, ^{31}P, ^{nat}S and ^{nat}Si, using uniform thick targets were systematically measured and simulated as described in sections 4.1 and 4.2 in the energy range 1-3.5 MeV, **in steps of 250 keV**, at 120.6°, 148.8° and 173.5° with an uncertainty of 0.1°. The results of this extensive/ benchmarking run are presented in the following paragraphs for each elastic backscattering and concern the analytical validation of the studied cross-section datasets, as thoroughly described in sections 4.1 and 4.2 being also treated for the roughness effect (4.3). It should be noted here that contributions of contaminant yields originating from elastic backscattering on surface carbon and oxygen were negligible and were thus not included in the simulations (to avoid further complications and uncertainty factors). A complementary uncertainty assessment is also described where needed, with respect to the already presented one in section 4.4.

The figures, along with the numerical results in the Tables that follow, concern the comparison of the near-surface experimental yield to the simulated one and present analytical results of the corresponding validation of the studied evaluated cross-section data both qualitatively (in Figures, e.g. for resonance yield) and quantitatively. The extension of the evaluations is moreover enabled, both with the use of the acquired experimental thick target spectra (see the beginning of this chapter concerning the feedback process in the evaluation procedure) and by validating experimental cross-section datasets in the absence of evaluated ones (cases of ^{23}Na(p,p) and ^{31}P(p,p)).

The targets used were high-purity (>99.99%), highly pressurized tablets of NaBr and MoS_2 in the case of ^{23}Na and ^{nat}S, and polished crystalline GaP and Silicon wafers in the case of ^{31}P and ^{nat}Si respectively. A thin layer of gold was evaporated on top of all the used targets in order to protect them from corrosion and for charged/solid angle normalization purposes, according to the followed methodology. It should be mentioned here, that this is the case of the performed GVM machine calibration, illustrated in section 4.2.1, which showed the excellent energy linearity (see Figure 4.3).

4.8.1 The ^{nat}S(p,p) case

For the ^{nat}S(p,p) backscattering evaluated cross-section data range from 1500 keV up to 3500 keV [25], as plotted in Figure 4.20 for the backscattering angle at 148.8°. The benchmarking results of the present work, using a MoS_2 pellet with a thin layer of gold on top, as target, concerning these data, are shown in Figures 4.21 and 4.22 and in Table 4.1 in numerical form. It is thereby shown that the simulated spectra, using the evaluated cross sections reproduce the experimental ones in an excellent way (within 1-8%) for all the backward angles studied, up to 3287 keV, which was the last benchmark point, where the simulation and the experiment perfectly agree. Cross sections for all intermediate backward detection angles, typically used for EBS measurements, are thereby also validated. In Figures 4.21 and 4.22, it is seen that using the evaluated results from SigmaCalc 1.6 for the ^{nat}S(p,p) backscattering, there are discrepancies between the experiment and the simulation around 3.5 MeV. Following the benchmarking results of the present work, the evaluation was revised (SigmaCalc 2.0) [88, 25], as seen in Figure 4.23, leading to a very good reproduction of the experimental spectra, as illustrated in Figure 4.24. A comparison between the cross sections obtained using the previous and the current SigmaCalc versions (1.6 and 2.0 respectively) is presented in Figure 4.23.

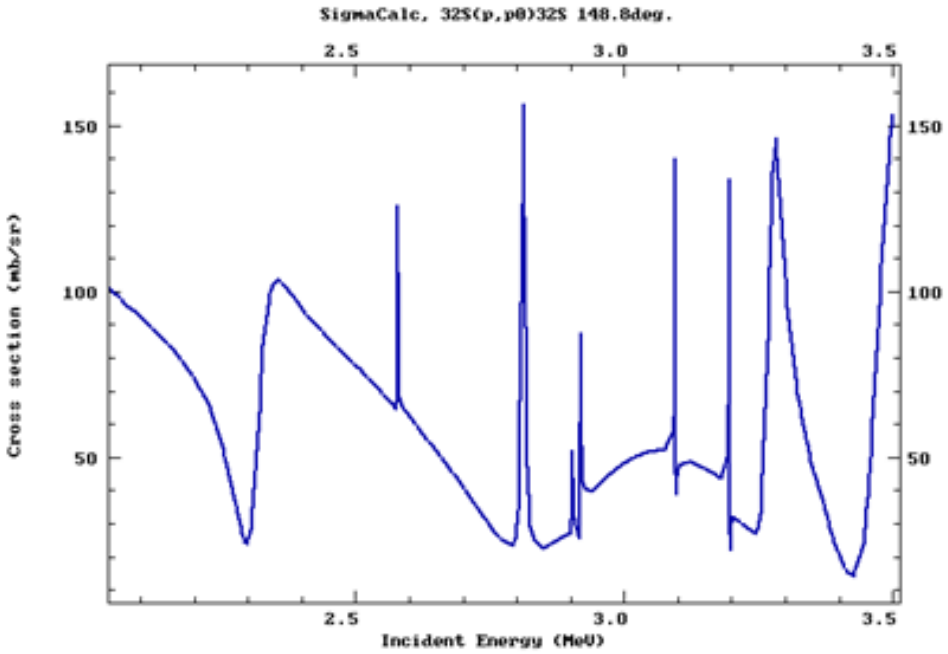

Figure 4.20: Evaluated cross-section data for ^{32}S(p,p) reaction at 148.8° [25].

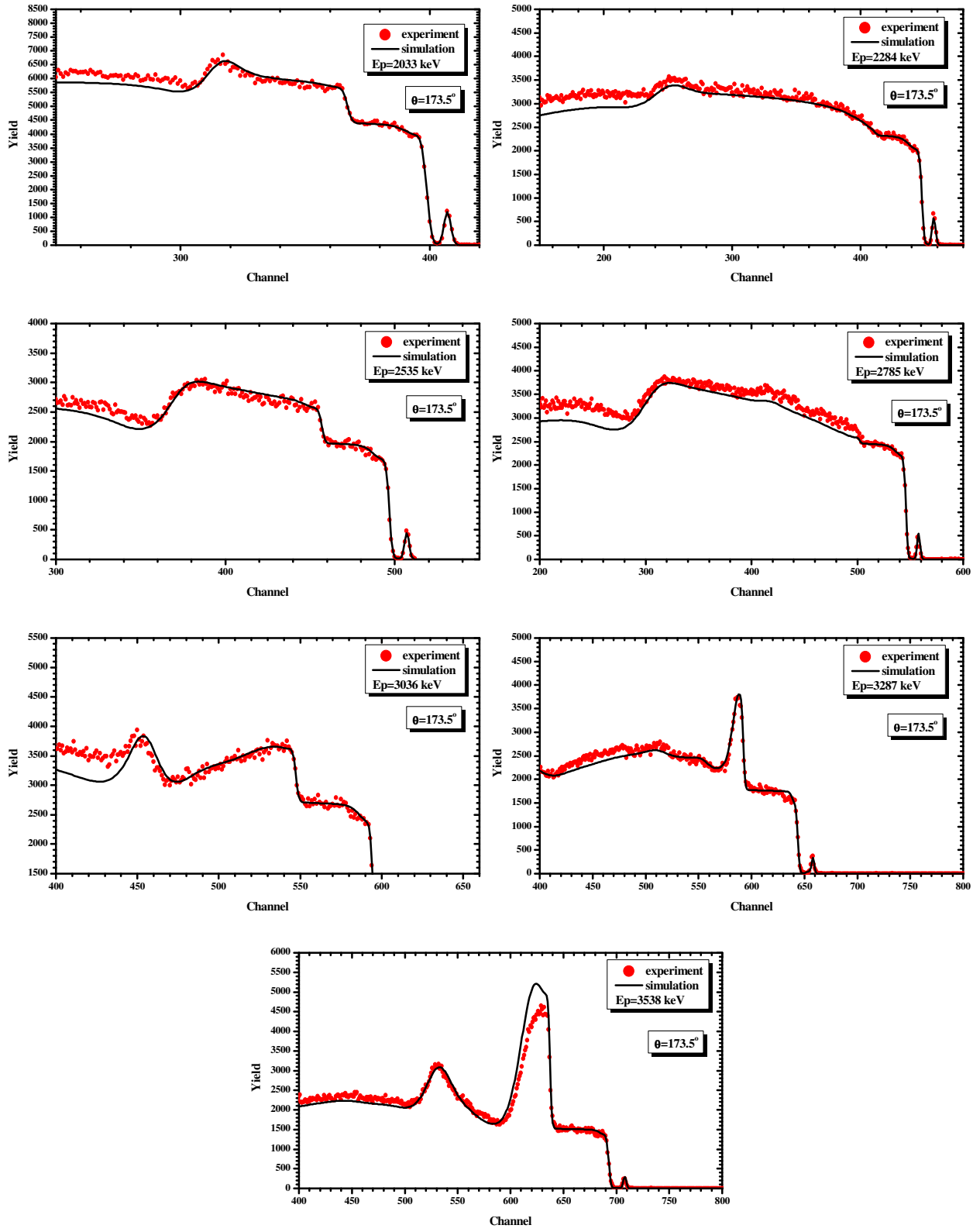

Figure 4.21: Benchmarking spectra at 173.5° on MoS_2 with a thin gold layer on top, along with the corresponding simulations using the DataFurnace code [82].

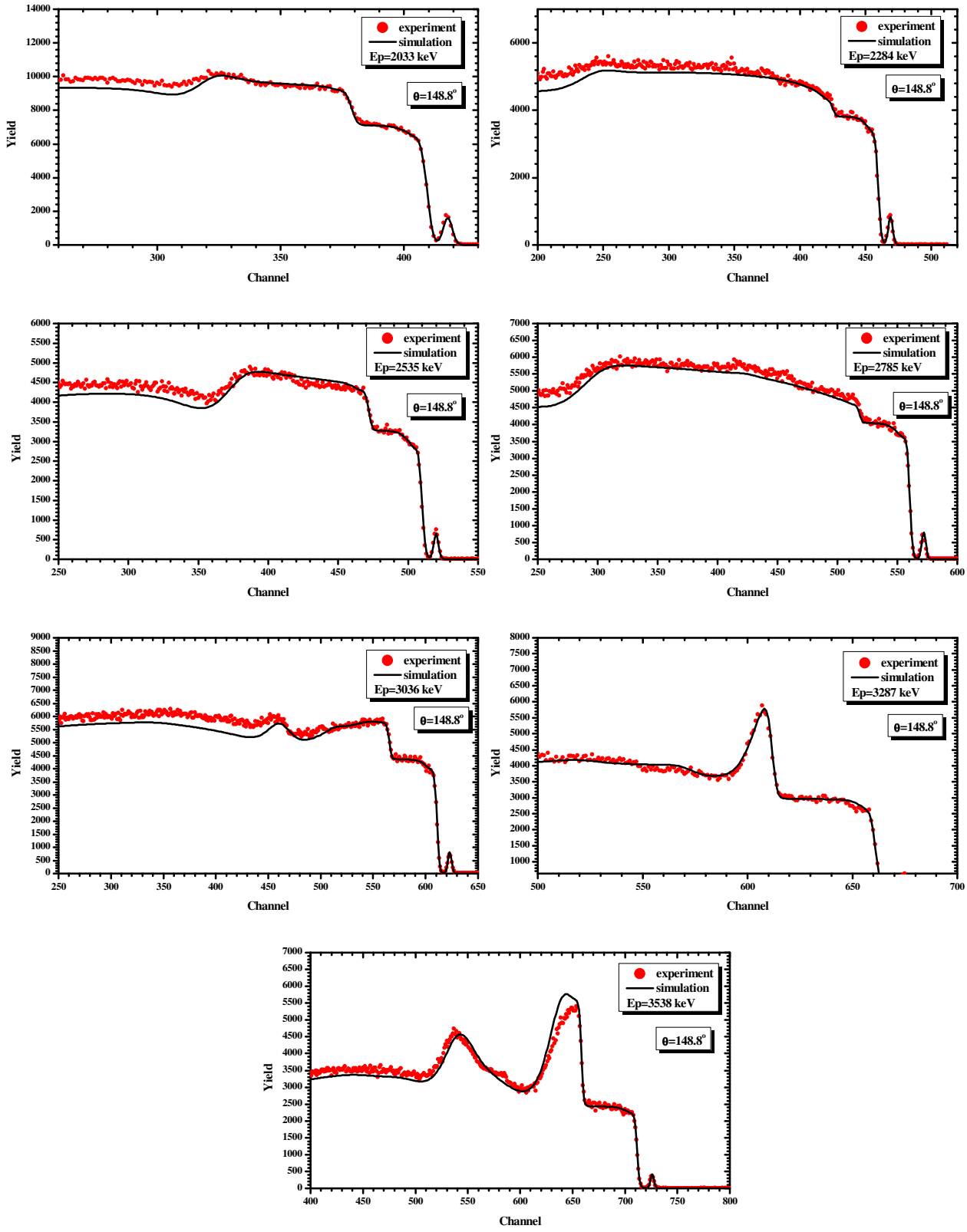

Figure 4.22: Benchmarking spectra at 148.8° on MoS_2 with a thin gold layer on top, along with the corresponding simulations using the DataFurnace code [82].

Table 4.1: Differences between the integrated experimental and simulated yields.

Spectrum Energy (keV) / Angle	148.8°	173.5°
1788-2033	+2%	+5%
2039-2284	-5%	+8%
2290-2535	+8%	+8%
2791-3036	+1%	+3%
3042-3287	+4%	+6%

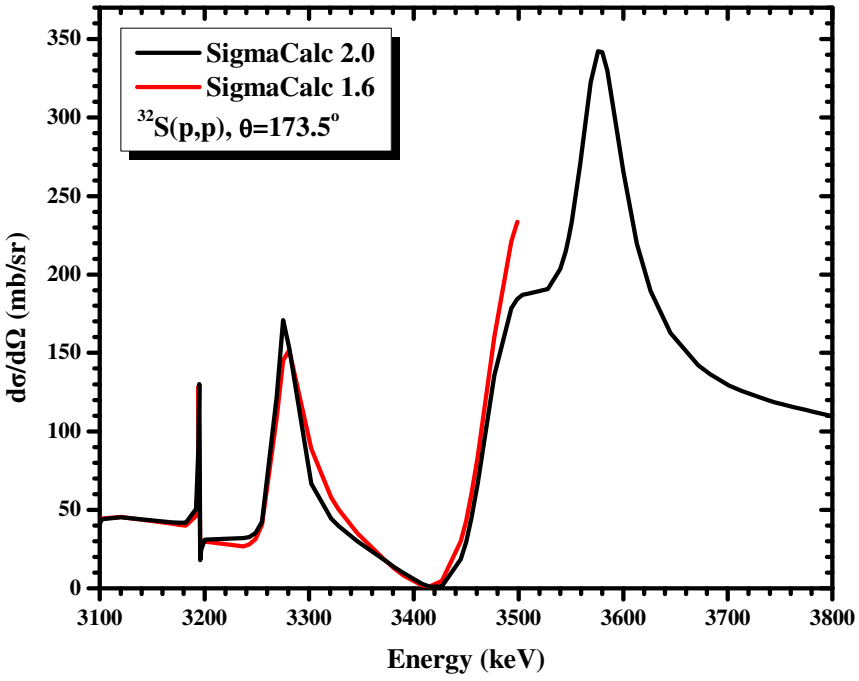

Figure 4.23: Evaluated cross-section data for ^{32}S(p,p) reaction at 173.5° [25].

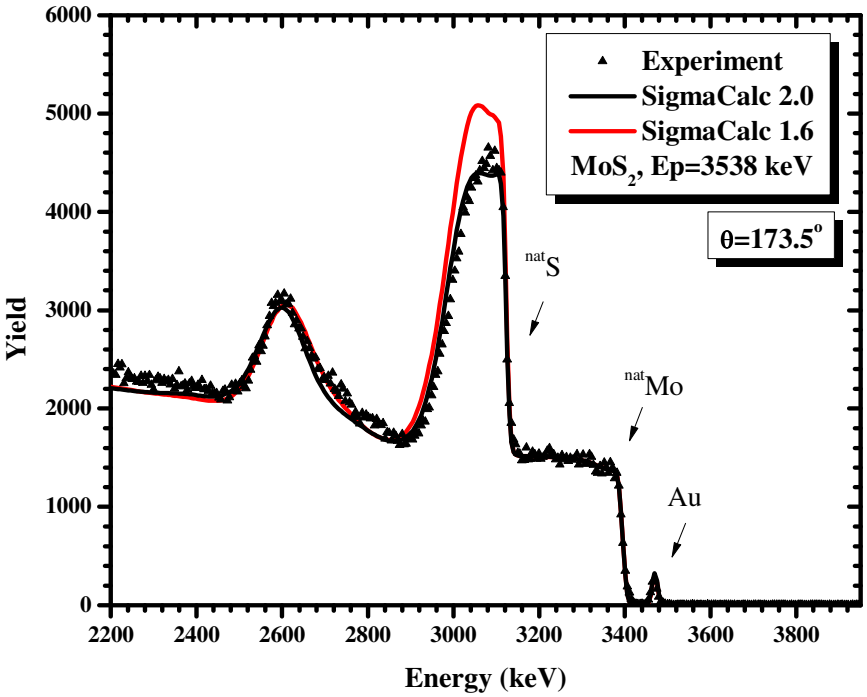

Figure 4.24: Benchmarking results using both versions of evaluated data.

4.8.1.1 Benchmarking database

The obtained results for the benchmarking on the proton backscattering on ^{nat}S can be demonstrated online in SigmaCalc website [25]. There exists a full database with all the relevant acquired thick target spectra (along with the corresponding information and characteristics) and one can directly perform simulations using any existing (relevant) cross-section dataset online, in order to validate the specific data, as illustrated in the following Figure 4.25.

The most significant feature of this initial benchmark database is that the benchmarked cross-section datasets are now "tagged" giving immediate information about their reliability to all the users. Moreover, there is the ability to validate any other relevant cross-section dataset, thus directly (online) checking their reliability before use.

sigmacalc.iate.obninsk.ru/cgi-bin/select_run.pl

$^{32}S(p,p_0)^{32}S$

The experimental data presented in the table is an excerpt from IBANDL database maintained by the IAEA.

Angle	Energy(keV)	Reference	Benchmark	File	Plot
170	1400-3600	Evaluated cross-section Recalculate	Benchmark	File	
170°	1500-2690	E.Rauhala, M.Luomajarvi. Nucl.Instr.& Meth. v.B33 (1988) 628	Benchmark	File	
167.4°	1420-3950	Olness, J.W., Haeberli, W. and Lewis, H.W. Phys. Rev. 112 (1958) 1702.	Benchmark	File	
155°	1500-2690	E.Rauhala, M.Luomajarvi. Nucl.Instr.& Meth. v.B33 (1988) 628	Benchmark	File	
155°	1840-2700	A. Li-Scholz et al. Appl. Phys. Lett. 56 (1990) 2696	Benchmark	File	

Cross-section from SigmaCalc at 170°, E_{max}=3600 keV

Benchmark spectra

No.	Angle	Energy(keV)	Target	Reference	File	Plot
1	173.5	3538	MoS_2	V.Paneta et al. Nucl. Instr. and Meth. B328 (2014) 1.	File	Plot
2	173.5	3287	MoS_2	V.Paneta et al. Nucl. Instr. and Meth. B328 (2014) 1.	File	Plot
3	173.5	3036	MoS_2	V.Paneta et al. Nucl. Instr. and Meth. B328 (2014) 1.	File	Plot
4	173.5	2785	MoS_2	V.Paneta et al. Nucl. Instr. and Meth. B328 (2014) 1.	File	Plot
5	173.5	2535	MoS_2	V.Paneta et al. Nucl. Instr. and Meth. B328 (2014) 1.	File	Plot
6	173.5	2284	MoS_2	V.Paneta et al. Nucl. Instr. and Meth. B328 (2014) 1.	File	Plot
7	173.5	2033	MoS_2	V.Paneta et al. Nucl. Instr. and Meth. B328 (2014) 1.	File	Plot
8	173.5	1782	MoS_2	V.Paneta et al. Nucl. Instr. and Meth. B328 (2014) 1.	File	Plot
9	173.5	1531	MoS_2	V.Paneta et al. Nucl. Instr. and Meth. B328 (2014) 1.	File	Plot
10	173.5	1230	MoS_2	V.Paneta et al. Nucl. Instr. and Meth. B328 (2014) 1.	File	Plot
11	148.8	3538	MoS_2	V.Paneta et al. Nucl. Instr. and Meth. B328 (2014) 1.	File	Plot
12	148.8	3287	MoS_2	V.Paneta et al. Nucl. Instr. and Meth. B328 (2014) 1.	File	Plot

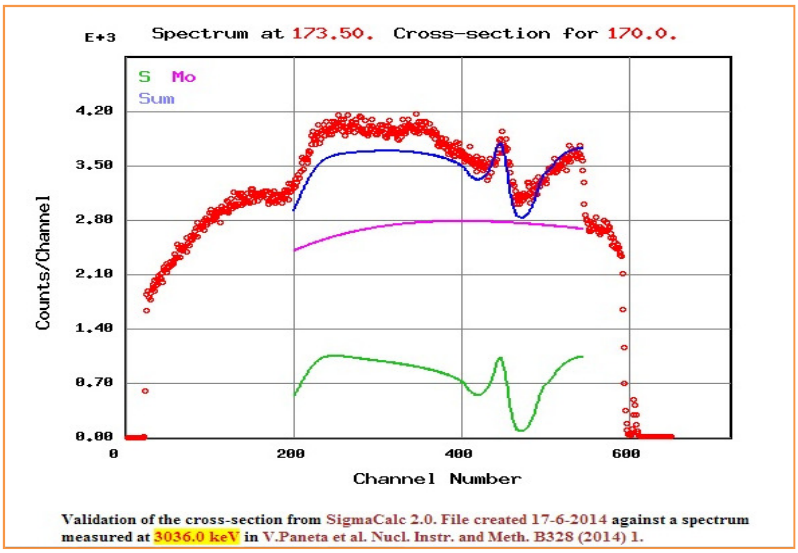

Figure 4.25: The existing cross-section datasets [23], along with the available benchmarking spectra for proton backscattering on ^{nat}S at 170° and the corresponding graph of the highlighted case [25].

4.8.2 The ^{23}Na(p,p) case

The existing evaluation in the case of ^{23}Na(p,p) covers a limited energy range, up to 1500 keV, as plotted in Figure 4.26. Concerning the ^{23}Na(p,p) backscattering using a NaBr pellet with a thin layer of gold evaporated on top, one can see in Figures 4.27 the benchmarks of the present study, using the evaluated cross-section data for the simulations. At such low energies, as it is shown in Figures 4.27, the spectra are dominated by the signal of the heaviest element in the compound target, which is Br. The benchmarking at higher energies was performed using the data of Caciolli *et al.*[89] at 150°, plotted in Figure 4.28. The results of this validation procedure are shown in Figures 4.29, while all the corresponding numerical results are seen in Table 4.2.

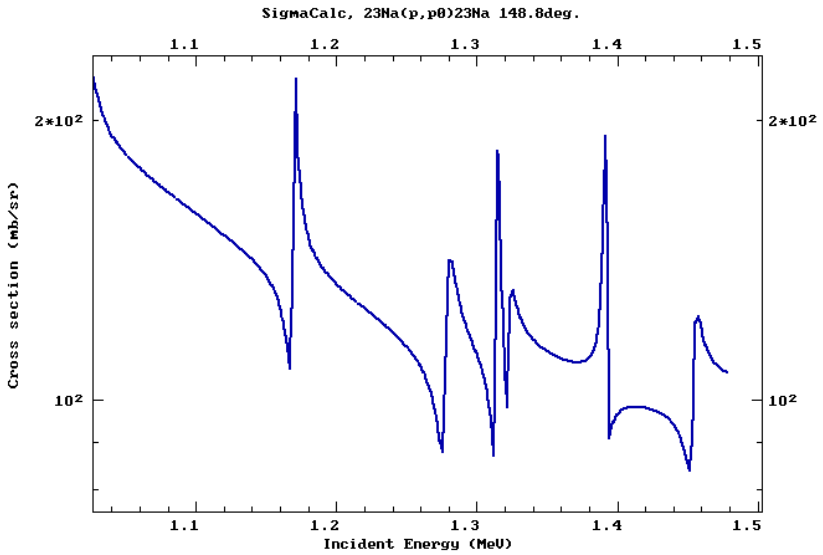

Figure 4.26: Evaluated cross-section data for ^{23}Na(p,p) reaction at 148.8° [25].

Concerning the validation of the evaluated data (Figures 4.27) one can observe that despite the resulting poor statistics (5% uncertainty in the worst case), originating from the subtraction of the large Rutherford Br signal from the total experimental one (over the whole integrated region corresponding to 250 keV from the surface), the simulation seems to reproduce the experimental spectra quite well for all the studied angles and the evaluation is thus in principle validated. At higher energies, where the only existing dataset relevant to the detection angles studied in the present work, is the one of Caciolli *et al.* [89] at 150°, covering the energy range between 2210 and 5200 keV, the Rutherford cross section for ^{nat}Br(p,p) is reduced and the sodium signal is more pronounced. The simulations using these experimentally determined differential cross sections, as shown in Figures 4.29, are in excellent agreement with the experimental spectra within the total experimental uncertainty (4%) except for the low energy case (at 2284 keV) where the agreement is within 7%. This dataset is thus validated and can be recommended for EBS analytical purposes. Moreover, it can be used for the extension of the evaluation to higher energies. As far as ^{nat}Br(p,p) is concerned, the results from the present work at 148.8° up to 3.6 MeV showed no significant deviation from the Rutherford formula as reported in [37] at 150°.

Table 4.2: Differences between the integrated experimental and simulated yields.

Spectrum Energy (keV) / Angle	**120.6°**	**148.8°**	**173.5°**
980-1230	-2%	-4%	-20%
1281-1531	+11%	+5%	-11%
2140-2284*		-7%	
2535-2785*		-3%	
3037-3287*		-1%	
3288-3538*		-5%	

***** Using data from [89]

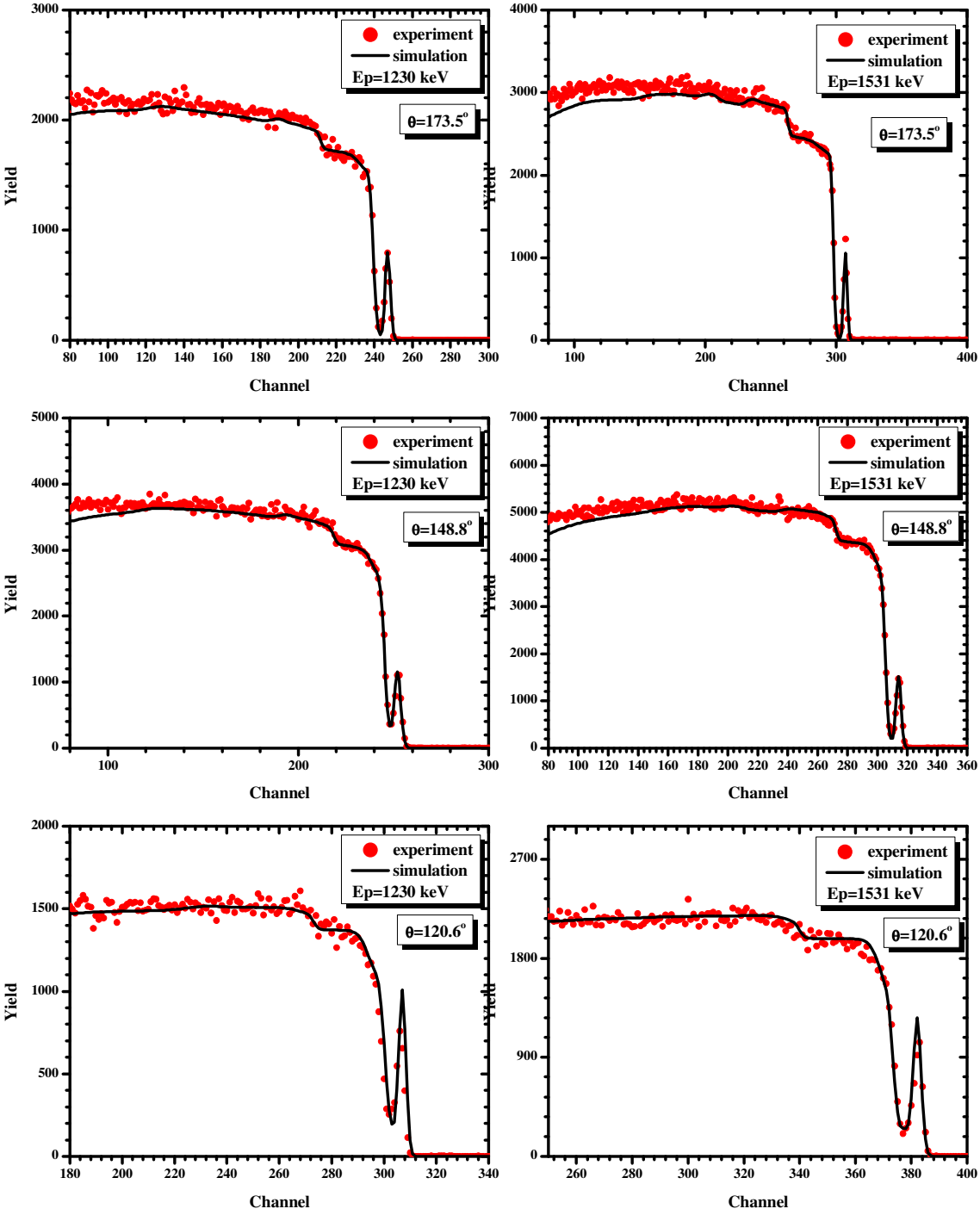

Figure 4.27: Benchmarking spectra on a NaBr pellet with a thin gold layer on top, along with the corresponding simulations using the DataFurnace code [82].

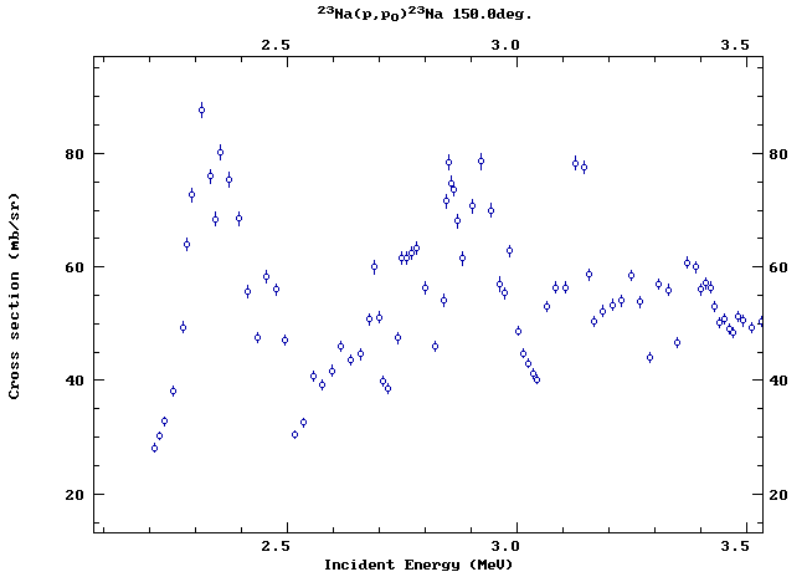

Figure 4.28: Experimental cross-section data for ^{23}Na(p,p) reaction at 150° by Caciolli et al. [89].

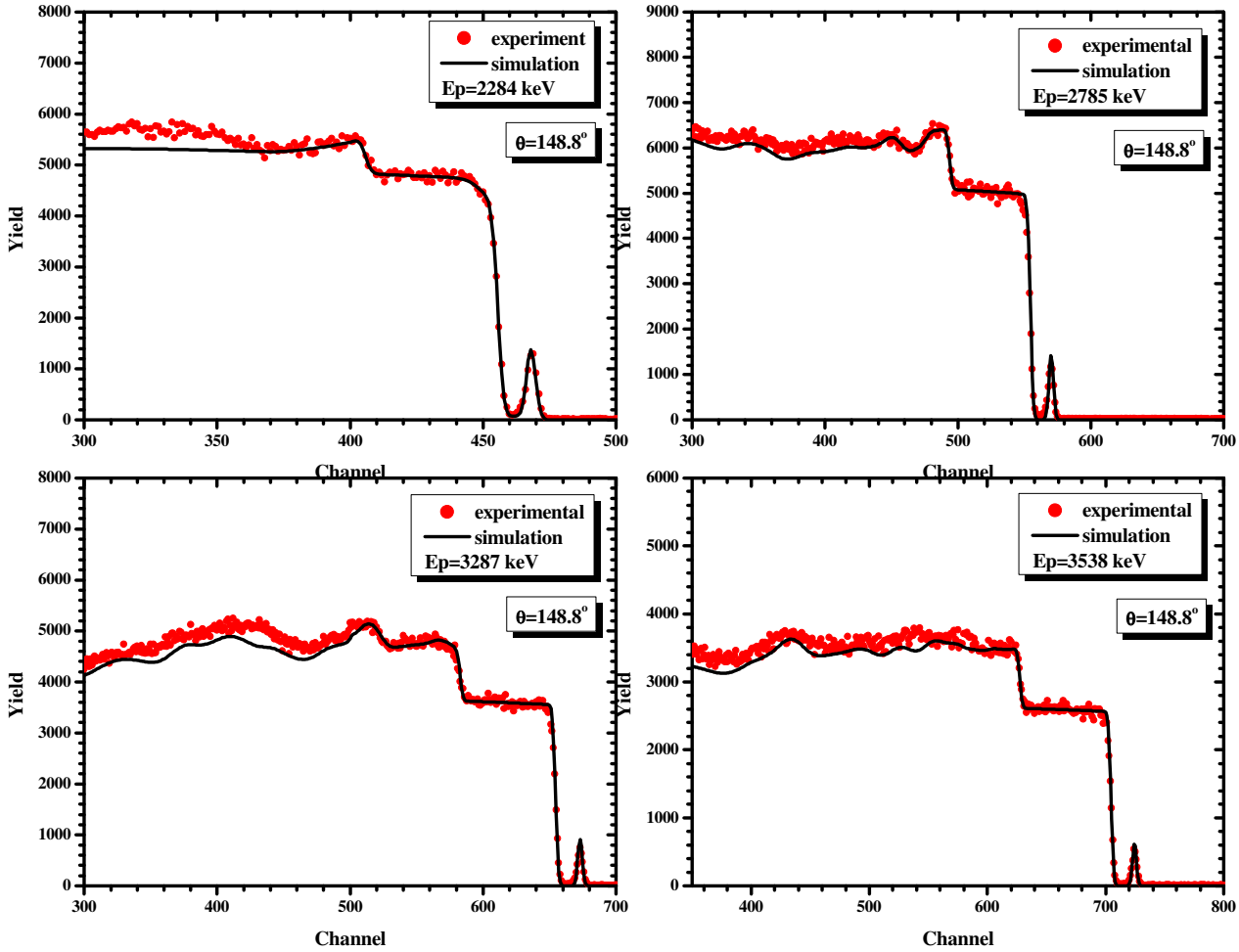

Figure 4.29: Benchmarking spectra on NaBr pellet with a thin gold layer on top, along with the corresponding simulations using the data of Caciolli et al. [89], with the DataFurnace code [82].

4.8.3 The ^{31}P(p,p) case

The evaluated cross sections for the ^{31}P(p,p) backscattering exist up to 2000 keV [25] showing a rather complicated structure with narrow resonances, as seen in Figure 4.30. The results of the corresponding benchmarking using a GaP wafer with a thin layer of gold on top as target, are presented in Figures 4.31 and 4.32, whereas numerical results concerning the comparison between the experiment and the simulations are seen in Table 4.3.

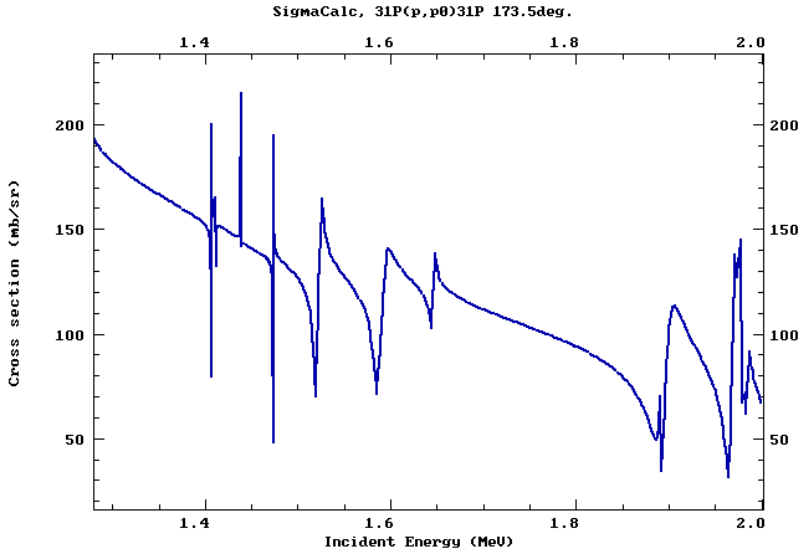

Figure 4.30: Evaluated cross-section data for ^{31}P(p,p) reaction at 173.5° [25]

In Figures 4.31, concerning the energy range up to 1782keV, the agreement between the simulations, using the evaluated data from SigmaCalc 1.6, and the experimental spectra is good (within 3-4%, over a small energy window, as seen in Table 4.3). At higher energies the only existing experimental dataset, related to the detection angles studied in the present work, is the one by Karadzhev *et al.* [90] up to 3500 keV for the ^{31}P(p,p) backscattering at 150°, plotted in Figure 4.33. The benchmarking results at ~2000 keV using both the evaluated data and the ones by [90] are shown in Figures 4.32. The results shown in Figures 4.34 were produced using only the data of [90] up to ~3.5 MeV. It can be seen in these figures (4.34) that there are serious discrepancies between the simulated and measured spectra (actually it seems that the data of Karadzhev *et al.* are systematically underestimated). This dataset cannot thus be recommended for analytical purposes, despite the fact that there seems to be a clear qualitative agreement. Consequently, it cannot be directly incorporated in the evaluation procedure at higher energies and therefore further experimental studies, in addition to the already existing ones (at different backward angles and/or energy range [91] and [92]), are needed in this case.

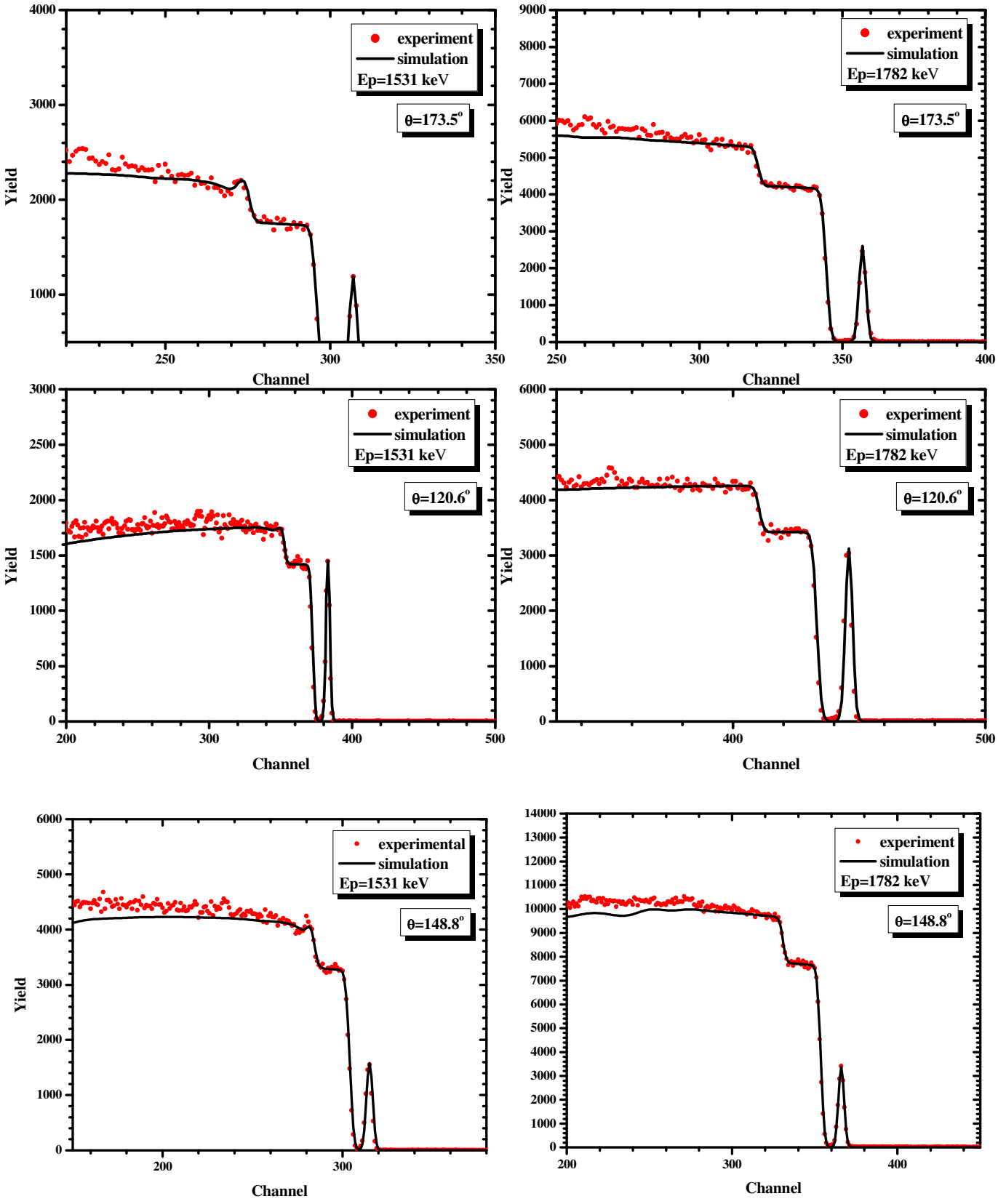

Figure 4.31: Benchmarking spectra on GaP wafer with a thin gold layer on top, along with the corresponding simulations using the DataFurnace code [82].

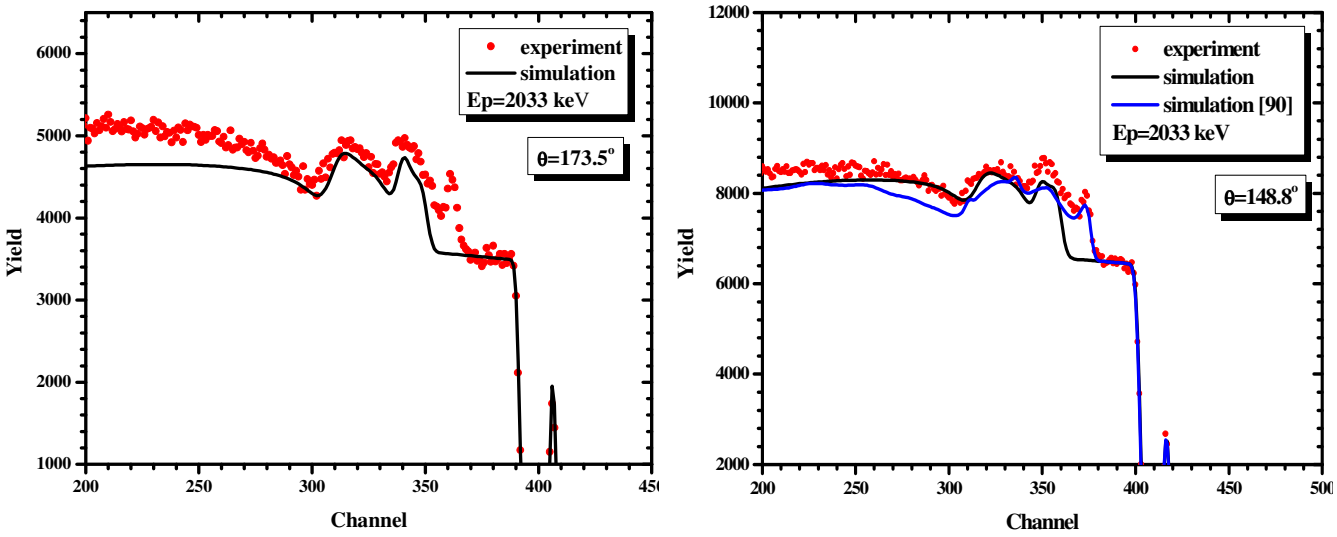

Figure 4.32: Benchmarking spectra on GaP wafer with a thin gold layer on top, along with the corresponding simulations using the DataFurnace code [82].

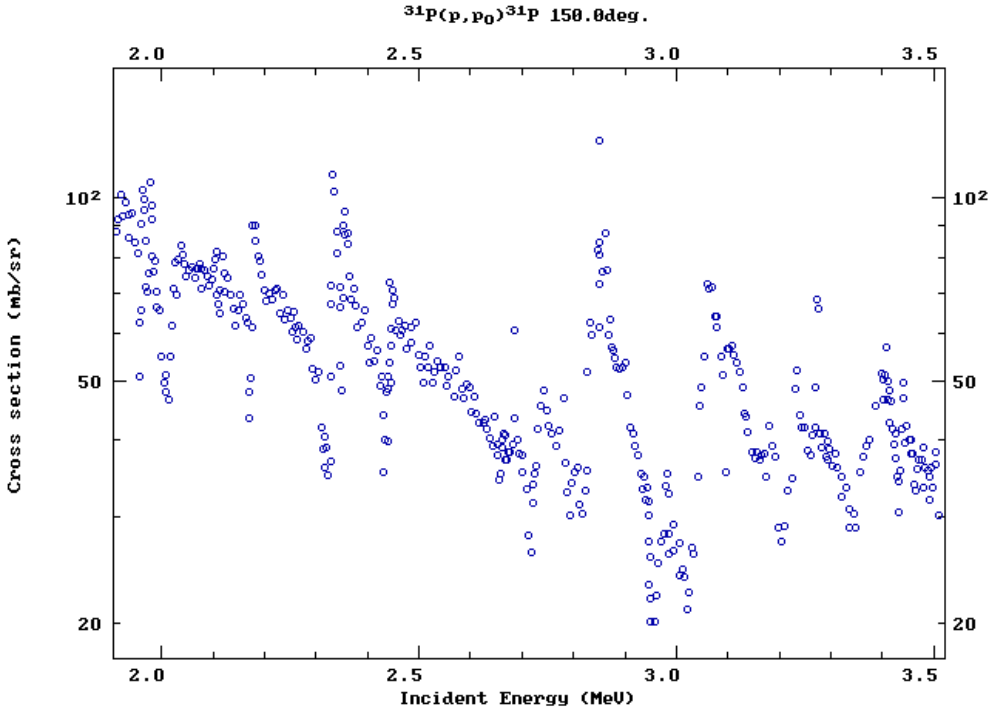

Figure 4.33: Experimental cross-section data for ^{31}P(p,p) reaction at 150° by Karadzhev et al. [90].

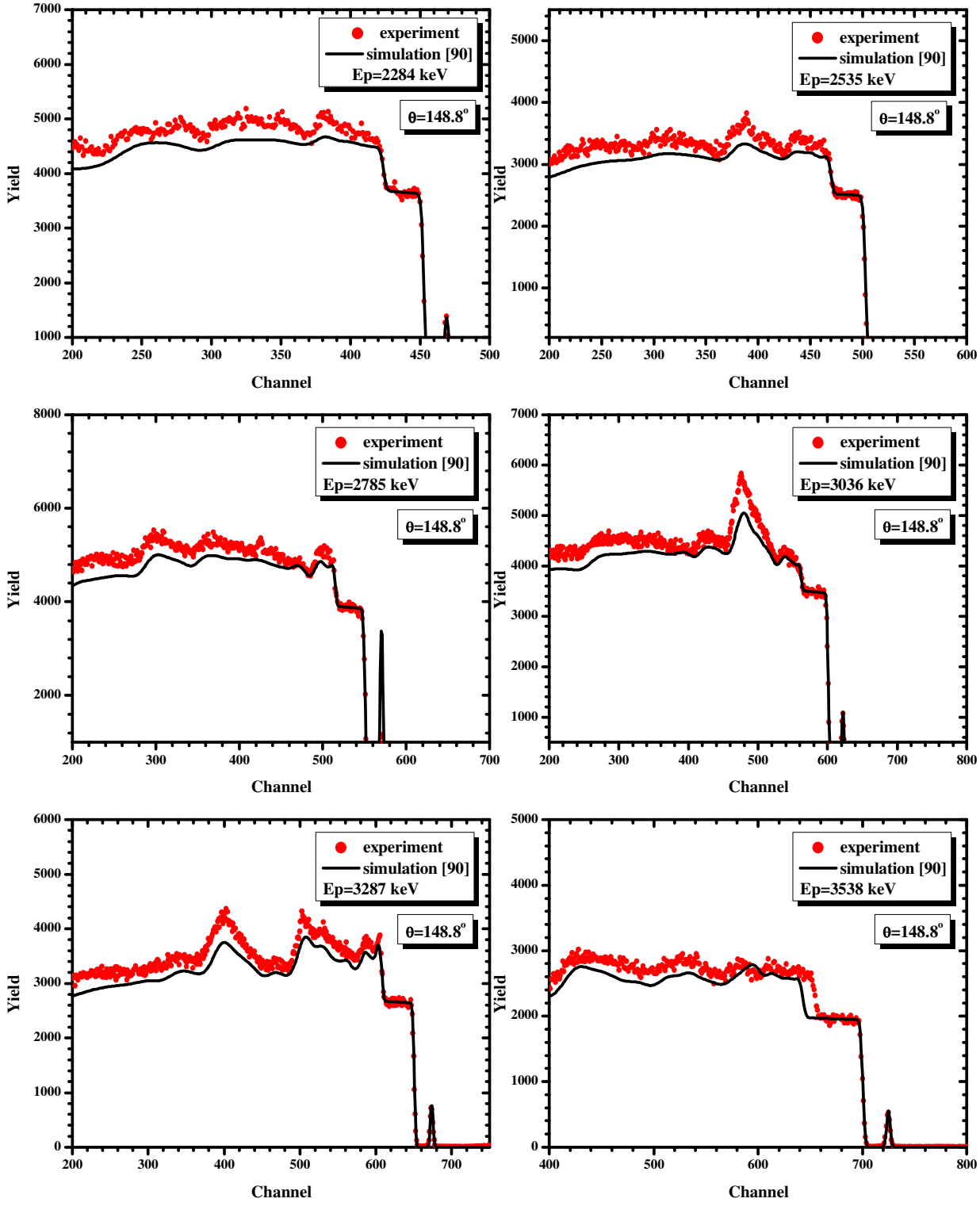

Figure 4.34: Benchmarking spectra on GaP wafer with a thin gold layer on top, along with the corresponding simulations using the data of [90] with the DataFurnace code [82].

Table 4.3: Differences between the integrated experimental and simulated yields.

Spectrum Energy (keV) / Angle	120.6°	148.8°	173.5°
1369-1531	-2%	-4%	-3%
1620-1782	-1%	-3%	-3%
1788-2033*		-19%	
2039-2284*		-21%	
2290-2535*		-22%	
2540-2785*		-16%	
2791-3036*		-15%	
3042-3287*		-20%	

* Using data from [90]

Following the benchmarking results of the present work, as in the case of natS(p,p), the revised [88] SigmaCalc 2.0 datasets (Figure 4.35) led to a very good reproduction of the experimental spectra, as shown in Figure 4.36. A comparison between the two versions of SigmaCalc is presented in Figure 4.35, showing the resonant structure and the extension of the evaluation up to 2.1 MeV [25].

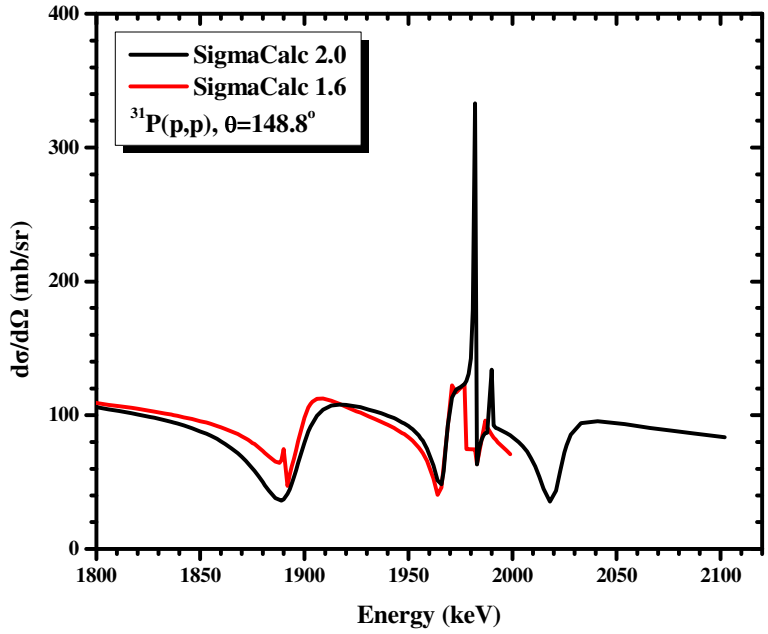

Figure 4.35: Evaluated cross-section data for ^{31}P(p,p) reaction at 148.8° [25]

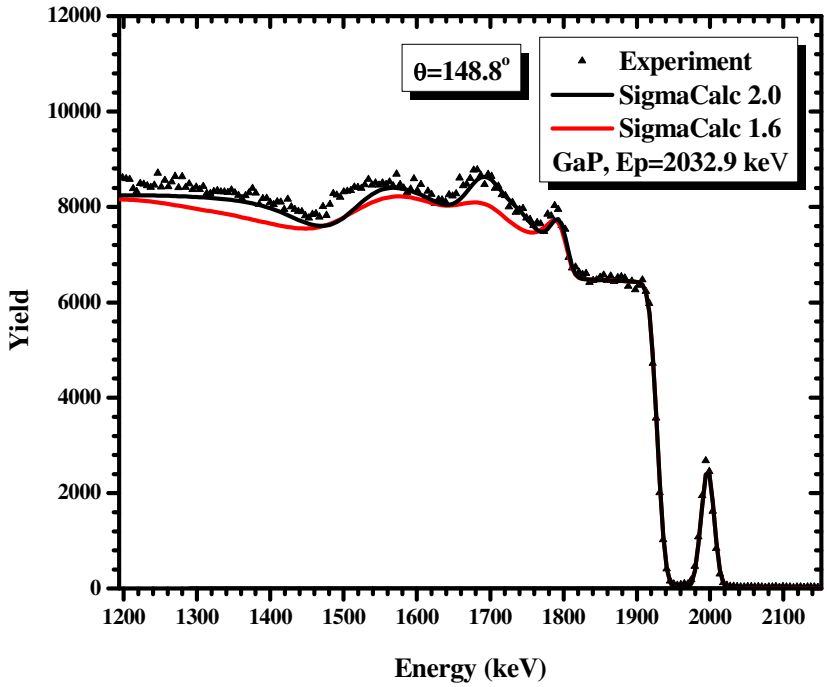

Figure 4.36: Benchmarking results using both versions of evaluated data.

4.8.4 The ^{nat}Si(p,p) case

The evaluated cross-section data for the elastic proton backscattering on silicon covers an energy range up to 3 MeV, as plotted in Figure 4.37 for the scattering angle at 170°, but no validation has ever been performed in a systematic way. The validation results of the present work using a silicon [111] wafer (which presents the narrowest channel among standard commercial Si orientations) as target, with a thin layer of gold on top, are presented in the figures below (4.38 and 4.39) for two studied scattering angles, namely at 148.8° and 173.5° concerning all the beam energy steps and following the proposed methodology (4.1-4.2). Numerical results concerning the comparison between the experiment and the simulations are seen in Table 4.4.

As seen in Figures 4.38 and 4.39, the benchmarking spectra show an excellent agreement between the experimental and the simulated spectra within 1-8% over the whole angular range studied up to ~2.2 MeV (the corresponding proton energy point was at 2284 keV). The smooth variation of the thick target spectra above this energy (at 2535 and 2785 keV) is attributed to the

contribution of the ^{29}Si(p,p), as demonstrated by the revised evaluated dataset for ^{nat}Si(p,p) [88,25].

It should be pointed out here, that the benchmarking procedure (up to 3.5 MeV) and subsequently the revision and extension of the data is still in progress, since there are some target dependent features, that are still under investigation in order to eliminate any relevant effects. These may include not only the channeling effect itself, but also stopping power effects being relevant to the tilting of the target during the measurements. A dedicated experimental run is foreseen in the near future using an unpolished Si wafer in order to clarify all unsolved issues and complete the validation procedure.

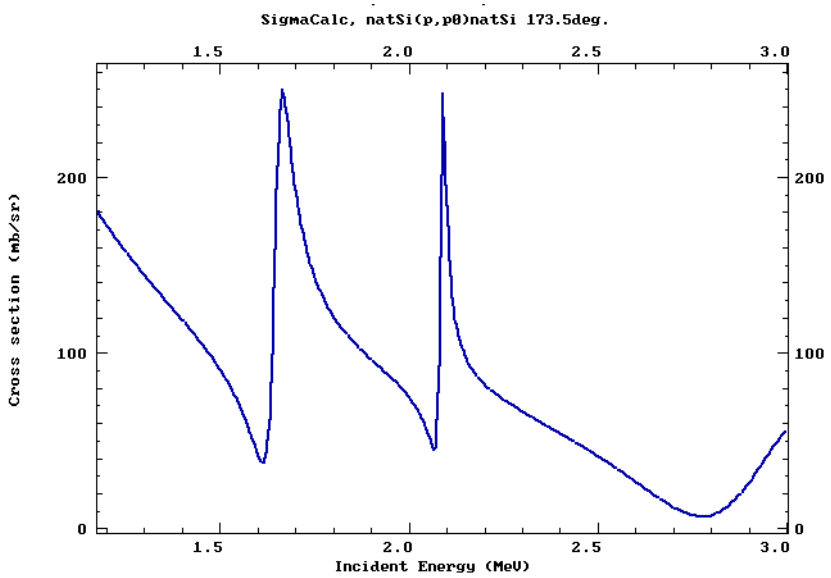

Figure 4.37: Evaluated cross-section data for ^{nat}Si(p,p) reaction at 173.5° [25]

Table 4.4: Differences between the integrated experimental and simulated yields.

Spectrum Energy (keV) / Angle	148.8°	173.5°
1532-1782	+2%	+6%
1783-2033	+4%	+8%
2034-2284	+5%	+8%
2285-2535	+6%	+1%
2535-2785	+2%	-17%

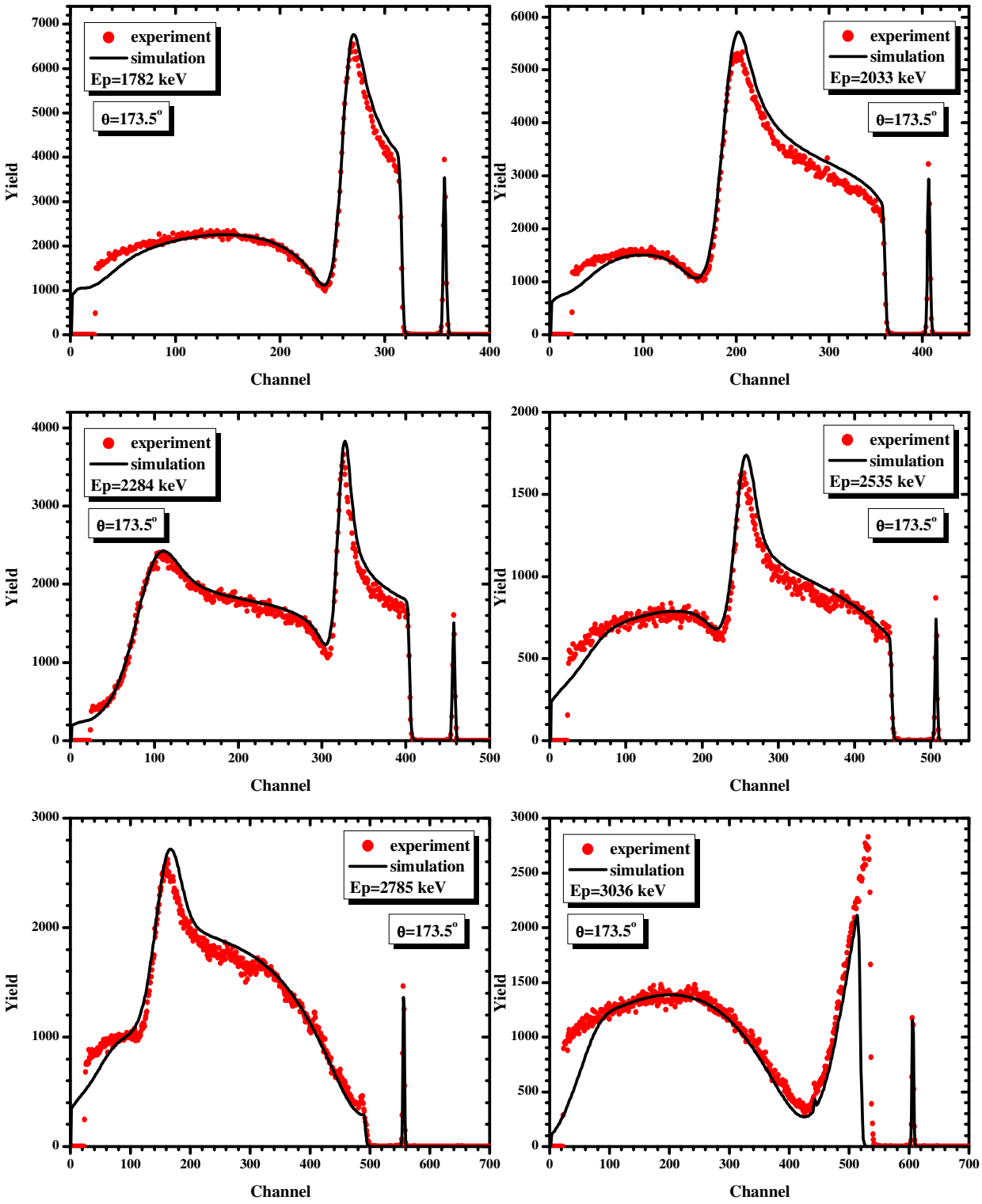

Figure 4.38: Benchmarking spectra on a silicon wafer with a thin gold layer on top, along with the corresponding simulations using the DataFurnace code [82].

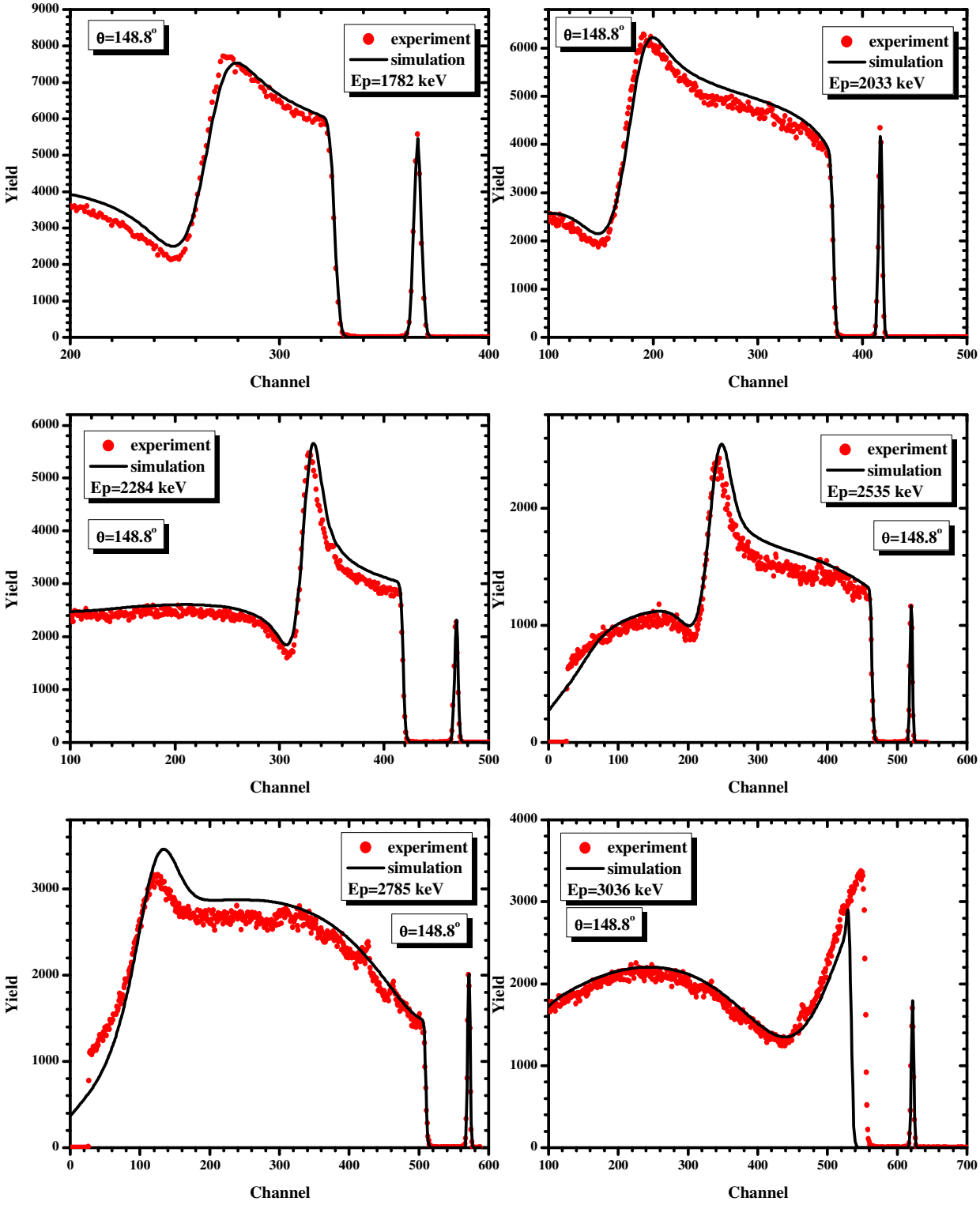

Figure 4.39: Benchmarking spectra on a silicon wafer with a thin gold layer on top, along with the corresponding simulations using the DataFurnace code [82].

CHAPTER 5

THEORETICAL INVESTIGATION OF THE ^{19}F(p,p) ELASTIC SCATTERING

The projectile interaction with a target nucleus can in principle be theoretically described as a sum of the elementary projectile-nucleon interactions, but the unknown scattering potential hinders such a procedure. Even assuming that comprehensive potential expressions can be provided, the insoluble many-body problem would nonetheless impede this theoretical description. A phenomenological approach is therefore applied [2 – chapter 3], considering the projectile interaction with a nucleus as a whole. The parameters of the used model and the appropriate potential, which represents the nucleus, are eventually found by fitting theoretical calculations to the available experimental data.

This phenomenological approach of the resonant elastic scattering cross sections within a theoretical framework is discussed in this chapter, concerning the main principles of the R-matrix theory. Both the hard-sphere, as the standard consideration of this framework, and the use of the optical model theory are analyzed here. The widely used analytical code AZURE implementing the corresponding calculations is subsequently introduced, along with a brief discussion about other existing programs. An implementation of such a procedure, concerns the study of the ^{19}F(p,p$_0$) scattering and is described in detail in section 5.2, which resulted in the extension of the corresponding evaluation up to Ep=2250 keV.

5.1 Main principles of the R-matrix theory

The review paper of Lane and Thomas in “R-matrix theory of nuclear reactions” [93] is certainly considered the reference paper in the field of resonance reactions, namely of the beam–nucleus interactions proceeding through the compound nucleus mechanism, where narrow resonances dominate the cross section. The reaction mechanisms and the required scattering theory fundamentals have already been described in chapter 1 (section 1.1.2), presenting the formalism of the scattering process in partial waves. It was shown along these lines, that the

differential cross section for elastic scattering can be calculated through the scattering amplitude function, being expressed through the phase shifts. The overall presentation of the R-matrix framework is however beyond the scope of this dissertation and therefore only the main principles will be in some extent analyzed here, concerning a complete but rather simple scattering case, namely the one of a spinless particle by a potential. The basic features of further analysis and formulae, corresponding to real nuclear problems, are only mentioned here and include the complications introduced by the spins and the multiplicity of both the reaction channels and the compound energy levels, as well as the modification of the calculations using the optical potential.

It should be noted here that among the various alternative frameworks, the R-matrix theory of Wigner and his collaborators turns out to be the most physical and appropriate one for the analysis of resonance reactions [94], as demonstrated in the basic concept description that follows, while the actual comparison between the frameworks can also be found in [94].

5.1.1 Concept

The basic concept [2, 94] of R-matrix theory lies in the division of the configuration space of the problem into an “internal” region, corresponding to the compound nucleus, and an “external” region, corresponding to the reaction alternatives, or channels, possible to reach the compound nucleus or emerge from it. This division of space represents the well defined radius of the atomic nucleus, which arises from the short range of the nuclear forces, and is made by a choice of the boundary of the compound nucleus. A nuclear radius is therefore chosen for each reaction alternative. The resonances displayed in the cross section are given by the boundary conditions of the wave functions chosen at each radius, matching the two regions of space. The construction of the appropriate boundary value problem to achieve stationary states, yields to a complete set of internal wave functions (expanded in eigenfunctions of the radial equation) that correspond to actual states of the compound nucleus. With the wave function and its derivative being known at the boundary of the nucleus, the wave function can be found everywhere outside the nucleus. The collision matrix elements, provided by the external region, (and therefore the scattering cross section) become thus expressed through the level parameters of the compound nucleus.

It should be pointed out here that the external region provides the scattering-theory features, such as the collision matrix, and phase shifts or penetration factors, while the internal one provides parameters pertaining to the nucleus, including energy levels, level widths and reduced widths (or spectroscopic factors). Considering also the aforementioned interpretation of the channel radii and the boundary condition numbers, the R-matrix framework indeed presents a rather physical approach to the description of resonance processes.

5.1.2 Scattering of a spinless particle by a potential

The R-matrix theory is described in this section, being implemented in the simple case study of the scattering of a spinless particle by a potential, for reasons of simplicity. Nonetheless, all the involved quantities in the R- matrix framework will be in some extent presented here, starting from the basic features.

It has already been shown in the first chapter (section 1.1.2) that within the scattering theory, the differential cross section is given by the following expression at each partial wave, in terms of the phase shifts δ_ℓ and the collision function $U_\ell = e^{2i\delta_\ell}$.

$$\frac{d\sigma}{d\Omega} = \left(\frac{1}{4k^2}\right)\left|\sum_l (2\ell+1)\left(1-U_\ell\right)P_\ell(cos\theta)\right)\right|^2 \qquad 5.1$$

while the integrated cross section is given by:

$$\sigma = \int \frac{d\sigma}{d\Omega} d\Omega = \left(\frac{\pi}{k^2}\right)\sum_l (2\ell+1)|1-U_\ell|^2 \qquad 5.2$$

The determination of the collision function U_ℓ, which is needed for the cross section calculation, is achieved through the division of the configuration space into two regions, an internal and an external one with respect to the nuclear radius, following the main principle of the R-matrix theory.

The **internal region** corresponds to the compound-nucleus domain, being represented by an assumed general potential well V(r). The internal radial equation is accordingly expanded in

eigenfunctions that correspond to actual states of the compound nucleus applying appropriate boundary conditions at the nuclear radius, as shown below.

The radial Schrödinger equation for stationary (resonant) waves X_λ is:

$$-\left(\frac{\hbar^2}{2m}\right)\frac{d^2X_{\lambda\ell}}{dr^2}+V(r)X_{\lambda\ell}=E_{\lambda\ell}X_{\lambda\ell} \qquad 5.3$$

along with the boundary condition

$$a_\ell \frac{dX_{\lambda\ell}}{dr}\Big|_{r=a} = b_\ell X_{\lambda\ell}(a_\ell) \qquad 5.4$$

where b_ℓ is the boundary condition number (real number) chosen for each partial wave and a_ℓ is the corresponding matching radius to separate the internal from the external region. The case of the s-wave neutron scattering by a square potential well is illustrated in Figure 5.1. The choice and the effect of these factors will be further discussed below (right after the mathematical description of the framework).

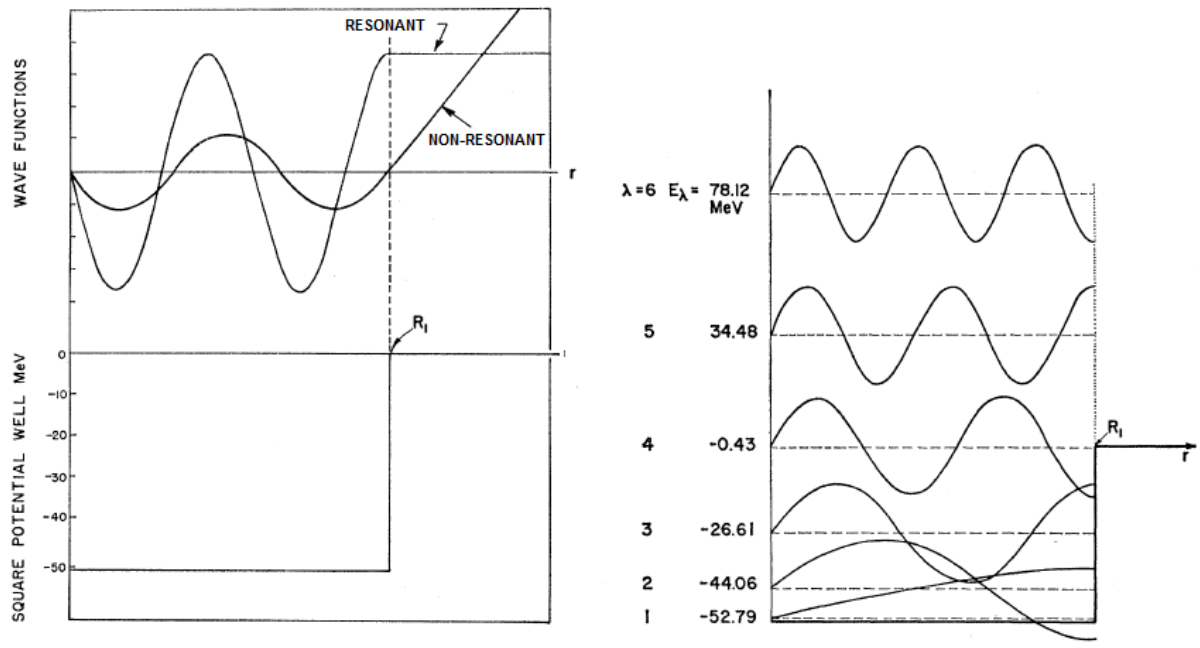

Figure 5.1: The square potential well for s-wave neutron scattering with the resonant and non-resonant neutron wave functions at low energies (left) and the first six standing waves of the well constructed with a boundary condition b=0 appropriate to low energy scattering, with R_1 being the square well radius [95].

In order to connect this resonant internal region with the external one, which describes the actual scattering (eq. 5.1), one needs to match the logarithmic derivatives of the corresponding wave functions evaluated at $r = a_\ell$.

The internal wave function φ_ℓ at arbitrary energy E certainly satisfies the same Schrödinger equation (5.5), while its logarithmic derivative ($\varphi'_\ell \equiv r\, d\varphi_\ell/dr$) can be expressed as follows, by applying the Green's theorem (multiplying the (5.5) by $X_\lambda^*(r)$ and the complex conjugate of (5.3) by φ_ℓ, subtracting and integrating) [96].

$$-\left(\frac{\hbar^2}{2m}\right)\frac{d^2\varphi_\ell}{dr^2} + V(r)\varphi_\ell = E\varphi_\ell \qquad 5.5$$

$$\varphi'_\ell/\varphi_\ell|_{r=a_\ell} = \left(\frac{1 + b_\ell R_\ell}{R_\ell}\right) \qquad 5.6$$

The R function, connecting the wave function with its derivative, is defined as:

$$R_\ell = \sum_\lambda \frac{\gamma_{\lambda\ell}^2}{E_{\lambda\ell} - E} \qquad 5.7$$

with the reduced width $\gamma_{\lambda\ell}^2$ of the level λ

:

$$\gamma_{\lambda\ell}^2 = \frac{\hbar^2}{2ma_\ell} X_{\lambda\ell}^2(a_\ell) \qquad 5.8$$

The **external wave function** φ is on the other hand more complicated, due to the centrifugal and Coulomb barriers. The corresponding radial equation is given by [94]:

$$\frac{d^2\varphi_\ell}{dr^2} - \left[\frac{\ell(\ell+1)}{r^2} + \frac{2m}{\hbar^2}\left(-E + \frac{Z_1 Z_2 e^2}{r}\right)\right]\varphi_\ell = 0 \qquad 5.9$$

This equation has regular solutions F_ℓ, which are finite at r=0, and irregular ones G_ℓ that are not finite at r=0. Their asymptotic behavior at large r is:

$$F_\ell \sim \sin\left[kr - \eta\, log(2kr) - \left(\frac{1}{2}\right)\ell\pi + \sigma_\ell\right] \quad 5.10$$

$$G_\ell \sim \sin\left[kr - \eta\, log(2kr) - \left(\frac{1}{2}\right)\ell\pi + \sigma_\ell\right] \quad 5.10$$

with the wave number being $k = mv/h$ and the Coulomb phase shift and parameter given respectively by:

$$\sigma_\ell = \arg(1 + \ell - i\eta) \qquad \eta = \frac{Z_1 Z_2 e^2}{hv} \quad 5.11$$

The incoming and outgoing waves, denoted as I_ℓ and O_ℓ respectively, are accordingly written as:

$$I_\ell = (G_\ell - iF_\ell)e^{i\omega_\ell} \qquad O_\ell = (G_\ell + iF_\ell)e^{-i\omega_\ell} \quad 5.12$$

with $\omega_\ell = \sum_{n=1}^{\ell} \tan\left(\frac{\eta}{n}\right)$ being the Coulomb phase, while the penetration factor P_ℓ, the shift function S_ℓ and the scattering phase shift Ω_ℓ are defined as follows:

$$P_\ell = (kr)/(F_\ell^2 + G_\ell^2) \quad 5.13$$

$$S_\ell = (F_\ell' F_\ell + G_\ell' G_\ell)/(F_\ell^2 + G_\ell^2) \quad 5.14$$

$$O_\ell^{-1} I_\ell = e^{2i\Omega_\ell} \quad \text{with} \quad \Omega_\ell = \omega_\ell - \tan(F_\ell/G_\ell) \quad 5.15$$

The scattering phase shift Ω_ℓ is apparently composed of two parts, the Coulomb (ω_ℓ) phase shift and the tan(F_ℓ/G_ℓ) one, being the phase shift of a hard sphere, in terms of the abrupt change in the potential at the matching radius.

Matching eventually the logarithmic derivative of the interval wave function with the one of the external wave function, one obtains the following form of the collision factor U_ℓ to be used in the cross section determination (see equations 5.1 and 5.2) defining $L \equiv O_\ell'/O_\ell - b_\ell$.

$$U_\ell = O_\ell^{-1}(1 - R_\ell L_\ell)^{-1}(1 - R_\ell L_\ell^*) I_\ell \quad 5.16$$

Substituting the exact expression of U_ℓ in the cross section formula (5.2), the final result for a single resonance λ in the R-function (5.7) is given by [94]:

$$\sigma = \left(\frac{\pi}{k^2}\right)(2\ell+1)\left|-e^{2i\Omega_\ell}\left\{1+\frac{i\Gamma_{\lambda\ell}}{[(E_{\lambda\ell}-E+\Delta_{\lambda\ell})-(i\Gamma_{\lambda\ell}/2)]}\right\}\right|^2 \qquad 5.17$$

The level width $\Gamma_{\lambda\ell}$ and level shift $\Delta_{\lambda\ell}$ are respectively:

$$\Gamma_{\lambda\ell} = 2P_\ell\gamma_{\lambda\ell}^2 \qquad \Delta_{\lambda\ell} = (S_\ell - b_\ell)\gamma_{\lambda\ell}^2 \qquad 5.18$$

The cross section contains thereby all the essential elements of a resonance [94], primarily being the outcome of the interference of the potential and resonance scattering and by having an energy dependent level shift $\Delta_{\lambda\ell}$ with clear dependence on the choice of the boundary condition number.

However, in order to describe a real nuclear reaction case, some other features need also to be taken into account, namely the complications introduced by the spins and the multiplicity of both the reaction channels and the compound energy levels. A brief description of these elements is presented in section 5.1.3.

It should be noted here, that the exact choice of the boundary conditions and the matching radii can be indeed arbitrary but when using sensible values, the so called “natural” ones, these auxiliary parameters tend to improve the connection of the results to nuclear structure [94]. More specifically, the “natural” boundary condition number, which should be real in order to preserve the Hermitian nature of the eigenvalue problem for the resonant states, is recommended to be equal to the shift functions S_l which vary slowly with energy. A proper choice of these functions would lead to almost zero values for the level shifts Δ_ℓ in the energy interval of the analyzed data, resulting to resonance energies $E_{\lambda\ell}$ which nearly coincide with the states of the compound nucleus. Similarly, the natural choice of the matching radius of a square-well potential would be the exact square-well radius, or the mid-point radius of the mean field in the case of Woods-Saxon type potential (described in section 5.1.3.3). Actually, it appears that for the latter case, the right choice for the matching radius would be approximately one fermi greater than the mid-point radius of the mean field, as discussed in [97]. These sensible values lead to reduced widths comparable to the results of nuclear structure calculations.

5.1.3 Further complications and modifications

The full nuclear problem, including reaction channels and energy levels, along with spin considerations, is briefly addressed here. The main principle of this matter lies mainly in the conversion of the preceding formula describing the collision function into a collision matrix and subsequently in the matrix inversion problem. The collision matrix, whose rows and columns pertain to channels, can be connected [93, 95] to an R-matrix and under some approximations the problem of matrix inversion in this space (pertaining to channels) can be transformed into a problem of matrix inversion in a space which pertains to levels. The former constitutes the few-channel, multi-level approximation, while the latter the few-level, multi-channel approximation of the R-matrix theory, which are thoroughly described in [93-95] but are only mentioned here.

Moreover, the consideration of a diffuse nuclear edge in the R-matrix calculations presents a different approach, described by the optical model of the nucleus, which is therefore also addressed in the following section 5.1.3.3.

5.1.3.1 The few-channel, multi-level R-matrix theory

In order to formulate nuclear resonances when retaining only few channels, the configuration space is divided into the internal region of the compound nucleus and the external one corresponding exactly to the various possible channels through which the compound nucleus can be formed or decay.

The total external wave function can be written as a sum of products, for each channel c, of the radial wave function φ_c with the channel wave function ψ_c, as follows:

$$\psi = \sum_c \Psi_c \, \varphi_c \qquad 5.19$$

The reaction channel c is specified by the quantum numbers $c \equiv (a, \ell, s, J, M_J)$, where the intrinsic spins I and i of the two particles (target and projectile or residual nucleus and ejectile, for incident or exit channel respectively) of the involved reaction pair α are coupled to form the channel spin s, which is then combined with the orbital angular momentum ℓ to form J. The corresponding vector additions are: $s = I + i$ and $J = \ell + s$.

Writing the radial wave function of the expression 5.19 in terms of incoming and outgoing waves and then using the collision matrix to connect these waves, one obtains the final form of the external radial wave function φ_c (having the incoming waves in the channel c and the outgoing ones in any channel c′) to be used in the calculations at the matching radius of the channel a_c (nuclear surface).

The internal wave function on the other hand is produced in a similar way as described in the previous section, applying boundary conditions at each piece of the channel surface (a_c) to the resonant states X_λ and eventually obtaining the following R-matrix:

$$R_{cc'} = \sum_{\lambda} \frac{\gamma_{\lambda c}\gamma_{\lambda c'}}{E_\lambda - E} \qquad 5.20$$

Matching the logarithmic derivatives of the two radial wave functions (of the internal and external region) on the channels surface a_c, the collision matrix gets the following form in terms of the R-matrix, which is similar to the one obtained above, in equation 5.16, although in channel space and matrices:

$$U_{cc'} = (k_c a_c)^{1/2}\, O_c^{-1} \sum_{c''} [1 - RL]^{-1}_{cc''} [\delta_{c''c'} - R_{c''c'} L^*_{c'}] I_{c'} (k_{c'} a_{c'})^{-1/2} \qquad 5.21$$

L is the diagonal matrix with the diagonal components $L_c \equiv O_c' O_c^{-1} - b_c \equiv S_c + iP_c$, where, as defined in 5.18, the shift function S_c leads to level shifts, while the penetrability P_c leads to level widths [95].

It should be noted here that the collision matrix is mainly used in the calculations in the following form (equation 5.22), which can be produced by observing that: $(k_c a_c)^{1/2} O_c^{-1} I_{c'} (k_{c'} a_{c'})^{-1/2} = \exp[i(\Omega_c + \Omega_{c'})] P_c^{1/2} P_{c'}^{1/2}$, where all quantities have been defined above (see equations 5.13-5.15).

$$U_{cc'} = \exp[i(\Omega_c + \Omega_{c'})]\, P_c^{1/2} P_{c'}^{-1/2} \sum_{c''} [1 - RL]^{-1}_{cc''} [\delta_{c''c'} - R_{c''c'} L^*_{c'}] \qquad 5.22$$

5.1.3.2 The few-level, multi-channel R-matrix theory

Treating the problem of inverting the channel matrix $[1 - RL]^{-1}$, as described by [95], an alternative form of the collision matrix is shown in equation 5.23 that follows [94], which refers to levels instead of channels. In this form many channels can be handled considering that there is a restriction in the number of the levels.

$$U_{cc'} = \exp[i(\Omega_c + \Omega_{c'})]\ (\delta_{cc'} + i\sum_{\lambda\lambda'} \Gamma_{\lambda c}^{1/2}\Gamma_{\lambda' c'}^{1/2}\, A_{\lambda\lambda'}) \qquad 5.23$$

where, (corresponding to equation 5.18):

$$\Gamma_{\lambda c} = 2P_c\gamma_{\lambda c}^2 \qquad \Delta_{\lambda\lambda'} = \sum_c (S_c - b_c)\,\gamma_{\lambda c}\gamma_{\lambda c'} \qquad 5.24$$

and

$$(A^{-1})_{\lambda\lambda'} = (E_\lambda - E)\delta_{\lambda\lambda'} + \Delta_{\lambda\lambda'} - (i/2)\Gamma_{\lambda\lambda'} \qquad 5.25$$

with

$$\Gamma_{\lambda\lambda'} = \sum_c 2P_c\,\gamma_{\lambda c}\gamma_{\lambda' c} \qquad 5.26$$

Thus, the inverse level matrix A will have the following form:

$$(A^{-1}) = \begin{pmatrix} E_1 + \Delta_1 - E - \frac{i}{2}\Gamma_1 & \Delta_{12} - \frac{i}{2}\Gamma_{12} & .. \\ \Delta_{21} - \frac{i}{2}\Gamma_{21} & E_2 + \Delta_2 - E - \frac{i}{2}\Gamma_2 & .. \\ .. & .. & .. \end{pmatrix}$$

5.1.3.3 Optical potential

The formal theory of the so-called optical potential is analytically described in [96], along with the corresponding empirical optical potential, usually referred to as the optical model. Only an overview of this widely used model is however presented here, in order to point out its significant role when implemented within the R-matrix framework, as the potential representing the scattering process.

A very brief presentation of the optical model has already been included in chapter 1, in section 1.1.2 (scattering theory). It has been pointed out, along those lines, that this model accounts for elastic scattering in a general way, with the interaction being determined by the bulk features of the nucleus, incorporating also the absorption effects. Let's note here that the name of the model derives exactly from the similarity of the treatment for the absorption effects, as shown below, to the ones for the scattering of light by a translucid glass [96].

The idea of the model is actually similar to the one of the shell model. It replaces the complicated interaction that a nucleon has with the rest of the nucleus with a **potential** that acts on the nucleon. The most commonly used form of the optical potential is the following (equation 5.27), with r being the distance between the center of mass of the two interacting nuclei. This potential contains parameters that can vary with the energy and the masses of the nuclei. These parameters should be adjusted to the experimental data (fitting procedure), as discussed below.

$$V(r) = U_R(r) + iW(r) + V_{SO}(r) + V_C(r) \qquad 5.27$$

The first term $U_R(r)$, is responsible for the elastic scattering of the projectile by the target nucleus, while the imaginary part, W(r), for the absorption. The rest correspond to spin-orbit and Coulomb terms, respectively.

The $U_R(r)$ part is **real** and is similar to the shell-model potential representing a nuclear well with depth V which is described, with some energy dependent modifications, by the Woods-Saxon form factor [1, 96], as given below, considering a diffuse nuclear surface (α), namely a **smooth edge of the potential**, around the mean nuclear radius R. The parameters V, R and α which define the well (with round borders) are to be adjusted to the experimental data in each case.

$$U_R(r) = -Vf(r, R, \alpha) \qquad 5.28$$

$$f(r,R,\alpha) = \frac{1}{1+\exp\left[\frac{r-R}{\alpha}\right]} \qquad 5.29$$

The **absorption** effects are taken into account by including a volume (W_I) and a surface (W_D) imaginary part in the potential, as shown in the following expressions (of Saxon-Woods type, equation 5.29). An imaginary part in the potential produces a term of decreasing exponential type [96] in the internal wavefunction, which therefore corresponds to absorption.

$$W(r) = W_I + W_D = -Wf(r,R_1,\alpha_1) + 4\alpha_1 W_D \frac{df(r,R_1,\alpha_1)}{dr} \qquad 5.30$$

The first term is responsible for the absorption in the whole volume of the nucleus, while the second one, with the derivative of the f function, acts specifically in the region near the surface, where the form factor f presents the largest variation. These two parts have complementary strengths: At low energies, where interactions take mostly place at the surface since there are no available unoccupied states for nucleons inside the nucleus, the surface term is important and the volume one can be ignored, while, in the opposite case, at high energies, where the incident particle has larger penetration, the volume part is the important one. The parameters of the potential concerning its depth W and W_D, along with the nuclear radius R_1 and diffuseness α_1 need also to be fitted to the experimental data.

The **spin-orbit** interaction leads to asymmetric scattering due to the different signs of the product $\boldsymbol{s}\cdot\boldsymbol{l}$ as the projectile passes by one or the other side of the nucleus. The presence of the spin-orbit term in the used potential is therefore necessary to describe the polarization effect. This term is usually written in the following form, with m_π the mass of the pion (seen in the corresponding normalization factor) and the product $\boldsymbol{s}\cdot\boldsymbol{l}$ of the corresponding spin and angular orbital momentum operators.

$$V_{SO} = \boldsymbol{s}\cdot\boldsymbol{l}\left(\frac{\hbar}{m_\pi c^2}\right)^2 V_S \frac{1}{r}\frac{df(r,R_S,\alpha_S)}{dr} \qquad 5.31$$

This term is important only near the surface of the nucleus, since it contains the derivative of the form function (5.29) like the previously mentioned surface imaginary part. The values of V_S , R_S and α_S must be correspondingly adjusted by the experiments.

The last contributing part in equation 5.27 is the well known **Coulomb potential**, concerning the case where the scattering involves charged particles. This potential has already been described in 1.1.2 under the assumption that the nucleus is a homogeneously charged sphere of radius equal to R, which defines the region of predominance of each force, the nuclear or the Coulomb one.

The **implementation** of the optical model, namely the theoretical calculations using the optical potential of equation 5.27, leads to a very good reproduction of the experimental cross section data with smooth variations (oscillations), originating from the modified well's properties.

Narrow resonances cannot however, be described using the optical model, since they concern the detailed compound nucleus structure (its energy levels and widths), but they can be very well reproduced in the R-matrix framework (when their corresponding energies and widths are introduced in the equations), as analyzed in the previous sections. Therefore, a unified approach, combining R-matrix and optical model has been shown [97,105,107] to be the most appropriate one for cross-section calculations in the case of low energy charged particle scattering. In this approach a Woods – Saxon real potential well along with a surface absorption part are used – together with the standard Coulomb and spin–orbit terms – for the calculation of phase shifts instead of the hard-sphere ones and, as a result, broad, single-particle resonances naturally occur, without being artificially, *ab initio,* introduced as in standard R-matrix approaches. This seems to constitute a more physical description of the scattering problem, since these resonances are not actually related to the compound nucleus eigenstates, as the other R-matrix components. Moreover, the introduction of the diffuse nuclear edge of the optical potential into the R-matrix theory, instead of using the hard sphere phase shifts ($(\tan(F_\ell/G_\ell)$, equation 5.15), removes both the artificial reflection of the incident wave by the abrupt square well and the artificial cross-section dependence on the nuclear radii. Comparing the results obtained with the use of the optical potential to those with a square well, the difference in the level widths lies mainly in the change of the penetrability, by an amount equal to the so-called reflection factor f [97]. Following this approach, a new, more versatile R-matrix code has been developed, which actually constitutes the core of the SigmaCalc online calculator [25] for the evaluated differential cross sections found in IBANDL [23]. This code can perform standard R-matrix calculations with hard-sphere or optical model potential phase shifts, and it can also incoherently add – when required –

contributions to the cross-section values originating from the direct reaction mechanism, by incorporating DWBA calculations using the well-known code DWUCK [106] as a subroutine. However, in the present work only the publicly available AZURE code has been implemented, which performs only standard hard-sphere R-matrix calculations, as will be discussed in the following paragraphs.

5.2 Theoretical investigation of the p+^{19}F system

The $^{19}F(p,p_0)$ scattering up to E_p=2.25 MeV has been investigated in the present dissertation within the R-matrix framework using the AZURE code [98]. The existing experimental data for the p+^{19}F system and especially of the $^{19}F(p,p_0)$ scattering, as well as the nuclear parameters of the excited states of the compound nucleus ^{20}Ne, play a key role in the implementation of the theoretical calculations and hence in the evaluation procedure. The contribution of benchmarking spectra is also of high importance in producing and also in validating the theoretical scattering data. The corresponding adopted steps of the evaluation process are therefore presented in section 5.2.2, while the final results are summarized and discussed in 5.2.2.3 and 5.2.2.4.

5.2.1 AZURE code

AZURE [98] is a publicly available, multichannel, multilevel R-matrix computer code, designed to model low-energy nuclear reactions involving charged particles, γ-rays and neutrons, focusing on the extraction of level energies, observed partial widths and bound state normalization parameters from the analysis of experimental excitation functions and angular distributions and on the determination of S factors at or near the energies of interest to nuclear astrophysics. The corresponding publication of the code structure by Azuma et al. [98] includes a demonstration of its applicability and versatility for a number of reaction cases relevant to stellar hydrogen burning, but it is designed to be easily adaptable to a variety of reactions.

The AZURE code is linked to the fitting package MINUIT [85] for the fitting procedure to experimental data and the χ^2 minimization, while the used R-matrix formalism is based on the work of Barker et al [99], which introduced a full multilevel multichannel R-matrix approach that allows resonant and non-resonant reaction contributions to be combined in a self-consistent

manner. A number of additional expressions and transformations from experimental to theoretical parameter space (and vice versa) are also adopted in the code as noted in [98], allowing one to use experimental resonance energies and widths directly as starting parameters in the fitting procedure. These are automatically converted into the proper reduced width amplitudes and pole energies and are eventually transformed back into physical parameters, following the R-matrix analysis. Many other analytical options are available in AZURE, including beam energy convolution, target thickness effects and inverse kinematics. The various features offered by AZURE, along with its technical and computational aspects are described in detail in the user manual, which is available online at the AZURE website [100], along with the source code, the graphical user interface (GUI) and several examples.

The multichannel aspect of the code permits the inclusion of all the allowed channels, in terms of the angular momentum conservation, for as many compound state decay reactions as desired, whereas all the allowed interferences are automatically taken into account. It can simultaneously fit as many channels as desired, offering the important advantage of more strict constraints on the fitted parameters. It should be noted here that the respective channels that can populate a given R-matrix (one for each grouping of like J^{π} levels) are restricted by conservation of both angular momentum and parity.

One important feature of actually implementing the R-matrix theory in a code, concerns the accurate calculation of the cross section in terms of the used eigenvalues of the internal region. More specifically, one must include all the energy levels in the compound nucleus to take into account all the possible eigenfunctions (see equation 5.3 in section 5.1.2), but this would be practically and computationally impossible. This is treated in AZURE by including all the levels of the given compound nucleus within the energy range of interest and by adding a background resonance for each of the relevant J^{π} groups above the energy range of interest (background poles) to simulate the tails of higher energy resonances [101].

Moreover, the graphical user interface of the AZURE package, developed to expedite the data management and the program configuration, makes it quite friendly to use. For instance, the user can easily add or delete entire reaction channels, turn on, off or edit resonances and their associated parameters and even swap datasets in and out. Configuration flags, that can be toggled using the GUI, actually control many analysis options within AZURE, as described in the manual of the code [100].

5.2.2 Evaluation procedure

The theoretical investigation of cross sections within the R-matrix theory is in general a complicated procedure, since it relies on the relevant existing experimental data, the nature of which justify, in reverse, the importance of the evaluation in the first place. The possible fine structure of the measured cross section and/or its strong angular dependence (if present) may well be missed in an experiment (e.g. due to the used target, the experimental conditions, etc.). Moreover, the experimental datasets are in many cases quite discrepant and/or scarce (both on energy and angle). The production of evaluated cross sections, incorporating the data measured under different experimental conditions at different scattering angles into the framework of a unified theoretical approach is therefore mandatory [2 – chapter 3]. The produced evaluated cross sections can thereafter be calculated at any scattering angle with **reliability** exceeding that of any individual measurement.

The evaluation procedure involves several steps, as schematically shown in Figure 5.2, which mostly depend on the existing data. More specifically, the compiled datasets should firstly be critically examined in terms of the reported experimental conditions and errors. Then the apparently reliable experimental points are selected to be used in the implementation of the theoretical model, the R-matrix theory, whereas the used free parameters are manually adjusted or automatically fitted to the selected data points. The produced cross sections are checked using benchmark experiments, providing feedback to the theoretical calculations, along with additional cross section measurements (when required) in order to find the optimal set of nuclear parameters.

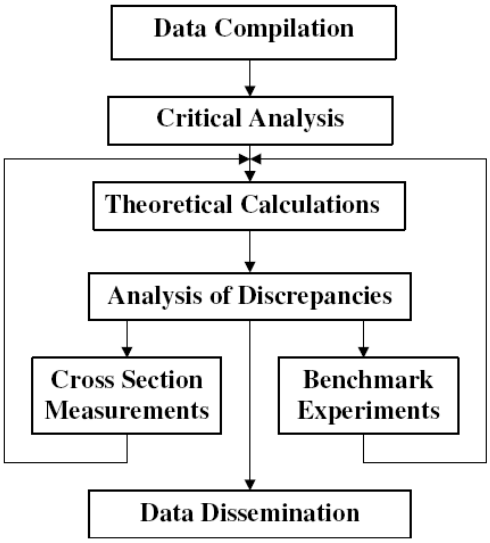

Figure 5.2: Evaluation procedure [25].

Concerning the proton elastic scattering on ^{19}F, which is investigated in the present thesis, the corresponding already made evaluation ranges up to 1730 keV [25]. The adopted steps for reproducing the evaluated data with the use of AZURE and extending them to higher energies (~2250 keV) are described in the following sections.

5.2.2.1 Data survey

The evaluation of the $^{19}F(p,p_0)$ scattering differential cross sections certainly requires the theoretical investigation of the $p+^{19}F$ system in total. In particular, experimental data on all the relevant reaction channels are useful, and especially the ones of the $^{19}F(p, p_0)$ scattering itself. A comprehensive compilation of all the corresponding charged particle data is found in IBANDL [23], and is listed here in Table 5.1, concerning the energy range of interest (up to ~3 MeV). The corresponding spectroscopy/properties of the compound nucleus ^{20}Ne have been studied in some extent in the past and a compilation of the different works can be found in [102-104]. A list of the energy levels of ^{20}Ne nucleus is presented in Table 5.2.

Table 5.1: Studied particle reactions in ^{19}F, in the range of 1.5-3 MeV [23].

Reaction	Energy range (keV)	Scattering angle	Reference
(p,p_0)	*650-1800*	135, 145	[48]
(p,p_0)	1400-2710	165	[47]
(p,p_0)	1000-1880	153	[46]
(p,p_0)	550-1810	159	[39]
(p,p_0)	2490-4790	150	[37]
(p,p_0)	500-2060	160, 140, 125	[35]
(p,p_0)	1800-2680	95, 123, 137	[34]
(p,α_0)	500-1880	150	[40]
(p,α_0)	1190-5270	160,90	[41]
(p,α_0)	690-2020	150, 90	[30]

(p,p) (p,α_3)	3000-7100	150, 135	[26]
(p,p_{0-4}), (p,α_{0-4})	1520-3430	161, 159, 149, 145, 138, 125, 123, 113, 111, 98, 95, 82, 69, 67, 65, 54,	[36]

Table 5.2: Levels of ^{20}Ne from $^{19}F(p,p)$ and $^{19}F(p,\alpha_0)$ studies [102].

Excitation Energy (MeV)	**J^π**	**Γ (keV)**	**Γ_p/Γ**
13.416	2^-	35	0.012
13.483	1^+	7.1	0.98
13.649	0^+	22	0.996
13.677	2^-	4.9	0.21
13.736	1^+	7	0.17
14.126	2^-	4.3	0.067
14.151	2^-	14	0.17
14.198	1^+	13.9	0.85
14.472	0^+	86	0.8
14.648	0^+	24	0.3
14.693	(1^+)	38	0.5
14.776	(1^-)	67	0.75
14.85	$(2^+),(4^+)$	71	
15.04	(2^+)	86	
15.27	(1^-)	285	

5.2.2.2 Data assessment

In order to extend the existing evaluation of the $^{19}F(p,p_0)$ cross sections, which ranges up to 1730 keV, one must carefully examine the corresponding experimental data found in literature, focusing on the datasets in the energy range above 1.5 MeV (Table 5.1). Taking into account the results presented in chapter 3, concerning the structure and the energy step of the relevant data (Figures 3.12a-d), as well as the available corresponding benchmarking spectra that range up to 2250 keV, as seen in the following section, the present evaluation procedure covers the energy range up to ~2.25 MeV. The cross section in this interval presents several interfering (overlapping) resonant structures, as seen in the following plots of the available data at 140° and 160°, in Figures 5.3.

The work of Ouichaoui et al. [36] is of great importance and relevance, since it concerned a systematic analysis of the p+^{19}F system within the R-matrix theory up to E_p=3.4 MeV. It included the study of the $^{19}F(p,p_{0\text{-}4})$ and $^{19}F(p,\alpha_{0\text{-}4})$ reactions at several forward and backward angles. The reported theoretical investigation was focused on the level extraction and characterization of the compound nucleus ^{20}Ne, in terms of allowed excitations and angular distributions. The absolute values of the obtained cross sections present, however, discrepancies compared to the majority of the other datasets in various energy regions, as can be seen in Figures 5.3 concerning the elastic channel. More specifically, comparing the data of Ouichaoui et al. [36] to the results obtained in the present work [71], which have been benchmarked (chapter 4, section 4.5), one excludes the case of a systematic error in the data of Ouichaoui, since there are indeed regions, namely at ~1.8-1.95 MeV and ~2.05-2.1 MeV, where the data agree very well (Figures 5.3). The discrepancies could be attributed either to the insufficient charge collection of the Faraday cup or, less likely, to the gas target used by Ouichaoui et al. The reported experimental information of this work [36] is actually quite poor and one cannot exclude larger uncertainties than the reported 10%. Being guided however by the absolute values of the present work [71], the cross sections of Ouichaoui, which qualitatively agree with the other available datasets in energy regions, where the present data are quite sparse, provide valuable information for the evaluation procedure.

On the other hand, the cross-section data of Jesus et al [47] are systematically underestimated compared to the other datasets. A factor of 18% seems however to be adequate to correct the results. Studying the experimental conditions of the other sources as well, and then comparing all the relevant data, as plotted in Figures 5.3, one concludes that there are three energy regions,

where special attention needs to be drawn. More specifically, there are structures (maxima) at ~1.75, ~1.9 and ~1.95 MeV that are described quite poorly by the present data [71] and need to be taken into account in the calculations.

Considering all the above, and using the reported excited states of the compound nucleus ^{20}Ne (Table 5.2), theoretical calculations for the p+^{19}F system were performed using the AZURE code, focusing on the $^{19}F(p,p_o)$ scattering cross section.

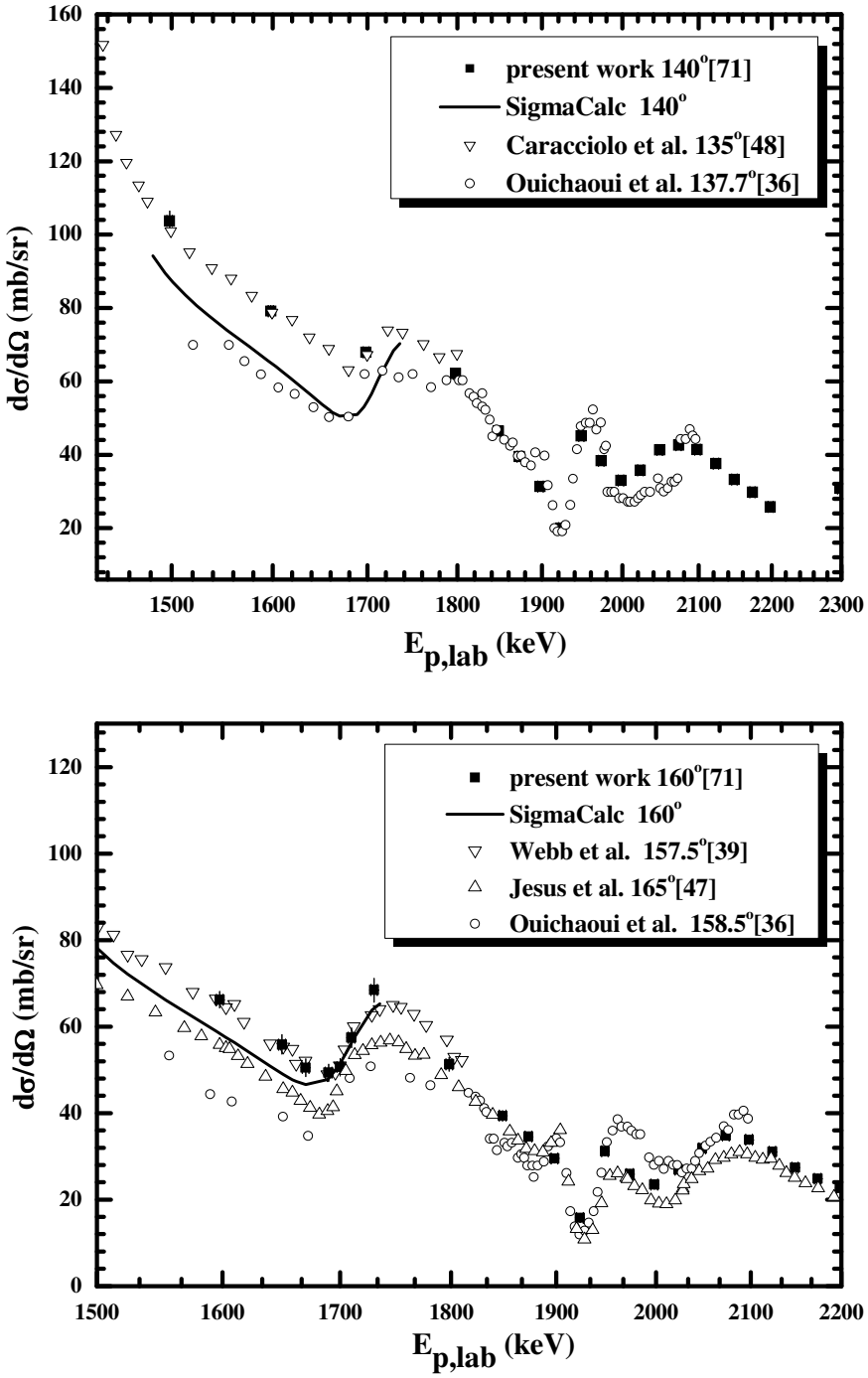

Figures 5.3: Existing differential cross sections of the $^{19}F(p,p)$ at 140° and 160° [23].

5.2.2.3 Results

The final input parameters for the theoretical calculations of the p+^{19}F system with the AZURE code are given in Table 5.3, while the obtained $^{19}F(p,p_0)$ cross sections for several scattering angles are plotted in Figures 5.4 and 5.5, along with the existing evaluated data (SigmaCalc [25]) and the available experimental values from literature, respectively.

All the reported levels from literature (Table 5.2) were used in the calculations with minimal energy shifts and differences in widths. However, in order to reproduce the pronounced resonant structure around 1.92 MeV (at ~14.67 MeV excitation energy of ^{20}Ne), which presents a rather negligible angular dependence, an additional overlapping 2^- level was introduced very close to the ambiguous reported 1^+ broad one. The width of the latter was also tuned accordingly.

Table 5.3: Final input parameters of ^{20}Ne used in AZURE (along with R_0=1.4 fm).

Excitation Energy (MeV)	**J^π**	**Γ_p (keV)**	**Γ (keV)**
13.479	1^+	6.9	6.9
13.646	0^+	20.13	2.0.15
13.673	2^-	0.9	0.9
13.733	1^+	1	4.7
14.149	2^-	8.4	17.2
14.194	1^+	13.5	20.1
14.468	0^+	27.1	64.8
14.63	0^+	29.4	49.9
14.669	2^-	6.4	16
14.693	1^+	0.3	9.7
14.745	1^-	94	141.9
14.87	2^+	71.4	265
15.21	1^+	464	613.5

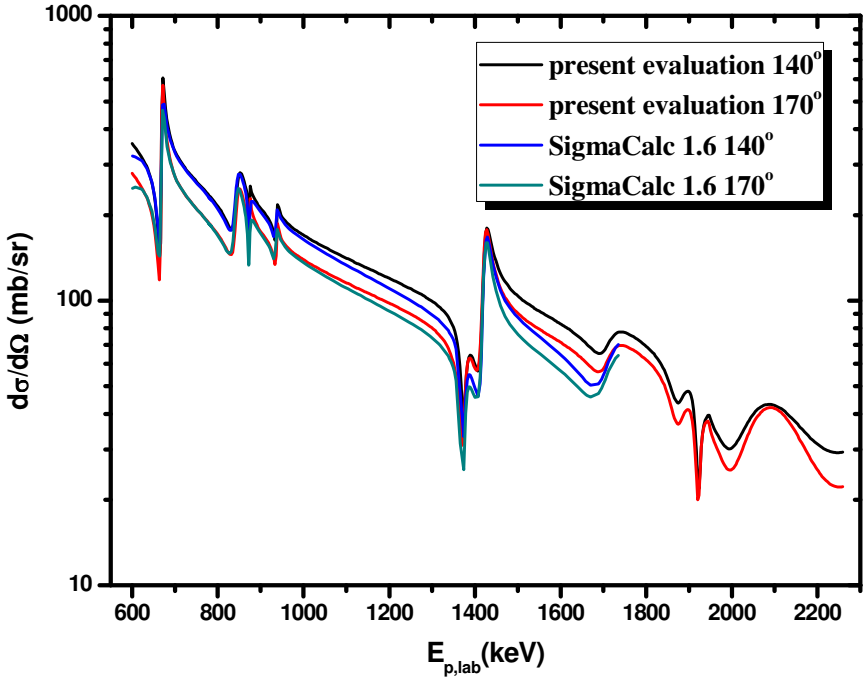

Figure 5.4: Comparison between the present evaluated data and the existing ones at 140° and 170°.

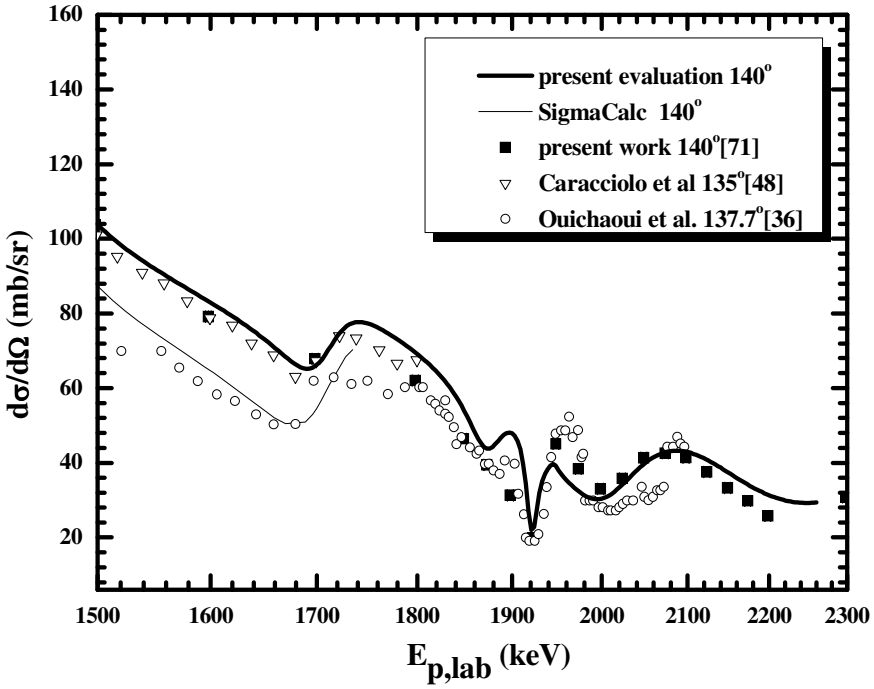

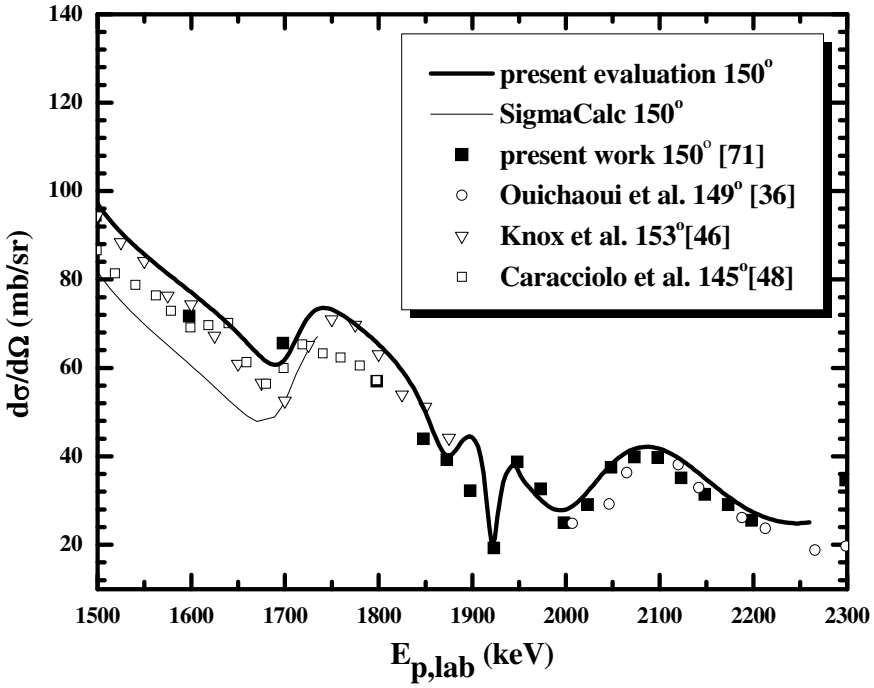
present evaluation 150°
SigmaCalc 150°
present work 150° [71]
Ouichaoui et al. 149° [36]
Knox et al. 153°[46]
Caracciolo et al. 145°[48]
dσ/dΩ (mb/sr)
E p,lab (keV)

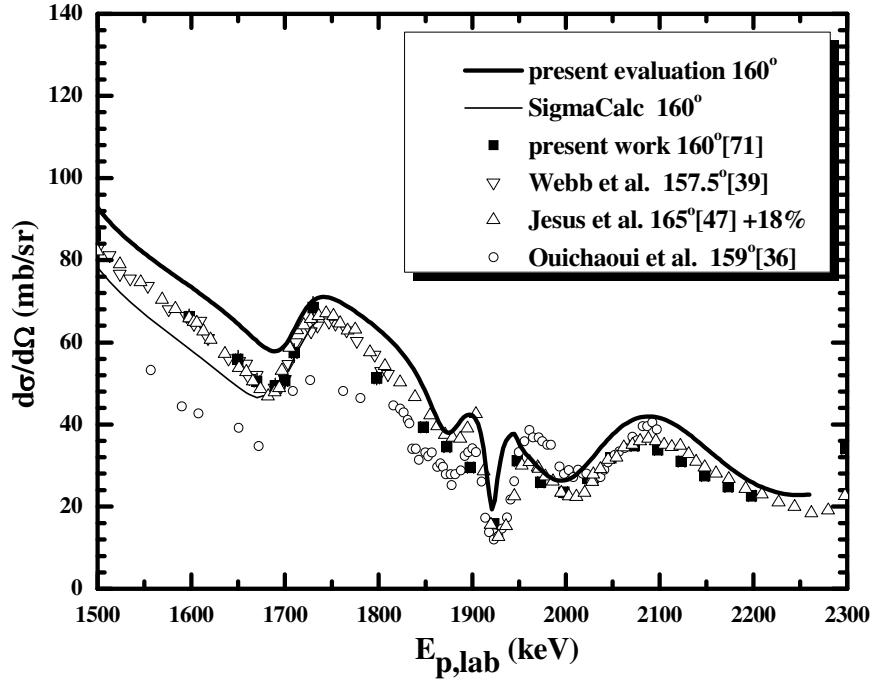
present evaluation 160°
SigmaCalc 160°
present work 160°[71]
Webb et al. 157.5°[39]
Jesus et al. 165°[47] +18%
Ouichaoui et al. 159°[36]
dσ/dΩ (mb/sr)
E p,lab (keV)

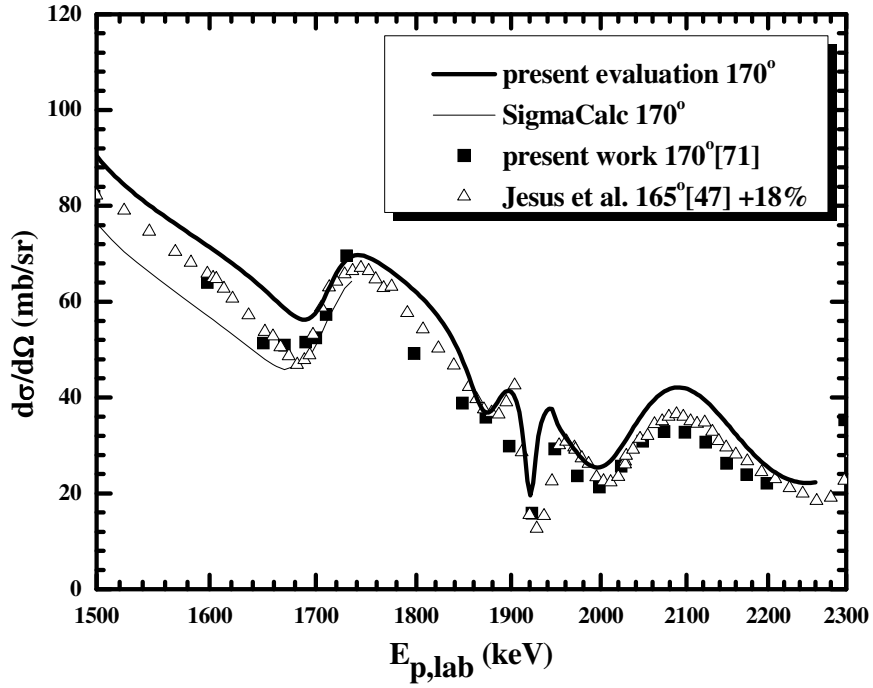

Figures 5.5: The final results of the present evaluation along with selected existing data at 140°, 150°, 160° and 170°.

5.2.2.4 Benchmarking

The benchmarking, namely the validation, of the calculated cross-section data is a very important intermediate step in the evaluation procedure. It provides feedback to the obtained calculations in all stages of the process. More specifically, in the beginning of the evaluation, the benchmarking spectra indicate both qualitatively and quantitatively the cross-section structure, thus justifying the existing data assessment. As the evaluation progresses, benchmarking spectra are eventually used for the final tuning of the nuclear parameters of the theoretical calculations, gradually leading to the final results.

The validation of the calculated cross-section values has been achieved, using experimental thick target spectra and the corresponding simulations, as described in chapter 4 (4.1-4.4). More specifically, a ZnF_2 pellet was used for the benchmarking measurements and the proton scattering on the target has been studied at 1730, 2000 and 2250 keV at 140°, 150°, 160° and 170°. The simulation of the $^{nat}Zn(p,p)$ signal enabled the determination of the QΩ factor, while the roughness code was used to incorporate the corresponding surface effects of the spectra.

The obtained final benchmarking results are shown in Figures 5.6 and 5.7, regarding the scattering at 140° and at 170° respectively (where statistical errors were minimal, while angular range was maximal), whereas the corresponding simulations were performed using the final evaluated cross sections for the elastic scattering on ^{19}F and the Rutherford ones for the $^{nat}Zn(p,p)$ scattering. The comparison between the experimental and the simulated spectra was limited to a narrow energy window near the surface peak of $^{19}F(p,p_0)$, at about 150 keV (see section 4.2.4), which corresponds to ~40 channels, in order to exclude any possible carbon contaminations and to further minimize the effect of plural scattering on the ^{nat}Zn substrate in the calculations.

Due to the kinematics of the $^{19}F(p,\alpha)$ reactions, there is a background contribution in the spectra originating from $^{19}F(p,\alpha_3)$ and $^{19}F(p,\alpha_4)$ reactions, but it is indeed negligible in the spectra acquired at 1730 and 2250 keV, as seen in the experimental yields. The contributions of the edges of the two signals seem to be of the order of 1%.

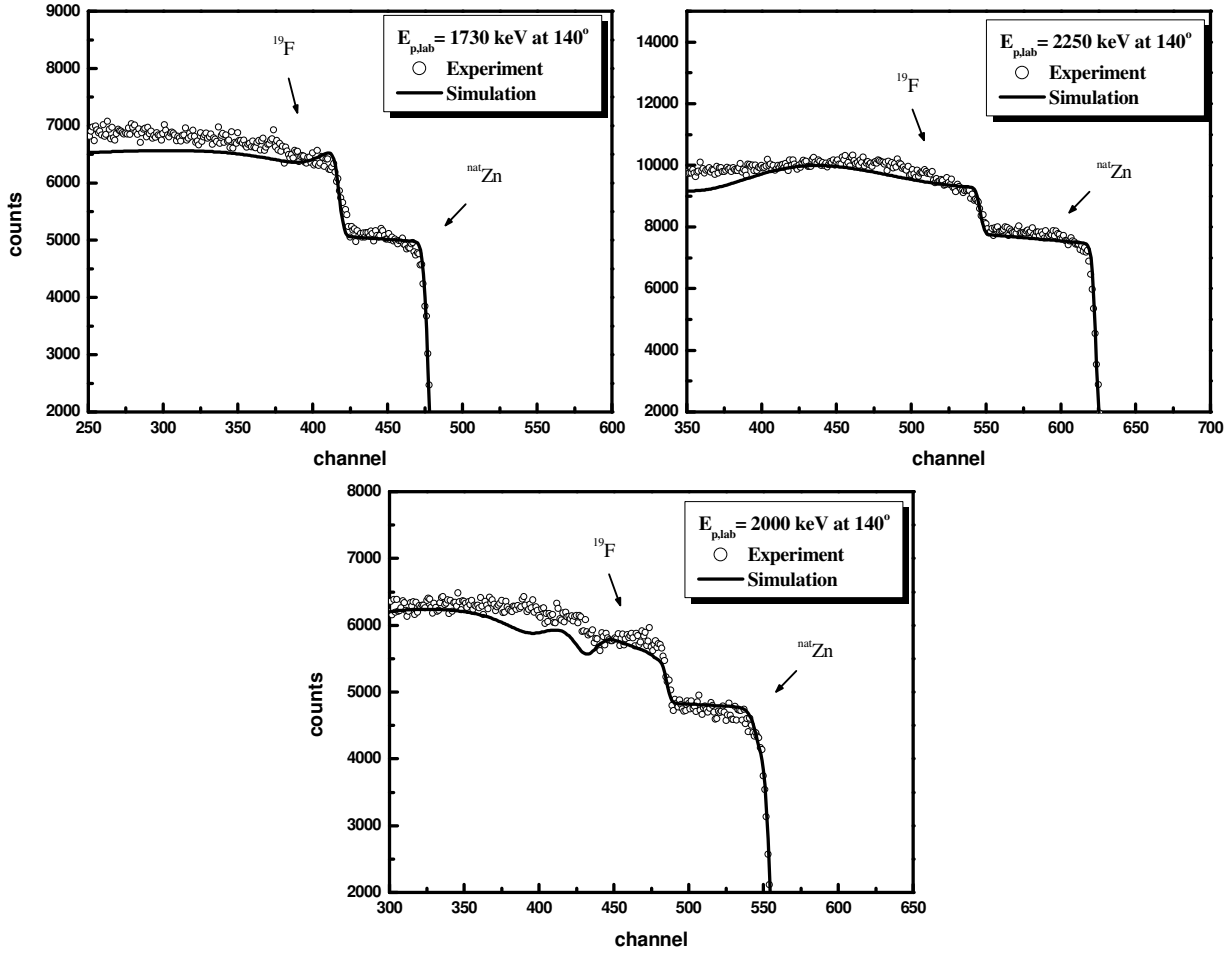

Figures 5.6: Benchmarking spectra on ZnF_2 pellet at 140°, along with the corresponding simulations using the SIMNRA code [70].

The only available cross section data of the two exit channels ($^{19}F(p,\alpha_3)$ and $^{19}F(p,\alpha_4)$) are the experimentally determined ones by Ouichaoui et al. [36], which range up to 2100 and 1960 keV respectively. This study shows that the cross section of the $^{19}F(p,\alpha_3)$ reaction is indeed very low compared to the elastic scattering over the whole studied energy range, while the data concerning the $^{19}F(p,\alpha_4)$ reaction present a structure with a relatively wide maximum at ~1.9 MeV, comparable to the elastic cross section values, as seen in Figure 5.8 (top). It should be noted here that the $^{19}F(p,\alpha_0)$ cross section of Ouichaoui et al [36] is in good agreement with the ones presented in chapter 3 [71] which are benchmarked (see 3.2 and 4.5). Therefore the $^{19}F(p,\alpha_3)$ and $^{19}F(p,\alpha_4)$ data of [36], despite the absence of other experimental data in literature,

can be considered to be at least indicative concerning their absolute values, since all experimental data were simultaneously acquired as reported in [36].

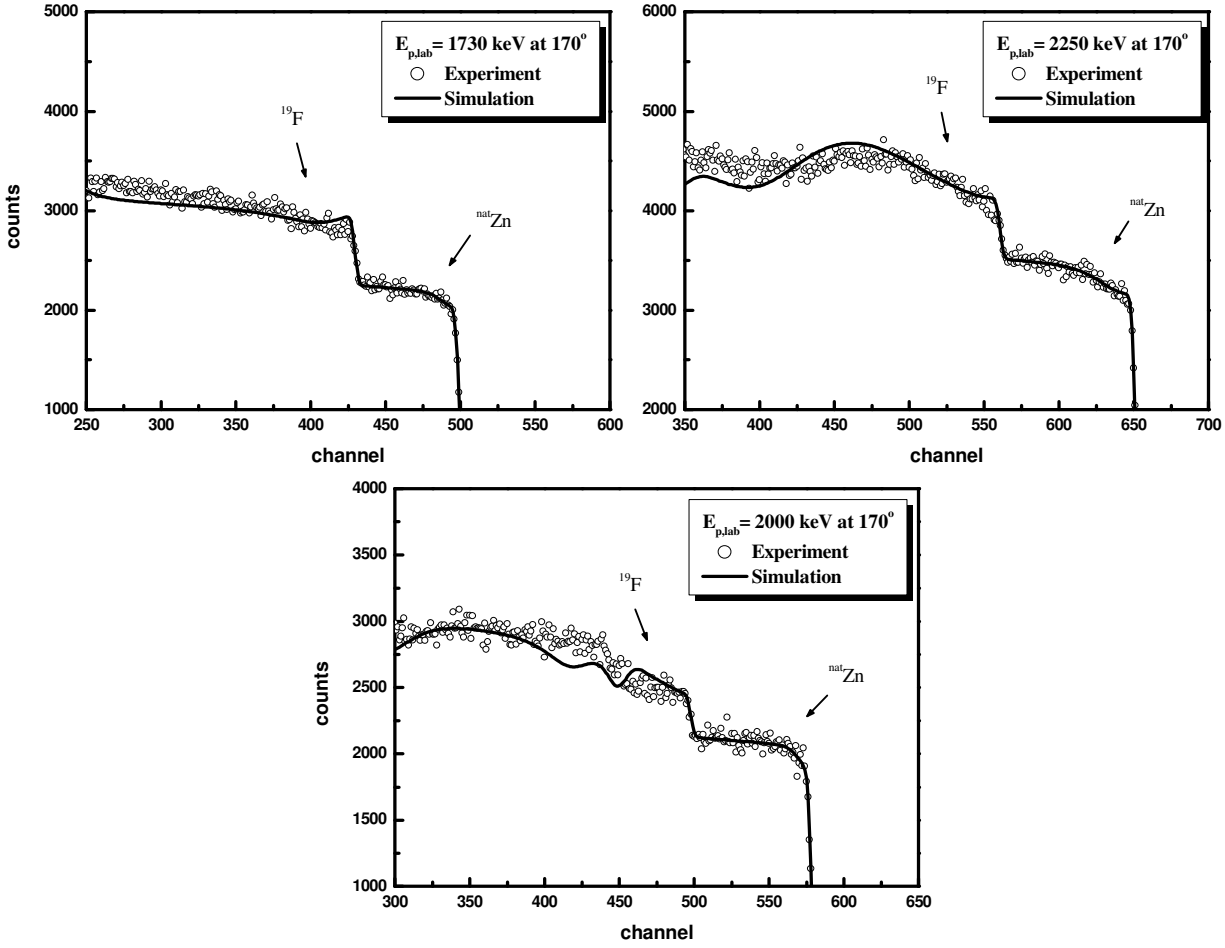

Figures 5.7: Benchmarking results on ZnF_2 pellet at 170°, along with the corresponding simulations using the SIMNRA code [70].

It is also shown in [36] that there is only a slight angular dependence of the $^{19}F(p,\alpha_4)$ differential cross section data (with $\sigma_{140°}<\sigma_{170°}$), while the ^{nat}Zn (p,p) scattering cross section at 140° is ~26% higher than the one at 170°. The contribution of the $^{19}F(p,\alpha_4)$ counts in the ^{nat}Zn (p,p) yield acquired at 140° is therefore insignificant in the case of the incident proton energy at 2MeV, where the edge of the $^{19}F(p,\alpha_4)$ signal is expected at a slightly higher energy than the one of the ^{nat}Zn signal, and it did not affect the determination of the QΩ factor (by simulating the ^{nat}Zn (p,p) yield). However, the higher $^{19}F(p,\alpha_4)$ cross-section values for lower incident energies

(inside the target) contribute to the $^{19}F(p,p)$ yield with the maximum values being present below channel ~550 in the corresponding Figure 5.6 (bottom), changing the shape of the spectrum and giving a qualitative discrepancy between the experimental and simulated thick target yields in the range between ~1850-1950 keV. Therefore, the spectra at 2 MeV cannot be used for the validation of the evaluated cross sections of $^{19}F(p,p)$ in this energy region (below 2 MeV). Using nevertheless the data by [36] for the (p,α) reactions in the simulation (with a gap of data in the region 1.96-2 MeV for the (p,α_4) one, which is not studied by Ouichaoui et al.), the difference between the experimental and the simulated spectra minimizes from 13% to 9 %, as shown in Figure 5.8 (bottom) but this procedure remains inaccurate.

It should be pointed out here, that all differential cross-section measurements using thin targets show a strong fine structure in the cross section in this particular energy region of ~1850-1950 keV (see Figures 5.3 for example). In this case, and in the absence of reliable ("clean") benchmarking spectra, the evaluated differential cross-section values were rather tuned according to the selected experimental data points. A possible set of additional benchmarking spectra measured exactly in this problematic energy region with proton-alpha particle separation (e.g by using ΔE/E detectors) and/or with the use of a different target could clarify this point and lead to a better fine tuning of the level parameters involved in the AZURE calculations, since the evaluation is a dynamic process.

Nevertheless, with the exception of this problematic region, comparing in absolute values the spectra at 1730 and 2250 keV in an energy region near the surface, which corresponds to ~40 channels in average for both detectors (at 140° and at 170°), the corresponding evaluated cross-section values are validated, since the difference of the integrated yields (subtracting the $^{nat}Zn(p,p)$ contribution) is in all cases within 3-7%, as seen in Table 5.3.

Table 5.3: Differences between the integrated experimental and simulated yields.

Spectrum energy (keV) / Angle	**140°**	**170°**
~1580-1730	-4%	+7%
~2100-2250	-4%	+3%

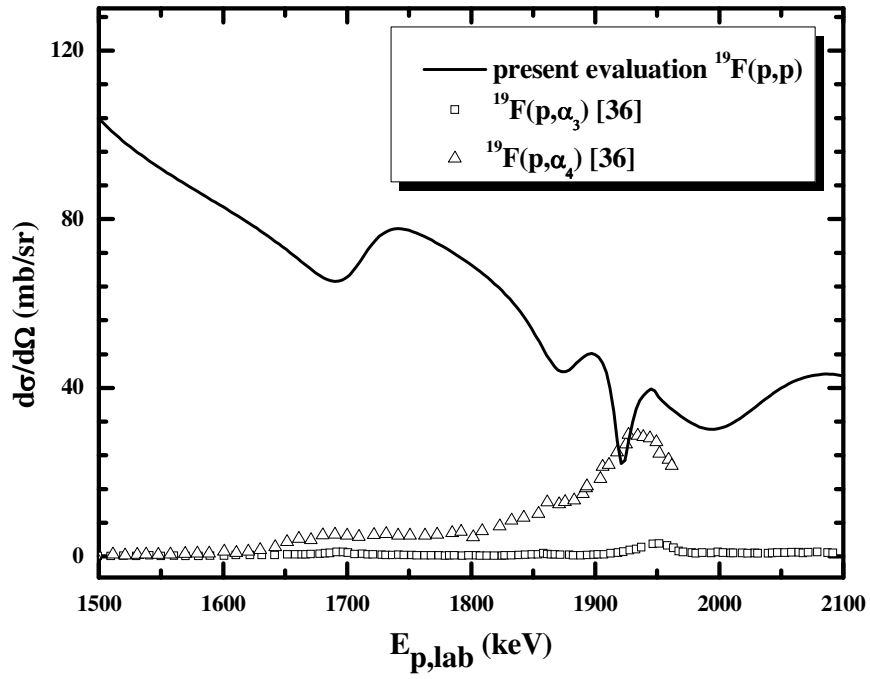

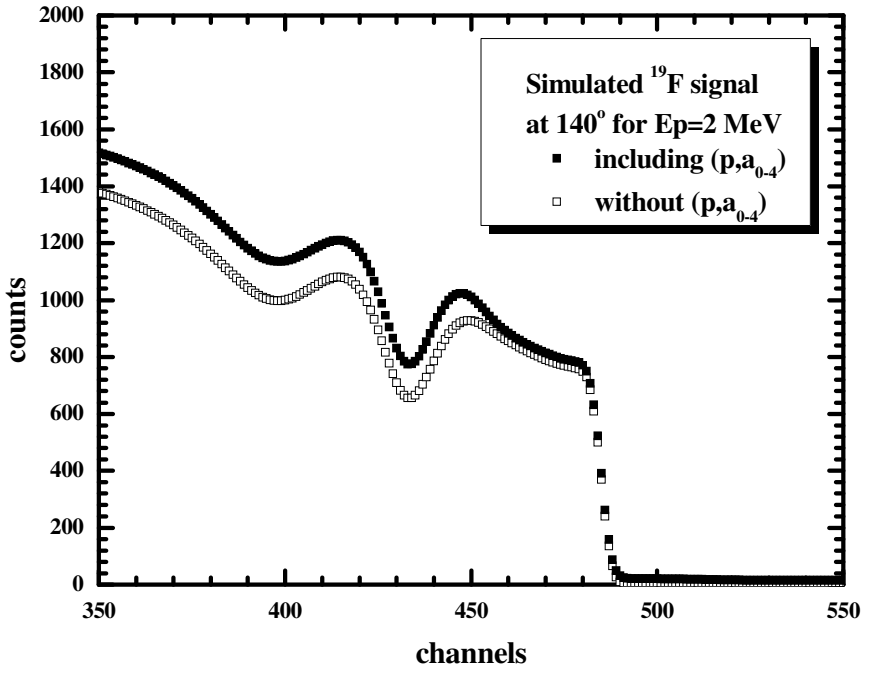

Figures 5.8: Evaluated differential cross sections for the proton elastic scattering on ^{19}F at 140°, along with the experimental $^{19}F(p,\alpha_{3,4})$ ones by Ouichaoui et al. [36] (**top**). Simulated ^{19}F signal at 140° for E_p=2MeV with and without the $^{19}F(p,\alpha_{0-4})$ contribution. The $^{19}F(p,\alpha_4)$ reaction has been measured only up to 1960 keV, which corresponds to channel ~460 **(bottom)**.

CONCLUSIONS – FUTURE PERSPECTIVES

The contribution of the present dissertation in the field of Ion Beam Analysis (IBA) lies on the measurements, the benchmarking and the theoretical investigation of differential cross sections suitable for EBS and NRA studies.

More specifically, selected differential cross sections have been experimentally determined regarding the p+^{7}Li, p+^{19}F and d+^{nat}Mg systems, where the available data in literature are quite sparse and/or discrepant. More than 1000 new cross-section values have been added to IBANDL (Ion Beam Analysis Nuclear Data Library) through this work, concerning several reactions, which in most of the cases have been measured for the first time in this angular and energy range, thus enhancing the implementation of the corresponding IBA techniques.

These reactions are:

- ^{7}Li(p,p$_0$)^{7}Li, ^{7}Li(p,p$_1$)^{7}Li, ^{7}Li(p,α_0)^{4}He και ^{19}F(p,p$_0$)^{19}F,^{19}F(p,α_0)^{16}O, ^{19}F(p,$\alpha_{1,2}$)^{16}O in the energy range of 1.5–7 MeV at several backward detection angles, namely at 140°, 150°, 160° and 170°.
- ^{nat}Mg(d,d$_0$), ^{24}Mg(d,p$_0$,p$_1$,p$_2$)^{25}Mg in the energy range of 1.3–2.05 MeV at 55°, 70°, 90°, 125°,140°, 150°, 160° and 170°.

Additionally, a benchmarking methodology has been developed and documented in the present thesis regarding the validation of charged particle differential cross sections, using thick target yield. This procedure has been implemented to validate not only the obtained cross-section values for the aforementioned reactions, but also the evaluated (and/or the existing experimental) cross-section datasets, concerning other critical reactions (elements) for IBA.

In particular, the benchmarking of the present cross section datasets for the p+^{7}Li, p+^{19}F and d+^{nat}Mg systems yielded quite satisfactory results, thus validating all the obtained data. The extra benchmarking measurements involved the validation of the existing differential cross sections of proton elastic scattering on ^{23}Na, ^{31}P, ^{nat}S, and ^{nat}Si. The corresponding studied evaluated data were found to be valid in most of the cases (in terms of energy regions and scattering angles), while selected benchmarks of experimentally determined cross sections (in the absence of evaluated ones at higher energies) indicated the reliable datasets, which could potentially be used in the corresponding evaluation process in order to extend it to higher energies.

The theoretical approach of calculating resonant elastic cross sections within the R-matrix framework has also been presented in this dissertation, followed by the implementation of such a procedure regarding the p+^{19}F system using the AZURE code. This work resulted in the reproduction of the existing evaluated cross-section data (SigmaCalc), which range up to 1730 keV, using a different code and their extension to ~2250 keV.

Nonetheless, special effort in the study of differential cross sections is in overall still required, in order to improve the accuracy and the reliability of all depth profiling IBA techniques. First of all, differential cross-section measurements are still needed, especially concerning the cases where the existing work in literature is poor, as in the case of deuteron elastic scattering on light elements. This would facilitate for example the simultaneous (and complementary) application of both EBS and NRA techniques, leading to far more accurate analytical IBA studies. It is also of crucial importance to validate all the existing cross-section data prior to their use, and especially the evaluated ones which are considered to be the most reliable datasets, since they are produced by incorporating all the corresponding experimental studies into the framework of a unified theoretical approach. The benchmarking procedure is therefore expected to become an important field of research in the following years, including and incorporating different techniques (e.g. using ΔE/E detectors) and/or using different targets.

Moreover, the extension of the existing evaluations to higher beam energies is indeed needed for the implementation of the IBA profiling techniques at higher depths. New cross-section measurements, along with the corresponding benchmarking spectra will enable such extensions of the evaluated cross section data, but can also facilitate the theoretical calculations to be applied in problematic cases, like the ^{nat}B(p,p) scattering, where no evaluated data exist, although highly needed by the IBA community.

It should also be noted that the present study of the d+^{nat}Mg system revealed an unexpected resonant-like structure, due to the existence of several, possibly overlapping resonances. There is however no reference in all nuclear compilation reports in literature to the corresponding excited states of the compound nucleus ^{26}Al for the center of mass energy range covered in the present work. The relevant comprehensive datasets of the present work cover a wide angular range and several exit channels and can therefore possibly contribute to a future level characterization.

APPENDIX A

Table 1: Differential cross-section values of the proton elastic scattering on ^{7}Li.

E_{lab} (keV)	δE_{lab} (keV)	$\sigma \pm \delta\sigma$ (mb/sr), ^{7}**Li(p,p$_0$)**							
		140º		150º		160º		170º	
1498	3	31.5	0.7	27.6	0.6	27.4	0.5	27.9	0.6
1598	3	32.3	0.6	27	0.6	26.8	0.5	26.6	0.9
1698	3	32.3	0.5	25.6	0.5	25.1	0.7	26.9	1.0
1798	3	29.0	0.6	25.2	0.4	20.1	0.5	19.6	0.5
1848	3	39.9	0.5	32.3	0.6	34.1	0.4	28.3	0.4
1873	3	35.7	0.5	31.7	0.4	30.3	0.4	26.9	0.6
1898	3	39.4	0.5	36.3	0.5	37.1	0.4	37.9	0.5
1923	3	51.4	0.6	51.5	0.5	46.8	0.5	52.1	0.5
1948	3	64.7	0.7	66.5	0.6	65.3	0.6	68.0	0.6
1973	3	77.4	0.8	80.9	0.6	80.9	0.6	82.3	0.7
1998	3	84.8	0.8	90.9	0.6	92.0	0.7	92.6	0.7
2023	3	84.1	0.8	93.9	0.7	96.2	0.7	99.1	0.7
2048	3	86.3	0.8	93.2	0.6	97.3	0.7	99.7	0.7
2073	4	81.6	0.8	90.5	0.6	93.2	0.7	95.8	0.7
2098	4	73.2	0.7	81.8	0.6	84.6	0.6	86.9	0.7
2123	4	60.8	0.6	67.6	0.5	71.3	0.6	73.2	0.6
2148	4	48.9	0.5	53.7	0.5	56.8	0.5	59.1	0.5
2173	4	35.4	0.5	38.7	0.4	40.5	0.5	40.8	0.5
2198	4	25.1	0.4	25.9	0.3	27.7	0.4	27.3	0.4
2298	4	52.1	0.6	53.8	0.5	55.8	0.5	56.3	0.5
2398	4	68.9	0.8	71.8	0.6	78.3	0.7	81.1	0.7
2499	4	68.9	0.7	76.7	0.6	80.0	0.6	85.9	0.7
2599	4	67.3	0.7	75.5	0.6	77.8	0.6	81.3	0.7
2699	5	66.4	0.7	72.4	0.6	76.2	0.6	79.1	0.6
2799	5	63.7	0.7	71.9	0.6	74.9	0.6	77.7	0.6
2899	5	66.5	0.7	72.9	0.6	76.2	0.6	82.1	0.7
2999	5	69.1	0.7	77.0	0.6	82.9	0.6	86.2	0.7
3099	5	71.3	0.7	80.3	0.6	86.4	0.7	90.9	0.7
3199	5	73.6	0.7	81.0	0.6	92.4	0.7	94.2	0.7
3299	6	74.9	0.7	87.2	0.6	95.1	0.7	99.1	0.7
3399	6	77.0	0.7	88.4	0.5	97.4	0.6	101.5	0.7
3499	6	78.6	0.7	89.1	0.5	100.3	0.6	105.4	0.7
3599	6	80.1	0.7	91.8	0.5	102.9	0.6	108.5	0.7
3699	6	81.6	0.7	96.0	0.5	103.7	0.6	112.2	0.7
3799	6	82.6	0.7	95.9	0.5	107.3	0.6	113.4	0.7
3899	7	84.5	0.7	104.4	0.5	110.6	0.6	118.0	0.7
3999	7	86.2	0.7	105.2	0.5	113.1	0.6	116.7	0.7
4099	7	81.3	0.5	88.9	0.4	103.6	0.5	107.6	0.6
4199	7	81.2	0.5	91.7	0.4	105.5	0.5	109.6	0.6
4299	7	81.6	0.5	91.4	0.4	104.2	0.5	108.7	0.6

4399	7	79.8	0.5	89.4	0.4	100.5	0.5	104.5	0.6
4499	8	76.8	0.5	85.6	0.4	97.1	0.5	100.7	0.5
4599	8	71.8	0.4	78.8	0.4	88.0	0.4	91.2	0.5
4699	8	65.1	0.4	71.5	0.4	78.6	0.4	77.1	0.4
4799	8	58.6	0.4	63.7	0.3	-			
4899	8	52.3	0.4	56.8	0.4	-			
4999	8	47.1	0.3	55.2	0.3	-	-		
5099	9	-	-	-	-	46.3	1.2	46.2	0.4
5199	9	-	-	-	-	39.0	0.3		
5299	9	38.5	0.3	35.9	0.3	-	-		
5399	9	36.3	0.3	35.9	0.6	-	-		
5499	9	35.5	0.3	33.2	1.8	33.8	0.4		
5599	10	34.6	0.3	29.7	0.3	-	-		
5699	10	34.3	0.3	29.5	0.2	-	-		
5799	10	32.6	0.2	28.8	0.2	-	-	33.8	0.3
5899	10	-	-	-	-	32.5	0.4	32.6	0.3
5999	10	-	-	-	-	32.3	0.4	32.2	0.2
6099	10	-	-	-	-	31.0	0.2	30.8	0.2
6199	11	-	-	-	-	29.4	0.2	29.7	0.2
6299	11	-	-	-	-	29.8	0.2	30.0	0.2
6399	11	29.1	0.2	28.1	0.2	29.8	0.2	29.7	0.2
6499	11	27.6	0.1	27.0	0.2	28.5	0.2	29.0	0.2
6599	11	27.3	0.3	26.8	0.2	27.9	0.2	28.2	0.2
6699	11	26.0	0.3	26.1	0.2	26.9	0.2	26.9	0.2
6799	12	25.0	0.2	25.2	0.2	26.1	0.2	25.9	0.2
6899	12	24.4	0.2	24.3	0.2	24.6	0.2	24.7	0.2
6999	12	22.8	0.2	23.0	0.2	23.8	0.2	23.9	0.2

Table 2: Differential cross-section values of the $^{7}Li(p,p_1)^{7}Li$ reaction.

E_{lab} (keV)	δE_{lab} (keV)	$\sigma \pm \delta\sigma$ (mb/sr), **$^{7}Li(p,p_1)$**							
		140º		150º		160º		170º	
1498	3	4.5	0.2	3.8	0.3	4.3	0.3	5.5	0.2
1598	3	4.8	0.2	5.3	0.2	5.3	0.3	4.7	0.2
1698	3	5.5	0.2	6.6	0.3	6.3	0.3	5.9	0.3
1798	3	5.4	0.4	6.1	0.2	5.5	0.3	5.9	0.2
1848	3	6.0	0.2	6.4	0.2	6.2	0.2	6.6	0.2
1873	3	5.2	0.2	5.7	0.2	5.7	0.2	5.5	0.2
1898	3	5.2	0.2	5.5	0.2	6.0	0.2	5.4	0.2
1923	3	5.1	0.5	5.3	0.2	5.7	0.3	6.2	0.2
1948	3	4.3	0.3	5.2	0.3	4.4	0.3	5.1	0.2
1973	3	5.7	0.2	6.5	0.2	5.1	0.2	5.1	0.2
1998	3	5.6	0.5	6.2	0.2	6.7	0.3	6.1	0.3
2023	3	5.5	0.3	6.1	0.2	6.8	0.2	6.8	0.2
2048	3	5.9	0.2	6.4	0.2	6.2	0.2	5.8	0.2
2073	4	5.8	0.3	6.0	0.2	6.6	0.2	6.5	0.2
2098	4	5.4	0.3	6.3	0.2	6.3	0.2	6.6	0.2
2123	4	5.9	0.3	6.1	0.2	6.0	0.2	5.6	0.2

2148	4	5.4	0.3	6.4	0.2	6.5	0.3	5.8	0.2
2173	4	5.8	0.4	5.7	0.2	6.8	0.2	6.0	0.2
2198	4	6.1	0.3	6.5	0.2	6.3	0.2	6.3	0.2
2298	4	6.3	0.3	6.5	0.2	7.0	0.2	6.4	0.2
2398	4	6.0	0.4	6.0	0.2	7.0	0.3	6.0	0.2
2499	4	7.1	0.3	8.0	0.3	7.0	0.2	7.0	0.2
2599	4	7.3	0.3	8.7	0.3	8.6	0.3	8.1	0.2
2699	5	8.8	0.3	8.7	0.2	8.0	0.3	8.0	0.3
2799	5	8.9	0.3	9.0	0.2	8.9	0.3	9.1	0.2
2899	5	10.4	0.5	10.6	0.3	10.1	0.1	9.8	0.3
2999	5	10.7	0.2	10.7	0.2	11.4	0.1	11.0	0.2
3099	5	10.5	0.3	12.0	0.3	11.7	0.1	11.9	0.3
3199	5	12.0	0.3	12.8	0.3	11.8	0.3	12.8	0.3
3299	6	12.2	0.3	12.3	0.3				
3399	6	12.4	0.4						
3499	6	9.9	0.2						
3599	6							12.4	0.2
3699	6					12.2	0.3		
3799	6			11.5	0.1				
3899	7	10.7	0.2						
3999	7								
4099	7	10.4	0.1	10.6	0.1				
4199	7	10.5	0.1						
4299	7	10.1	0.4						
4399	7								
4499	8					12.9	0.2		
4599	8			10.9	0.2	11.8	0.2		
4699	8			10.9	0.2	11.4	0.1	11.3	0.1
4799	8	8.8	0.2	10.9	0.1	11.0	0.2	11.4	0.1
4899	8	8.1	0.2	10.9	0.1	11.5	0.1	11.2	0.1
4999	8					13.2	0.2		
5099	9	10.8	0.2	12.7	0.2	13.1	0.2	12.6	0.1
5199	9	11.9	0.3	13.1	0.2	13.6	0.2	13.6	0.2
5299	9	15.1	0.3	15.4	0.2	16.0	0.2	15.6	0.2
5399	9	14.7	0.3	14.8	0.2	15.0	0.2	15.0	0.2
5499	9	13.1	0.2	13.9	0.1	15.0	0.2	14.7	0.2
5599	10	14.5	0.3	15.4	0.2	16.0	0.2	16.3	0.2
5699	10	14.3	0.2	15.2	0.2	15.2	0.2	14.6	0.3
5799	10	13.2	0.1	14.1	0.2	14.1	0.2	13.0	0.5
5899	10	11.3	0.2	13.2	0.3			12.3	0.7
5999	10	10.0	0.2	11.6	0.1				
6099	10	9.3	0.2	10.2	0.1				
6199	11	8.9	0.2	10.2	0.2				
6299	11	9.1	0.2						
6399	11								
6499	11								
6599	11								
6699	11			9.9	0.1				

Table 3: Differential cross-section values of the $^{7}Li(p,\alpha_0)^{4}He$ reaction.

E_{lab} (keV)	δE_{lab} (keV)	$\sigma \pm \delta\sigma$ (mb/sr), **$^{7}Li(p,\alpha_0)$**							
		140º		150º		160º		170º	
1498	3	1.97	0.07	2.02	0.08	2.21	0.09	2.15	0.08
1598	3	2.25	0.07	2.26	0.09	2.49	0.09	2.3	0.1
1698	3	2.34	0.07	2.5	0.09	2.9	0.1	2.6	0.1
1798	3	2.49	0.07	2.82	0.08	2.66	0.08	2.68	0.07
1848	3	2.55	0.08	2.8	0.1	2.8	0.1	2.76	0.09
1873	3	2.59	0.08	3.0	0.1	2.9	0.1	2.81	0.09
1898	3	2.83	0.08	2.91	0.09	2.8	0.1	3.06	0.09
1923	3	2.79	0.08	3.0	0.1	3.0	0.1	2.93	0.09
1948	3	2.98	0.08	3.2	0.1	3.2	0.1	3.3	0.1
1973	3	2.93	0.08	3.3	0.1	3.1	0.1	3.2	0.1
1998	3	3.07	0.09	3.3	0.1	3.5	0.1	3.3	0.1
2023	3	3.17	0.09	3.5	0.1	3.3	0.1	3.5	0.1
2048	3	3.22	0.09	3.5	0.1	3.5	0.1	3.6	0.1
2073	4	3.41	0.09	3.6	0.1	3.5	0.1	3.7	0.1
2098	4	3.35	0.09	3.7	0.1	3.7	0.1	3.6	0.1
2123	4	3.62	0.09	3.7	0.1	3.7	0.1	3.8	0.1
2148	4	3.75	0.10	4.1	0.1	3.8	0.1	3.8	0.1
2173	4	3.95	0.10	4.2	0.1	4.0	0.1	4.1	0.1
2198	4	3.96	0.10	4.3	0.1	3.9	0.1	4.0	0.1
2298	4	4.23	0.10	4.6	0.1	4.7	0.1	4.4	0.1
2398	4	4.86	0.11	4.9	0.1	4.8	0.2		
2499	4	5.11	0.12	5.1	0.1				
2599	4	5.61	0.12			5.9	0.2	5.7	0.1
2699	5	5.97	0.14			6.1	0.1	5.7	0.1
2799	5			6.0	0.2	5.8	0.1	5.7	0.1
2899	5			6.3	0.1	5.6	0.1	5.5	0.1
2999	5	5.88	0.16	5.9	0.1	5.4	0.1	5.2	0.1
3099	5	5.71	0.14	5.4	0.1	4.4	0.1	4.3	0.1
3199	5	5.31	0.12	4.2	0.1	3.6	0.1	3.4	0.1
3299	6	4.14	0.10	3.6	0.1	3.0	0.1	2.70	0.09
3399	6	3.47	0.07	2.85	0.07	2.27	0.07	2.12	0.06
3499	6	2.80	0.06	2.21	0.06	1.89	0.06	1.60	0.05
3599	6	2.26	0.06	1.89	0.06	1.47	0.05	1.32	0.05
3699	6	1.87	0.05	1.62	0.05	1.18	0.04	1.06	0.04
3799	6	1.62	0.04	1.40	0.04	1.14	0.04	0.95	0.03
3899	7	1.45	0.04	1.30	0.04	0.99	0.04	0.87	0.03
3999	7	1.29	0.03	1.17	0.04	0.99	0.04	0.81	0.03
4099	7	1.09	0.03	0.95	0.03	0.81	0.03	0.71	0.02
4199	7	0.95	0.03	0.93	0.03	0.83	0.03	0.71	0.02
4299	7	0.94	0.03	0.93	0.03	0.83	0.03	0.71	0.02
4399	7	0.89	0.03	0.85	0.03	0.79	0.03	0.65	0.02
4499	8	0.81	0.03	0.85	0.03	0.76	0.03	0.67	0.02
4599	8	0.77	0.02	0.80	0.03	0.71	0.03	0.64	0.02
4699	8	0.70	0.02	0.71	0.03	0.64	0.03	0.59	0.02
4799	8	0.64	0.02	0.68	0.03	0.58	0.02	0.49	0.02

4899	8	0.63	0.02	0.63	0.02	0.53	0.02	0.45	0.02
4999	8	0.67	0.02	0.57	0.02	0.45	0.02	0.32	0.02
5099	9	0.76	0.02	0.59	0.02	0.42	0.02	0.24	0.01
5199	9	0.94	0.03	0.68	0.03	0.43	0.02	0.19	0.01
5299	9	1.23	0.03	0.81	0.03	0.5	0.02	0.26	0.02
5399	9	1.62	0.04	1.15	0.03	0.6	0.03	0.36	0.02
5499	9	1.99	0.04	1.33	0.04	0.85	0.03	0.51	0.02
5599	10	2.22	0.04	1.51	0.04	1.10	0.03	0.75	0.03
5699	10	2.32	0.04	1.71	0.04	1.22	0.04	0.94	0.03
5799	10	2.26	0.04	1.82	0.04	1.40	0.04	1.04	0.03
5899	10	2.22	0.04	1.83	0.04	1.47	0.04	1.19	0.03
5999	10	2.31	0.04	1.90	0.04	1.65	0.04	1.25	0.03
6099	10	2.27	0.04	1.86	0.04	1.57	0.04	1.34	0.03
6199	11	2.09	0.04	1.87	0.04	1.55	0.04	1.35	0.03
6299	11	2.03	0.04	1.70	0.04	1.55	0.04	1.32	0.03
6399	11	1.96	0.04	1.74	0.04	1.53	0.04	1.24	0.03
6499	11	1.90	0.04	1.73	0.04	1.49	0.04	1.21	0.03
6599	11	1.89	0.04	1.58	0.04	1.48	0.04	1.13	0.03
6699	11	1.90	0.04	1.69	0.04	1.39	0.04	1.18	0.03
6799	12	1.88	0.04	1.70	0.04	1.41	0.04	1.18	0.03
6899	12	1.92	0.04	1.68	0.04	1.48	0.04	1.20	0.03
6999	12	1.85	0.04	1.76	0.04	1.48	0.04	1.30	0.03

APPENDIX B

Table B1: Differential cross-section values of the proton elastic scattering on ^{19}F.

E_{lab} (keV)	δE_{lab} (keV)	$\sigma \pm \delta\sigma$ (mb/sr), $^{19}F(p,p_0)$							
		140º		150º		160º		170º	
1498	3	103.7	2.4	95	4	86	4	82	3
1598	3	79.1	1.4	72	3	66.2	1.9	64.0	2.0
1650	3					55.9	2.2	51.4	2.1
1670	3					51.0	2.0	50.9	2.0
1690	3					49.0	2.0	51.5	2.1
1698	3	67.8	1.3	65.6	2.0				
1700	3					50.6	2.0	52.5	2.1
1710	3					57.4	2.3	57.3	2.3
1730	3					68.4	2.7	69.6	2.8
1798	3	62.1	1.1	57.0	1.1	51.2	1.5	49.2	2.0
1848	3	46.4	1.0	44.0	2.0	39.3	1.1	38.8	1.5
1873	3	39.4	1.0	39.3	1.5	34.6	0.7	35.8	1.4
1898	3	31.3	0.9	32.2	0.9	29.5	0.7	29.8	1.4
1923	3	19.9	0.7	19.3	0.6	15.8	0.5	15.8	0.7
1948	3	45.1	1.2	38.8	0.9	31.2	0.5	29.2	0.7
1973	3	38.4	0.9	32.6	0.8	25.9	0.5	23.6	0.7
1998	3	33.0	0.9	25.0	0.5	23.5	0.5	21.3	0.7
2023	3	35.8	0.9	29.1	0.9	26.9	0.5	25.6	0.7
2048	3	41.3	0.9	37.6	0.9	31.8	0.5	30.9	0.7
2073	4	42.5	0.9	39.9	0.9	34.7	0.7	32.9	0.7
2098	4	41.4	0.9	39.7	0.9	33.8	0.7	32.7	0.7
2123	4	37.6	0.9	35.2	0.9	31.0	0.5	30.6	0.7
2148	4	33.3	0.9	31.4	0.9	27.4	0.5	26.3	0.7
2173	4	29.7	0.9	29.1	0.9	24.8	0.5	23.9	0.7
2198	4	25.8	0.7	25.5	0.9	22.6	0.5	22.1	0.7
2298	4	30.7	0.9	34.7	0.9	34.1	0.7	35.3	0.7
2398	4	45.1	1.2	43.9	0.9	38.1	0.7	36.5	0.7
2499	4	26.3	0.9	24.7	0.9	21.1	0.7	19.8	0.5
2599	4	31.8	0.9	28.9	0.9	24.0	0.7	22.1	0.4
2699	5	46.6	1.2	43.7	0.9	35.4	0.7	34.5	0.5
2799	5	46.4	1.2	36.0	0.9	30.4	0.7	26.2	0.5
2899	5	41.9	0.9	31.8	0.9	27.8	0.5	25.5	0.4
2999	5	37.3	0.9	33.4	0.9	27.2	0.7	24.7	0.4
3099	5	31.3	0.9	30.3	0.9				
3199	5	18.9	0.7	17.8	1.2				
3299	6	28.7	0.9						
3599	6					25.0	0.9		
3799	6			38.3	1.1				
3899	7	50.4	0.8						
3999	7	45.9	0.7						
4099	7	25.5	0.5						

4199	7	23.9	0.7						
4299	7					21.3	0.5	17.3	0.4
4399	7					21.3	0.3	19.6	0.4
4499	8			12.9	0.5	11.8	0.2	10.7	0.2
4599	8			19.1	0.5	14.4	0.2	12.0	0.2
4699	8	16.8	0.4	13.3	0.5	11.7	0.2	10.7	0.2
4799	8	21.1	0.4	15.8	0.5	10.6	0.2	6.6	0.2
4899	8	16.1	0.5	13.0	0.5	10.7	0.2	9.9	0.2
4999	8	22.2	0.4	20.8	0.5	19.7	0.2	19.2	0.3
5099	9	20.4	0.4	16.5	0.5	13.0	0.5	11.9	0.4
5199	9	19.3	0.4	16.8	0.5	12.9	0.5	10.7	0.4
5299	9	25.4	0.5	19.9	0.5	13.3	0.5	9.6	0.2
5399	9	24.3	0.5	18.1	0.5	11.5	0.5	5.8	0.2
5499	9	24.4	0.5	18.5	0.5	10.3	0.5	5.5	0.2
5599	10	20.2	0.4	15.0	0.5	8.3	0.5	4.0	0.2
5699	10	18.2	0.4	13.7	0.5	7.3	0.5	3.4	0.2
5799	10	14.0	0.4	10.3	0.5	5.9	0.5	2.9	0.2
5899	10	13.3	0.4	10.3	0.5	9.5	0.5	8.8	0.2
5999	10	18.1	0.4	17.8	0.5	17.8	0.5	18.3	0.2
6099	10	20.4	0.4	16.2	0.5	12.7	0.5	11.6	0.2
6199	11	18.1	0.4	13.6	0.5	9.4	0.5		
6299	11	15.7	0.4	12.3	0.5	9.2	0.5		
6399	11	14.2	0.3	13.0	0.5				
6499	11			13.7	0.4				

Table B2: Differential cross-section values of the $^{19}F(p,\alpha_0)^{16}O$ reaction.

E_{lab} (keV)	δE_{lab} (keV)	$\sigma \pm \delta\sigma$ (mb/sr), **$^{19}F(p,\alpha_0)$**							
		140º		150º		160º		170º	
1498	3	0.56	0.04	0.49	0.04	0.37	0.03	0.36	0.03
1598	3	1.08	0.05	1.33	0.09	1.49	0.10	1.57	0.08
1698	3	0.92	0.05	0.69	0.06	0.71	0.05	0.69	0.05
1798	3	2.97	0.11	3.76	0.13	4.03	0.15	4.26	0.10
1848	3	3.77	0.14	4.48	0.18	5.36	0.22	5.63	0.14
1873	3	3.15	0.13	4.12	0.17	4.11	0.20	4.76	0.13
1898	3	2.36	0.11	2.77	0.13	2.99	0.16	3.35	0.11
1923	3	1.89	0.10	2.06	0.08	2.21	0.13	2.26	0.08
1948	3	1.37	0.08	1.60	0.07	1.69	0.13	1.72	0.07
1973	3	1.11	0.08	1.07	0.05	0.98	0.07	1.15	0.07
1998	3	0.78	0.07	0.71	0.05	0.67	0.05	0.62	0.04
2023	3	0.66	0.06	0.68	0.05	0.51	0.05	0.53	0.04
2048	3	0.71	0.06	0.62	0.04	0.49	0.03	0.43	0.03
2073	4	0.54	0.06	0.54	0.04	0.46	0.03	0.40	0.03
2098	4	0.79	0.07	0.72	0.05	0.53	0.05	0.44	0.03
2123	4	1.11	0.08	0.73	0.05	0.48	0.03	0.32	0.03
2148	4	1.04	0.07	0.78	0.05	0.61	0.05	0.43	0.03
2173	4	0.97	0.07	0.99	0.05	0.9	0.05	0.83	0.05
2198	4	1.22	0.08	1.11	0.09	1.09	0.08	1.01	0.08

2298	4	3.91	0.14	4.69	0.17	5.06	0.2	5.10	0.19
2398	4	2.09	0.11	2.38	0.08	2.46	0.16		
2499	4	2.67	0.12	3.20	0.15				
2599	4	3.05	0.13					3.86	0.15
2699	5	2.05	0.12			2.29	0.13	2.42	0.12
2799	5			1.13	0.09	0.82	0.07	0.63	0.04
2899	5			1.56	0.10	1.50	0.07	1.58	0.07
2999	5			1.73	0.10	1.41	0.07	1.35	0.07
3099	5	2.26	0.11	2.82	0.14	2.94	0.10	3.15	0.10
3199	5	3.04	0.13	3.39	0.15	3.73	0.12	4.04	0.11
3299	6	2.46	0.12	3.20	0.15	3.94	0.12	4.71	0.12
3399	6	0.54	0.04	0.87	0.06	1.20	0.05	1.43	0.05
3499	6	1.09	0.05	0.88	0.05			0.41	0.02
3599	6	0.89	0.05	0.86	0.05			1.27	0.07
3699	6	1.13	0.05					2.28	0.08
3799	6	1.41	0.05					3.23	0.06
3899	7	1.47	0.05					4.25	0.10
3999	7	1.12	0.05					3.49	0.06
4099	7	0.61	0.03					3.07	0.08
4199	7	0.33	0.02					0.23	0.02
4299	7	0.78	0.03					1.00	0.03

Table B3: Differential cross-section values of the $^{19}F(p,\alpha_{1,2})^{16}O$ reaction.

E_{lab} (keV)	δE_{lab} (keV)	$\sigma \pm \delta\sigma$ (mb/sr), **$^{19}F(p,\alpha_{1,2})$**							
		140º		150º		160º		170º	
1498	3	1.6	0.1	1.8	0.1	2.0	0.1	1.83	0.07
1598	3	2.8	0.1	2.8	0.1	2.8	0.1	2.79	0.11
1698	3	3.0	0.1	2.7	0.1	2.6	0.1	2.86	0.13
1798	3	1.9	0.1	2.1	0.1	2.3	0.1	2.25	0.07
1848	3	3.6	0.1	4.0	0.1	4.2	0.1	4.29	0.11
1873	3	3.5	0.1	3.7	0.1	4.5	0.1	4.49	0.12
1898	3	3.5	0.1	3.7	0.1	4.6	0.1	4.44	0.11
1923	3	4.5	0.1	4.6	0.1	4.8	0.1	4.92	0.12
1948	3	2.9	0.1	3.0	0.1	3.2	0.1	3.31	0.10
1973	3	2.0	0.1	2.0	0.1	1.7	0.1	1.91	0.07
1998	3	1.7	0.1	1.3	0.1	1.1	0.1	0.88	0.05
2023	3	2.0	0.1	1.3	0.1	0.8	0.1	0.47	0.04
2048	3	2.3	0.1	1.5	0.1	0.8	0.1	0.44	0.03
2073	4	2.1	0.1	1.4	0.1	0.8	0.1	0.46	0.04
2098	4	1.9	0.1	1.4	0.1	0.8	0.1	0.57	0.04
2123	4	2.1	0.1	1.5	0.1	1.1	0.1	0.88	0.05
2148	4	2.7	0.1	2.5	0.1	2.1	0.1	1.68	0.07
2173	4	3.0	0.1	2.8	0.1	2.6	0.1	2.22	0.08
2198	4	3.0	0.1	3.0	0.1	2.9	0.1	2.77	0.09
2298	4	4.5	0.1	4.5	0.1	3.6	0.1	3.66	0.10
2398	4	4.7	0.1	4.4	0.1	3.6	0.1	3.28	0.10

2499	4	10.7	0.2	10.5	0.2	10.2	0.2	9.94	0.17
2599	4	8.6	0.2	9.2	0.2	8.7	0.2	8.50	0.16
2699	5	3.9	0.1	4.3	0.1	4.1	0.1	4.23	0.11
2799	5	5.1	0.1	4.9	0.1	4.6	0.1	4.47	0.11
2899	5	2.5	0.1	2.3	0.1	1.6	0.1	1.24	0.06
2999	5	3.0	0.1	2.9	0.1	2.9	0.1	3.13	0.09
3099	5	5.6	0.1	5.7	0.1	5.4	0.1	4.97	0.12
3199	5	4.5	0.1	4.8	0.1	4.6	0.1	4.41	0.11
3299	6	3.4	0.1	3.0	0.1	2.1	0.1	1.48	0.07
3399	6	2.4	0.1	2.4	0.1	2.2	0.1	2.38	0.07
3499	6	4.2	0.1	3.5	0.1	3.2	0.1	2.68	0.09
3599	6	2.8	0.1	2.6	0.1	2.6	0.1		
3699	6	2.4	0.1	2.6	0.1				
3799	6	3.0	0.1						
3899	7	3.7	0.1						

APPENDIX C

Table C1: Differential cross-section values of the proton elastic scattering on ^{nat}Mg at 55 º-125 º.

E_{lab} (keV)	δE_{lab} (keV)	$\sigma \pm \delta\sigma$ (mb/sr), ^{nat}**Mg(d,d$_0$)**							
		55º		70º		90º		125º	
1663	6	1540	80	610	30	249	12	98	5
1668	6	1510	80	600	30	248	12	96	5
1673	6	1460	70	600	30	244	12	96	5
1678	6	1520	80	600	30	247	12	95	5
1683	6	1490	70	600	30	244	12	96	5
1688	6	1460	70	600	30	245	12	96	5
1693	6	1500	80	588	29	242	12	96	5
1698	6	1470	70	589	29	241	12	95	5
1703	6	1430	70	581	29	238	12	96	5
1708	6	1460	70	580	29	237	12	95	5
1713	6	1440	70	575	29	235	12	95	5
1718	6	1400	70	566	28	236	12	94	5
1723	6	1420	70	564	28	232	12	93	5
1728	6	1400	70	558	28	231	12	93	5
1733	6	1360	70	560	28	231	12	90	5
1738	6	1390	70	557	28	228	11	89	4
1743	6	1370	70	549	27	226	11	88	4
1748	6	1400	70	551	28	224	11	86	4
1753	6	1370	70	545	27	222	11	85	4
1758	6	1330	70	545	27	220	11	85	4
1763	6	1350	70	535	27	216	11	85	4
1768	6	1330	70	528	26	216	11	84	4
1773	6	1300	70	531	27	214	11	82	4
1778	6	1330	70	525	26	213	11	82	4
1783	6	1300	70	521	26	213	11	83	4
1785	6	1290	70	518	26	211	11	82	4
1787	6	1270	60	511	26	209	10	81	4
1789	6	1270	60	517	26	210	11	81	4
1791	6	1260	60	517	26	210	11	80	4
1793	6	1310	70	512	26	208	10	80	4
1795	6	1300	70	510	26	207	10	81	4
1797	6	1280	60	511	26	207	10	80	4
1799	6	1270	60	506	25	206	10	79	4
1801	6	1270	60	512	26	206	10	79	4
1803	6	1260	60	509	25	205	10	78	4
1808	6	1280	60	508	25	204	10	79	4
1813	6	1260	60	509	25	202	10	78	4
1818	6	1270	60	502	25	200	10	78	4
1823	6	1280	60	497	25	197	10	77	4
1828	6	1250	60	494	25	195	10	77	4
1834	6	1230	60	489	24	194	10	77	4
1839	6	1260	60	481	24	191	10	76	4

1844	6	1220	60	479	24	187	9	77	4
1849	6	1190	60	473	24	186	9	77	4
1854	6	1210	60	463	23	184	9	77	4
1859	6	1190	60	459	23	181	9	78	4
1864	6	1150	60	452	23	182	9	79	4
1869	6	1170	60	450	23	182	9	79	4
1874	6	1150	60	448	22	181	9	81	4
1879	6	1170	60	440	22	181	9	83	4
1884	6	1150	60	441	22	183	9	84	4
1889	6	1120	60	443	22	184	9	84	4
1894	6	1140	60	437	22	185	9	85	4
1899	6	1110	60	442	22	184	9	84	4
1904	6	1100	60	439	22	185	9	85	4
1909	6	1120	60	442	22	186	9	84	4
1914	6	1100	60	437	22	184	9	83	4
1919	6	1090	50	436	22	183	9	83	4
1924	6	1120	60	438	22	184	9	82	4
1929	6	1100	60	436	22	183	9	81	4
1934	6	1120	60	429	21	181	9	80	4
1939	6	1100	60	433	22	180	9	80	4
1944	6	1090	50	427	21	178	9	80	4
1949	6	1060	50	426	21	177	9	79	4
1954	6	1070	50	418	21	175	9	78	4
1959	6	1050	50	416	21	175	9	78	4
1964	6	1060	50	415	21	174	9	79	4
1969	6	1050	50	411	21	174	9	78	4
1974	6	1030	50	412	21	172	9	78	4
1979	6	1050	50	412	21	172	9	77	4
1984	6	1030	50	405	20	171	9	77	4

Table C2:Differential cross-section values of the proton elastic scattering on ^{nat}Mg at 140 °-170 °

E_{lab} (keV)	δE_{lab} (keV)	$\sigma \pm \delta\sigma$ (mb/sr), **^{nat}Mg(d,d$_0$)**				E_{lab} (keV)	δE_{lab} (keV)	$\sigma \pm \delta\sigma$ (mb/sr), **^{nat}Mg(d,d$_0$)**			
		140º		150º				150º		170º	
1300	1			123	6	1663	6	68	4	60	3
1350	1			113	6	1668	6	68	4	60	3
1400	1			105	5	1673	6	69	4	60	3
1450	1			94	5	1678	6	68	4	61	3
1500	2	101	5	88	4	1683	6	68	4	60	3
1550	2	92	5	81	4	1688	6	69	4	61	3
1600	2	84	4	73	4	1693	6	69	4	62	3
1625	2	81	4	74	4	1698	6	71	4	64	3
1650	2	78	4	70	4	1703	6	71	4	63	3
1675	2	73	4	65	3	1708	6	69	4	63	3
1700	2	75	4	68	3	1713	6	70	4	63	3
1725	2	76	4	68	3	1718	6	68	4	61	3

1750	2	69	3	62	3	1723	6	67	4	60	3
1775	2	67	3	60	3	1728	6	66	3	59	3
1790	2	66	3	59	3	1733	6	65	3	57	3
1800	2	64	3	57	3	1738	6	63	3	56	3
1810	2	65	3	57	3	1743	6	63	3	56	3
1825	2	63	3	58	3	1748	6	63	3	55	3
1850	2	64	3	59	3	1753	6	62	3	55	3
1875	2	70	3	65	3	1758	6	61	3	54	3
1885	2	73	4	68	3	1763	6	61	3	54	3
1900	2	73	4	68	3	1768	6	61	3	53	3
1910	2	73	4	67	3	1773	6	61	3	54	3
1925	2	70	3	65	3	1778	6	60	3	53	3
1950	2	67	3	62	3	1783	6	60	3	52	3
1975	2	67	3	62	3	1785	6	60	3	53	3
2000	2	62	3	56	3	1787	6	59	3	53	3
2025	2	57	3	53	3	1789	6	59	3	52	3
2050	2	56	3	51	3	1791	6	59	3	52	3
						1793	6	59	3	52	3
						1795	6	60	3	53	3
						1797	6	59	3	52	3
						1799	6	59	3	52	3
						1801	6	59	3	53	3
						1803	6	58	3	52	3
						1808	6	58	3	53	3
						1813	6	58	3	53	3
						1818	6	59	3	54	3
						1823	6	59	3	53	3
						1828	6	60	3	54	3
						1834	6	60	3	54	3
						1839	6	60	3	55	3
						1844	6	60	3	56	3
						1849	6	60	3	55	3
						1854	6	62	3	56	3
						1859	6	62	3	57	3
						1864	6	63	3	58	3
						1869	6	64	3	59	3
						1874	6	65	3	61	3
						1879	6	66	3	62	3
						1884	6	67	4	63	3
						1889	6	68	4	62	3
						1894	6	68	4	63	3
						1899	6	67	4	63	3
						1904	6	67	4	62	3
						1909	6	67	4	62	3
						1914	6	66	3	61	3
						1919	6	66	3	61	3
						1924	6	65	3	60	3
						1929	6	65	3	60	3
						1934	6	64	3	60	3
						1939	6	63	3	59	3

						1944	6	63	3	59	3
						1949	6	63	3	59	3
						1954	6	63	3	59	3
						1959	6	62	3	58	3
						1964	6	63	3	57	3
						1969	6	62	3	57	3
						1974	6	61	3	56	3
						1979	6	61	3	56	3
						1984	6	60	3	56	3

Table C3: Differential cross-section values of the $^{24}Mg(d,p_0)\,^{25}Mg$ reaction at 55 º-125 º.

E_{lab} (keV)	δE_{lab} (keV)	$\sigma \pm \delta\sigma$ (mb/sr), **$^{24}Mg(d,p_0)$**							
		55º		70º		90º		125º	
1663	6	0.72	0.05	0.48	0.04	0.40	0.03	0.34	0.04
1668	6	0.70	0.04	0.50	0.04	0.37	0.03	0.35	0.06
1673	6	0.72	0.04	0.48	0.04	0.39	0.04	0.39	0.05
1678	6	0.74	0.05	0.46	0.03	0.36	0.05	0.45	0.05
1683	6	0.65	0.04	0.50	0.04	0.41	0.04	0.44	0.05
1688	6	0.66	0.04	0.44	0.03	0.46	0.04	0.48	0.05
1693	6	0.72	0.04	0.48	0.04	0.47	0.04	0.51	0.06
1698	6	0.73	0.05	0.53	0.04	0.55	0.04	0.56	0.05
1703	6	0.67	0.04	0.59	0.04	0.53	0.04	0.57	0.05
1708	6	0.79	0.05	0.62	0.04	0.60	0.04	0.64	0.07
1713	6	0.82	0.05	0.67	0.05	0.60	0.04	0.61	0.07
1718	6	0.78	0.05	0.74	0.05	0.62	0.04	0.69	0.07
1723	6	0.82	0.05	0.79	0.05	0.65	0.04	0.59	0.05
1728	6	0.91	0.05	0.90	0.06	0.66	0.04	0.61	0.05
1733	6	0.90	0.05	0.88	0.06	0.70	0.05	0.62	0.06
1738	6	1.01	0.06	0.87	0.06	0.83	0.06	0.67	0.06
1743	6	1.00	0.06	0.90	0.06	0.83	0.06	0.66	0.06
1748	6	1.11	0.06	1.03	0.06	0.88	0.06	0.74	0.08
1753	6	1.11	0.06	1.11	0.07	0.97	0.06	0.73	0.07
1758	6	1.11	0.06	1.17	0.07	0.99	0.06	0.77	0.06
1763	6	1.22	0.07	1.20	0.07	1.19	0.08	0.84	0.06
1768	6	1.19	0.07	1.27	0.08	1.18	0.08	0.88	0.08
1773	6	1.43	0.08	1.40	0.08	1.27	0.08	1.00	0.10
1778	6	1.55	0.09	1.54	0.09	1.32	0.08	0.90	0.09
1783	6	1.60	0.09	1.60	0.09	1.44	0.09	0.96	0.09
1785	6	1.74	0.10	1.69	0.10	1.51	0.09	0.94	0.09
1787	6	1.60	0.09	1.73	0.10	1.49	0.09	1.05	0.09
1789	6	1.66	0.09	1.74	0.10	1.54	0.10	0.96	0.09
1791	6	1.69	0.09	1.75	0.10	1.54	0.09	0.96	0.09
1793	6	1.82	0.10	1.86	0.11	1.57	0.09	1.01	0.10
1795	6	1.89	0.10	1.90	0.11	1.64	0.10	1.06	0.10
1797	6	1.89	0.10	1.93	0.11	1.66	0.10	1.01	0.09
1799	6	1.86	0.10	1.93	0.11	1.74	0.11	1.03	0.09
1801	6	1.94	0.11	2.05	0.12	1.78	0.11	1.06	0.08

1803	6	1.96	0.11	1.98	0.11	1.75	0.11	1.07	0.08
1808	6	2.12	0.12	2.17	0.12	1.88	0.11	1.16	0.08
1813	6	2.12	0.12	2.23	0.13	1.82	0.11	1.16	0.10
1818	6	2.17	0.12	2.22	0.12	1.88	0.14	1.22	0.09
1823	6	2.32	0.13	2.12	0.12	1.84	0.11	1.12	0.09
1828	6	2.32	0.13	2.12	0.13	1.86	0.11	1.10	0.08
1834	6	2.29	0.12	2.21	0.12	1.82	0.14	1.10	0.08
1839	6	2.28	0.12	2.27	0.13	1.75	0.11	1.16	0.08
1844	6	2.36	0.13	2.08	0.13	1.80	0.11	1.11	0.08
1849	6	2.39	0.13	2.31	0.13	1.78	0.11	1.08	0.08
1854	6	2.41	0.14	2.23	0.14	1.75	0.12	1.15	0.08
1859	6	2.38	0.14	2.14	0.12	1.72	0.11	1.06	0.10
1864	6	2.50	0.14	2.17	0.12	1.78	0.12	1.12	0.12
1869	6	2.36	0.13	2.15	0.13	1.90	0.12	1.15	0.10
1874	6	2.33	0.13	2.07	0.12	1.84	0.12	1.21	0.09
1879	6	2.52	0.14	2.08	0.12	1.68	0.11	1.20	0.09
1884	6	2.28	0.13	1.99	0.12	1.61	0.11	1.21	0.10
1889	6	2.22	0.13	2.05	0.12	1.62	0.11	1.23	0.10
1894	6	2.17	0.13	1.93	0.11	1.59	0.10	1.19	0.08
1899	6	1.95	0.11	1.96	0.12	1.47	0.09	1.15	0.10
1904	6	2.00	0.11	1.81	0.11	1.61	0.11	1.13	0.08
1909	6	1.86	0.10	1.75	0.10	1.43	0.10	1.14	0.08
1914	6	1.77	0.10	1.62	0.10	1.35	0.10	1.21	0.09
1919	6	1.68	0.10	1.61	0.10	1.35	0.09	1.19	0.09
1924	6	1.85	0.10	1.63	0.10	1.28	0.10	1.17	0.08
1929	6	1.64	0.09	1.45	0.10	1.28	0.14	1.11	0.09
1934	6	1.77	0.10	1.36	0.09	1.25	0.09	0.99	0.09
1939	6	1.72	0.10	1.49	0.09	1.14	0.10	1.03	0.09
1944	6	1.81	0.10	1.48	0.09	1.12	0.08	1.04	0.09
1949	6	1.72	0.10	1.33	0.08	1.10	0.08	1.02	0.09
1954	6	1.72	0.10	1.42	0.09	1.11	0.09	1.10	0.10
1959	6	1.71	0.09	1.49	0.09	1.12	0.08	1.09	0.08
1964	6	1.73	0.10	1.35	0.08	1.10	0.08	0.99	0.11
1969	6	1.57	0.09	1.30	0.08	1.06	0.08	1.08	0.09
1974	6	1.51	0.08	1.30	0.08	1.03	0.08	1.14	0.11
1979	6	1.53	0.08	1.21	0.07	1.06	0.08	1.09	0.11
1984	6	1.44	0.09	1.30	0.07	0.98	0.07	1.06	0.10

Table C4: Differential cross-section values of the $^{24}Mg(d,p_1)\,^{25}Mg$ reaction at 55 º-125 º.

E_{lab} (keV)	δE_{lab} (keV)	$\sigma \pm \delta\sigma$ (mb/sr), **$^{24}Mg(d,p_1)$**							
		55º		70º		90º		125º	
1663	6	0.69	0.04	1.15	0.07	1.49	0.09	1.08	0.10
1668	6	0.73	0.05	1.09	0.07	1.50	0.09	1.18	0.09
1673	6	0.65	0.04	1.16	0.07	1.55	0.13	1.21	0.09
1678	6	0.69	0.04	1.18	0.07	1.50	0.09	1.25	0.09
1683	6	0.65	0.04	1.19	0.08	1.54	0.09	1.26	0.09
1688	6	0.65	0.04	1.18	0.07	1.52	0.09	1.19	0.08

1693	6	0.75	0.05	1.32	0.08	1.64	0.09	1.20	0.09
1698	6	0.87	0.05	1.32	0.08	1.56	0.09	1.13	0.09
1703	6	0.85	0.05	1.37	0.08	1.58	0.09	1.15	0.09
1708	6	0.95	0.06	1.44	0.09	1.61	0.09	1.27	0.10
1713	6	1.04	0.06	1.47	0.09	1.57	0.09	1.44	0.09
1718	6	1.07	0.06	1.55	0.09	1.66	0.10	1.46	0.09
1723	6	1.09	0.06	1.56	0.09	1.79	0.10	1.54	0.10
1728	6	1.18	0.07	1.68	0.10	1.80	0.10	1.72	0.11
1733	6	1.26	0.07	1.83	0.10	1.85	0.11	1.77	0.12
1738	6	1.3	0.07	1.78	0.10	1.94	0.11	1.85	0.12
1743	6	1.29	0.07	1.76	0.10	2.09	0.12	2.03	0.12
1748	6	1.36	0.08	1.86	0.11	2.09	0.12	1.84	0.11
1753	6	1.45	0.08	1.9	0.11	2.14	0.12	1.98	0.12
1758	6	1.55	0.09	1.96	0.11	2.12	0.12	2.01	0.12
1763	6	1.59	0.09	1.98	0.12	2.18	0.12	2.15	0.13
1768	6	1.58	0.09	1.97	0.11	2.18	0.12	2.20	0.13
1773	6	1.65	0.09	2.00	0.11	2.01	0.11	2.48	0.14
1778	6	1.65	0.09	1.92	0.11	2.23	0.12	2.51	0.14
1783	6	1.56	0.09	1.80	0.10	2.17	0.12	2.68	0.15
1785	6	1.62	0.09	1.79	0.10	2.09	0.12	2.73	0.15
1787	6	1.56	0.09	1.70	0.10	2.08	0.11	2.77	0.16
1789	6	1.48	0.08	1.68	0.10	2.23	0.12	2.76	0.16
1791	6	1.44	0.08	1.75	0.10	2.10	0.12	2.74	0.15
1793	6	1.45	0.08	1.59	0.10	2.15	0.12	2.71	0.15
1795	6	1.41	0.08	1.51	0.09	2.02	0.11	2.77	0.16
1797	6	1.38	0.08	1.47	0.09	2.05	0.12	2.74	0.15
1799	6	1.35	0.08	1.41	0.09	2.04	0.12	2.75	0.15
1801	6	1.24	0.08	1.40	0.09	2.04	0.12	2.72	0.15
1803	6	1.09	0.06	1.39	0.08	1.95	0.11	2.84	0.17
1808	6	0.95	0.06	1.24	0.08	1.89	0.11	2.67	0.16
1813	6	0.87	0.06	1.09	0.08	1.94	0.11	2.47	0.14
1818	6	0.76	0.05	1.03	0.07	1.71	0.10	2.37	0.14
1823	6	0.77	0.05	1.06	0.07	1.72	0.10	2.03	0.12
1828	6	0.67	0.05	1.00	0.06	1.64	0.10	1.99	0.13
1834	6	0.57	0.04	1.10	0.08	1.56	0.09	1.88	0.13
1839	6	0.74	0.05	1.17	0.08	1.61	0.13	1.70	0.11
1844	6	0.8	0.06	1.17	0.07	1.38	0.11	1.48	0.10
1849	6	0.84	0.06	1.27	0.08	1.50	0.12	1.37	0.12
1854	6	0.96	0.06	1.27	0.09	1.50	0.12	1.45	0.14
1859	6	1.01	0.06	1.39	0.08	1.51	0.11	1.38	0.13
1864	6	0.98	0.06	1.33	0.08	1.49	0.10	1.35	0.11
1869	6	0.98	0.06	1.36	0.08	1.56	0.12	1.45	0.12
1874	6	1.00	0.06	1.37	0.08	1.72	0.12	1.49	0.13
1879	6	1.02	0.06	1.40	0.09	1.73	0.12	1.61	0.13
1884	6	1.01	0.06	1.34	0.08	1.84	0.13	1.71	0.13
1889	6	1.07	0.07	1.61	0.10	1.91	0.13	1.95	0.12
1894	6	1.20	0.08	1.69	0.10	1.98	0.13	1.88	0.12
1899	6	1.33	0.08	1.88	0.11	1.98	0.13	1.93	0.13
1904	6	1.30	0.08	1.82	0.11	2.18	0.14	1.86	0.13
1909	6	1.39	0.08	1.79	0.11	2.01	0.13	1.79	0.12
1914	6	1.38	0.08	1.62	0.11	1.89	0.12	1.66	0.11

1919	6	1.19	0.07	1.49	0.09	1.78	0.11	1.54	0.12
1924	6	1.37	0.08	1.47	0.09	1.61	0.11	1.42	0.10
1929	6	1.22	0.07	1.32	0.09	1.37	0.14	1.36	0.11
1934	6	1.15	0.07	1.25	0.09	1.37	0.11	1.08	0.09
1939	6	1.17	0.07	1.23	0.09	1.34	0.11	1.00	0.09
1944	6	1.08	0.07	1.13	0.07	1.17	0.09	0.92	0.09
1949	6	1.06	0.07	1.17	0.07	1.15	0.09	0.84	0.07
1954	6	1.15	0.07	1.22	0.08	1.11	0.08	0.67	0.07
1959	6	1.12	0.07	1.12	0.07	1.04	0.07	0.62	0.06
1964	6	1.08	0.06	1.26	0.08	1.11	0.08	0.58	0.08
1969	6	1.13	0.07	1.22	0.08	1.00	0.07	0.50	0.07
1974	6	1.12	0.06	1.13	0.07	0.92	0.07	0.42	0.06
1979	6	1.12	0.06	1.08	0.06	0.90	0.07	0.40	0.05
1984	6	1.08	0.06	1.07	0.07	0.93	0.07	0.34	0.05

Table C5: Differential cross-section values of the $^{24}Mg(d,p_2)\,^{25}Mg$ reaction at 55 º-125 º.

E_{lab} (keV)	δE_{lab} (keV)	$\sigma \pm \delta\sigma$ (mb/sr), **$^{24}Mg(d,p_2)$**							
		55º		70º		90º		125º	
1663	6	1.19	0.08	1.26	0.08	1.35	0.08	1.16	0.11
1668	6	1.15	0.08	1.26	0.08	1.37	0.08	1.17	0.13
1673	6	1.24	0.09	1.15	0.09	1.34	0.08	1.19	0.19
1678	6	1.18	0.07	1.20	0.07	1.20	0.08	1.29	0.12
1683	6	1.21	0.07	1.10	0.08	1.16	0.07	1.26	0.09
1688	6	1.05	0.06	1.04	0.06	1.06	0.07	1.20	0.11
1693	6	1.06	0.07	0.91	0.06	0.98	0.06	1.20	0.13
1698	6	1.01	0.07	0.96	0.07	0.90	0.07	1.10	0.07
1703	6	0.94	0.06	0.79	0.05	0.79	0.06	0.93	0.08
1708	6	0.83	0.05	0.72	0.05	0.64	0.05	0.92	0.07
1713	6	0.84	0.06	0.70	0.05	0.67	0.05	0.91	0.07
1718	6	0.76	0.06	0.69	0.05	0.66	0.06	0.92	0.08
1723	6	0.84	0.05	0.69	0.05	0.65	0.05	1.01	0.07
1728	6	0.89	0.06	0.69	0.05	0.73	0.05	1.03	0.08
1733	6	0.88	0.06	0.75	0.05	0.77	0.06	1.10	0.07
1738	6	0.91	0.06	0.70	0.05	0.90	0.07	1.17	0.08
1743	6	0.84	0.05	0.81	0.05	0.91	0.06	1.25	0.08
1748	6	1.08	0.07	0.85	0.06	0.98	0.06	1.33	0.09
1753	6	1.07	0.06	0.90	0.06	1.10	0.07	1.45	0.10
1758	6	1.03	0.06	0.89	0.06	1.10	0.07	1.40	0.09
1763	6	1.12	0.07	1.00	0.06	1.08	0.07	1.56	0.10
1768	6	1.04	0.06	0.94	0.06	1.08	0.07	1.60	0.09
1773	6	1.09	0.07	0.97	0.06	1.14	0.07	1.52	0.12
1778	6	1.23	0.07	1.07	0.07	1.11	0.07	1.56	0.10
1783	6	1.30	0.08	1.11	0.07	1.20	0.07	1.48	0.10
1785	6	1.37	0.08	1.08	0.07	1.13	0.07	1.50	0.10
1787	6	1.38	0.08	1.07	0.07	1.15	0.07	1.64	0.12
1789	6	1.33	0.08	1.04	0.07	1.15	0.07	1.51	0.11
1791	6	1.44	0.08	1.24	0.08	1.19	0.08	1.50	0.10
1793	6	1.52	0.09	1.17	0.07	1.25	0.08	1.50	0.10

1795	6	1.49	0.09	1.29	0.10	1.26	0.08	1.47	0.09
1797	6	1.49	0.09	1.37	0.08	1.23	0.08	1.57	0.11
1799	6	1.46	0.09	1.24	0.07	1.32	0.08	1.54	0.11
1801	6	1.63	0.10	1.35	0.08	1.38	0.09	1.52	0.10
1803	6	1.72	0.10	1.40	0.09	1.37	0.08	1.50	0.10
1808	6	1.71	0.10	1.40	0.08	1.50	0.09	1.36	0.09
1813	6	1.81	0.10	1.49	0.09	1.58	0.10	1.55	0.10
1818	6	1.85	0.09	1.62	0.10	1.57	0.10	1.60	0.11
1823	6	2.01	0.11	1.65	0.10	1.62	0.10	1.64	0.14
1828	6	2.00	0.11	1.83	0.10	1.76	0.11	1.69	0.12
1834	6	1.94	0.11	1.79	0.10	1.79	0.11	1.66	0.15
1839	6	2.15	0.12	1.80	0.10	1.80	0.11	1.80	0.13
1844	6	2.15	0.12	1.84	0.11	1.84	0.12	1.78	0.12
1849	6	2.13	0.12	1.95	0.11	1.87	0.12	1.94	0.13
1854	6	2.09	0.12	1.92	0.11	1.82	0.12	1.91	0.14
1859	6	2.05	0.11	1.81	0.11	1.86	0.12	1.95	0.16
1864	6	2.07	0.12	1.88	0.11	1.80	0.12	1.91	0.17
1869	6	1.96	0.12	1.76	0.10	1.77	0.11	1.84	0.14
1874	6	1.89	0.11	1.71	0.10	1.68	0.11	1.81	0.15
1879	6	1.83	0.11	1.57	0.09	1.53	0.11	1.62	0.13
1884	6	1.71	0.10	1.43	0.09	1.35	0.09	1.57	0.12
1889	6	1.59	0.10	1.22	0.08	1.23	0.09	1.38	0.10
1894	6	1.58	0.09	1.31	0.08	1.07	0.07	1.18	0.09
1899	6	1.38	0.08	1.15	0.08	0.92	0.07	1.07	0.08
1904	6	1.36	0.10	1.07	0.07	0.95	0.07	1.00	0.09
1909	6	1.33	0.08	1.12	0.08	0.94	0.07	1.08	0.09
1914	6	1.22	0.07	1.02	0.08	0.75	0.06	0.96	0.09
1919	6	1.11	0.07	0.96	0.09	0.76	0.07	0.91	0.10
1924	6	1.22	0.07	1.00	0.07	0.81	0.06	1.04	0.08
1929	6	1.23	0.08	0.83	0.07	0.83	0.07	0.95	0.09
1934	6	1.31	0.08	0.96	0.09	0.90	0.08	1.01	0.09
1939	6	1.32	0.10	1.00	0.07	0.98	0.09	1.09	0.09
1944	6	1.25	0.08	1.05	0.07	1.04	0.09	1.05	0.12
1949	6	1.31	0.08	1.02	0.07	1.06	0.08	1.13	0.11
1954	6	1.45	0.09	1.12	0.07	1.12	0.08	1.11	0.10
1959	6	1.21	0.07	1.07	0.07	1.03	0.07	1.14	0.10
1964	6	1.38	0.08	1.14	0.07	1.16	0.08	1.24	0.09
1969	6	1.35	0.08	1.21	0.07	1.22	0.08	1.17	0.08
1974	6	1.24	0.07	1.17	0.07	1.19	0.08	1.27	0.08
1979	6	1.26	0.07	1.23	0.07	1.18	0.08	1.16	0.09
1984	6	1.35	0.08	1.22	0.07	1.23	0.08	1.12	0.10

Table C6: Differential cross-section values of the $^{24}Mg(d,p_0)\,^{25}Mg$, $^{24}Mg(d,p_1)\,^{25}Mg$ and $^{24}Mg(d,p_2)\,^{25}Mg$ reactions at 140º and 160º.

E_{lab} (keV)	δE_{lab} (keV)	$\sigma \pm \delta\sigma$ (mb/sr), **$^{24}Mg(d,p_0)$**				$\sigma \pm \delta\sigma$ (mb/sr), **$^{24}Mg(d,p_1)$**				$\sigma \pm \delta\sigma$ (mb/sr), **$^{24}Mg(d,p_2)$**			
		140º		160º		140º		160º		140º		160º	
1300	1	0.160	0.015	0.131	0.012	0.188	0.018	0.257	0.024	0.346	0.028	0.363	0.028
1350	1	0.186	0.018	0.162	0.018	0.225	0.020	0.146	0.017	0.303	0.022	0.249	0.020

1400	1	0.155	0.017	0.142	0.021	0.388	0.028	0.46	0.04	0.56	0.04	0.50	0.04
1450	1	0.163	0.016	0.162	0.016	0.45	0.03	0.42	0.03	0.388	0.029	0.370	0.028
1500	2	0.309	0.025	0.270	0.023	0.51	0.04	0.48	0.04	0.70	0.05	0.65	0.04
1550	2	0.189	0.013	-	-	0.71	0.04	0.77	0.05	0.353	0.023	0.302	0.023
1600	2	0.198	0.015	0.154	0.014	1.12	0.06	1.08	0.07	0.66	0.04	0.64	0.04
1625	2	0.199	0.017	0.164	0.021	0.97	0.06	0.69	0.05	0.77	0.05	0.64	0.04
1650	2	0.208	0.015	0.116	0.011	0.53	0.03	0.71	0.05	0.54	0.03	0.51	0.04
1675	2	0.344	0.023	0.300	0.026	-	-	0.61	0.05	1.21	0.07	1.20	0.08
1700	2	0.54	0.04	0.51	0.05	0.94	0.06	0.78	0.08	1.40	0.08	1.84	0.13
1725	2	0.61	0.04	0.61	0.06	1.46	0.09	1.57	0.11	1.09	0.07	1.37	0.11
1750	2	0.64	0.04	0.57	0.04	1.97	0.11	2.19	0.20	1.36	0.08	1.43	0.12
1775	2	0.70	0.05	0.51	0.05	2.49	0.15	2.67	0.16	1.79	0.11	1.73	0.11
1790	2	0.67	0.06	0.58	0.08	3.09	0.20	3.35	0.22	1.91	0.16	2.03	0.16
1800	2	0.77	0.05	0.55	0.04	-	-	3.44	0.20	1.72	0.10	1.80	0.12
1810	2	0.87	0.08	0.56	0.06	3.08	0.23	3.25	0.23	1.69	0.18	1.72	0.14
1825	2	0.94	0.06	0.51	0.04	-	-	2.90	0.17	1.63	0.10	1.52	0.10
1850	2	0.84	0.05	0.48	0.03	-	-	1.39	0.08	-	-	1.74	0.10
1875	2	1.06	0.07	0.95	0.06	-	-	1.36	0.08	1.21	0.08	2.05	0.12
1885	2	1.13	0.10	1.15	0.10	-	-	1.67	0.12	1.67	0.12	1.83	0.15
1900	2	1.18	0.08	1.22	0.08	-	-	1.90	0.12	1.29	0.08	1.48	0.10
1910	2	1.18	0.10	1.32	0.11	1.77	0.15	1.91	0.16	1.05	0.10	1.34	0.11
1925	2	1.23	0.08	1.27	0.08	-	-	1.63	0.11	1.15	0.08	1.47	0.10
1950	2	1.04	0.07	1.04	0.06			1.06	0.07	1.27	0.08	1.48	0.10
1975	2	1.10	0.07	1.14	0.07			0.66	0.05	1.26	0.08	1.33	0.09
2000	2	1.21	0.08	1.23	0.08			0.49	0.04	0.87	0.07	0.95	0.07
2025	2	1.07	0.07	1.02	0.07			0.33	0.03	0.69	0.05	0.72	0.05
2050	2	0.91	0.06	0.58	0.05			0.94	0.07	0.74	0.06	0.81	0.06

Table C7: Differential cross-section values of the $^{24}Mg(d,p_0)\,^{25}Mg$, $^{24}Mg(d,p_1)\,^{25}Mg$ and $^{24}Mg(d,p_2)\,^{25}Mg$ reactions at 150º and 170º.

E_{lab} (keV)	δE_{lab} (keV)	$\sigma \pm \delta\sigma$ (mb/sr), **$^{24}Mg(d,p_0)$**				$\sigma \pm \delta\sigma$ (mb/sr), **$^{24}Mg(d,p_1)$**				$\sigma \pm \delta\sigma$ (mb/sr), **$^{24}Mg(d,p_2)$**			
		150º		170º		150º		170º		150º		170º	
1300	1	0.173	0.015	0.141	0.014	0.211	0.022	0.267	0.021	0.336	0.016	0.300	0.023
1350	1	0.176	0.014	0.146	0.012	0.183	0.018	0.149	0.014	0.307	0.013	0.275	0.023
1400	1	0.146	0.013	0.123	0.013	0.44	0.03	0.50	0.04	0.48	0.03	0.54	0.04
1450	1	0.141	0.012	0.168	0.014	0.411	0.029	0.333	0.024	0.35	0.03	0.388	0.026
1500	2	0.289	0.022	0.265	0.020	0.46	0.04	0.39	0.03	0.69	0.03	0.66	0.05
1550	2	0.125	0.010	0.056	0.007	0.73	0.04	0.73	0.05	0.31	0.05	0.291	0.021
1600	2	0.144	0.011	0.162	0.012	1.07	0.06	1.07	0.07	0.64	0.07	0.63	0.05
1625	2	0.151	0.012	0.130	0.012	0.81	0.05	0.63	0.04	0.68	0.05	0.58	0.04
1650	2	0.157	0.011	0.100	0.009	0.66	0.04	0.38	0.03	0.74	0.04	0.68	0.04
1663	6	0.27	0.04	0.200	0.020	0.71	0.05	0.40	0.03	1.11	0.06	0.99	0.06
1668	6	0.30	0.04	0.300	0.020	0.65	0.05	0.48	0.03	1.12	0.06	1.22	0.07
1673	6	0.33	0.04	0.240	0.020	0.69	0.05	0.45	0.03	1.19	0.07	1.30	0.08
1675	2	0.322	0.022	0.266	0.021	0.78	0.05	0.50	0.03	1.15	0.05	1.14	0.08
1678	6	0.39	0.04	0.36	0.03	0.70	0.06	0.55	0.04	1.38	0.08	1.43	0.08
1683	6	0.44	0.04	0.36	0.03	0.83	0.05	0.58	0.04	1.45	0.08	1.57	0.09
1688	6	0.46	0.04	0.45	0.03	0.81	0.06	0.63	0.06	1.55	0.09	1.69	0.10

1693	6	0.44	0.03	0.45	0.03	0.76	0.06	0.69	0.06	1.54	0.09	1.71	0.10
1698	6	0.51	0.03	0.51	0.04	0.93	0.06	0.72	0.06	1.50	0.08	1.74	0.10
1700	2	0.52	0.04	0.5	0.04	0.81	0.06	0.72	0.05	1.57	0.05	1.77	0.11
1703	6	0.54	0.03	0.49	0.03	1.03	0.06	0.83	0.05	1.52	0.08	1.66	0.09
1708	6	0.59	0.04	0.58	0.04	1.15	0.07	0.99	0.07	1.44	0.08	1.64	0.09
1713	6	0.5	0.03	0.58	0.04	1.26	0.07	1.21	0.07	1.34	0.08	1.49	0.09
1718	6	0.58	0.04	0.55	0.04	1.33	0.08	1.34	0.08	1.34	0.08	1.49	0.09
1723	6	0.63	0.05	0.56	0.04	1.47	0.08	1.54	0.09	1.27	0.07	1.42	0.08
1725	2	0.56	0.04	0.67	0.06	1.43	0.09	1.54	0.11	1.35	0.09	1.49	0.11
1728	6	0.56	0.04	0.55	0.04	1.69	0.09	1.68	0.10	1.30	0.07	1.41	0.08
1733	6	0.57	0.04	0.54	0.04	1.78	0.10	1.87	0.11	1.34	0.08	1.41	0.08
1738	6	0.6	0.04	0.55	0.04	1.9	0.10	1.90	0.11	1.36	0.08	1.41	0.08
1743	6	0.6	0.04	0.52	0.04	2.02	0.11	2.05	0.12	1.42	0.08	1.38	0.09
1748	6	0.59	0.04	0.48	0.03	2.18	0.12	2.10	0.12	1.49	0.09	1.41	0.08
1750	2	0.56	0.04	0.49	0.03	2.08	0.12	2.16	0.13	1.37	0.12	1.46	0.09
1753	6	0.51	0.04	0.54	0.04	2.22	0.12	2.23	0.13	1.55	0.09	1.52	0.09
1758	6	0.59	0.04	0.51	0.03	2.19	0.12	2.32	0.13	1.64	0.09	1.57	0.09
1763	6	0.6	0.05	0.51	0.03	2.39	0.13	2.41	0.13	1.74	0.09	1.73	0.10
1768	6	0.65	0.04	0.46	0.03	2.53	0.13	2.59	0.14	1.78	0.10	1.64	0.10
1773	6	0.53	0.04	0.48	0.03	2.78	0.15	2.64	0.14	1.84	0.10	1.73	0.10
1775	2	0.6	0.04	0.52	0.04	2.54	0.15	2.54	0.17	1.78	0.15	1.66	0.18
1778	6	0.52	0.05	0.46	0.03	2.94	0.16	2.99	0.16	1.68	0.09	1.83	0.10
1783	6	0.63	0.05	0.51	0.04	3.04	0.16	3.03	0.16	1.73	0.09	1.75	0.10
1785	6	0.6	0.04	0.41	0.03	3.02	0.16	3.08	0.17	1.60	0.09	1.75	0.10
1787	6	0.57	0.04	0.46	0.03	3.09	0.16	3.04	0.17	1.75	0.10	1.72	0.10
1789	6	0.58	0.04	0.45	0.03	3.25	0.17	3.13	0.17	1.73	0.10	1.65	0.09
1790	2	0.6	0.06	0.46	0.05	2.98	0.19	3.40	0.22	1.67	0.21	1.70	0.13
1791	6	0.59	0.04	0.46	0.03	3.14	0.17	3.23	0.17	1.69	0.09	1.65	0.10
1793	6	0.58	0.04	0.48	0.03	3.25	0.17	3.22	0.17	1.80	0.10	1.74	0.10
1795	6	0.65	0.04	0.5	0.03	3.32	0.17	3.35	0.18	1.67	0.09	1.59	0.09
1797	6	0.66	0.04	0.48	0.03	3.32	0.17	3.46	0.19	1.73	0.09	1.68	0.09
1799	6	0.61	0.04	0.46	0.03	3.28	0.17	3.35	0.18	1.66	0.09	1.72	0.10
1800	2	0.62	0.04	0.425	0.028	3.36	0.18	3.45	0.20	1.77	0.19	1.75	0.11
1801	6	0.62	0.04	0.43	0.03	3.16	0.17	3.36	0.18	1.71	0.09	1.68	0.09
1803	6	0.6	0.04	0.54	0.04	3.15	0.17	3.40	0.18	1.54	0.09	1.62	0.09
1808	6	0.68	0.04	0.52	0.04	3.17	0.17	3.29	0.17	1.54	0.09	1.49	0.08
1810	2	0.73	0.08	0.59	0.07	3.29	0.23	3.36	0.22	1.69	0.26	1.66	0.13
1813	6	0.67	0.04	0.48	0.03	3.01	0.16	3.01	0.16	1.58	0.09	1.47	0.08
1818	6	0.73	0.04	0.40	0.03	2.80	0.15	2.86	0.15	1.65	0.09	1.47	0.08
1818	6	0.69	0.04	0.41	0.03	2.76	0.15	2.88	0.16	1.53	0.08	1.46	0.08
1823	6	0.63	0.04	0.41	0.03	2.55	0.14	2.62	0.14	1.61	0.09	1.47	0.08
1825	2	0.71	0.05	0.42	0.04	2.73	0.15	2.81	0.18	1.57	0.16	1.48	0.09
1828	6	0.67	0.04	0.38	0.03	2.20	0.12	2.31	0.13	1.69	0.09	1.55	0.09
1834	6	0.67	0.04	0.36	0.03	2.03	0.11	1.98	0.11	1.69	0.09	1.51	0.09
1839	6	0.69	0.04	0.44	0.03	1.61	0.09	1.45	0.1	1.71	0.09	1.52	0.09
1844	6	0.6	0.04	0.40	0.04	1.61	0.09	1.39	0.11	1.81	0.10	1.57	0.09
1849	6	0.62	0.04	0.49	0.04	1.35	0.08	1.17	0.1	1.71	0.10	1.71	0.12
1850	2	0.63	0.04	0.427	0.028	1.38	0.08	1.30	0.08	1.74	0.08	1.68	0.10
1854	6	0.75	0.05	0.52	0.04	1.24	0.08	1.03	0.08	1.89	0.10	1.77	0.10
1859	6	0.72	0.05	0.54	0.04	1.30	0.08	1.06	0.08	1.97	0.11	1.93	0.11
1864	6	0.85	0.06	0.68	0.04	1.34	0.08	1.03	0.06	1.87	0.10	1.89	0.11

1869	6	0.88	0.07	0.81	0.05	1.40	0.09	1.14	0.11	2.03	0.11	1.92	0.11
1874	6	0.94	0.06	0.88	0.06	1.45	0.10	1.30	0.10	1.92	0.11	1.89	0.11
1875	2	0.95	0.06	0.84	0.05	1.39	0.08	1.30	0.08	1.33	0.09	1.99	0.12
1879	6	1.03	0.06	1.02	0.06	1.53	0.10	1.37	0.11	1.90	0.11	1.86	0.11
1884	6	1.06	0.06	1.07	0.07	1.70	0.10	1.50	0.12	1.76	0.10	1.91	0.11
1885	2	0.92	0.09	1.18	0.09	1.52	0.11	1.61	0.12	1.82	0.12	1.91	0.14
1889	6	1.12	0.07	1.11	0.07	1.85	0.11	1.57	0.12	1.49	0.08	1.54	0.09
1894	6	1.17	0.07	1.16	0.07	1.87	0.10	1.70	0.10	1.53	0.09	1.52	0.09
1899	6	1.15	0.07	1.23	0.07	1.81	0.11	1.78	0.13	1.29	0.07	1.43	0.08
1900	2	1.13	0.07	1.15	0.08	1.83	0.12	1.90	0.12	1.32	0.11	1.53	0.10
1904	6	1.21	0.07	1.19	0.07	1.83	0.11	1.65	0.09	1.21	0.07	1.33	0.08
1909	6	1.24	0.07	1.22	0.07	1.85	0.11	1.65	0.09	1.40	0.08	1.65	0.09
1910	2	1.15	0.10	1.30	0.09	1.82	0.15	1.95	0.14	1.26	0.14	1.51	0.12
1914	6	1.21	0.07	1.25	0.07	1.71	0.10	1.66	0.10	1.31	0.07	1.44	0.09
1919	6	1.25	0.08	1.27	0.08	1.64	0.10	1.63	0.09	1.25	0.07	1.46	0.10
1924	6	1.26	0.07	1.41	0.08	1.44	0.09	1.42	0.08	1.26	0.07	1.43	0.10
1925	2	1.29	0.08	1.43	0.09	1.55	0.10	1.51	0.09	1.30	0.09	1.48	0.09
1929	6	1.20	0.07	1.24	0.07	1.41	0.08	1.32	0.10	1.39	0.08	1.45	0.09
1934	6	1.13	0.07	1.18	0.07	1.15	0.07	1.22	0.07	1.38	0.08	1.43	0.08
1939	6	1.15	0.07	1.24	0.07	1.09	0.06	1.05	0.09	1.34	0.08	1.48	0.09
1944	6	1.15	0.07	1.07	0.07	1.06	0.06	1.08	0.09	1.29	0.07	1.42	0.08
1949	6	1.12	0.07	0.99	0.06	0.88	0.06	0.92	0.08	1.36	0.08	1.40	0.08
1950	2	1.03	0.06	1.05	0.07	0.93	0.06	1.02	0.07	1.36	0.06	1.47	0.09
1954	6	1.08	0.06	0.95	0.06	0.84	0.06	0.78	0.10	1.33	0.08	1.48	0.09
1959	6	1.08	0.06	0.99	0.06	0.69	0.04	0.78	0.08	1.34	0.08	1.39	0.08
1964	6	1.08	0.06	0.90	0.05	0.69	0.05	0.56	0.06	1.30	0.07	1.19	0.07
1969	6	1.13	0.06	0.98	0.06	0.60	0.05	0.56	0.05	1.24	0.07	1.16	0.07
1974	6	1.13	0.07	1.14	0.07	0.55	0.03	0.65	0.04	1.19	0.07	1.27	0.07
1975	2	1.05	0.07	1.07	0.07	0.58	0.05	0.77	0.05	1.27	0.04	1.25	0.09
1979	6	1.26	0.07	1.16	0.07	0.52	0.05	0.49	0.05	1.11	0.06	1.15	0.07
1984	6	1.13	0.06	1.14	0.06	0.43	0.04	0.50	0.05	1.08	0.07	1.06	0.06
2000	2	1.21	0.08	1.29	0.09	0.35	0.04	0.48	0.05	0.85	0.03	0.99	0.07
2025	2	0.98	0.06	1.00	0.07	0.32	0.04	0.176	0.022	0.60	0.03	0.73	0.06
2050	2	0.69	0.05	0.5	0.04	1.03	0.07	0.73	0.06	0.72	0.08	0.89	0.06

REFERENCES

[1] P. E. Hodgson, E. Gadioli and E. Gadioli Erba, “Introductory Nuclear Physics”, Clarendon Press, Oxford, 1997.

[2] Y. Wang and M. Nastasi, “Handbook of Modern Ion Beam Materials Analysis”, Materials Research Society, 2009.

[3] K. S. Krane, “Introductory Nuclear Physics”, John Wiley & Sons, 1988.

[4] W.-K. Chu, J. W. Mayer and M.-A. Nicolet, “Backscattering Spectroscopy”, Chapters 2 and 3, Academic Press, 1978.

[5] J.F. Ziegler, J.P. Biersack, M.D. Ziegler, The Stopping and Range of Ions in Matter, Lulu Press Co., NC 27560, USA, 2013.

[6] J.F. Ziegler, J.P. Biersack, and U. Littmark. The Stopping and Ranges of Ions in Matter. Pergamon Press, New York, 1985.

[7] J.F. Ziegler and J.M. Manoyan. Nucl. Instr. Meth. B 35 (1988) 215.

[8] M. Mayer, SIMNRA User's Guide, Report IPP 9/113, Max-Planck-Institut für Plasmaphysik, Garching, Germany, 1997

[9] O. Schmelmer, G. Dollinger, C.M. Frey, A. Bergmaier, and S. Karsch. Nucl. Instr. Meth. B 145 (1998) 261.

[10] F. Besenbacher, J.U. Andersen, E. Bonderup, Nucl. Instr. Meth. 168 (1980) 1.

[11] Q. Yang, D.J. O’Connor, and Z. Wang. Nucl. Instr. Meth. B 61 (1991) 149.

[12] M.A. Kumakhov and F.F. Komarov. Energy Loss and Ion Ranges in Solids. Gordon and Breach Science Publishers, New York, London, Paris, 1981.

[13] J.R. Bird and J.S. Williams, Eds. Ion Beams for Materials Analysis. Academic Press, Sydney, New York, Tokyo, 1989.

[14] J. Tirira, Y. Serruys, and P. Trocellier. Forward Recoil Spectrometry. Plenum Press, New York, London, 1996.

[15] P.V. Vavilov. Soviet Physics J.E.T.P. 5 (1957) 749.

[16] N. Bohr. Mat. Fys. Medd. Dan. Vid. Selsk. 18 (8), 24 (19), (1948).

[17] J.W. Mayer and E. Rimini. Ion Handbook for Material Analysis. Academic Press, New York, San Francisco, London, 1977.

[18] M.G. Payne. Phys. Rev. 185, 2 (1969) 611.

[19] C. Tschalär. Nucl. Instr. Meth. 61 (141), 64 (237), (1968).

[20] W.K. Chu. Phys. Rev. 13 (1976) 2057.

[21] J. Lindhard, M. Scharff, Mat. Fys. Medd. Dan. Vid. Selsk. 27 (1953) 15.

[22] E. Bonderup, P. Hvelplund, Phys. Rev. A 4 (1971) 562.

[23] https://www-nds.iaea.org/exfor/ibandl.htm

[24] https://www-nds.iaea.org/exfor/exfor.htm

[25] SigmaCalc: http://sigmacalc.iate.obninsk.ru, www-nds.iaea.org/exfor/ibandl.htm

[26] A. Caciolli, M. Chiari, A. Climent-Font, M.T. Fernandez-Jimenez, G. García-López b, F. Luca-relli, S. Nava, A. Zucchiatti, Nucl. Instr. Meth. B 249 (2006) 95.

[27] U. Fasoli, D. Toniolo, G. Zago, Nuovo Cimento 34 (1964) 542.

[28] P.R. Malmberg, Phys.Rev. 101 (1956) 114.

[29] N. Sarma, K.S. Jayaraman, C.K. Kumar, Nucl. Phys. 44 (1963) 205.

[30] D. Dieumegard, B. Maurel, G. Amsel, Nucl. Instr. Meth. 168 (1980), 93.

[31] H. Orihara, M. Baba, M. Akiyama, S. Iwasaki, T. Nakagawa, H. Ueno, M. Watanabe, Journal of the Physical Society of Japan 29 (3), (1970) 533.

[32] P.D. Forsyth et al., Nucl. Phys. 67, 517-528 (1965).

[33] I.I. Bondouk, S. Saad, Atomkernenergie 29 (4), (1977) 270.

[34] P.Cuzzocrea, A. De Rosa, G. Inglima, E. Perillo, E. Rosato, M. Sandoli, G. Spadaccini, Nuovo Cimento 2, 28, (1980) 515.

[35] G. Dearnaley, Philos. Mag. (1956) 821.

[36] S.Ouichaoui, H. Beaumevieille, N. Bendjaballah, C. Chami, A. Dauchy, B. Chambon, D. Drain, C. Pastor, Nuovo Cimento A 86 (1985) 170.
S. Ouichaoui, H. Beaumevieille, N.Bendjaballah, A. Genoux-Lubain, Nuovo Cimento 94 (1986) 133.

[37] I. Bogdanovic, S. Fazinic, M. Jaksic, T. Tadic, O. Valkovic, V. Valkovic, Nucl. Instr. Meth. B 79 (1993) 524.

[38] H.M. Kuan, G.L. Latshaw, W. J. O'Connell, D.W. Heikkinen, E.G. Adelberger, A.V. Nero, S.S Hanna, Nucl. Phys. A193 (1972) 497.

[39] T.S. Webb, F.B. Hagedorn, W.A. Fowler, C.C. Lauritsen, Phys. Rev. 99 (1955) 138.

[40] I.Golicheff, M. Loeuillet, Ch. Engelmann, Journal of Radioanalytical Chemistry 22 (1974) 113.

[41] W.A.Ranken, T.W. Bonner, J.H. McCrary, Phys. Rev.109 (1958) 1646.

[42] D.M. Stanojevic, S.D. Cirilov, M.M. Ninković, Nucl. Phys. 73 (1965) 657.

[43] A.Z. El-Behay, M.A. Farouk, V.J. Gontchar, V.A. Loutsik, M.H. Nassef, I.I. Zaloubovsky,

Nucl. Phys. 56 (1964) 224.

[44] A.Z. El-Behay, M.A. Farouk, M.H. Nassef, I.I. Zaloubovsky, Nucl. Phys. 61 (1965) 282.

[45] L. Mesko, B. Schlenk, G. Somogyi, A. Valek, Nucl. Phys. A 130 (1969) 449.

[46] J.M. Knox, J.F. Harmon, Nucl. Instrum. Meth. B 44 (1989) 41.

[47] A.P. Jesus, B. Braizinha, J. Cruz, J.P. Ribeiro, Nucl. Instrum. Meth. B 174 (2001) 229.

[48] R. Caracciolo et al., Lettere al Nuovo Cimento 11 (1974) 33.

[49] Nagamatsu, N. Nakagawa, T. Muranaka, Y. Zenitani, and J. Akimitsu, Nature 410 (2001) 63.

[50] A. F. Gurbich, C. Jeynes, *Nucl. Instr. And Meth.* **B265** (2007)

[51] H. M. Omar, I. I. Zaloubovsky, M. H. S. Bakr, R. Zaghloul, and V. J. Gontchar, *Nucl. Phys.* **56** (1964).

[52] A. Gallmann, P. Wagner, P.E. Hodgson, Nuclear Physics 88 (1966) 675.

[53] S.M. Lee, Y. Hiratate, K. Miura, S. Kato, S. Morita, Nuclear Physics A 122 (1968) 97.

[54] A. Simon, C. Jeynes, R.P. Webb, R. Finnis, Z. Tabatabian, P.J. Sellin, M.B.H. Breese, D.F. Fellows, R. van den Broek, R.M. Gwilliam, Nucl. Instrum. Meth. B 219 (2004) 405.

[55] J.W. Mous, A. Gottdang, R. van den Broek, R.G. Haitsma, Nucl. Instrum. Meth. B 99 (1995) 697.

[56] B. Beckhoff, B. Kanngiesser, N. Langhoff, R. Wedell, H. Wolff (Eds.), Handbook of Practical X-Ray Fluorescence Analysis, (Eds.), Springer (2006)

[57] https://www-nds.iaea.org/public/libraries/larelkin/

[58] http://personal.ph.surrey.ac.uk/~phs1wc/kinematics/

[59] https://www.ikp.uni-koeln.de/misc/doc/Tv_user-manual/archive/Tv_user-manual.pdf

[60] C. Chronidou, K. Spyrou, S. Harissopulos, S. Kossionides, T. Paradellis, Eur. Phys. J. A 6 (1999) 303.

[61] J.B. Marion, Accelerator calibration energies, Rev. Mod. Phys. 38 (1966) 660.

[62] P. Rao, S. Kumar, S. Vikramkumar, V.S. Raju, Nucl. Instr. Meth. B 269 (2011) 2557; P.M. Endt, Nucl. Phys. A 633 (1998) 1.

[63] V. Paneta, J.L. Colaux, A.F. Gurbich, C. Jeynes, M. Kokkoris, Nucl. Instr. Meth. B 328 (2014) 1.

[64] J. Räisänen, P.O.Tikkanen, Nucl. Instr. Meth. A 723 (2013) 5.

[65] C. Rolfs, W.S. Rodney, Cauldrons in the Cosmos, The University of Chicago Press, (1988).

[66] A.G. Karydas, personal communication

[67] INDC(NDS)-0634, Accuracy of Experimental and Theoretical Nuclear Cross-Section Data for Ion Beam Analysis and Benchmarking, Summary Report of the Consultants' Meeting, 2013.

[68] E.V. Gai, A.F. Gurbich, Evaluated $^{12}C(^{4}He,^{4}He)^{12}C$ cross-section and its uncertainty, Nucl. Instr. Meth. B 296 (2013) 87.

[69] R.B. Firestone, V.S. Shirley, C.M. Baglin, S.Y. Frank Chu, J. Zipkin, Table of Isotopes, eighth ed., vol. 1, John Wiley & Sons, Inc., New Jersey, (1996).

[70] M. Mayer, *SIMNRA, a Simulation Program for the Analysis of NRA, RBS and ERDA*, Proceedings of the 15th International Conference on the Application of Accelerators in Research and Industry, J. L. Duggan and I.L. Morgan (eds.), American Institute of Physics Conference Proceedings 475 (1999) 541.

[71] V. Paneta, A. Kafkarkou, M. Kokkoris, A. Lagoyannis, Nucl. Instr. Meth B 288 (2012) 53.

[72] N. Patronis, X. Aslanoglou, M. Axiotis, A. Georgiadou, M. Kokkoris, A. Lagoyannis, P. Misaelides, V. Paneta, Nucl. Instr. and Meth. B 337 (2014) 97.

[73] V. Paneta, X. Aslanoglou, M. Axiotis, P. Gastis, M. Kokkoris, A. Lagoyannis, P. Misaelides, N. Patronis, R. Vlastou, Nucl. Instr. and Meth. B 319 (2014) 34.

[74] K.A. Chipps et al., Phys. Rev. C 86 (2012) 014329.

[75] P.M. Endt, Nucl. Phys. A633, (1998) 1.
P.M. Endt, Nucl. Phys. A521, (1990) 1.
P.M. Endt, Nucl. Phys. A529, (1991) 763.
P.M. Endt, Nucl. Phys. A564, (1993) 609.

[76] H.M. Omar , V.Y. Gontchar, M.H.S. Bakra and M.A. Ali, Annalen der Physik 7 (26) 1 (1971), 8.

[77] D. Abriola, A.F. Gurbich, M. Kokkoris, Nucl. Instr. Meth. B301 (2013) 41.

[78] A.F. Gurbich, Evaluated differential cross-sections for IBA, Nucl. Instr. Meth. B 268 (2010) 1703.

[79] D. Abriola, A.F. Gurbich, M. Kokkoris, A. Lagoyannis, V. Paneta, Nucl. Instr. Meth. B 269 (18) (2011) 2011.

[80] I.B. Radovic, Z. Siketic, M. Jakšic, A.F. Gurbich, J. Appl. Phys. 104 (7) (2008). art. no. 074905.

[81] A.F. Gurbich, C. Jeynes, Nucl. Instr. Meth. B 265 (2) (2007) 447.

[82] N.P. Barradas, C. Jeynes, Advanced physics and algorithms in the IBA DataFurnace, Nucl. Instrum. Meth. B 266 (8) (2008) 1338.

[83] S.L. Molodtsov, A.F. Gurbich, Simulation of the pulse pile-up effect on the pulse-height spectrum, Nucl. Instrum. Meth. B 267 (2009) 3484.

[84] S.L. Molodtsov, A.F. Gurbich, C. Jeynes, Accurate ion beam analysis in the presence of

surface roughness, J. Phys. D: Appl. Phys. 41 (2008) 205303.

[85] CN/ASD Group. MINUIT, Users Guide, nProgram Library D506. CERN, 1993.

[86] H.H. Andersen, J.F. Ziegler, Hydrogen – Stopping Powers and Ranges in All Elements, Pergamon Press, New York, 1977.

[87] Pakou, A., Alamanos, N., Clarke, N. M., Davis, N. J., Doukelis, G., Kalyva, G., Kokkoris, M., Lagoyannis, A., Mertzimekis, T.J., Musumarra, A., Nicolis, N. G., Papachristodoulou, C., Patronis, N., Perdikakis, G., Pierroutsakou, D., Roubos, D., Rusek, K., Spyrou, A., Zarkadas, Ch. The 6Li exclusive breakup on 28Si at 13 MeV. Phys. Lett. B 633 (6), (2006) 691.

[88] Dr. A.F. Gurbich, personal communication.

[89] A. Caciolli, G. Calzolai, M. Chiari, A. Climent-Font, G. Garcia, F. Lucarelli, S. Nava, Proton elastic scattering and proton induced c-ray emission cross-sections on Na from 2 to 5 MeV, Nucl. Instrum. Meth. B 266 (8) (2008) 1392.

[90] K.V. Karadzhev et al., YadernayaFizika 7 (1968) 242. Available from: http://www-nds.iaea.org/exfor/ibandl.htm.

[91] D.F. Fang, E.G. Bilpuch, C.R. Westerfeldt, Proton resonances in ^{32}S from Ex = 9.83–12.74 MeV, Phys. Rev. C 37 (1988) 28.

[92] M. Cenja, M. Duma, C. Hategan, M. Tanase, The (p, n) threshold anomaly in proton elastic scattering on 23Na, 27Al, 31P, 35Cl and 34S, Nucl. Phys. A 307 (1978) 65.

[93] A.M. Lane, R.G. Thomas, Rev. Mod. Phys. 30 (1958) 257.

[94] E. Vogt notes, R-Matrix Theory, JINA, Notre Dame 2004.

[95] E. Vogt, Resonance reactions, Nuclear Reactions, Vol.1, P.M. Endt and M. Demeur, North-Holland Publ. Co. (1959).

[96] C.A. Bertulani, P. Danielewicz, Introduction to Nuclear Reactions, IoP, 2004.

[97] E. Vogt, Rev. Mod. Phys. 34 (1962) 723.

[98] R.E Azuma et al., Phys. Rev. C 81 (2010) 045805.

[99] F.C. Barker, T. Kajino, Aust. J. Phys. 44 (1991) 369.

[100] AZURE user manual available online at http://azure.nd.edu/.

[101] E.C. Simpson, Master thesis, R-matrix Analysis of CNO Cycle Reactions, 2006.

[102] D.R. Tilley et al. Nucl. Phys. A 636 (1998) 249.

[103] F. Ajzenberg-Selove, Nucl. Phys. A 475 (1987) 1.

[104] http://www.nndc.bnl.gov/

[105] C.H. Johnson, Phys. Rev. C 7 (2) (1973) 561.

[106] P.D. Kunz, A DWBA Reaction Code DWUCK4, University of Colorado, Boulder (1987)

http://spot.colorado.edu/~kunz/DWBA.html.

[107] A. Gurbich, Nucl. Instr. Meth. B 266 (2008) 1193.

[108] K. Kilian, G. Clausnitzer, W. Dürr, D. Fick, R. Fleischmann, H.M. Hofmann, Jour. Nuclear Physics A 126 (1969) 529.

[109] R. Gleyvod, N.P. Heydenburg, I.M. Naqib, Jour. Nuclear Physics 63 (1965) 650.